Doctoral Dissertation

博士論文

Design, Growth, and Characterization of InGaAs/GaAsP Superlattice for High Efficiency Ge-based Multi-junction Solar Cells

高効率 Ge ベース多接合太陽電池に向けた
InGaAs/GaAsP 超格子の設計・評価および
結晶成長に関する研究

Hiromasa Fujii

藤井宏昌

Department of Electrical Engineering and Information Systems,

School of Engineering, The University of Tokyo

Abstract

Terrestrial application of III-V compounds multi-junction solar cells under concentrated sunlight is a promising concept for realizing high-efficiency, low-cost solar photovoltaic power generation. The most widely used lattice-matched triple-junction structure, InGaP (1.85 eV)/(In)GaAs (1.42 eV)/Ge (0.67 eV), has a limitation in performance due to the current-mismatch with the wide bandgap of the middle cell, and further enhancement in cell efficiency is expected by lowering it to approximately 1.2 eV. Toward this target, this research aims at development of InGaAs/GaAsP superlattice (SL), in which narrow-gap InGaAs light absorbing layers with a large lattice constant and GaAsP layers with a small lattice constant are alternately grown to compensate the strains.

The major challenges in InGaAs/GaAsP SL solar cells exist both in design and growth. The challenge for the structural design is the trade-off between light absorption and carrier collection. In other words, incorporation of more number of wells for sufficient light absorption makes the carrier transport through the SL more difficult and inefficient. A challenge for crystal growth is partial lattice relaxation that is likely to occur during formation of the hetero-interfaces between the oppositely strained layers. Moreover, the growth of SLs on vicinal substrates, which are necessary for Ge-based application, tends to be unstable due to formation of step bunching and resultant severe layer undulation.

In this study, carrier collection efficiency (CCE) was defined as a parameter to evaluate the carrier transport in solar cells. The CCE is defined as the fraction of carriers photo-generated in the active p-n junction area of a cell, and can be calculated by normalizing the illumination-induced current enhancement to its saturation value at reverse bias. By combining wavelength- and bias-dependent CCE analyses, influence of electric field distribution in the i-region has been examined and carrier transport problems with typical SL design have been clarified.

In order to overcome the challenges in structural design and crystal growth, stepped tunnel SL (STSL) was proposed as a design principle for higher SL cell performance. Its fundamental strategies are; 1) InGaAs wells should be thinner and deeper for a given bandgap for efficient light absorption and for lower compressive strain accumulation, 2) Insertion of few-nm-thick GaAs interlayers is effective for band narrowing without additional compressive strain, and for suppressing crystal degradation, and 3) GaAsP barriers should be thinner than 3 nm to facilitate tunneling transport, and their phosphorus content should be minimized while avoiding detrimental lattice relaxation. The effectiveness of the proposed design was experimentally demonstrated with structural optimization.

Aiming at implementation of STSL on Ge substrates, MOVPE technique for SLs on vicinal substrates has been established. Low temperature growth is necessary for stable growth of SLs on vicinal substrates with control of step bunching formation, but it is accompanied with problems such as high defect densities and high impurity levels. Substitution of TMGa with TEGa as the gallium source significantly improved the crystal quality of the low-temperature grown SL, and also greatly suppressed the carbon incorporation. Using TEGa, the growth temperature and layer undulation of the SL was further optimized with respect to photovoltaic performance.

Consequently, implementation of a 100-period $In_{0.30}Ga_{0.70}As$ (3.4 nm)/GaAs (2.7 nm)/$GaAs_{0.60}P_{0.40}$ (2.5 nm)/GaAs (2.7 nm) STSL with a bandgap of 1.21 eV into an N-on-P GaAs solar cell on a 6°-off substrate achieved 1.11 times higher efficiency with 36% current enhancement as a middle cell performance.

Contents

1   Introduction

1.1 Solar photovoltaics: a potential energy source in the future

1.1.1 Renewable electricity for sustainable energy supply

Sustainable energy supply-demand has been a focus of recent international attention from the viewpoint of energy security. Approximately 90% of the primary energy is supplied by fossil fuels such as oil, coal, and natural gas at present, and their usage have been rapidly increasing especially along with economic development in Asia [1]. Energy supply-demand structure mostly relying on fossil energy, however, has various risks in terms of sustainability. First, fossil fuels are unable to be used for eternity due to their limited resources, as are indicated by the reserve-production ratios (R/P) of 53 for oil, 55 for natural gas, and 113 for coals [2]. It is true that the proved reserve amounts have been continuously increasing year by year, and sufficient supply should be possible in the medium term, but the uncertainty for the future production and supply cannot be eliminated.

Second problem is the uneven distribution of petroleum. Natural gases and coals are distributed all over the world with large amount existing in regions where the geopolitical statuses are relatively stable. In contrast, approximately half of the oil resource exists in the Middle East where conflicts among countries take place frequently, and thus import of oil in the future is always accompanied by geopolitical risks [2]. The shale gas revolution, which happened in the US, has drastically opened the possibility of oil and gas productions that had been difficult previously, but its technical development and deployment are the next concern.

Thirdly, not a few developed countries including Japan, rely mostly on the import for the supply of oil and natural gases due to their poor annual production, though they are much dependent on fossil fuels for the primary energy supply. In case of Japan, for example, nearly 100% of oil has been supplied from abroad, and the dependence on the import from OPEC has remained 80-90% for decades [3]. Although sufficient natural gas and coals had been produced domestically in the past, the fraction of import has been rapidly increasing since the 70's, and reached nearly 100% at present [3].

These backgrounds suggest that achieving sustainable energy supply-demand, especially in nations that are poor in fossil resources, requires the dependence on fossil energy to be lowered. One of the realistic approaches is to substitute the secondary energy of heat or fuels, for which heating oil or gasoline have been used, with "electricity" by spreading the use of electric heaters and electric

vehicles etc., and then to supply the demanded power by nuclear electricity or renewable electricity such as solar, wind, and biomass. Needless to say, it is impossible to mention what is the universally-ideal energy system for all the regions in the world since the amount of resources, political situation, and the climatic and geographic characteristics differ from country to country. Nevertheless, the fraction of electricity in the energy consumption is fairly high in advanced countries that have developed urban area in general, and substituting fossil-fuel power plants with other types of power generation is a universal challenge.

Fig. 1-1 shows historical electricity generation in OECD countries [4]. Over the past decade, fossil fuel power generation has been occupying 60% in average. Despite the future decrease of the population in advanced countries and the expectation for more improvement in energy-saving technologies, the expansion of economies in the emergent nations are expected to be continuously accelerating, making the substitution of fossil fuel power generation already an internationally urgent theme. Among various types of electricity generations, nuclear power is advantageous with respect to the stable operation and large capacity, but it has been used as base power source avoiding load-follow operation in many countries. Therefore, its generation output is not supposed to be actively adjusted to the demand change within a day in principle. Moreover, the R/P ratio of uranium is only 92 at present [5]. Sustainable use of nuclear power generation, therefore, requires (1) establishment of fast breeding reactors (FBR) technologies and (2) disposal of high-level radioactive wastes, but these issues imposes us of not only engineering challenges but also social receptivity and international control.

On the other hand, renewable energies except for conventional hydro power generation, e.g. solar, wind, geothermal, and biomasses, occupy less than 10% of electricity supply in OECD, and their further deployment is desired for the future. (Note that the Fig. 1-1 shows the averaged plots, and the detail of supply structure quite differs among the countries). The energy potential and the power operation stabilities strongly depend on the climatic and geographic characteristics, and thus the types of energy sources should be appropriately selected and adopted by each region. Among various renewable energies, solar energy has large potential in many countries, and has been intensely paid attention to as a driving force of deployment of renewable energy all over the world. Medium scale renewable power generators such as large windmills, dams, or geothermal power plants sometimes have serious influences on the surrounding environments, and hence may require throughout environmental assessments and negotiation with local communities. In contrast, solar power generation, which just requires vacant area to place solar panels, generally does not have serious impacts on the surrounding environments, and small scale application is also available for individual usage. Therefore, solar photovoltaics is a very promising energy source if the current challenges preventing its spread are solved.
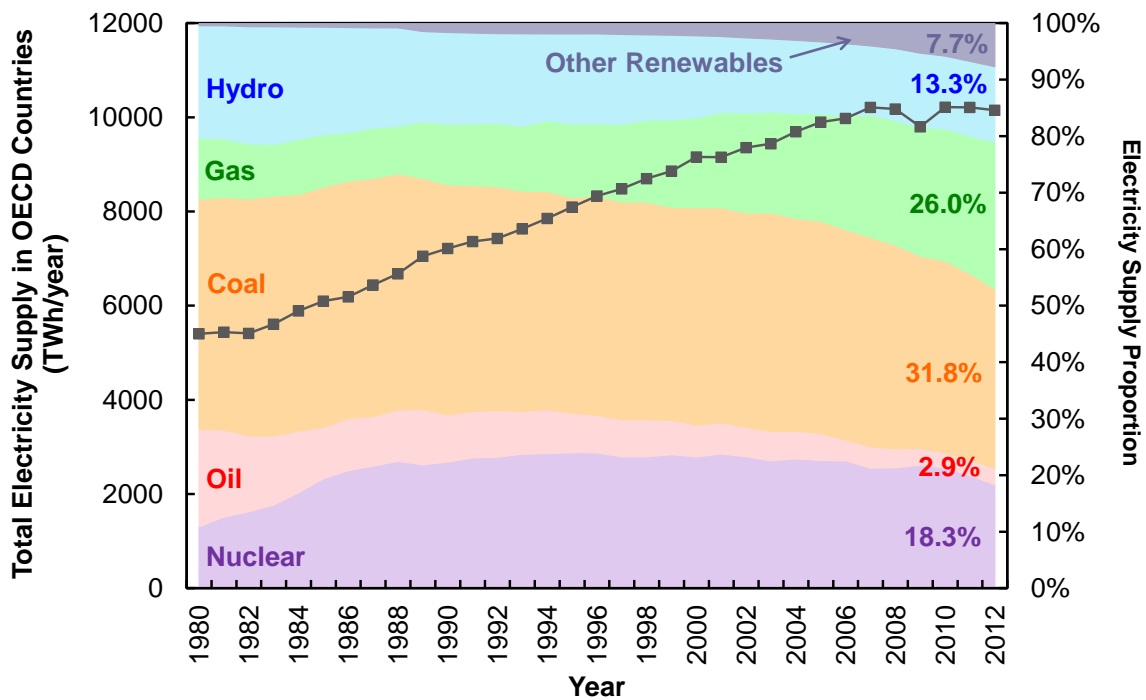
Fig. 1-1   Total electricity generation and the supply proportion from 1980 in OECD countries **[4]**.

1.1.2 Challenges of photovoltaics: Cost & Efficiency

Solar photovoltaics has two major challenges: "high power generation cost" and "Low energy conversion efficiency". The generation cost is determined by the system cost and the operation years, and thus contains not only "solar modules" but also surrounding equipment such as power conditioners, distribution boards, and batteries (if necessary), and also balance of system (BOS) including installation and maintenances. Using crystalline silicon (c-Si) based solar cells, however, approximately 40-60% of the system cost is accounted by the modules cost [6]. Power generation cost of photovoltaics has been gradually lowered over the past decades, but still remains comparatively higher in most regions than those of conventional large-scale power generation methods. The grid-parity condition for photovoltaics is dependent on the applications: in case of Japan, ¥23/kWh for residential use, ¥14/kWh for industrial use, and ¥7/kWh for utility applications. Although the discussion on the cost target is not so simple for this reason, drastic cost reduction is indispensable to achieve grid parity for power generation businesses. Therefore, reduction in the manufacturing costs for solar modules, which take approximately the half of the entire system, is very important to make photovoltaics commercially competitive in the market.

For this challenge, thin-film solar cells, which are sometimes called second generation solar cells, are recently paid much attention to owing to their advantages of low manufacturing processes and low material consumption. Various materials are used for thin-film technologies such as amorphous silicon

3

(a-Si), CuInGaSe$_2$ (CIGS), and CdTe, and the learning curves of their average module selling prices are shown in Fig. 1-2. At a same cumulative production volume, the price of thin-film technologies is lower than crystalline silicon technologies by a factor of 1/3. Crystalline silicon is the mainstream in the current market, and the global share of thin-film type manufactures is still low with a small cumulative production capacity. Nonetheless, both technologies have more or less reached the grid-parity for residential applications ($1.0 /Wp). On the other hand, the grid-parity for the utility application ($0.5 /Wp) is yet to be achieved, and further scaling-up in production volumes are required to realize it for both generation technologies. In other words, continuous market expansion and technological development are expected to enable photovoltaics to generate electricity at as low cost as conventional power plants.
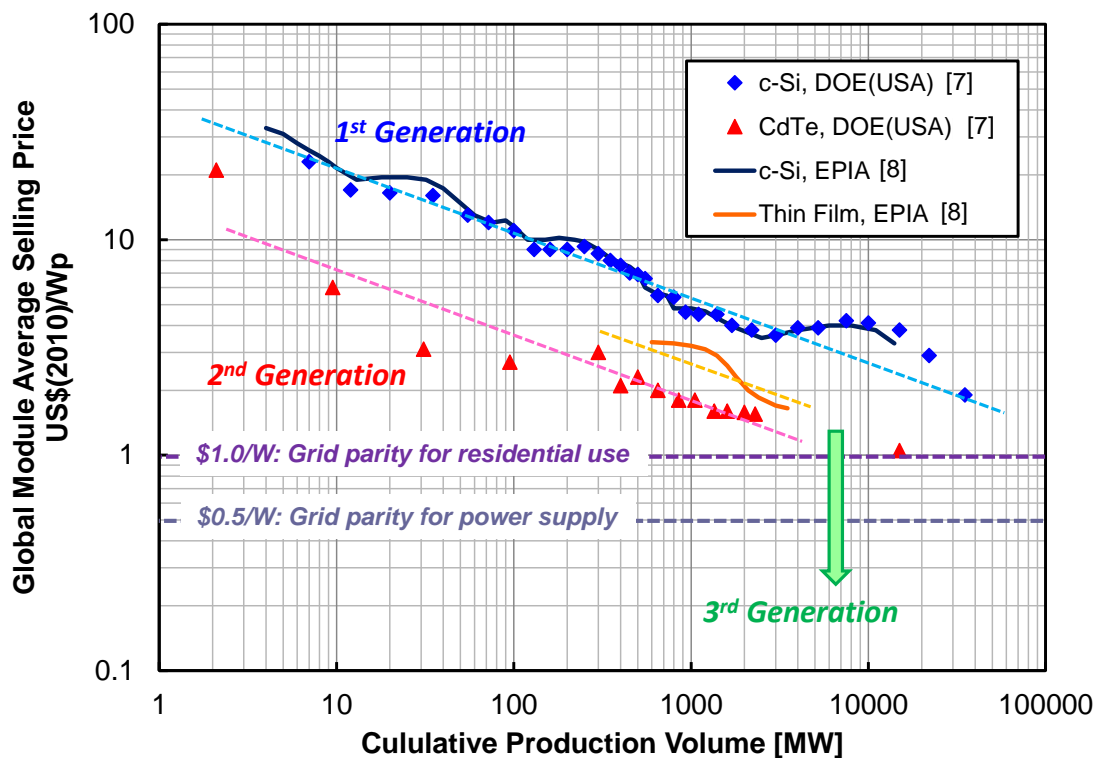
Fig. 1-2 Global module average selling price for crystalline silicon technology (first generation) and thin-film technologies (second generation) versus the cumulative production volume [7, 8].

The power conversion efficiency, on the other hand, is mostly determined by the solar cells and modules, and thus cell design with as low energy loss as possible with new material system and device architectures, as well as with innovative physical effects have been researched from various viewpoints.

Fig. 1-3 shows the historic chart of the best recorded efficiency of research cells with various material systems [9]. Mono-crystalline silicon solar cells, which are the mainstream products in the current market, have been recording comparatively high efficiency and long-term stability since their early start. PEAL cell invented in UNSW in 1999 [10] had kept the world record of 24.7% for over ten years, but several manufacturing companies such as Panasonic, Sharp, and Sunpower, have exceeded 25% in the past few years with design known as HIT or back contact structure [11, 12]. Accordingly, modules with efficiency higher than 20% are already commercially available with mono-crystalline silicon cells [13].

Thin-film solar cells (a-Si, CIGS, CdTe) are advantageous for low cost, but their efficiencies are still lower than that of c-Si. One of the major challenges for a-Si solar cells, in particular, is the Staebler-Wronski effect, which deteriorates cell performance under light illumination [14]. In spite of this, a-Si/µc-Si tandem cells have achieved over 13% stabilized efficiency [15]. Efficiencies of compound semiconductor based thin-film solar cells such as CIGS and CdTe are relatively higher. Over 20% cell efficiencies and around 15% module efficiencies, which are comparable values to the multi-crystalline silicon technologies, have been already reported, and thus further technological developments in this category will surely gather more attention [16, 17].
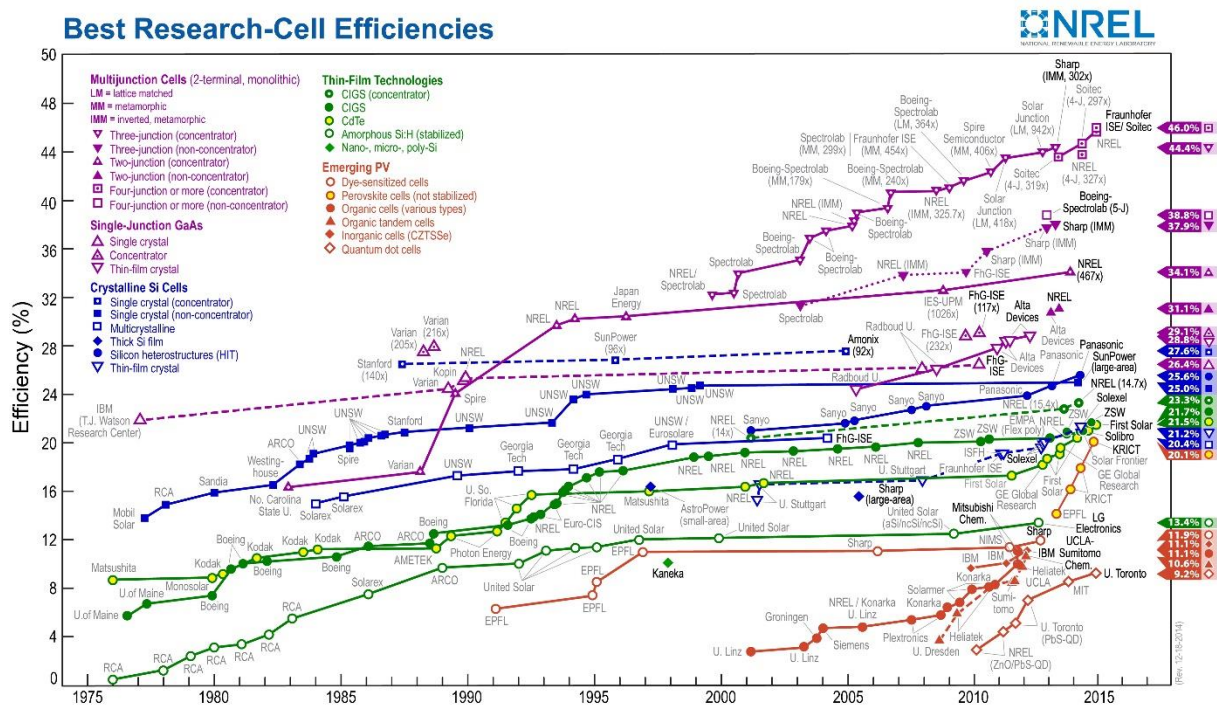
Fig. 1-3 Historic chart of world recorded efficiency of research cells with various material technologies (NREL chart) [9].

1.1.3 Concentration photovoltaics (CPV)

III-V compounds based multi-junction solar cells have achieved the highest efficiency among various types of photovoltaic devices especially under concentrated illumination condition: concentration photovoltaics (CPV). Although III-V semiconductors are generally 10 times as expensive as bulk silicon per unit volume, light concentration can make the required cell area to receive the same amount of light much smaller and hence contribute to drastic reduction of the cell cost. The efficiency of solar cells in general increases under concentration (as will be discussed in the Chapter 2), and III-V multi-junction cells are suitable for concentrated operation owing to the good thermal properties and low current density to reduce the joule heat production. 44.4% in triple-junction, 46.5% in quad-junction configurations have been achieved by Sharp and Fraunhofer ISE, respectively [18, 19].

In CPV, the sunlight is focused by a factor of several hundreds or a thousand by means of lens or mirrors. A concentration system consists of a primary optics to concentrate the light and a secondary optics including a homogenizer to make the concentrated light uniform. Cooling of the photovoltaic chips, typically with fins, is important because the cell temperature easily increases under high concentration. In addition, a tracking system is indispensable since the optics is designed to focus the direct solar radiation.

Fig. 1-4 (b) shows CPV system cost with various cell efficiencies (30% - 50%) and numbers of junction (3J, 4J) calculated based on the typical component costs summarized in the article [20]. The system cost greatly decreases as the concentration ratio increases. Considering that the current c-Si based PV system cost is typically \$3-5/Wp (with large variety depending on the manufacturers), light concentration by a factor of 100 ~ 1000 enables even lower power generation cost. At a low concentration ratio less than 100, the CPV system cost is much higher than conventional PV system due to the high material cost for III-V based cells. Therefore, a system design that is durable at high concentration is desired, and reduction of series resistance and improvement in cooling efficiency are important in this regard. Very high concentration higher than 1000, however, does not contribute much to the reduction of the system cost since the cost proportion for the photovoltaic cells becomes sufficiently small. In such high concentration cases, enhancement in energy conversion efficiency is the most effective driving force to reduce the cost. Among the triple junction cells in Fig. 1-4 (b), the system cost is reduced in an inversely proportional manner to the cell efficiency. Comparing the 50% cell between 3J and 4J, the difference in the system cost is large at low concentration but becomes negligibly small at higher concentration. This suggests that improvement in cell efficiency even by increasing the cell cost is more reasonable than trying to reduce the manufacturing cost preserving the cell efficiency. For these reasons, CPV has been expected as a promising technology that can achieve high energy conversion efficiency and low power generation cost simultaneously.
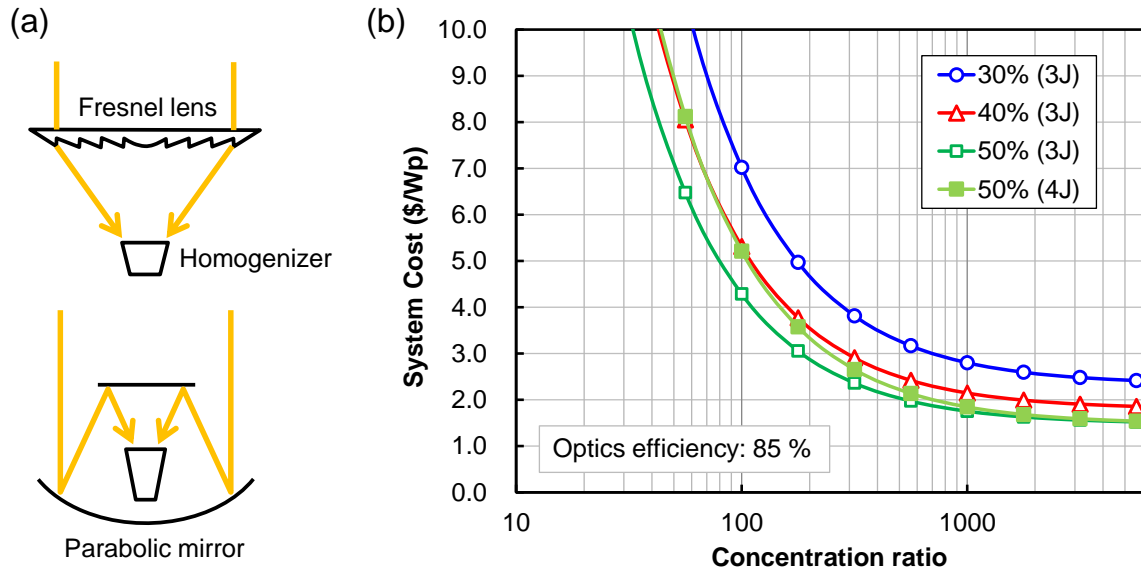
Fig. 1-4   (a) Schematics of concentration photovoltaics (CPV) using lens or mirrors, and (b) CPV System cost with various cell efficiencies (30%-50%) and numbers of junction (3J, 4J) calculated with current component costs based on the reference [20]. The assumed optics efficiency is 85% in the cost estimation.

1.2 Fundamental principle of solar cells

1.2.1 Solar spectrum

Fig. 1-5 and Fig. 1-6 shows spectra of sunlight illuminated on earth [21]. AM0 represents the sunlight vertically irradiated on the earth outside the aerosphere. AM1.5 represents sunlight irradiated on the ground by an angle of 41.8°, taking account of light scattering and absorption by the atmosphere; the light path to the ground through the air is 1.5 times longer than the case of vertical irradiation. AM1.5 is generally referred as the average sunlight spectrum on the land surface, and widely used for solar cell characterizations. The spectrum shape of sunlight is quite different whether the *x*-axis is wavelength for photon energy, and whether the *y*-axis is energy flux or photon flux. The total sunlight irradiation energy can be obtained by integrating the spectra in Fig. 1-5: 1.36×10^3 W/m^2 and 1.00×10^3 W/m^2 for AM0 and AM1.5, respectively (The former value is called solar constant). The total photon number, on the other hand, is obtained by integrating the spectra in Fig. 1-6: 6.16×10^{21} s^{-1}m^{-2} and 4.31×10^{21} s^{-1}m^{-2}, for AM0 and AM1.5, respectively.

The solar spectrum is known to be similar to that of a black body radiation at a temperature of 5800 K. The energy flux I [Wm^{-2}nm^{-1}] in wavelength range between $\lambda \sim \lambda + d\lambda$ in the radiation from the surface of a black body at temperature of T can be described by Planck's Law as

7

$$I(T,E)dE = I(T,\lambda)d\lambda = \frac{2\pi}{h^3c^2}\left(\frac{E^3}{e^{E/kT}-1}\right)dE = \frac{2\pi}{h^3c^2}\left(\frac{E^3}{e^{E/kT}-1}\right)\frac{hc}{\lambda^2}d\lambda . \tag{1-1}$$

$I(T, E)$ can be converted to photon flux $F(T, E)$ as

$$F(T,E)dE = F(T,\lambda)d\lambda = \frac{2\pi}{h^3c^2}\left(\frac{E^2}{e^{E/kT}-1}\right)dE = \frac{2\pi}{h^3c^2}\left(\frac{E^2}{e^{E/kT}-1}\right)\frac{hc}{\lambda^2}d\lambda . \tag{1-2}$$

The angular separation between the earth and the sun θ_{sun} is 0.26°. If a 5800-K black body exists at the sun's location, therefore, the energy or photon flux received by the earth surface are obtained by multiplying I (5800 K, λ) or F (5800 K, λ) by $\sin^2\theta_{sun}$ ($\sim$2.15×10^{-5}). They are plotted as red lines in Fig. 1-5 and Fig. 1-6, showing good agreement with the actual solar spectra.
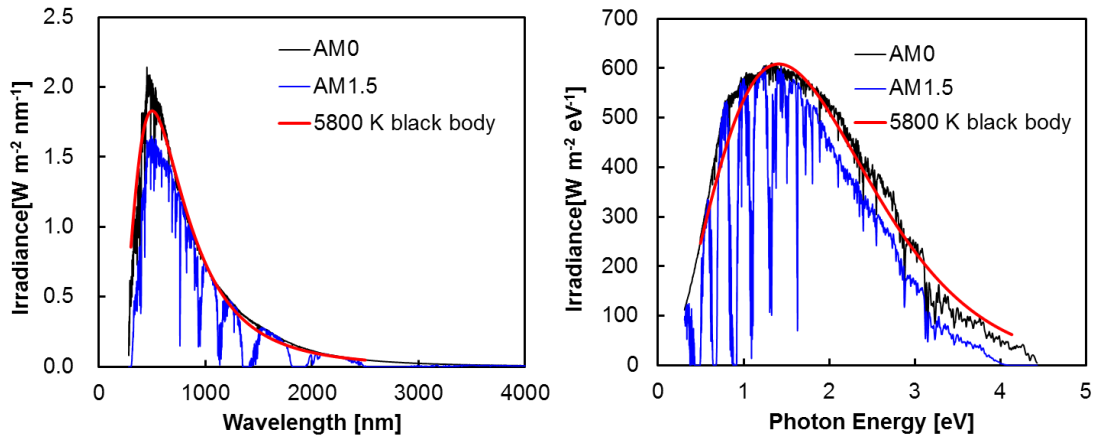
Fig. 1-5   Energy flux of sunlight as functions of (a) wavelength and (b) photon energy.
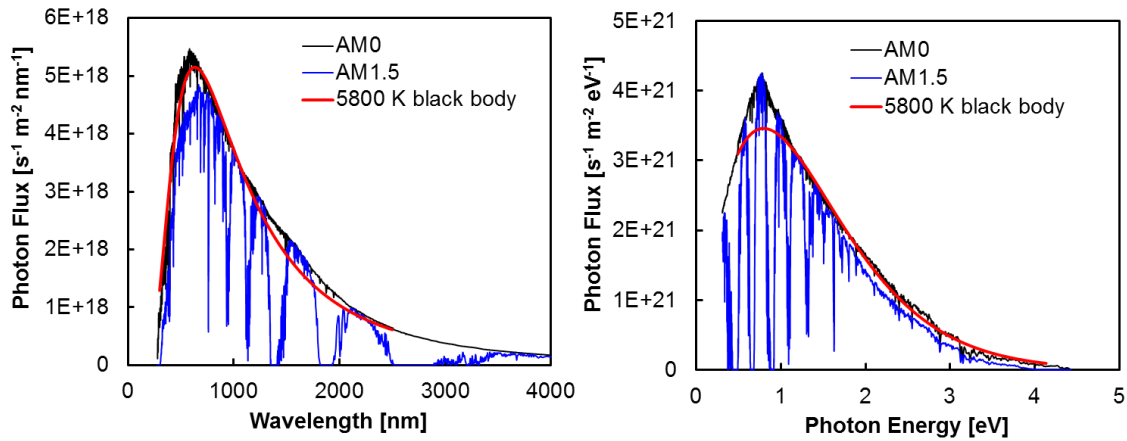
Fig. 1-6   Photon flux of sunlight as functions of (a) wavelength and (b) photon energy.

1.2.2 **Principle of solar cells**

Basic structure of a semiconductor-based solar cell is a p-n junction. Photons with energy above the bandgap E_g are absorbed in the p-n junction area forming electron-hole pairs. The photo-excited electrons and holes are transported by the electric field to the n-region and p-region, respectively, and are extracted by the external circuit as photo-current. The applied voltage V is the difference between the quasi-Fermi levels of the holes in the p-region and that of the electrons in the n-region.

Since the structure of a solar cell is same as a diode in principle, the ideal current-voltage characteristic can be described by adding the photo-current due to light absorption J_L to the diode characteristic as

$$J(V) = J_L - J_0(e^{\frac{qV}{kT}} - 1),\qquad (1\text{-}3)$$

where J is the current density, V is the applied bias, J_0 is the saturation current of the diode, q is the elementary charge, and k is the Boltzmann constant. Ideally J_L is constant, but in reality it is dependent on the applied voltage (see chapter 2 for the detail).

Since sunlight has a wide spectrum from $0 - 4$ eV in photon energy as shown in Fig. 1-5 and Fig. 1-6, there are two major energy losses in a solar cell [22].

(i) Transmission loss

Photons with energy less than the bandgap E_g are transmitted and not absorbed.

(ii) Thermalization loss

Photo-excited carriers are subsequently thermalized to the bandedge by rapidly exchanging heat energy with the surrounding lattice. This takes place on a pico-second time scale [23].
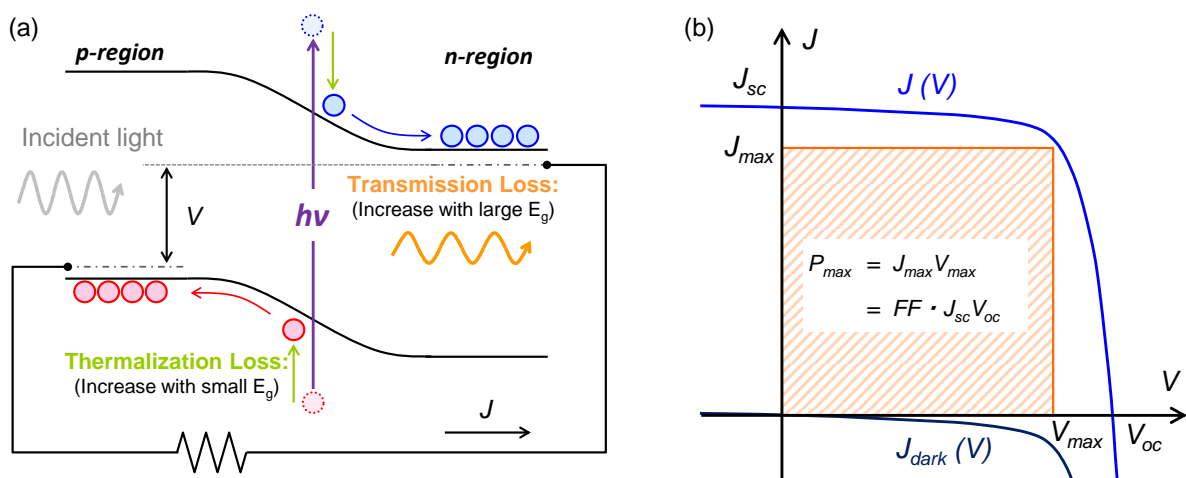
Fig. 1-7 (a) Fundamental principle of a p-n junction photovoltaic cell, and (b) its typical J-V characteristic.

There are various other loss mechanisms such as reflection loss at the front surface, non-radiative recombination loss occurring at crystal defects, surface recombination loss, and ohm loss in the electrodes, though the above two losses in Fig. 1-7 (a) are inevitable in principle. These two energy losses are dependent on the material bandgap; the transmission loss increases with wider bandgap (reduction of J_{sc}), and the thermalization loss increases with narrower bandgap (reduction of V_{oc}). Therefore, theoretical efficiency limit of a single-junction cell composed of a homogeneous material is determined by the bandgap, with maximum efficiency limit of approximately 30% at 1.4 eV, which is called "Shockley-Queisser Limit" [24]. (The detailed derivation will be discussed in Chapter 2).

1.3 Multi-junction solar cells

Cell concepts to exceed the Shockley-Queisser (S-Q) Limit are called third generation photovoltaics, and various device concepts have been proposed and researched:

1) Intermediate band solar cells (IBSC) where multiple photon absorption takes place via intermediate bands in the forbidden band in the bulk semiconductor formed with densely-aligned quantum dots [25, 26], by band anticrossing in highly mismatched alloys [27], or as impurity bands [28].

2) Multiple exciton generation (MEG) cells where the thermalization energy of the carriers excited by high-energy photons generate additional electron-hole pairs [29, 30].

3) Hot carrier solar cells (HCSC) where photo-excited carriers are rapidly extracted by external circuit through energy selective contacts before thermalization [31, 32].

These concepts can theoretically achieve much higher efficiency than the S-Q limit, but are still on the stage of fundamental research at present in order to verify the desired physics phenomena.

The most successful third generation concept has been multi-junction solar cells, or tandem solar cells shown in Fig. 1-8. Multi-junction cells consist of several p-n junctions with different bandgaps that are connected in series with tunnel junctions. They can reduce both the transmission loss and the thermalization loss by absorbing light in decreasing order of the photon energy; the top cell absorbs high-energy photons and the bottom cell absorbs the transmitted low-energy photons.

Multi-junction concepts have been studied and applied in many material systems, such as CIGS solar cells with different compositions [33, 34], or thin-film silicon cells with combination of a-Si, μc-Si, and a-SiGe [35, 36]. Owing to the available materials and the established growth technology, III-V semiconductors have been the most widely used for tandem devices [20, 37]. In particular, Ge-based triple junction cells using InGaAsP compounds have been already used for space application, and also a focus of recent research aiming at application for terrestrial CPV [38, 39, 40, 41].
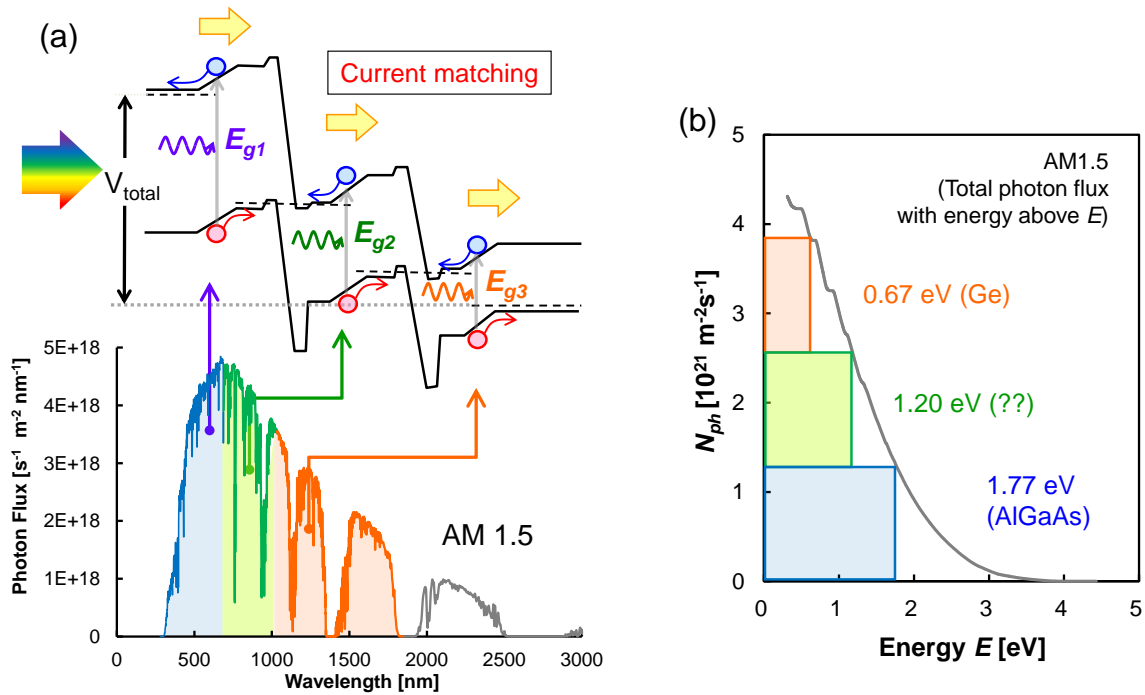
Fig. 1-8 (a) Schematic of multi-junction a solar cell, and (b) simplified current-match condition in Ge-based triple junction cells under AM1.5 irradiation.

1.4 Current match in multi-junction solar cells

Current match condition is a very important design restriction in tandem solar cells. If the photocurrents output differ among the sub-cells, the overall current in the whole device is limited to the minimum values among them since each sub cell is connected in series. The sub-cells producing higher currents are operated under non-optimized condition by losing the excessive current via recombination. Combination of sub-cell bandgaps, therefore, must be appropriately chosen in order to achieve high efficiency.

Assuming that the maximum power output current of each sub-cell is approximately same as the photocurrent due to the light absorption, the current match condition is well satisfied when the numbers of the absorbed photons in each cell are equal (Note that this assumption is not strictly accurate, and detailed theory will be discussed in Chapter 2.). Fig. 1-8 (b) shows the total photon flux with energy of E in the x-axis, in other words, the number of photons that a semiconductor with a bandgap E can absorb. The bandgap combination in Ge ($E_g = 0.67$ eV) based 3-junction cell to achieve equal light absorption can be simply derived from the graph: 0.67 eV/ 1.19 eV / 1.77 eV.

1.4.1 Middle cell materials for triple junction cells

III-V multi-junction solar cells have been mostly developed based on the lattice constant of GaAs and Ge, and InGaP(1.88 eV)/(In)GaAs(1.42 eV)/Ge (0.67 eV) lattice-matched triple junction cells have been conventionally used [38, 42]. Although this structure has achieved over 40% efficiency under concentration [43], it does not satisfy the current match condition due to the wide bandgap of the middle cell. Further improvement in device performance is expected by narrowing the middle cell bandgap to approximately 1.2 eV, and both lattice-matched and lattice mismatched materials have been researched. GaInNAs alloy is the only bulk material that can be lattice-matched to GaAs or Ge and can achieve bandgap lower than 1.4 eV [44, 45, 46], and its epitaxy has been developed mostly using MBE. One of the problems with such dilute nitrides is formation of crystal defects such as N-As or N-N bonds, which act as non-radiative recombination centers [47]. Various growth methods to avoid this issue have been reported such as irradiation of atomic hydrogen [48, 49] or use of Sb as a surfactant [50], but degradation of open-circuit voltage due to low mobility is still a big challenge. Despite this problem, high-efficiency tandem cells using GaInNAs (not as the middle cell) have been already demonstrated [51]. Yet, it is still difficult to grow high-quality crystal using MOVPE, which is more suitable for mass production.

InGaAs is the most widely used lattice-mismatched material for the middle cell in inverse metamorphic (IMM) architectures. Since InGaAs has larger lattice constant than GaAs or Ge, it is typically grown over buffer layers with graded indium composition to reduce the threading dislocation density. This technology achieved higher efficiency than conventional InGaP/GaAs/Ge tandem cells under light concentration [43, 52, 53]. Nevertheless, several-micro-meter-thick graded buffer layers are indispensable, and introduction of recombination centers due to residual dislocation cannot be completely avoided.
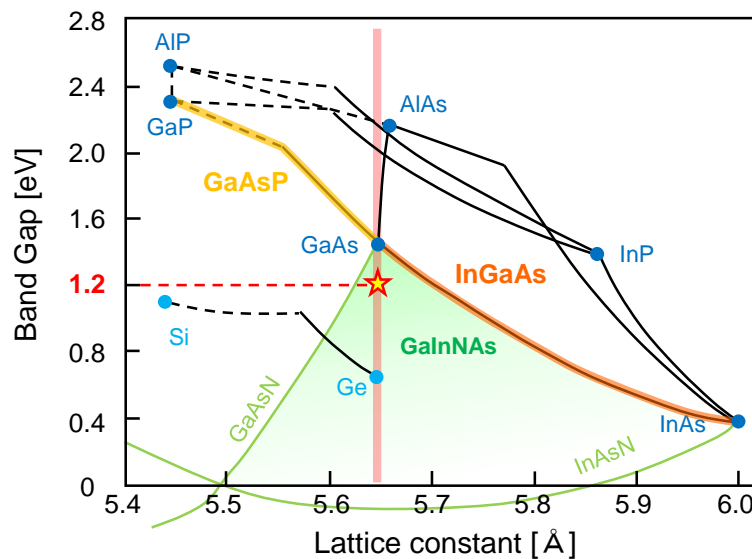
Fig. 1-9   Bandgaps and lattice constants of typical semiconductor materials.

1.5 InGaAs/GaAsP strain balanced superlattice

InGaAs/GaAsP strain balanced superlattice (SL) is a concept to alternately grow InGaAs narrowgap layers with a large lattice constant and GaAsP strain compensation layer with a small lattice constant. Then the lattice relaxation can be prevented by canceling out the compressive strain in InGaAs and the tensile strain in GaAsP. This concept was proposed by Bedair et al. [54], with following demonstration of LED and solar cells [55]. Other opto-electronic devices such as laser diodes [56, 57], photo detectors [58], and modulators [59] have also been so far demonstrated.

Application of this SL to multi-junction solar cells was proposed by Ekins-Daukes et al. [60]. Target bandgap of ~1.2 eV can be achieved as an effective value due to quantum confinement effects by adjusting the composition and thickness of each layer.

Since the bandgap is wider in GaAsP than in InGaAs, the band-lineup in the SL forms periodically aligned potential wells, which are also often referred as multiple quantum wells (MQW). In this study, such a structure is expressed as "superlattice (SL)" instead of MQW, because the primary aim for using InGaAs/GaAsP periodic layers in this work is not to utilize the quantum effects in QWs, but to balance the strain for successful epitaxial growth; the literal definition of "superlattice" is a periodic layer structure of several materials, which is closer to the concept in this work.

Strain balance condition in an InGaAs/GaAsP SL is satisfied when the average lattice constant in the SL region $<a>$ is equal to that of the substrate $a_{substrate}$ as

$$<a> = \frac{t_{InGaAs}a_{InGaAs} + t_{GaAsP}a_{GaAsP}}{t_{InGaAs} + t_{GaAsP}} = a_{substrate} \qquad (1\text{-}4)$$

where a_{InGaAs}, a_{GaAsP}, t_{InGaAs}, t_{GaAsP} are the lattice constants and thicknesses of InGaAs wells and GaAsP barriers, respectively. As an option, strain-neutral GaAs can be inserted between the two layers. With thick interlayers, the band-lineup becomes step-like potential.

In solar cells, the SL-region is typically inserted in the intrinsic region of a p-i-n GaAs cell as shown in Fig. 1-10. Carriers photo-excited by low-energy photons in InGaAs wells subsequently escape via thermionic process or tunneling transport. Suppression of lattice relaxation with strain-compensation technique has been shown to be effective to prevent degradation in photovoltaic performances. Use of InGaAs/GaAsP strain-balanced SLs instead of InGaAs/GaAs strained SLs can greatly reduce the dark current [60, 61]. The impact of net strain on the cell performance was reported by Sodabanlu et al., showing that the cell efficiency becomes the best at the strain-balance condition, and larger accumulation of strain either to compressive or tensile direction deteriorates the device performance [62].

Ge-based triple junction cells including such InGaAs/GaAsP SLs have been already demonstrated. JDSU has achieved over 40% efficiency under light concentration using 100-period SLs with

bandedge extended to 930 nm (E_g = 1.33 eV) [63]. For ideal current match condition, however, the band-edge must be further extended beyond 1000 nm, which corresponds to a bandgap below 1.24 eV.
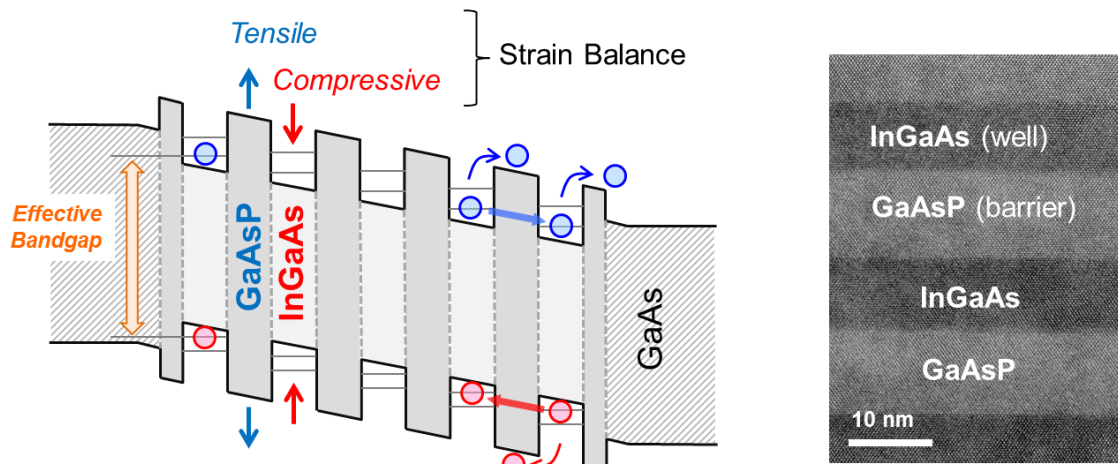
Fig. 1-10   Schematic of an InGaAs/GaAsP SL solar cell, and a bright-field TEM image of typical SLs.

1.5.1 General characteristics of SL solar cells

Use of a superlattice or MQW for high-efficiency multi-gap solar cells was initially proposed by Barnman [64], and since then, various material systems have been studied such as GaAs/AlGaAs, InGaAsP/InP, and InGaAs/GaAsP.

Fig. 1-11 shows typical I-V characteristics and quantum efficiency of InGaAs/GaAsP SL solar cells with various SL period numbers. Spectral response beyond the band-edge of the host material (GaAs) can be obtained due to absorption of low-energy photons in the SLs. As the period number increases, J_{sc} is enhanced by the additional photocurrent though the collection of all the photo-excited carriers becomes difficult especially at forward bias that weakens the built-in field. As a result, the photocurrent J_L in eq. (1-3) decreases as the forward bias increases to degrade the *FF*. Furthermore, V_{oc} tends to be lowered in SL cells compared to a reference cell composed of only the host material, since implementation of narrow-gap SLs generally increases recombination current due to high carrier concentrations in the quantum wells [65, 66]. Therefore, the total cell efficiency becomes lower if the influence of reduction in *FF* and V_{oc} exceeds the contribution of additional photocurrent.

Araújo et al. [67] argued that efficiency limit of SL or MQW solar cells cannot exceed that of the optimal single-gap cell, based on a detailed-balance theory assuming that the quasi-Fermi level splitting $\Delta\phi_F$ is uniform in the entire device and equal to the applied bias voltage. On the other hand, comparison between simulation and experiments for electroluminescence suggested that $\Delta\phi_F$ in quantum well solar cells is not uniform in reality and lower than the applied bias in the well region due to carrier escape processes [68]. Using AlGaAs/GaAs, GaInP/GaAs, and InP/InGaAs SL systems,

efficiency gains due to SL incorporation with contribution of increased J_{sc} larger than decreased V_{oc}, have been experimentally demonstrated [69]. Comparable efficiency using an InGaAs/GaAsP SL to that of a GaAs p-i-n cell, whose bandgap is almost optimal for a single junction device, has been also already reported [70, 62].
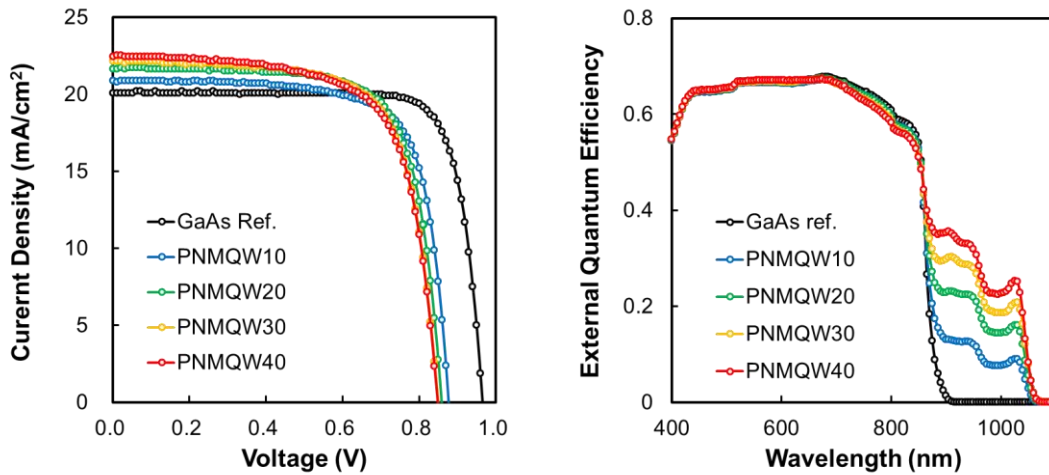
Fig. 1-11   I-V curves and EQE of typical InGaAs/GaAsP SL cells with various period numbers (Data in the ref. [66] are replotted).

1.5.2 Challenges in InGaAs/GaAsP SL solar cells

For practical application of InGaAs/GaAsP to Ge-based multi-junction solar cells, there are still several challenges both in design and crystal growth, as briefly summarized below. The details for each will be discussed in the corresponding chapters.

(I) Design of SL
- The major challenge is the trade-off between light absorption and carrier collection. For complete absorption of the photons with energy above the effective bandgap of the SL, the excitation between electrons and holes in their ground states, i.e. 1e-1hh transition, must be sufficiently large. This necessity, however, requires a large number of wells to be stacked, resulting in more difficulty in extracting carriers through the MQW regions because of the weakened electric field in the thickened i-region. The SL structure, therefore, must be designed 1) to absorb sufficient photons with as many wells as possible, and 2) to extract carriers as efficiently as possible.
- For current match condition, a SL with a large number of periods (typically 100-period) with bandgap of 1.24-1.20 eV ($\lambda_{bandedge} > 1000$ nm) are required. To date, however, most research

efforts related to this material system have introduced SLs with band-edge limits of 950 nm, or periods below 70. Therefore, it is needed to clarify the carrier transport problems that would emerge with a 100-period SL with a bandedge extended beyond 1000 nm, and to design the suitable SL structure to achieve enhancement of cell performance with such required properties for the SL.

- I-V and QE have been the most widely used characterization methods for SL-cells similarly as for other types of solar cells. These output characterization and comparison of microscopic properties e.g. J_{sc}, V_{oc} and *FF* are suitable to evaluate how well the cell performs as a device, but have difficulties in examining the underlying problem with respect to the carrier transport (chapter 4). Physical phenomena in quantum wells have been uncovered by particularly-designed equipment such as low-temperature or time-resolved measurements. Although these characterizations are effective, specialized measurement setups are required.

(II) Growth of SL

- In theory, the SLs can be infinitely grown if the compressive strain in InGaAs and the tensile strain in GaAsP well balance out each other. In reality, however, partial lattice relaxation occurs during formation of hetero-interfaces between the two oppositely strained layers, and the crystal can be easily degraded as more layers are stacked.

- InGaAs/GaAsP SLs solar cells have been mostly demonstrated on exact-oriented GaAs (0 0 1) substrates, though vicinal substrates are generally used for growth of III-V on Ge in order to prevent formation of anti-phase domains. When strained SLs are grown on vicinal substrate, however, layers tend to be undulated due to formation of step bunching, which easily induces lattice relaxation (chapter 6).

- These difficulty in crystal growth becomes more serious as the indium composition is increased for band narrowing and the SL period number is increased for sufficient light absorption. Therefore, development in growth technology for the SL with a bandgap as low as 1.2 eV and a period number as large as 100 on vicinal GaAs or Ge substrates is required.

1.6 Research outline

The purpose of this study is to develop InGaAs/GaAsP SL solar cells with required middle cell properties for current-matched Ge-based triple junction cells. The aimed target is to achieve higher N-on-P type cell performance than a GaAs reference cell, by incorporating a 100-period SL with bandedge wavelength extended beyond 1000 nm on 6º-off substrate.

Table 1-1 Quantitative targets in this study

Cell performance	• Higher middle cell efficiency than GaAs ref. • Current under operation J_{max} = 17 mA/cm^2 • N-on-P structure
InGaAs/GaAsP SL	• Period number = 100 • Bandedge > 1000 nm (bandgap < 1.24 eV)
Substrate	Vicinal (0 0 1) substrates: 6º misorientation

Milestones toward the research goals are:

(1) Establishment of evaluation method for carrier transport through quantum structures.
(2) Clarification of carrier transport challenges in InGaAs/GaAsP SL cells that would emerge for practical application.
(3) Proposition of a SL design principle for higher efficiency, and its experimental demonstration.
(4) Development of MOVPE technique to grow high-quality SLs on vicinal substrates.
(5) Implementation of SL into N-on-P solar cells on vicinal GaAs substrates

In the main context, fundamental theories related to this work are firstly summarized in chapter 2, and the experimental equipment and their principles are introduced in chapter 3.

In chapter 4, Carrier Collection Efficiency (CCE) is proposed and the validity of its definition is verified. Using this evaluation measure, the effects of quantum structures on the transport of the photo-generated carriers especially under operational condition are examined.

In chapter 5, stepped tunnel superlattice (STSL) is proposed as a design principle to overcome the trade-off between light absorption and carrier collection, and its design criterion are discussed.

In chapter 6, MOVPE of high quality SLs with growth stability and low background carbon incorporation on vicinal substrates is developed using triethylgallium as the Ga source.

In chapter 7, the designed 100-period SL with bandgap of 1.2 eV is implemented into an N-on-P GaAs cell on a vicinal substrate.

The research will be concluded in chapter 8.

> **_Purpose_**
>
> **To develop InGaAs/GaAsP superlattice solar cells for current matched
> Ge-based triple junction cells.**

Chapter 1) Introduction

Chapter 2) Fundamental theories

➤ Physics of solar cells
➤ Physics of SLs: quantum confinement, light absorption, carrier transport

Chapter 3) Experimental equipment

➤ MOVPE, XRD, Solar simulator, PL(CW/TR), FTIR

Chapter 4) Evaluation of carrier transport in SL solar cells

➤ CCE: Carrier Collection Efficiency
   – Definition & Validation
➤ Demonstration of CCE evaluation
   – Effectiveness of compensation-doping
   – Challenges for 100-period SL cell (E_g = 1.2 eV)

Evaluation method

Chapter 5) Design of SL structure for higher performance

➤ Stepped tunnel SL (STSL)
   – Design criteria for the component layers
   – Demonstration of a 100-period SL cell with efficiency gain

Design principle

Chapter 6) MOVPE of SLs on vicinal substrates

➤ Low temperature growth with TEGa
   – Improvement in crystal quality and uniformity
   – Suppression of carbon background doping

Growth technique

Chapter 7) Implementation of SL into N-on-P cells

➤ Optimization of growth temperature for SL cell on vicinal substrates
➤ N-on-P cell on a vicinal substrate with a 100-period SL (E_g = 1.2 eV)
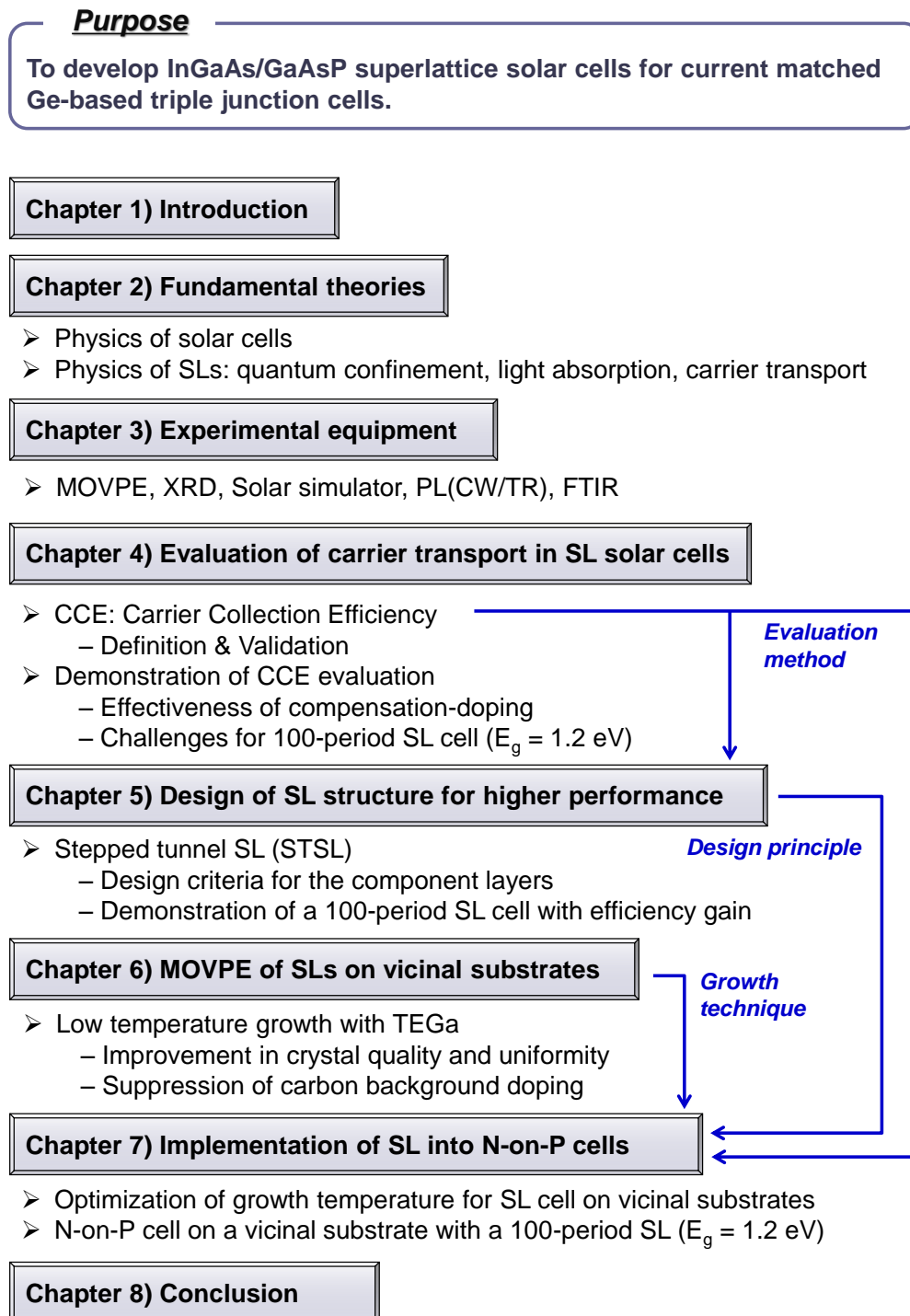
Chapter 8) Conclusion

Fig. 1-12   Purpose and outline of this research

2   Fundamental theories

2.1 Theory of solar cells

In Chapter 1, qualitative principle of solar cells was introduced. In this section, more detailed physics theories that determine the photovoltaic characteristics are overviewed.

There are two major theories that derive solar cell characteristics: detailed-balance theory based on macroscopic photon balance described by statistical mechanics, and drift-diffusion theory based on microscopic phenomena inside the device such as light absorption and carrier transport. Both theory can derive the same current-voltage characteristics of solar cells as introduced in chapter 1:

$$J(V) = J_{sc} - J_0 (e^{\frac{qV}{kT}} - 1) . \tag{2-1}$$

Real solar cells shows more or less same characteristics, but sometimes not. Therefore it is important to understand what assumptions underlie this theoretical characteristic.

2.1.1 Detailed Balance theory

The brief principle of the detailed balance theory is that the current-voltage characteristics of a solar cells is determined by the balance of photon absorption and emission. In other words, a solar cell is regarded as a light emitter as well as a light absorber, and the difference between the absorption and emission corresponds to the number of remaining photo-excited carriers that are extracted by the external circuit as the current. (Also this relation holds true at all the photon energies.)

Photon flux from a light emitter with temperature of T_c and chemical potential of $\Delta\mu$ to a medium with refractive index of n_c can be described by generalized Planck's radiation law as

$$F(T_c, E, \Delta\mu) = \int_\Omega \frac{2n_c^2}{h^3 c^2} \frac{E^2}{e^{(E-\Delta\mu)/kT_c} - 1} d\Omega = (\pi \sin^2 \theta_c) \frac{2n_c^2}{h^3 c^2} \frac{E^2}{e^{(E-\Delta\mu)/kT_c} - 1} , \tag{2-2}$$

where h is the Planck's constant and c is the light velocity [71, 23]. θ_c is the angle within which emission is allowed, and thus θ_c is $\sin^{-1}(n_0/n_c)$ due to Snell's law if photons are radiated from inside the emitter to the air (with refractive index of n_0). Since the refractive index of the air is near unity, the eq. (2-2) can be written as

$$F(T_c, E, \Delta\mu) = \frac{2\pi}{h^3 c^2} \frac{E^2}{e^{(E-\Delta\mu)/kT_c} - 1} . \tag{2-3}$$
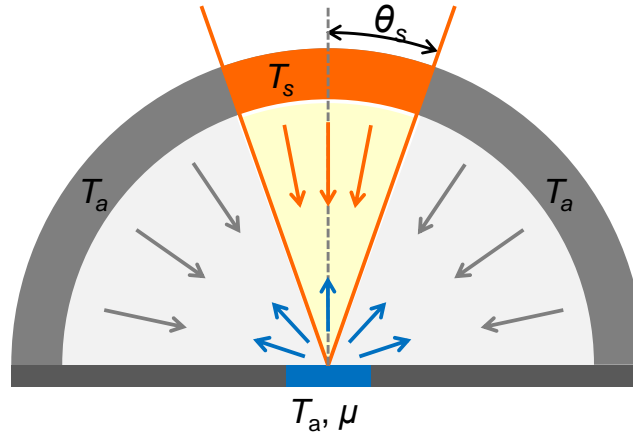
Fig. 2-1 A schematic of a flat plate solar cell receiving the sunlight [72].

Fig. 2-1 shows a schematic of a solar cell under sunlight illumination. The sun is regarded as a blackbody at a temperature of T_s. The cell receives the sunlight (eq. (1-2)) within an angle range $\theta < \theta_s$, and receives radiation from the atmosphere at temperature T_a in $\theta > \theta_s$. Current attributed to absorption of photon with energy E can be described as

$$j_{abs}(E) = q(1 - R(E))a(E)[f_s F(T_s, E, 0) + (1 - f_s)F(T_a, E, 0)],\qquad(2\text{-}4)$$

where $R(E)$ is the reflectivity, $a(E)$ is the absorptivity, and f_s (= $\sin^2\theta_s$) is the geometrical factor representing the angular range of the sun. On the other hand, the current attributed to emission can be described by considering the cell temperature T_c equals to T_a as

$$j_{emit}(E) = q(1 - R(E))\varepsilon(E)F(T_a, E, \Delta\mu),\qquad(2\text{-}5)$$

where $\varepsilon(E)$ is the emissivity, which is always equal to $a(E)$, not only under thermal equilibrium state ($f_s = 0$, $\Delta\mu = 0$, $j_{abs}(E)=j_{emit}(E)$), but also under an arbitrary situation [73].

To derive solar cell efficiencies based on the detailed balance theory, the ideal situation are assumed as follows [72].

- The surface reflectance is negligible: $R(E) = 0$.
- All the photons with energy above the bandgap are absorbed, and all the photons with energy below the bandgap are transmitted: $a(E) = 0$ ($E > E_g$), $a(E) = 1$ ($E < E_g$).
- Exact one electron-hole pair is generated when a photon is absorbed.
- The photo-excited electrons and holes are subsequently thermalized until the carrier temperature becomes equal to T_a.
- Photo-excited carriers are completely separated and transported to the external circuit without loss.
- Carriers recombine only radiatively.

- Quasi-Fermi-level splitting (or the chemical potential) in the entire cell equals to the applied voltage *V.*

To simplify the equations, functions *N* and *L* are defined as

$$N(E_{\min}, E_{\max}, T, \Delta\mu) = \frac{2\pi}{h^3 c^2} \int_{E_{\min}}^{E_{\max}} \frac{E^2}{e^{(E-\Delta\mu)/kT} - 1} dE, \tag{2-6}$$

$$L(E_{\min}, E_{\max}, T, \Delta\mu) = \frac{2\pi}{h^3 c^2} \int_{E_{\min}}^{E_{\max}} \frac{E^3}{e^{(E-\Delta\mu)/kT} - 1} dE. \tag{2-7}$$

N ($E_{\min}$, $E_{\max}$, *T*, $\Delta\mu$) and *L* ($E_{\min}$, $E_{\max}$, *T*, $\Delta\mu$) represents photon flux and energy flux that are absorbed from / emitted into the entire hemisphere by the solar cell at temperature of *T* and chemical potential of $\Delta\mu$ [72]. Using these functions, the obtained current density at a bias voltage of *V* can be described based on the assumptions above as

$$J(V) = q[Xf_s N(E_g, \infty, T_s, 0) + (1 - Xf_s)N(E_g, \infty, T_a, 0) - N(E_g, \infty, T_a, qV)], \tag{2-8}$$

where E_g is the bandgap of the cell, and *X* is the concentration ratio. The first and the second terms represent the absorption from the sun and the atmosphere, respectively, and the third term represents the emission from the cell. This equation becomes (2-1) by assuming "$e^{(E-\Delta\mu)/kT} \gg 1$" in the eq. (2-7) and (2-8).

Since the power output is the product of *J(V)* and *V*, the maximum energy conversion efficiency is

$$\eta_{\max} = \frac{[J(V) \cdot V]_{\max}}{Xf_s L[0, \infty, T_s, 0]}. \tag{2-9}$$

Assuming that the sun is a blackbody with temperature of 6000 K, the theoretical maximum efficiency of single junction solar cells based on detailed balance calculation is 31%, which is called the Shockley-Queisser Limit [24].

In the discussion above, the solar spectrum was described as a blackbody radiation spectrum at temperature of T_s, but it can be substituted with an arbitrary photon flux spectrum. Fig. 2-2 shows efficiency limits calculated for AM1.5 spectrum at different concentration ratios; *X* = 46200 (= $1/\sin^2\theta_s$) is the maximum concentration ratio. The efficiency limit takes the maximum of 33% at 1.4 eV bandgap at 1 sun, and 44% at 1.1 eV bandgap under maximum concentration.
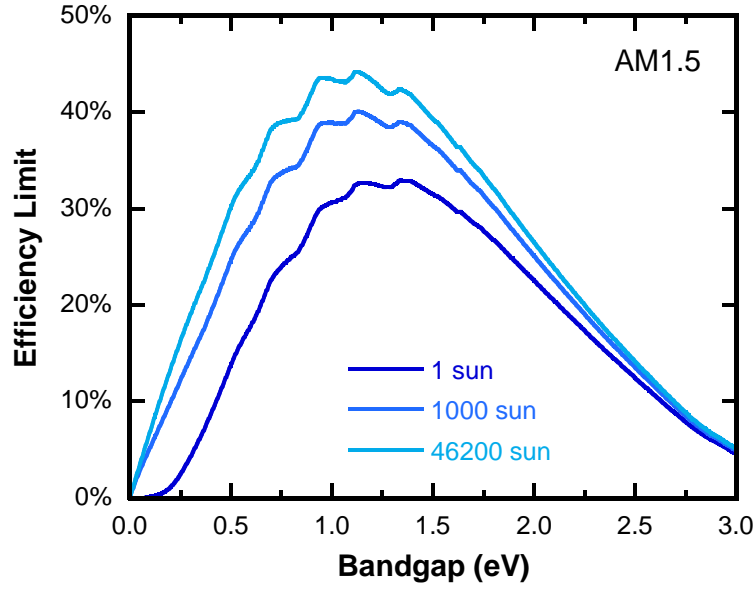
Fig. 2-2 Theoretical efficiency limit for single junction solar cells under AM1.5 spectrum at 1, 1000, 46200 (maximum) sun conditions.

Efficiency limits for multi-junction solar cells can be similarly calculated by detailed balance theory by taking account of the principle that the current in the entire device is limited to the minimum among the sub-cells as mentioned in the section 1.3. As the simplest case, the efficiency of dual-junction cells can be derived as follows.

The bandgaps for the top and the bottom cell are assumed to be E_{g1}, E_{g2}, and voltages applied to them are assumed to be V_1, V_2, respectively. The external voltage V is the sum of V_1 and V_2. The current density for the top and the bottom cell, $J_1(V_1)$ and $J_2(V_2)$ can be described as

$$J_1(V_1) = q[Xf_s N(E_{g1},\infty,T_s,0) + (1-Xf_s)N(E_{g1},\infty,T_a,0) - N(E_{g1},\infty,T_a,qV_1)] , \qquad (2\text{-}10)$$

$$J_2(V_2) = q[Xf_s N(E_{g2},E_{g1},T_s,0) + (1-Xf_s)N(E_{g2},E_{g1},T_a,0) - N(E_{g2},E_{g1},T_a,qV_2)] , \qquad (2\text{-}11)$$

where X is the concentration ratio, and N is the function defined in the eq. (2-6). The power output of the tandem cell is

$$P(V) = q[J_1(V_1)V_1 + J_2(V_2)V_2] . \qquad (2\text{-}12)$$

By calculating the maximum $P(V)$ with a condition of $J_1(V_1) = J_2(V_2) = J(V)$ the efficiency can be obtained by eq. (2-9).

Fig. 2-3 shows the efficiency limits for 2-junction and Ge-based 3-junction solar cells at 1 sun condition, calculated by substituting the illumination spectrum in the eq. (2-10) and (2-11) with AM1.5 spectrum. For the 3-junction case, the Ge (0.67 eV) is used as the bottom cell. The optimal bandgap combination is 1.60 eV/0.94 eV for 2-junction, and 1.79 eV/1.20 eV/0.67 eV for Ge-based 3-junction. This combination quite well agree with a simple estimation shown in Fig. 1-8 (b), in which the maximum power output current is assumed to be almost the same as the short circuit current. Note that the optimal combination of the bangap does not significantly change under high concentration illumination.
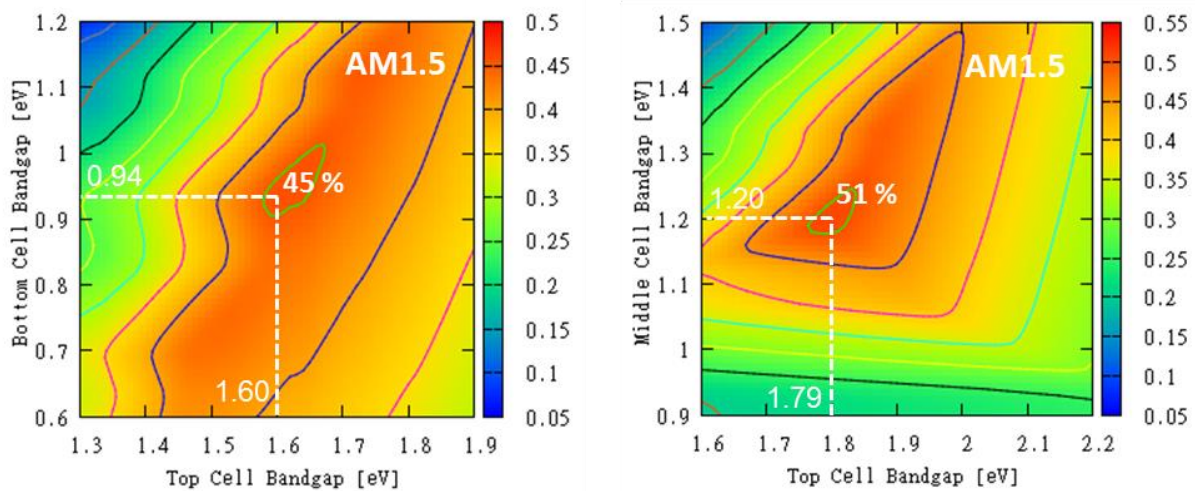
Fig. 2-3   Efficiency limits for 2-junction and Ge-based 3-junction solar cells under AM1.5 illumination, calculated based on detailed balanced theory. The maximum efficiency and corresponding bandgap combinations are shown together.

2.1.2 Semiconductor drift-diffusion theory

The detailed balance theory is solely based on the photon balance, and it derives the device characteristics independent of the cell structure. This section shows how the current-voltage characteristics are derived by a semiconductor device model, which takes account of carrier dynamics inside the cell.

The basic structure of a solar cell is a p-n junction, and it can be simplified as a 1-dimensional structure in most cases as shown in Fig. 2-4. By self-consistently solving the Poisson's equation and the current continuity equations under appropriate boundary conditions, e.g. semi thermal equilibrium at the contacts, the band-lineup of the entire cell, and profiles of carrier concentration, quasi-Fermi levels, and current density can be uniquely determined.

i) Poisson's equation

$$\frac{\partial^2 \phi(x)}{\partial x^2} = -\frac{q}{\varepsilon}\left[N_D(x) - N_A(x) + p(x) - n(x)\right]. \tag{2-13}$$

ii) Electron current continuity equation

$$\frac{\partial n}{\partial t} = 0 = \frac{1}{q}\frac{\partial}{\partial x}\left[-q\mu_n n(x)\frac{\partial \phi(x)}{\partial x} + qD_n\frac{\partial n(x)}{\partial x}\right] + g(x) - r(x). \tag{2-14}$$

iii) Hole current continuity equation

$$\frac{\partial p}{\partial t} = 0 = -\frac{1}{q}\frac{\partial}{\partial x}\left[-q\mu_p p(x)\frac{\partial \phi(x)}{\partial x} - qD_p\frac{\partial p(x)}{\partial x}\right] + g(x) - r(x). \tag{2-15}$$

In the above equations, $\phi(x)$ is the electrical potential, $n(x)$ and $p(x)$ are electron and hole concentrations, q is the elementary charge, ε is the permittivity, $N_D(x)$ and $N_A(x)$ are the donor and the acceptor concentrations, μ_n and μ_p are the electron and hole mobilities, D_n and D_p are the electron and hole diffusion coefficients, $g(x)$ is the carrier generation rate, and $r(x)$ is the recombination rate.
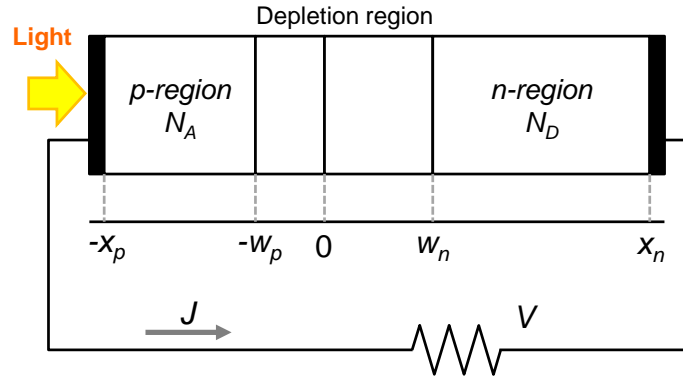
Fig. 2-4   A p-n junction device. The p-side is illuminated with light.

Analytical solutions for (2-13)-(2-15) can be obtained with the following assumptions:

- Injection is sufficiently low, and thus the majority carrier concentrations in the neutral regions are constant and unaffected by the external bias V.
- Quasi-Fermi levels are constant in the depletion region and split by V.
  → Minority carrier concentrations at $x = -w_p$, w_n are determined as a boundary condition.
- Minority carrier diffusions at the device terminals are determined by surface recombination.
  → Boundary conditions at $x = -x_p$, x_n
- Electric field in the neutral regions is negligible.

Carrier generation rate due to light absorption is described as

$$g(E,x) = (1 - R(E))\alpha(E)F(E)e^{-\alpha(E)(x+x_p)},$$ (2-16)

where E is photon energy, $\alpha(E)$ is the light absorption coefficient, $F(E)$ is irradiated photon number density.

Recombination in the neutral p-region and n-region are written as

$$r|_{p-region} = \frac{n - n_0}{\tau_n}, \qquad r|_{n-region} = \frac{p - p_0}{\tau_p},$$ (2-17)

where τ_n and τ_p are minority carrier lifetimes, n_0 and p_0 are electron and hole concentration in the p- and the n- region under the thermal equilibrium condition.

(1) p-region

By solving the electron current continuity equation

$$\frac{d^2 n(x)}{dx^2} - \frac{n - n_0}{L_n^2} + \frac{g(E,x)}{D_n} = 0 \qquad (x < -w_p),$$ (2-18)

with boundary conditions of

$$n(-w_p) - n_0 = \frac{n_i^2}{N_A}(e^{\frac{qV}{kT}} - 1), \qquad D_n \frac{dn}{dx} = S_n[n(-x_p) - n_0],$$ (2-19)

where S_n is the surface recombination velocity, the electron current at $x = -w_p$ under bias of V for photon energy of E, can be derived as

$$j_n(E, -w_p) = \frac{q(1-R)F\alpha L_n}{\alpha^2 L_n^2 - 1} \left[\frac{e^{-\alpha(x_p - w_p)}\left(\frac{S_n L_n}{D_n}\cosh\frac{x_p - w_p}{L_n} + \sinh\frac{x_p - w_p}{L_n}\right) - \left(\frac{S_n L_n}{D_n} + \alpha L_n\right)}{\frac{S_n L_n}{D_n}\sinh\frac{x_p - w_p}{L_n} + \cosh\frac{x_p - w_p}{L_n}} + \alpha L_n e^{-\alpha(x_p - w_p)} \right]$$

$$- \frac{qD_n n_0(e^{\frac{qV}{kT}} - 1)}{L_n} \left[\frac{\frac{S_n L_n}{D_n}\cosh\frac{x_p - w_p}{L_n} + \sinh\frac{x_p - w_p}{L_n}}{\frac{S_n L_n}{D_n}\sinh\frac{x_p - w_p}{L_n} + \cosh\frac{x_p - w_p}{L_n}} \right] = j_{illu,n}(E, -w_p) + j_{dark,n}(V, -w_p)$$ (2-20)

where the first and the second term are defined as $j_{illu,n}$ and $j_{dark,n}$. The total electron current density at $x = -w_p$ can be obtained by integrating the eq. (2-20) with respect to photon energy E as

$$J_n(-w_p) = \int_{AM1.5} j_{illu,n}(E, -w_p)dE + j_{dark,n}(V, -w_p).$$ (2-21)

(2) n-region

By solving the hole current continuity equation

$$\frac{d^2 p(x)}{dx^2} - \frac{p - p_0}{L_p^2} + \frac{g(E,x)}{D_p} = 0 \qquad (x > w_n), \tag{2-22}$$

with boundary conditions of

$$p(w_n) - p_0 = \frac{n_i^2}{N_D}(e^{\frac{qV}{kT}} - 1), \quad -D_p \frac{dp}{dx} = S_p[p(x_n) - p_0], \tag{2-23}$$

the hole current at $x = w_n$ under bias of V for photon energy of E, can be derived as

$$j_p(E,w_n) = \frac{q(1-R)F\alpha L_p}{\alpha^2 L_p^2 - 1} e^{-\alpha(x_p + w_n)} \left[\frac{\left(\frac{S_p L_p}{D_p}\cosh\frac{x_n - w_n}{L_p} + \sinh\frac{x_n - w_n}{L_p}\right) - \left(\frac{S_p L_p}{D_p} - \alpha L_p\right)e^{-\alpha(x_n - w_n)}}{\frac{S_p L_p}{D_p}\sinh\frac{x_n - w_n}{L_p} + \cosh\frac{x_n - w_n}{L_p}} - \alpha L_p \right]$$

$$- \frac{qD_p p_0 (e^{\frac{qV}{kT}} - 1)}{L_p} \left[\frac{\frac{S_p L_p}{D_p}\cosh\frac{x_n - w_n}{L_p} + \sinh\frac{x_n - w_n}{L_p}}{\frac{S_p L_p}{D_p}\sinh\frac{x_n - w_n}{L_p} + \cosh\frac{x_n - w_n}{L_p}} \right] = j_{illu,p}(E,w_n) + j_{dark,p}(V,w_n) \tag{2-24}$$

where the first and the second term are defined as $j_{illu,p}$ and $j_{dark,p}$. The total hole current density at $x = w_n$ can be obtained by integrating the eq. (2-24) with respect to photon energy E as

$$J_p(w_n) = \int_{AM1.5} j_{illu,p}(E,w_n)dE + j_{dark,p}(V,w_n). \tag{2-25}$$

(3) Space charge region (Depletion region)

Current contribution from the space charge region J_{scr} is described as the difference between the carrier generation rate g and the recombination rate r. Recombination occur radiatively or nonradiatively (typically via SRH processes). The carrier generation current J_{gen}, radiative recombination current J_{rad}, SRH recombination current J_{SRH} can be described as

$$J_{gen} = \int_{AM1.5} j_{gen}(E)dE = \int_{AM1.5} q(1-R)Fe^{-\alpha(x_p - w_p)}(1 - e^{-\alpha(w_p + w_p)})dE, \tag{2-26}$$

$$J_{rad} = q\int_{-w_p}^{w_n} \frac{2\pi}{h^3 c^2}\left[\int_0^\infty \frac{\alpha(E)E^2}{e^{(E-qV)/kT} - 1}dE - \int_0^\infty \frac{\alpha(E)E^2}{e^{E/kT} - 1}dE\right]dx \approx q\int_{-w_p}^{w_n} B_{rad}n_i^2(e^{\frac{qV}{kT}} - 1)dx, \tag{2-27}$$

$$J_{SRH} = q\int_{-w_p}^{w_n} \frac{np - n_i^2}{\tau_n(p + p_t) + \tau_p(n + n_t)}dx \approx \frac{qn_i(w_n + w_p)}{\sqrt{\tau_n \tau_p}}\frac{2\sinh(qV/2kT)}{q(V_{bi} - V)/kT}\frac{\pi}{2}, \tag{2-28}$$

where $j_{gen}(E)$ is the photon-energy E component of the carrier generation current, B_{rad} is the radiative recombination coefficient, p_t, n_t, τ_n, τ_p are the trap-center densities and the recombination time constants for holes and electrons, respectively [72]. For the approximation in (2-28), it is assumed that the quasi Fermi levels are constant in the space charge region, and that the vacuum level changes linearly along the *x*-axis [72]. Using these equations, the net generation current in the space charge region can be

$$J_{scr} = J_{gen} - J_{rad} - J_{SRH} \; . \tag{2-29}$$

The current-voltage characteristic of a solar cell under light illumination is then given as

$$J(V) = J_n(-w_p) + J_p(w_n) + J_{scr} \; . \tag{2-30}$$

Importantly, $J_n(-w_p)$, $J_p(w_n)$ and J_{scr} are expressed as the sum of two terms: one representing light absorption, and the other representing the bias dependency. Therefore, the photocurrent J_L attributed to light absorption can be simply given by substituting $V = 0$ as

$$J_L = J(0) = \int_{AM1.5} [j_{illu,n}(E, -w_p) + j_{illu,p}(E, w_n) + j_{gen}(E)] dE \; . \tag{2-31}$$

The dark current is obtained by substituting $F = 0$ in the eq. (2-20), (2-24) and (2-26). Since the bias dependent terms in $J_n(-w_p)$, $J_p(w_n)$, and J_{rad} are approximately proportional to $(e^{qV/kT} - 1)$ and J_{SRH} is approximately proportional to $(e^{qV/2kT} - 1)$, the dark current can be simply approximated as sum of the two diode characteristics with ideal factors of 1 and 2 as

$$J_{dark}(V) \approx -J_1(e^{\frac{qV}{kT}} - 1) - J_2(e^{\frac{qV}{2kT}} - 1) \; . \tag{2-32}$$

In an ideal solar cell, non-radiative recombination does not occur, and therefore, its current-voltage characteristic can be expressed as superposition of photocurrent J_L and the dark current J_{dark} as

$$J(V) = J_L - J_0(e^{\frac{qV}{kT}} - 1) \; , \tag{2-33}$$

which is the same expression as the eq. (1-3). Since the short circuit current J_{sc} equals to J_L as can be seen in the eq. (2-31), the open circuit voltage V_{oc} can be written as

$$V_{oc} = \frac{kT}{q} \ln\left[\frac{J_{sc}}{J_0} + 1\right] . \tag{2-34}$$

Consequently, the energy conversion efficiency is given as

$$\eta = \frac{[J(V) \cdot V]_{max}}{\int_0^\infty E \cdot F(E) dE} = \frac{J_{sc} \cdot V_{oc} \cdot FF}{\int_0^\infty E \cdot F(E) dE} \; . \tag{2-35}$$

where *FF* is the fill-factor, which is the ratio of the shaded-area in Fig. 1-7 to the area determined by $J_{sc} \times V_{oc}$.

Quantum Efficiency (QE) is defined as the ratio of the number of electrons extracted by the external circuit to the number of either illuminated photons or absorbed photons. The former is called external QE (EQE), and the latter is called internal QE (IQE):

$$EQE = \frac{\{j_n(E,-w_p) + j_p(E,w_n) + j_{gen}(E)\} - J_{dark}}{qF(E)},$$

(2-36)

$$IQE = \frac{\{j_n(E,-w_p) + j_p(E,w_n) + j_{gen}(E)\} - J_{dark}}{q(1-R(E))F(E)(1-e^{-\alpha(E)(x_p+x_n)})}.$$

(2-37)

QE can be defined bias-dependently, but it is mostly characterized under short circuit condition as one of the widely-used evaluation measures for solar cells.

2.2 Fundamental physics in superlattice

In this section, several important physics related to InGaAs/GaAsP superlattice solar cells are summarized: quantum confinement in quantum wells consisting of strained layers, light absorption in quantum wells, and carrier escape from the wells.

2.2.1 Bandgap in quantum wells

2.2.1.1 Effects on strains on the bandgap

When lattice mismatched materials are grown on substrates, the epitaxial layers are strained. In InGaAs/GaAsP SLs on GaAs on Ge substrates, GaAsP with a smaller lattice constant is tensely strained, and InGaAs with a larger lattice constant is compressively strained.

Strain in zinc blende crystals such as InGaAsP alloy can be described with biaxial stresses, and change in the lattice constant in the lateral direction is accompanied with its change in the vertical direction. Strain ε and stress σ tensors are described as

$$\sigma_i = \sum_j c_{ij}\varepsilon_j,$$

(2-38)

where c_{ij} is the elastic stiffness constant. Assuming that the lattice constant of the substrate and the epitaxial layer are a_{sub} and a_{epi}, respectively, the strain due to lattice mismatch is

$$\varepsilon_{xx} = \varepsilon_{yy} = \varepsilon = \frac{a_{sub} - a_{epi}}{a_{epi}} = \Delta a, \quad \varepsilon_{zz} = 0, \quad \varepsilon_{xy} = \varepsilon_{yz} = \varepsilon_{zx} = 0,$$

(2-39)

where z is the growth direction. Due to lattice mismatch, the grown plane is subjected to biaxial stress while no stress is produced in the growth direction, and thus

$$\sigma_{xx} = \sigma_{yy} = \sigma, \quad \sigma_{zz} = 0, \quad \sigma_{xy} = \sigma_{yz} = \sigma_{zx} = 0.$$

(2-40)

From(2-39) and (2-40), the elastic stiffness tensor can be simplified as

$$
\begin{bmatrix} \sigma \\ \sigma \\ 0 \\ 0 \\ 0 \\ 0 \end{bmatrix} = \begin{bmatrix} c_{11} & c_{12} & c_{12} & 0 & 0 & 0 \\ c_{12} & c_{11} & c_{12} & 0 & 0 & 0 \\ c_{12} & c_{12} & c_{11} & 0 & 0 & 0 \\ 0 & 0 & 0 & c_{44} & 0 & 0 \\ 0 & 0 & 0 & 0 & c_{44} & 0 \\ 0 & 0 & 0 & 0 & 0 & c_{44} \end{bmatrix} \begin{bmatrix} \varepsilon \\ \varepsilon \\ \varepsilon_{zz} \\ 0 \\ 0 \\ 0 \end{bmatrix},
\tag{2-41}
$$

from which the strain in the growth direction ε_{zz} can be derived as

$$
\varepsilon_{zz} = -\frac{2c_{12}}{c_{11}}\varepsilon .
\tag{2-42}
$$

Change of the conduction band-edge and the valence band-edge induced by strain can be derived by $\mathbf{k \cdot p}$ perturbation theory using Pikus-Bir Hamiltonian [72]. The volume deformation strain shifts the edges of both the conduction and the valence bands by

$$
\Delta E_{hy} = -a(\varepsilon_{xx} + \varepsilon_{yy} + \varepsilon_{zz}) = -2a\frac{c_{11} - c_{12}}{c_{11}}\Delta a .
\tag{2-43}
$$

where a is the hydrostatic deformation potential.
Shear deformation strain splits the valence band of heavy holes and that of light holes by

$$
\Delta E_{sh} = -b(\varepsilon_{xx} + \varepsilon_{yy} - 2\varepsilon_{zz}) = -2b\frac{c_{11} + 2c_{12}}{c_{11}}\Delta a .
\tag{2-44}
$$

where b is the shear deformation potential. The bandgap for heavy hole $E_{e\text{-}hh}$ and for light hole $E_{e\text{-}lh}$, can be approximated using (2-43) and (2-44) as

$$
E_{e-hh} = E_g - \Delta E_{hy} + \frac{1}{2}\Delta E_{sh} .
\tag{2-45}
$$

$$
E_{e-lh} = E_g - \Delta E_{hy} - \frac{1}{2}\Delta E_{sh} - \frac{(\Delta E_{sh})^2}{2\Delta_{SO}} .
\tag{2-46}
$$

where Δ_{SO} is the spin-orbit interaction energy and generally its contribution is very small. Therefore, the degenerated valence bands at the Γ point for heavy holes and light holes are split by strain, resulting in a narrower/wider bandgap for heavy holes with compressive/tensile strain, respectively. Fig. 2-5 shows a schematic of band deformation due to strain [75].
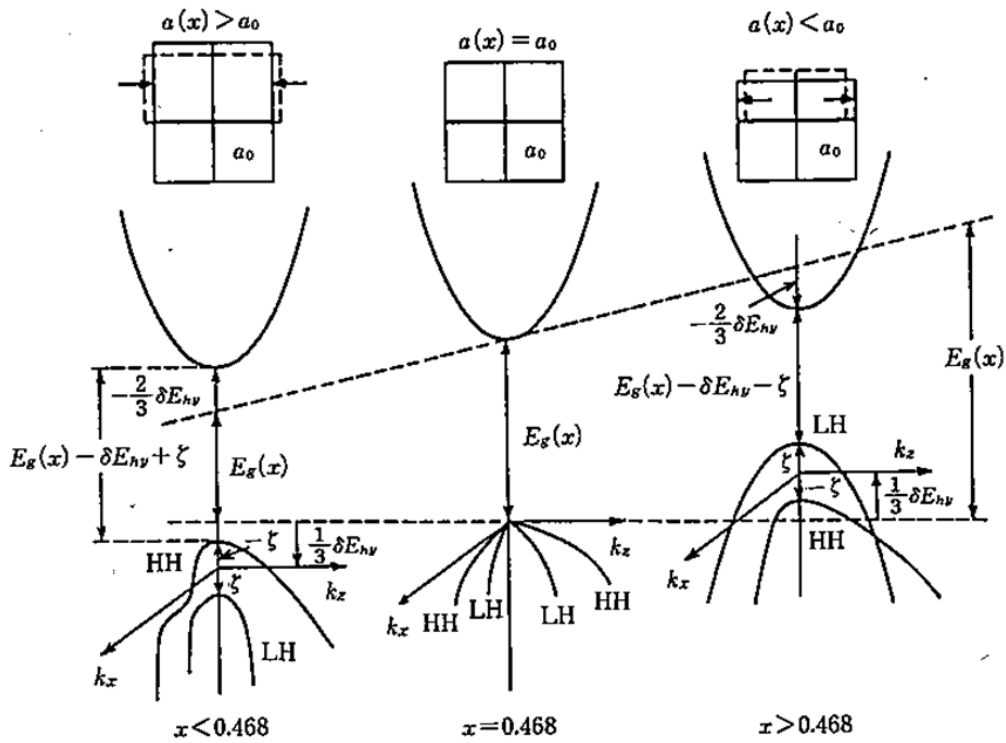
Fig. 2-5 Deformation of a band diagram in bulk induced by strain [75].

2.2.1.2 Quantum confinement in quantum wells

Carriers inside the quantum wells that compose a SL have discrete energies in the layer-stack direction (z) due to the quantum confinement effects. The Schrödinger equation for the envelop function in the z-direction $\phi(z)$ is written as

$$\left[-\frac{\hbar^2}{2m}\frac{d^2}{dz^2}+V(z)\right]\phi(z)=E\phi(z).$$ (2-47)

where $V(z)$ is the potential profile, m is the effective mass, and E is the energy of the carrier. Assuming a simple quantum wells system where no electric field is present as depicted in the Fig. 2-6, $V(z)$ can be written as

$$V(z)=\begin{cases} 0 \ \text{(well)} \\ V_B \ \text{(barrier)} \end{cases}$$ (2-48)

where V_B is the constant potential barrier height.

The general solutions of the Schrödinger equation (2-47) for the barrier and the well regions are expressed as

$$\text{(barrier)} \quad \phi(z) = A\exp(\kappa z) + B\exp(-\kappa z), \tag{2-49}$$

$$\text{(well)} \quad \phi(z) = C\sin(kz) + D\cos(kz), \tag{2-50}$$

where

$$k = \frac{\sqrt{2mE}}{\hbar}, \quad \kappa = \frac{\sqrt{2m(V_B - E)}}{\hbar}. \tag{2-51}$$

The boundary condition for the envelope functions is that

$$\phi(z), \quad \frac{1}{m}\frac{d\phi}{dz} \tag{2-52}$$

must be continuous at the hetero interfaces.
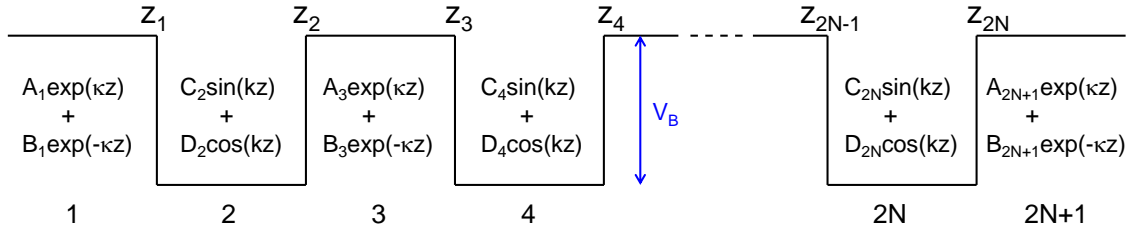
Fig. 2-6   Potential profile of multiple quantum wells with a period number of *N* and a constant barrier height of V_B. $z_1 \sim z_{2N}$ represent the boundaries between wells and barriers.

In a multiple quantum wells (MQW) with a period number of *N*, which is shown in the Fig. 2-6, the boundary conditions at all the interfaces ($z = z_1, z_2, z_3, \ldots.$) must be satisfied. Using

$$M_W = \begin{pmatrix} \sin(kz) & \cos(kz) \\ \dfrac{k}{m_W}\cos(kz) & \dfrac{-k}{m_W}\sin(kz) \end{pmatrix}, \quad M_B = \begin{pmatrix} \exp(\kappa z) & \exp(-\kappa z) \\ \dfrac{\kappa}{m_B}\exp(\kappa z) & \dfrac{-\kappa}{m_B}\exp(-\kappa z) \end{pmatrix}, \tag{2-53}$$

the boundary conditions at each interface can be described as

$$M_B(z_{2j-1})\begin{pmatrix} A_{2j-1} \\ B_{2j-1} \end{pmatrix} = M_W(z_{2j-1})\begin{pmatrix} C_{2j} \\ D_{2j} \end{pmatrix}, \quad M_W(z_{2j})\begin{pmatrix} C_{2j} \\ D_{2j} \end{pmatrix} = M_B(z_{2j})\begin{pmatrix} A_{2j+1} \\ B_{2j+1} \end{pmatrix}, \tag{2-54}$$

where *j* is an integer number (1, 2, 3, …., *N*), and thus the following matrix equation holds.

$$\begin{pmatrix} A_1 \\ B_2 \end{pmatrix} = M_B(z_1)^{-1} M_W(z_1) M_W(z_2)^{-1} M_B(z_2) \cdots M_W^{-1}(z_{2N}) M_B(z_{2N}) \begin{pmatrix} A_{2N+1} \\ B_{2N+1} \end{pmatrix}$$
$$= \begin{pmatrix} M_{11} & M_{12} \\ M_{21} & M_{22} \end{pmatrix} \begin{pmatrix} A_{2N+1} \\ B_{2N+1} \end{pmatrix}. \tag{2-55}$$

Since $\phi = 0$ at $z = \pm \infty$, $B_1 = A_{2N+1} = 0$, which can be substituted to the eq. (2-55) to obtain

$$M_{22}(E) = 0. \tag{2-56}$$

Energies that satisfy the eq. (2-56) are eigen-energies in the z-direction. All M_B and M_W are uniquely determined by each eigen-energy E, and thus the coefficients A, B, C, and D for the wave function in the individual layers are also determined as relative values (matrix transfer method). When interlayers with an intermediate potential of $V_I (< V_B)$ are inserted between wells and barriers, the eigen-energy E can be similarly obtained by the matrix transfer method by considering that the wave function in the interlayer can be written in the expression of (2-49) if $E < V_I$ or (2-50) if $E > V_I$.

In a MQW system with a period number of N, the wave functions corresponding to each eigen-energy obtained in the case of single quantum well (SQW) are coupled among the wells and are split into N states. A set of the split eigen-states can be regarded as a miniband when the energy gap among the states are small with a sufficiently large N.

2.2.2　Light absorption in quantum wells

In a bulk semiconductor, the wave functions for electrons in the valence band and the conduction band are described by the Bloch's theorem as

$$\psi_{V,\mathbf{k_V}}(\mathbf{r}) = u_{V,\mathbf{k_V}}(\mathbf{r}) \exp(i\mathbf{k_V} \cdot \mathbf{r}) \tag{2-57}$$

$$\psi_{C,\mathbf{k_C}}(\mathbf{r}) = u_{C,\mathbf{k_C}}(\mathbf{r}) \exp(i\mathbf{k_C} \cdot \mathbf{r}) \tag{2-58}$$

where $u_{V,\mathbf{k_V}}(\mathbf{r})$ and $u_{C,\mathbf{k_C}}(\mathbf{r})$ are the functions with periodicity of the lattice. The probability that an electron in the valence band with an energy of $E_V(\mathbf{k_V})$ is excited by a photon to a state in the conduction band with energy of $E_C(\mathbf{k_C})$ can be derived by the Fermi's golden rule using a Hamiltonian in which the electromagnetic field is expressed with vector potentials. Considering that absorption of photons with energy E can take place for various electron wavenumbers, the light absorption coefficient $\alpha(E)$ is given as the sum for all the possible transitions as

$$\alpha(E) = \frac{\pi q^2 \hbar}{m_0^2 \varepsilon_0 cnE} \sum_{\mathbf{k_V}, \mathbf{k_C}} |M|^2 \left[f_V(E_V(\mathbf{k_V})) - f_C(E_C(\mathbf{k_C})) \right] \delta(E_C(\mathbf{k_C}) - E_V(\mathbf{k_V}) - E), \tag{2-59}$$

where q is the elementary charge, m_0 is the free electron mass, ε_0 is the vacuum permittivity, c is the light velocity, n is the refractive index of the semiconductor, $f_V(E)$ and $f_C(E)$ are the Fermi distribution

functions for each energy states in the valence band and the conduction band, respectively, and M is the angular momentum matrix element. For the case of bulk material, M can be expressed as

$$M = \int u_{C,\mathbf{k}_C}(\mathbf{r}) * (\mathbf{e} \cdot \mathbf{p}) \, u_{V,\mathbf{k}_V}(\mathbf{r}) \, d\mathbf{r} = M_0 \delta(\mathbf{k}_C, \mathbf{k}_V), \tag{2-60}$$

where $\mathbf{e}$ is the unit vector of the vector potential for the electromagnetic field, and $\mathbf{p}$ is the momentum operator. The eq. (2-60) represents the conservation law with respect to the wave number for direct transitions.

For a quantum well where electrons are one dimensionally confined (in the z direction), the eigen-functions have to be expressed as

$$\psi_{V,\mathbf{k}_V}(\mathbf{r}) = u_{V,\mathbf{k}_V}(\mathbf{r}) \exp[i(k_{V,x}x + k_{V,y}y)]\phi_{h,n_h}(z) \tag{2-61}$$

$$\psi_{C,\mathbf{k}_C}(\mathbf{r}) = u_{C,\mathbf{k}_C}(\mathbf{r}) \exp[i(k_{C,x}x + k_{C,y}y)]\phi_{e,n_e}(z) \tag{2-62}$$

where ϕ_{h,n_h} and ϕ_{e,n_e} are the envelope functions in the z direction [76]. M is then expressed as

$$M = M_0 \delta(\mathbf{k}_{C//}, \mathbf{k}_{V//}) \cdot \left\langle \phi_{e,n_e} \middle| \phi_{h,n_h} \right\rangle, \tag{2-63}$$

where $\mathbf{k}_{C//}$ and $\mathbf{k}_{V//}$ are the wave number vectors in the x-y plane.

The light absorption coefficient are described as the sum for the available transitions, in which conservation laws for wave number and energy are satisfied. Assuming that the conduction and the valence band can be approximated as parabolic bands, the absorption coefficient in a bulk is derived as

$$\alpha_{\text{bulk}}(E) = \frac{q^2 (2\mu_r)^{3/2} |M_0|^2}{2\pi m_0^2 \varepsilon_0 c n E \hbar^2} (E - E_g)^{1/2}[F_V(E) - F_C(E)], \tag{2-64}$$

where E_g is the bandgap, and μ_r is the reduced mass, which is defined as

$$\frac{1}{\mu_r} = \frac{1}{m_e*} + \frac{1}{m_h*}, \tag{2-65}$$

where m_e* and m_h* are effective masses for an electron and a hole, respectively. $F_V(E)$ and $F_C(E)$ are the rewritten Fermi distribution terms in eq. (2-59) as functions of the photon energy, and they are expressed as

$$F_V \equiv \frac{1}{1 + \exp\left\{ -\left(\dfrac{\mu_r}{m_h*}\right)\dfrac{E - E_g}{kT} - \dfrac{E_{F,V} - E_V}{kT} \right\}}, \tag{2-66}$$

$$F_C \equiv \frac{1}{1 + \exp\left\{ \left(\dfrac{\mu_r}{m_e*}\right)\dfrac{E - E_g}{kT} - \dfrac{E_{F,C} - E_C}{kT} \right\}}, \tag{2-67}$$

where $E_{F,V}$ and $E_{F,C}$ are quasi-Fermi energy for the conduction band and the valence band, respectively.

The light absorption coefficient in a quantum well with a well thickness of L_W, on the other hand, is derived as

$$\alpha_{QW}(E) = \frac{1}{L_W} \cdot \frac{q^2 \hbar |M_0|^2}{m_0^2 \varepsilon_0 cnE} \left(\frac{\mu_r}{\hbar^2}\right) \sum_{n_e, n_h} \Theta(E - E_{QW}) \left| \left\langle \phi_{e,n_e} \middle| \phi_{h,n_h} \right\rangle \right|^2 [F_{V,n_h}(E) - F_{C,n_e}(E)], \quad (2\text{-}68)$$

where Θ is the step function representing the density of states. E_{QW} is the quantized transition energy, which is the sum of the bandgap of the well material (E_g) and the eigen-energies in the conduction and valence bands ($E_{C,n}$ and $E_{V,n}$):

$$E_{QW} = E_g + E_{C,n_e} + E_{V,n_h} . \quad (2\text{-}69)$$

The Fermi distribution functions in (2-68) are described as

$$F_{V,n_h} \equiv \frac{1}{1 + \exp\left\{ -\left(\frac{\mu_r}{m_h *}\right) \frac{E - E_{QW}}{kT} - \frac{E_{F,V} - E_V + E_{V,n_h}}{kT} \right\}} , \quad (2\text{-}70)$$

$$F_{C,n_e} \equiv \frac{1}{1 + \exp\left\{ \left(\frac{\mu_r}{m_e *}\right) \frac{E - E_{QW}}{kT} - \frac{E_{F,C} - E_C - E_{C,n_e}}{kT} \right\}} . \quad (2\text{-}71)$$

In the derivation of eq. (2-68), the summation of the absorption coefficient for each transition with respect to the **k** vector is given as the product of the summation in the *x-y* plane and that in the *z*-directions. The former term can be obtained by two dimensional integral with respect to $\mathbf{k}_{//}$. The latter term is given as the sum with respect to the quantum number *n* due to the discrete levels, which is then divided by the well thickness L_W taking account of the number of states per unit width.

As indicated in the eq. (2-68), the probability for the electric dipole transition in a quantum well is proportional to the overlap integral of the electron wave function and the hole wave function. Therefore, transition between states with different parities, e.g. 1e-2hh, is forbidden. In an infinite potential well, the overlap function is zero unless the quantum number is conserved ($n_e = n_h$), and thus only transitions between the same quantum numbers, e.g. 1e-1hh, 2e-2lh, are possible. In a finite potential well, however, transitions between different quantum numbers is possible if the parity is the same, e.g. 1e-3hh, because of the different shape of the envelope functions for an electron and for a hole with different potential heights and effective masses, but their probability is quite low. Furthermore, under strong electric field, the symmetry of the wave function is distorted and thus the transitions with $n_e \neq n_h$ becomes more apparent.

2.2.3 Carrier escape from quantum wells

The carrier escape from a quantum well is typically categorized into two mechanisms: thermionic escape and tunneling escape. The two processes are competing each other in real SL structure.

2.2.3.1   Thermionic escape

Carriers with energy above the potential height, which is in the continuum states, can be thermionically transported over the barriers. The electron density with energy $E \sim E+dE$ assuming 3D density of states can be written as

$$dn = \frac{1}{2\pi^2}\left(\frac{2m_e}{\hbar^2}\right)^{3/2}\sqrt{E-E_C} \cdot \exp\left(-\frac{E-E_F}{kT}\right)dE \;, \tag{2-72}$$

where m_e is the effective electron mass, E_C is the conduction band energy, and E_F is the Fermi level. The total carrier density n can be written as

$$n = \int_{E_C}^{\infty}dn = 2\left(\frac{m_e kT}{2\pi\hbar^2}\right)^{3/2} \cdot \exp\left(-\frac{E_C-E_F}{kT}\right). \tag{2-73}$$

Since E - E_C is the kinetic energy of the electrons, the thermionic emission current in the z direction when the electrons in the conduction band are subjected to a potential barrier with energy of V is given by

$$\begin{aligned}J_{thermionic} &= q\int_{E_C+V}^{\infty} v_z dn \\ &= qn\sqrt{\frac{kT}{2\pi m_e}}\exp\left(-\frac{V}{kT}\right).\end{aligned} \tag{2-74}$$

where the eq. (2-73) is used for the expression for E_F [77].

The thermionic emission current for holes in the valence band can be similarly derived.

Generalizing the eq. (2-74) to the carriers inside the quantum wells with quantized energies, the time constant of the thermionic escape can be written as

$$\begin{aligned}\frac{1}{\tau_{thermionic}} &= \frac{J_{thermionic}}{qnL_W} \\ &= \frac{1}{L_W}\sqrt{\frac{kT}{2\pi m_W}}\exp\left(-\frac{\Delta E_{C,V}-E_n-qFL_W/2}{kT}\right).\end{aligned} \tag{2-75}$$

where m_W is the effective mass in the well region, L_W is the well thickness, $\Delta E_{C,V}$ is the offset potential for electrons in the conduction band and holes in the valence band, E_n is the n-th eigen-energy of the corresponding carrier measured from the center of the well, and F is the electric field [78]. Note that the eq. (2-73) for the total carrier density assumes three dimension for the carrier density at the entire energy range in the well region, and thus the derived escape time here is an approximated expression.

Strictly speaking, 2D density of state has to be considered for the energy below the potential barrier, at which carriers are confined and quantized. However, the (2-75) gives general trends of thermionic transport in SL; the thermionic escape time becomes exponentially longer as the well becomes deeper and that the electric field plays an important rule to facilitate this process.

2.2.3.2   Tunneling escape

Carriers inside wells with energy below the potential barriers can be transported via tunneling escape. The time constant for the transport of a carrier through a set of a well and a barrier τ_{tunnel} is given as the product of the transmittance per barrier T and the inverse of the transport time per well. Assuming WKB approximation for T, τ_{tunnel} can be thus described as

$$
\begin{aligned}
\frac{1}{\tau_{tunnel}} &= \frac{v_x}{L_W} \exp\left[-\frac{2}{\hbar} \int_0^{L_B} \sqrt{2m_B(V(z) - E_n)}\,dz \right] \\
&= \frac{1}{L_W} \sqrt{\frac{2E_n}{m_W}} \exp\left[-\frac{2}{\hbar} \int_0^{L_B} \sqrt{2m_B(\Delta E_{C,V} - E_n - qFL_W/2 - qFz)}\,dz \right].
\end{aligned}
\tag{2-76}
$$

where $V(z)$ is the potential profile in the z-direction. The tunneling time increases exponentially with the barrier width L_B and the square root of barrier height $\Delta E_{C,V}$.

Another mechanism of tunneling transport is resonant tunneling, which takes place when a carrier has an energy exactly equal to an eigen-energy in the adjacent quantum well. Carrier transport via this process is feasible when a number of quantum wells are stacked as MQW, and the envelope wave functions in the wells are coupled to form minibands with a finite energy width where resonant tunneling is possible. In most SL or MQW solar cells, the quantum wells are included in the i-region where electric field is present, and thus the minibands easily breaks up into series of localized states.

3   Experimental equipment

3.1 Metal-Organic Vapor Phase Epitaxy (MOVPE)

MOVPE is one of the widely used crystal growth methods for III-V compounds materials, where metal organic gas sources are introduced in a high-temperature reactor, and epitaxial thin-film crystals are grown on substrates. Precursors injected in the reactor with carrier gas such as H_2, are diffused by the concentration gradient between the substrate and the gas flow region. The particular vapor region where the flow rate changes from the substrate surface to the main gas flow region is called boundary layer, in which the source molecules are decomposed by chemical reactions while diffusing. Then, the adatoms or radicals produced by the pyrolysis repeat adsorption, surface migration, and desorption, and finally are incorporated in the crystal. Fig. 3-1 shows the schematic of a horizontal MOVPE reactor (AIX200/4, AIXTRON) used in this research. The liquid metal organic precursors are kept in stainless containers called bubblers, and gas-state sources at the saturated vapor pressure are extracted by bubbling the liquid source with high purity H_2 carrier gas. The saturated vapor pressure for each precursor is dependent on the holding temperature, following the Antoine equations:

$$\log_{10} p_{sat}[\text{Torr}] = A - \frac{B}{T[K]}, \qquad\qquad (3\text{-}1)$$

where A and B are Antoine parameters, and T is the bubbler temperature.

In this research, trimethylgallium (TMGa: $(CH_3)_3Ga$), tryethylgallium (TEGa: $(C_2H_5)_3Ga$), trimethylindium (TMIn: $(CH_3)_3In$) are used as group III sources, and tertiarybutylarsine (TBAs: $(CH_3)_3CAsH_2$) and tertiarybutylphosphine (TBP: $(CH_3)_3CPH_2$) are used as group V sources. For p-type and n-type dopants, dimethylzinc (DMZn: $(CH_3)_2Zn$) and hydrogen sulfide (H_2S) are used, respectively. Note that H_2S is gas state at room temperature at atmospheric pressure and thus is directly injected from a cylinder. The Antoine parameters A, B, melting points T_M, boiling point T_B for each bubbler, and the holding temperatures and pressures in the experiments in this study are summarized in the Table 3-1.

Gas flow in the MOVPE system are all controlled by mass flow controllers and pneumatic valves. Precursors from the bubblers are diluted by H_2, and then either injected into the reactor through the Run-line or discarded into the Vent-line. Since even small change in total gas flow rate in the reactor disturbs the laminar flow and influences on crystal growth, when the precursor injection is switched on/off, dummy H_2 line is simultaneously closed/opened so that the total flow rate in the reactor is

37

always preserved. This control is especially important in growth with frequent gas switching, such as for superlattices. Differential pressure between the Run-line and the Vent-line is also controlled to zero to avoid flow disturbance during injection switching

For crystal growth of III-V compounds, there are several epitaxy techniques besides MOVPE: Liquid Phase Epitaxy (LPE), Molecular Beam Epitaxy (MBE), Atomic Layer Epitaxy (ALE). MOVPE is particularly suitable for mass production among these technologies because simultaneous growth on many substrates is possible in large-scale reactors.
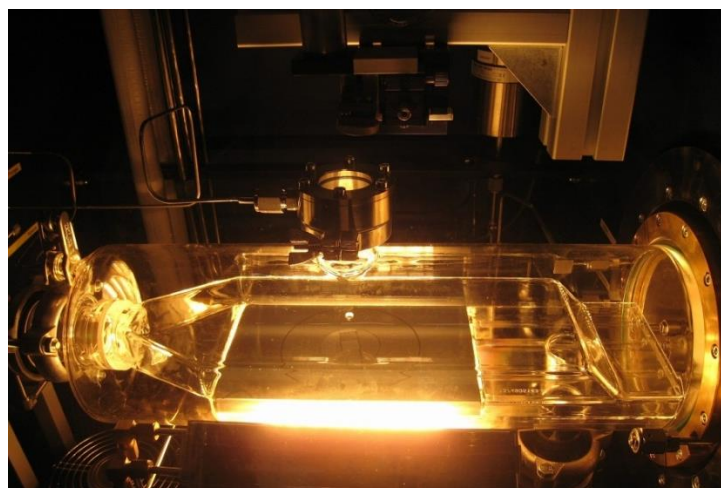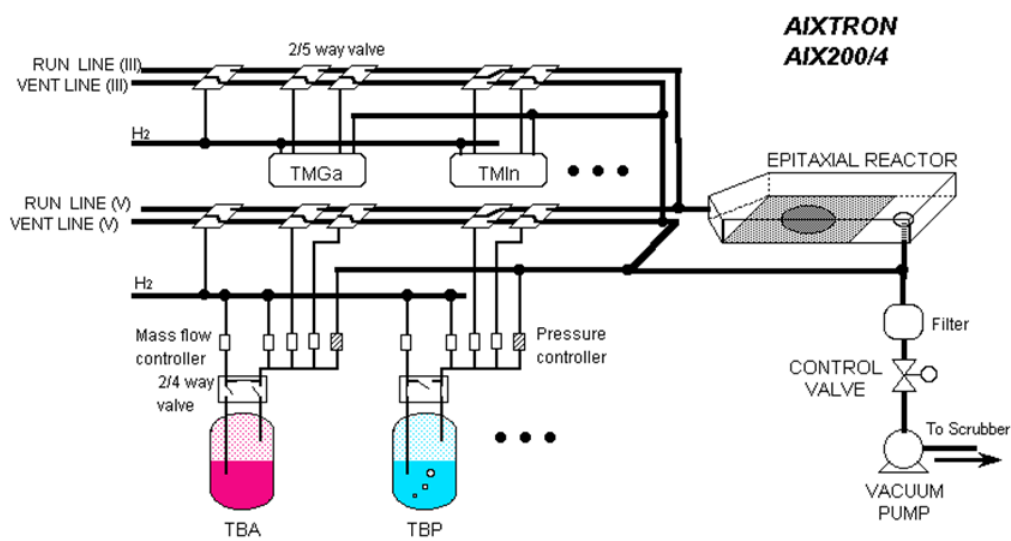

Fig. 3-1: A horizontal MOVPE reactor (AIX200/4, AIXTRON) used in this research

Table 3-1: Properties of metal-organic sources [79], and the holding temperatures ($T_{bubbler}$) and pressure $P_{bubbler}$ for each bubbler.

Source	*A*	*B*	T_M [°C]	T_B [°C]	$T_{bubbler}$[°C]	$P_{bubbler}$ [mbar]
TMGa	8.07	1703	-15.8	55.8	0.0	1000
TEGa	8.083	2162	-82.3	143	17.0	1000
TMIn	10.52	3014	88.4	133.8	17.0	400
TMAl	8.224	2135	15.4	127	17.0	1000
TBAs	7.243	1509	-1	69	17.0	1000
TBP	7.586	1539	4	56.1	17.0	1000
DMZn	7.802	1560	-42	46	-10.0	1000

3.1.1 *In-situ* reflectance monitoring

In-situ (DC/AC) reflectance measurement is a widely used characterizations for real-time growth monitoring in MOVPE [80]. In the MOVPE system used in this research, a commercial system (EpiR-M TT, Laytec) in installed for the measurement (Fig. 3-2). The incident light from a Xe lamp is focused on the sample after passing through a polarizer. The light reflected by the sample is subsequently reflected again by an anti-wobble mirror and then go back through the same light path as the incident beam. The returned light is then led through a photoelastic modulator, an analyzer and a monochromator, so that the chosen wavelength of light can be detected.

From AC component of the reflectance, the reflectance anisotropy (RA) can be evaluated. Although the bulk zinc blend crystal structure is isotropic, the atom arrangement on the surface is anisotropic due to surface reconstruction, resulting in angular dependency with periodicity of 180°. The reflectance is also angular dependent due to the optical misalignment such as inclination of the rotation disk, but this periodicity is 360°. To separate these components, the reflectance is monitored for a time period Δt for approximately one rotation, and then fit it with two parameters by extracting the rotation time t_{rot}: the AC component intensity Δr attributed to the anisotropy of the sample (with periodicity of $t_{rot}/2$) and the DC component intensity r including the background fluctuation (with periodicity of t_{rot}). By repeating this short-time measurement and collecting data for each period Δt, the time transient of the reflectance (r and Δr) is obtained.

Using r and Δr, the reflectance anisotropy (RA) is defined as

$$\mathrm{RA} = \frac{\Delta r}{r} = 2 \frac{r_x - r_y}{r_x + r_y}, \tag{3-2}$$

where r_x and r_y are complex reflectivities for the linearly polarized lights which are perpendicular to each other on the wafer, e.g. $r[1\,1\,0]$ and $r[1\,\bar{1}\,0]$ on a $(0\,0\,1)$ surface.

RA is primarily sensitive to the crystal's conditions in the near-vicinity of the surface, and

generally used for detecting surface reconstructions [81, 82], monolayer growth [83, 84] as well as estimating doping concentration [85, 86] and alloy composition [87]. RA can be also applied to the detection of growth abnormality and morphological change during SL growth, since it shows periodic time-transient corresponding to a set of quantum well, and its intensity and signal shape are unchanged if the each periodic unit structure is identical [80, 87, 88].
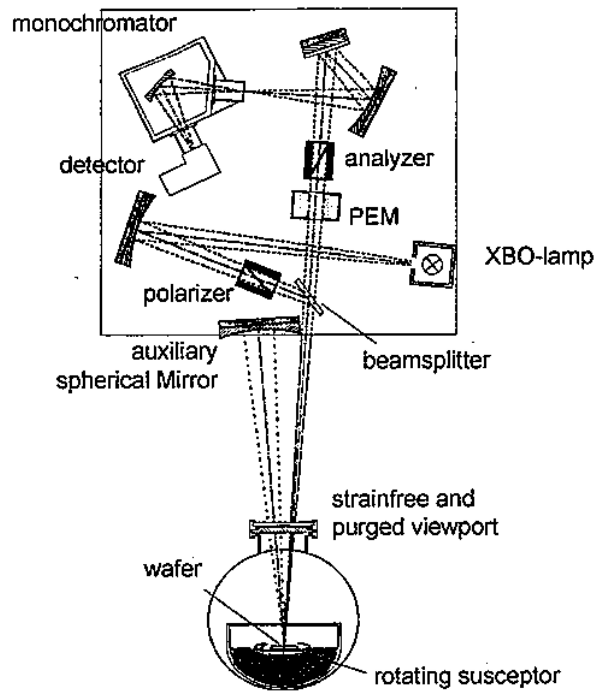
Fig. 3-2   Measurement system for in-situ reflectance monitoring (EpiR-M TT, Laytec)

3.2 X-ray diffraction (XRD)

X-ray diffraction (XRD) is a characterization tool to analyze crystals by irradiating the sample with X-ray and measuring the diffracted beam intensity. The incident X-ray vibrates the electrons in the component atoms in the crystal at the same frequency, thus generating X-ray with the same wavelength of the incident beam as a spherical wave from the atoms. Since this phenomenon is seen as though the incident X-ray were scattered by the lattice atoms, the generated X-ray is called scattered X-ray.

Fig. 3-3 (a) shows the basic mechanism for the diffraction. When X-ray is irradiated on the sample at an incident angle of θ, constructive interference of the scattered X-ray toward the same angle of θ occurs if

$$2d_{hkl} \sin \theta = n\lambda \,, \qquad\qquad (3\text{-}3)$$

where d_{hkl} is the spacing between the (*h k l*) planes of the atomic lattice, *n* is an integer, λ is the wavelength of the incident X-ray. This condition is known as Bragg's law. The scattered X-ray toward other directions for which the Bragg's condition is not satisfied destructively interferes.

Based on this principle, the detailed structure of the samples such as thickness and composition of the epitaxial layers, and the quality of the grown crystals such as lattice relaxation and mosaicity, can be examined by measuring the diffracted beam intensity at various angles for the incident beam and the detector. Fig. 3-3 (b) shows a schematic of diffractometer for such a measurement, in which the two arms, one for the X-ray source and the other for the detector, can independently move to determine the incident and detection angles.

Cu tube is one of the most widely used X-ray sources. In an X-ray tube, the target Cu is bombarded with electrons accelerated from the cathode filament by applying a high voltage (40-60 kV) between them. When the K-shell electrons of Cu is struck by the incident electron and ejected from the orbit, outer-shell electrons subsequently fall into the vacant K-shell, emitting a characteristic X-ray with an energy equivalent to the energy difference between the two orbits. For XRD, Cu-Kα X-ray, for which the emission is associated with the transition from the L-shell to the K-shell, is typically used.

The X-ray emitted from the Cu tube pass through the divergence slit (DS), which suppresses the horizontal dispersion of the incident beam, and is parallelized and purified in terms of the wavelength in the monochromator, in which the X-ray beam is reflected by Ge single crystals and parabolic mirrors. The incident beam is then irradiated on the sample after passing through a soller slit (SS) to reduce the vertical dispersion. The diffracted beam is finally detected by the X-ray counter, for which receiving slit (RS) is often inserted in front in order to enhance the measurement resolution.

The sample is located at the center of the diffractometer. The angles between the incident beam and the sample stage, and between the incident beam and the detector are defined as ω and 2θ. Scan with rotation of ω axis is called rocking curve measurement, and is used for evaluation of mosaicity of the crystal. Scan with $\Delta\omega : \Delta 2\theta = 1 : 2$ around the diffraction point is used to evaluate the crystal quality in a direction vertical to the corresponding crystal plane. For GaAs based epitaxial layer grown on (0 0 1) substrates, for example, ω-2θ scan is often performed around the (0 0 4) diffraction point ($\omega = 33.0239$ º, $2\theta = 66.0479$ º), for which the layer structure in the growth direction can be characterized. If the (0 0 1) plane is completely parallel to the sample stage, the constructive interference of the scattered X-ray takes place when $\omega = \theta$. In practice, however, offset between the ω and θ is generally non-negligible due to manual sample setting. Therefore, alignment of the each axis is typically carried out to makes the diffraction intensity highest prior to the main scan.

The Bragg's law described in the eq. (3-3) is synonymous with the Laue's condition:

$$\vec{H} = \frac{\vec{s}_o - \vec{s}}{\lambda},$$

(3-4)

where $\vec{H}$ is reciprocal lattice vector, $\vec{s}_o$ and $\vec{s}$ are the unit vectors for the incident and the diffracted X-ray, meaning that the constructive interference occur when the scattering vector of the X-ray is equal to $\vec{H}$ of the corresponding plane. Therefore, mapping of the diffracted X-ray intensity by sweeping the ω and 2θ within a particular angle range gives us more detailed information regarding the epitaxial films such as lattice constant and strain.

Since the reciprocal space is the Fourier transform of the real space, strong diffraction peaks are obtained for any periodic structures with larger periodicity than the unit lattice, or superlattice (SL). For example, one dimensional SL stacked in the vertical direction are represented by fringe spots near the substrate peak along the Q_y axis in the reciprocal space map (RSM). The thickness of the unit structure of the SL, which is typically a set of a well and a barrier, is described as

$$L = \frac{\lambda}{2\Delta\theta \cdot \cos\theta_B},$$

(3-5)

where $2\Delta\theta$ is the interval of the diffraction angle between two adjacent fringe peaks, θ_B is the Bragg angle for the substrate plane [86]. Although only the total unit thickness can be estimated by the intervals between the fringe peaks, thickness and compositions for the component layers can be further analyzed by fitting the relative intensities.
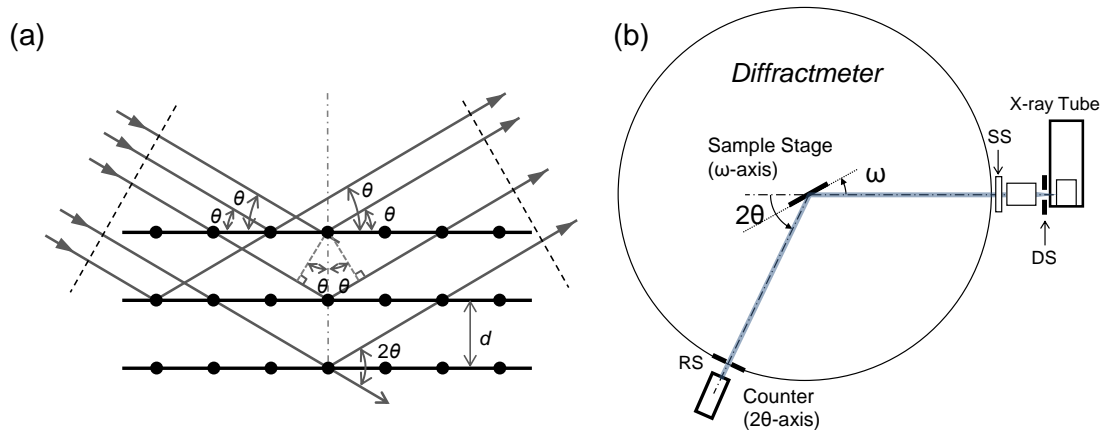

Fig. 3-3   (a) Principle of X-ray diffraction (XRD) by crystal with plane spacing of *d*, and (b) schematic of typical diffractmeter for XRD measurement.

3.3 Solar simulator

The photovoltaic performance of the fabricated solar cells, i.e. I-V and QE, are measured by a solar simulator (CEP-2000LS, Bunkokeiki).

For I-V measurement, 150 W Xe lamp is used as the light source with insertion of an AM1.5G filter (100 mW/cm^2) for 1-sun illumination. For QE measurement, the light from 300 W Xe lamp is monochromated, and led through a wedge ND filter to ensure a constant illumination intensity of 2.5 mW/cm^2. The reciprocal linear dispersion of the diffraction grating in the monochromator is 6 nm/mm. The slit width is 4 mm for sufficient light intensity, and thus the wavelength resolution is 24 nm in the QE spectra.

In order to evaluate the accurate QE values under sunlight, AM1.5 can be illuminated as the bias light for QE measurement. Since the monochromatic light is much weaker than AM1.5, the QE is measured in AC mode using a chopper and a lock-in amplifier, for which the current is converted to voltage by resistance as the input signal. The cell performance is thus measured by four terminal method so that the voltage applied to the solar cell device is independently controlled by the source meter.
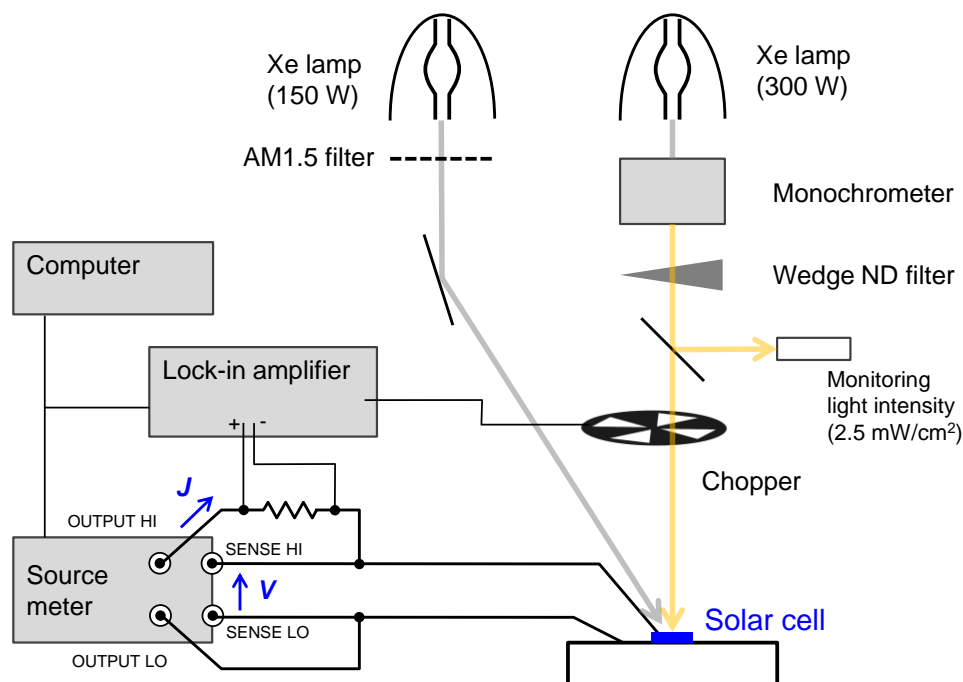

Fig. 3-4   Schematic of a solar simulator setup used in this research

3.4 **Photoluminescence (PL)**

PL spectroscopy is a characterization method for the luminescence due to radiative recombination of photo-generated carriers in a semiconductor. In this research, two types of PL are carried out: continuous wave PL (CWPL) and time resolved PL (TRPL). In CWPL, the luminescence from the sample is measured as a spectrum under continuous illumination by a laser. In TRPL, on the other hand, the time transient of the luminescence from the carriers excited by a short pulse illumination is measured, and thus it is more suitable for investigation of carrier dynamics.

Fig. 3-5 shows the experiment setup for PL measurement in this study. In CWPL, 532 nm DPSS laser (Nd:YVO$_4$) is used for excitation. The luminescent light from the sample passes through a long pass filter to cut the incident light, and is led to a spectrometer (iHR320, HORIBA). The dispersed light was then detected by CCD sensor.

In TRPL setup, 780 nm semiconductor pulse laser (88 ps) is used for excitation, which is repetitively triggered by the measurement unit at a repetition rate of 10 MHz. The time interval for the trigger should be sufficiently longer than the time necessary for the luminescence per excitation to completely diminish. The luminescence light from the sample is led to a monochromator, through which only the chosen wavelength light can come out to be detected by the photomultiplier tube (PMT). The measurement unit integrates the electrical signals from the photon counting unit versus the time after sending the trigger to the laser, and plots them as the time transient of the PL decay.

Since the response time of the system is finite, the measured and plotted PL intensity as a function of the time TRPL(t) is the result of the convolution integral between the actual luminescence decay PL(t) and the instrument response function IRF(t) as

$$\text{TRPL}(t) = \text{PL}(t) * \text{IRF}(t). \tag{3-6}$$

Note that the instrument response time for the TRPL equipment was approximately 0.5 ns, and thus the carrier dynamics faster than time scale cannot be accurately evaluated.
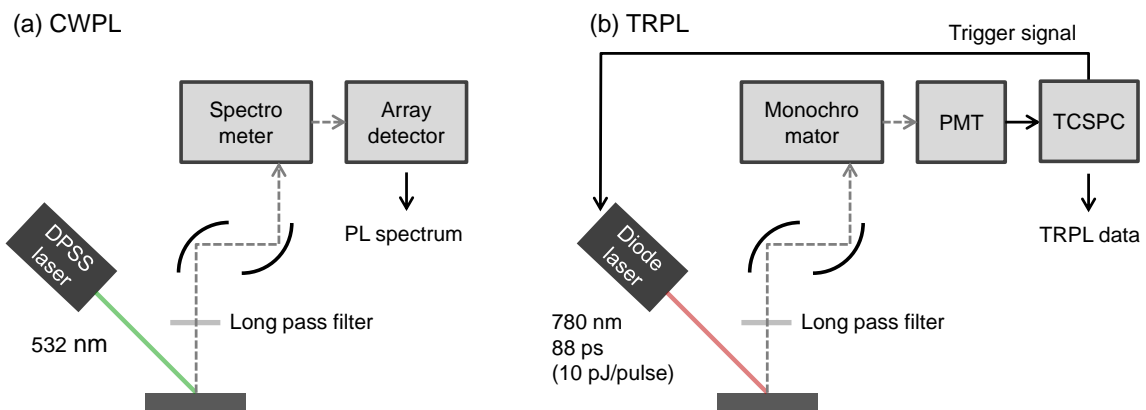

Fig. 3-5　Schematic of measurement setup for (a) CWPL and (b) TRPL

3.5 Fourier transform infra-red spectroscopy (FTIR)

The light absorption by the SL is measured by Fourier transform infrared spectroscopy (FTIR) in this study. As a schematic is shown in the Fig. 3-6, the measurement setup for FTIR consists of a halogen lamp (light source), a Michelson interferometer, and a detector. The white light from the halogen lamp is illuminated on the sample through the Michelson interferometer, where the moving mirror is oscillated at a constant speed so that each wavelength light is modulated with repetition of constructive and destructive interferences at a specific frequency. The transmitted light is detected by an InGaAs detector, and the electrical single is converted to digital signal by an AD converter. The transmission spectrum can then be obtained by Fourier transform of the digital signal.

As a detector for FTIR, pyroelectric sensors such as triglycine sulfate (TGS) and semiconductor sensor such as HgCdTe (MCT) are typically used. TGS is advantageous with respect to the wide detection wavelength range though its sensitivity is low. Semiconductor sensors, on the other hand, have high sensitivity above the bandgap, but cryogenic operation is necessary for some detectors.

FTIR is widely used in mid-infrared region for measurement of light absorption attributed to molecular vibration or rotation. Since the absorption in InGaAs/GaAsP SL is in the near infrared region (850-1100 nm), InGaAs detector is used for the measurement. An advantage of FTIR in comparison with other absorption evaluation method is that it does not use monochromator and thus high wavelength resolution in the spectra can be achieved.
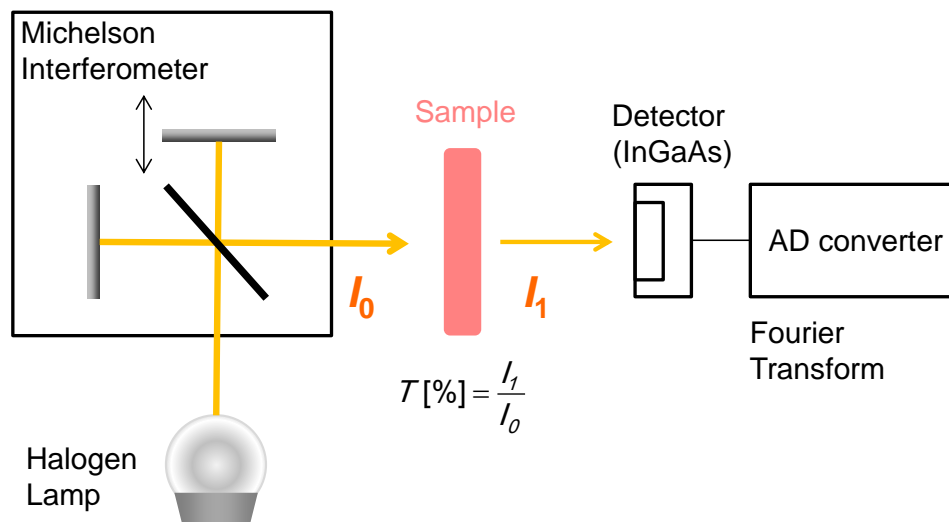

$$T\,[\%] = \frac{I_1}{I_0}$$

Fig. 3-6   Schematic of FTIR measurement.

4 Evaluation of carrier transport in SL solar cells

The major challenge to achieve high performance in SL solar cells is sufficient extraction of the photo-excite carriers, and thus it is very important to examine how the carriers photo-generated in each region of the device are transported under operational condition. As illustrated in Fig. 4-1, however, there are many processes related to carrier transport that occur simultaneously in SL cells, making the interpretation of the measured photovoltaic performance complicated. As mentioned in the chapter 1, currently the most widely used evaluation methods for solar cells are I-V characteristics under sunlight illumination and QE under short circuit condition, but these output characterization alone or simple comparison of macroscopic properties such as V_{oc}, J_{sc}, FF, and efficiency have limitation in revealing the underlying problem in carrier transport in detail.

This research proposes to evaluate SL solar cell by Carrier Collection Efficiency (CCE), which is defined as the fraction of the photo-excited carriers in the p-n junction area that are actually extracted as photo-current. In this chapter, the measurement and the evaluation procedures of CCE is introduced, and their validity will be comprehensively verified. And then two evaluation studies for SL solar cells using CCE will be shown to demonstrate the advantages and effectiveness of the proposed method: 1) the effect of band-flattening of the i-region due to background doping on the carrier transport, and 2) the challenges in carrier transport that emerge when a large number period SL with a desired bandgap of 1.2 eV is incorporated.
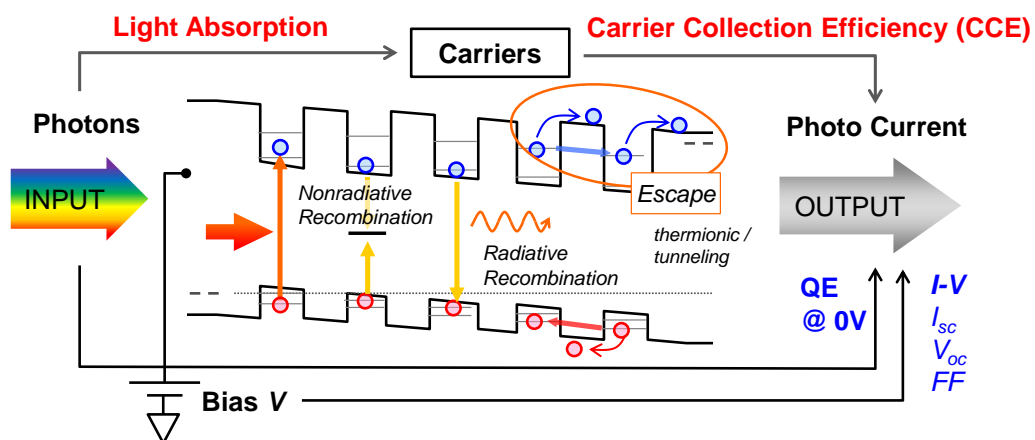

Fig. 4-1   Processes related to carrier transport in SL solar cells.

46

4.1 Carrier transport problem in SL solar cells

In this section, several important scientific knowledge related to carrier transport in SL solar cells that have been reported by other research groups are overviewed.

(1) Effects of well numbers and built-in field

A research group in Imperial College London, which has been one of the leading groups in this field, reported characterization of solar cells with various period number of $In_{0.10-0.11}GaAs$(8 - 9 nm)/$GaAsP_{0.08-0.09}$(18 – 19 nm) SLs. They reported increased efficiency with increase in the well number up to 50-period owing to the enhancement in J_{sc} and preservation of V_{oc} [90]. Beyond 50-period, however, the J_{sc} was not enhanced any longer and V_{oc} was dropped because of the weakened built-in field, resulting in degraded cell efficiency [91] (Fig. 4-2(a)).

Serdiukova et al. [92] characterized 10-period InP/InAsP SL cells with different well widths and compositions and hence various built-in fields. Assuming 100% carrier collection with current saturation at 0 V under sunlight illumination, they reported existence of a threshold built-in field above which total carrier collection becomes possible and V_{oc} becomes higher.

As has been reported by these studies, the electric field in the SLs is essential for efficient carrier transport. To date, however, most researches related to InGaAs/GaAsP system have introduced SLs with relatively shallow wells or limited period number below 70, and thus clarification of the carrier transport problems that would emerge with desired SL properties (period number of 100, bandedge beyond 1000 nm) is required for practical application.
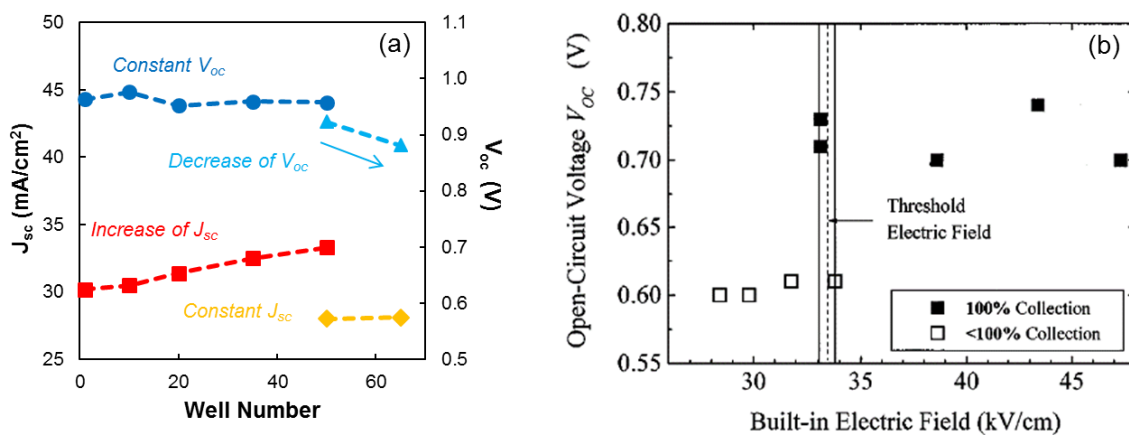

Fig. 4-2 (a) J_{sc} and V_{oc} in InGaAs/GaAsP SL solar cells with various well number (Data from [90] and [91] are plotted on the same graph), (b) Effect of built-in field in InP/InAsP-SL cells on V_{oc} and carrier collection [92].

(2) Effects of carrier escape sequence

An absorbed photon generates an electron and either a heavy hole or a light hole, and ideally, they simultaneously escape from the well and are collected by the circuit. Alemu et al. [93, 94] studied with 10-period InP/InAsP SL solar cells with various well and barrier widths, and reported that the photo-current extraction was affected by the carrier escape sequence and resultant charge accumulation in the wells. They investigated the sequence of the escape process by comparing the activation energy of photoluminescence (PL) and the simulated potential barriers for the carrier in the wells (Fig. 4-3). In InP/InAsP system, light holes are the first to escape in most SL designs, and thus negative charges are accumulated initially in the well region. If the next carriers to escape are electrons, then the net charge in the well is mitigated. If heavy holes escape prior to electrons, on the other hand, the negative charge in the well is accumulated more, resulting in electric screening that locally weakens the electric field and degrades V_{oc} [93].
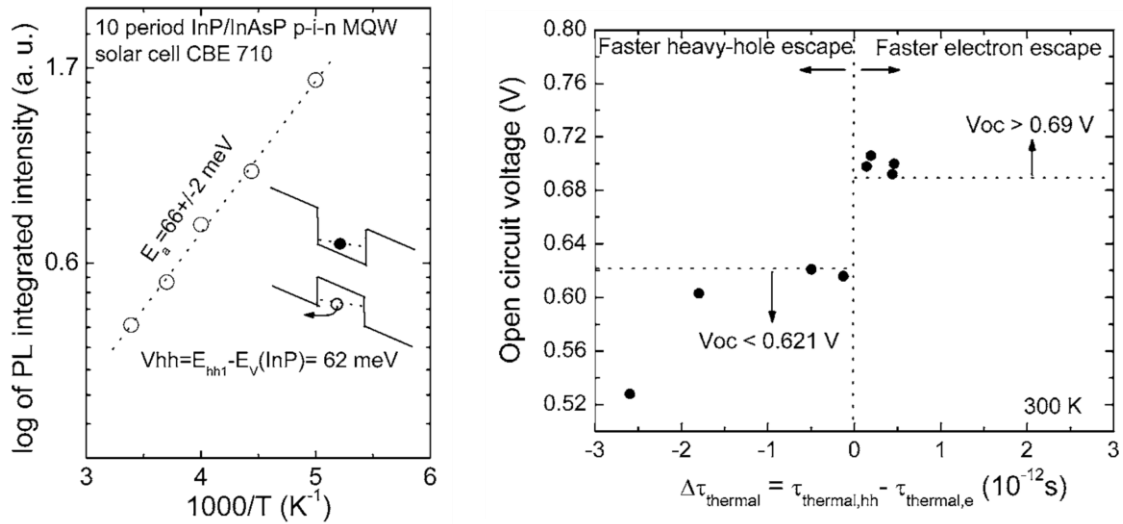
Fig. 4-3   Arrhenius plots of PL from InP/InAsP SL cells where heavy holes escape faster than electrons (left), and the effects of carrier sequence on V_{oc} (right) [93].

(3) Effects of Concentrated illumination

Charge accumulation inside the quantum wells affects the carrier transport dynamics due to electric screening, and this effect becomes more serious with higher carrier densities, in particular under concentrated illumination. Raisky et al. [95] studied room temperature PL of InGaAsP/InP SL solar cells, and reported that the PL becomes less bias-sensitive with strong luminescence remaining at reverse voltage under higher excitation power, a result suggesting that carrier escape is less efficient under concentrated light illumination. Simulation of the band lineup and the net charge density indicated that carriers are more likely to accumulate in the SL region under strong excitation, and

flatten the band of the i-region due to screen effects (Fig. 4-4 (a)).

Terrestrial applications of III-V based solar cells require CPV system to reduce the cell cost, and thus it is very important to clarify the carrier transport problem that especially emerge under highly concentrated illumination.

(4) Mechanism of carrier escape

Nelson et al. [96], Barnes et al. [97], and Zachariou et al. [98] studied photocurrent from AlGaAs/GaAs and InP/InGaAs single quantum well solar cells by selective excitation in the wells at various temperatures (50 K – 300 K) and biases (-0.8 ~ 0.8 V). At low temperature below 100 K, the current remained almost constant at each bias, and thus tunneling transport was suggested to be the dominant process for carrier escape. The photocurrent increased at higher temperatures, and became saturated above 200 K, indicating that the predominant transport mechanism shifted from tunneling to thermionic escape as the temperature increased.
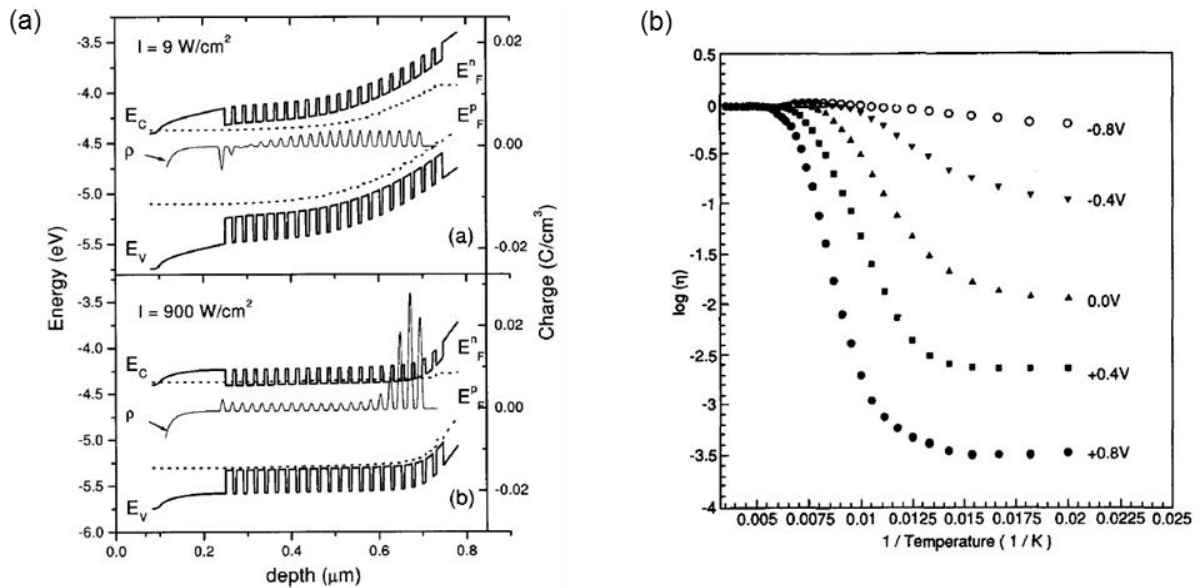

Fig. 4-4   (a) Simulation of the band-lineup and charge accumulation in InGaAsP/InP SL cells under different excitation intensities [95]. (b) Bias and temperature dependence of photo current in an AlGaAs/GaAs single quantum well solar cell [96]

4.2 Superposition approximation in SL solar cells

As shown in the eq. (2-33), the I-V characteristics of an ideal solar cell is given as the superposition of the photocurrent J_L and the dark current J_{dark}. In other words, the current under illumination can be obtained by shifting the diode characteristics by J_L. This approximation requires several conditions to be satisfied [72, 99].

<u>1) The effect of series resistance is negligible.</u>

The I-V characteristics with series resistance R_s and shunt resistance R_{sh} is described as

$$ J = J_L - J_1 \left[e^{\frac{q(V+JR_s)}{kT}} - 1 \right] - J_2 \left[e^{\frac{q(V+JR_s)}{2kT}} - 1 \right] - \frac{V + JR_s}{R_{sh}}, \qquad (4\text{-}1) $$

which can be obtained by the equivalent circuit model shown in Fig. 4-5. J_1 and J_2 are radiative and non-radiative recombination current coefficient respectively. When R_s and the JR_s are sufficiently small, the total current J is given as the sum of J_L and J_{dark} regardless of R_{sh} value. When the effects of R_s is not negligible, then the superposition approximation no longer holds because the voltage applied to the diode ($V+JR_s$) differs between cases with and without illumination at a given external voltage V.
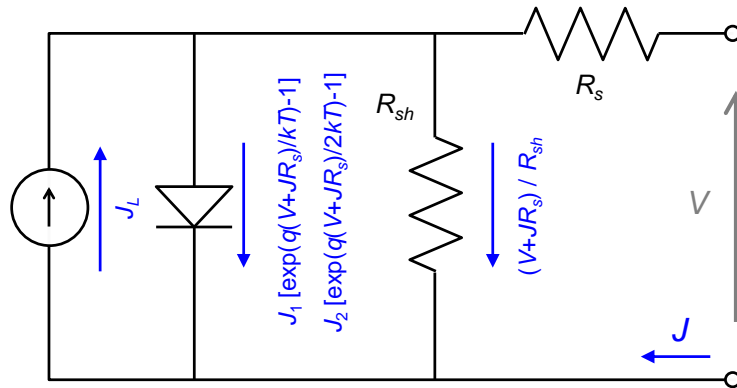
Fig. 4-5   Equivalent circuit of a solar cell with series and shunt resistances.

<u>2) Diode characteristics does not change under illumination.</u>

Diode current basically consists of the diffusion current in the neutral regions and the recombination current in the depletion region. Diode characteristics do not change as long as all the recombination rates are linear to the minority carrier concentration (eq. (2-17)), an approximation which is conserved under low-injection condition. Under high-injection condition due to high applied voltage or concentrated light illumination, however, the minority carrier concentration becomes

comparable to the majority carrier concentration, and thus the recombination rates are super-linear to the minority carrier concentration. In such a situation, the recombination behavior and hence diode characteristics changes with and without light illumination, resulting in inaccuracy of superposition approximation.

3) All the carriers photo-excited in the active region can be collected regardless of the bias.

This condition is the major concern in SL solar cells. As introduced in the previous section, the SL in the i-region blocks the carrier transport, and therefore, photo-excited electrons and holes easily recombine before reaching the n-region and the p-region, respectively. Since the carrier collection becomes more insufficient under a weaker electric field, the photo-current J_L in the eq. (2-33) generally is dependent on the bias V, meaning that superposition approximation with constant J_L does not hold in such devices.

Fig. 4-6 shows typical I-V curves of a GaAs pin cell and a SL solar cell, in comparison between the actually measured $J(V)$ and the ideal curves obtained by superposition approximation $J_{sp}(V)$. In the GaAs cell, $J(V)$ well matches with $J_{sp}(V)$, and superposition approximation is more or less conserved. In a SL cell, on the other hand, the deviation between the two curves becomes larger especially at forward bias, resulting degradation of *FF*. This is because the carrier transport is blocked by the SL, and the J_L is bias-dependently decreases. In this sense, the efficiency of carrier collection without recombination loss can be examined at each bias voltage by evaluating the degradation of the current output from $J_{sp}(V)$.
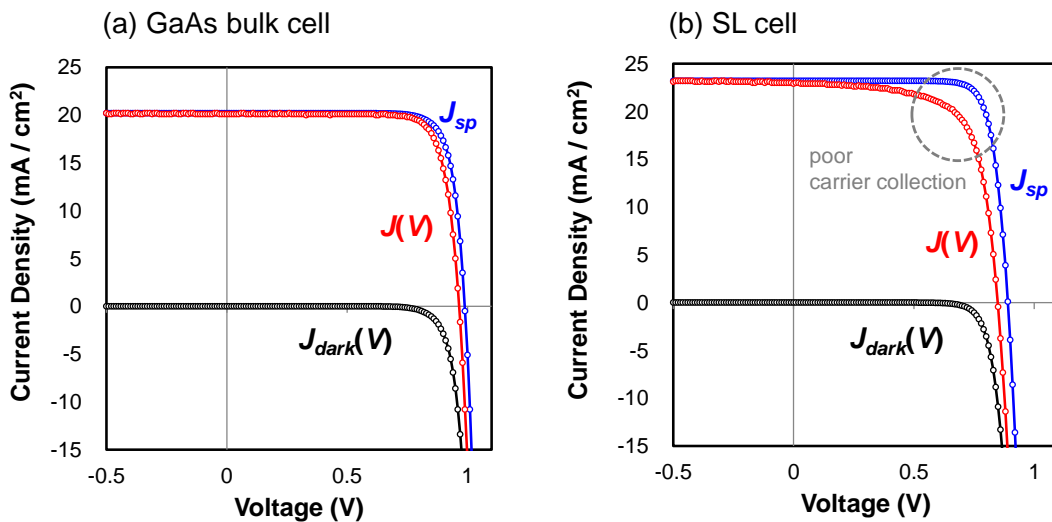

Fig. 4-6   Typical I-V curves of a GaAs pin cell and a SL solar cell, in comparison between the actually measured $J(V)$ and ideal curves obtained by superposition approximation $J_{sp}(V)$

4.3 Carrier Collection Efficiency (CCE)

This research proposes to use Carrier Collection Efficiency (CCE) as an evaluation measure for SL solar cells. CCE is defined as the fraction of carriers photo-excited in the active p-n junction area that are actually collected as photo-current. We use two types of CCE for which the evaluation procedures are explained below: collection efficiency of carriers excited by sunlight ($CCE_{AM1.5}(V)$), and by monochromatic illumination at wavelength of λ ($CCE(\lambda, V)$).

(1) Averaged CCE under sunlight: $CCE_{AM1.5}$

- Measure the currents in the dark $J_{dark}(V)$, and under AM1.5 light $J_{sun}(V)$ at bias of V.
- Calculate the difference between J_{dark} and J_{sun} as the collected current $\Delta J(V)$:

$$\Delta J(V) = J_{sun}(V) - J_{dark}(V) .$$ (4-2)

Since $\Delta J(V)$ is the additional current induced by light illumination, it can be regarded as bias-dependent photocurrent obtained by collection of photo excited carriers.

- Assuming 100% carrier collection when $\Delta J(V)$ is saturated to ΔJ_{sat} at reverse bias, CCE can be estimated as

$$CCE_{AM1.5}(V) = \frac{\Delta J(V)}{\Delta J_{sat}} .$$ (4-3)

$CCE_{AM1.5}$ indicates the total efficiency of the carrier transport in a solar cell under operation.

(2) Monochromatic CCE: $CCE(\lambda, V)$

- Measure the currents under AM1.5 irradiation, $J_{sun}(V)$, and under additional monochromatic light at wavelength λ at bias of V, $J_{mono}(\lambda, V)$
- Calculate the difference between J_{sun} and J_{mono} as the collected current $\Delta J(\lambda, V)$:

$$\Delta J(\lambda, V) = J_{mono}(\lambda, V) - J_{sun}(V) .$$ (4-4)

Since $\Delta J(V)$ is the incremental current induced by the additional monochromatic illumination, it can be regarded as current increase attributed to collection of carriers that are photo-excited at wavelength of λ.

- Assuming 100% carrier collection when $\Delta J(V)$ is saturated to ΔJ_{sat} at reverse bias, CCE can be estimated as

$$CCE(\lambda, V) = \frac{\Delta J(\lambda, V)}{\Delta J_{sat}(\lambda)} .$$ (4-5)

For evaluation of monochromatic CCE, AM1.5 should be illuminated as a bias light so that the estimated CCE (λ, V) reflects the carrier dynamics under actual cell operation under sunlight. In this sense, the intensity of monochromatic light should be sufficiently weaker than sunlight; 2.5 mA/cm^2 is used in this study.

CCE (λ, V) can be also described with QE. QE is typically evaluated at a short circuit condition, but its general expression at bias of V can be written as

$$\mathrm{EQE}(\lambda,V) = \frac{hc}{I\lambda q}[J_{mono}(\lambda,V) - J_{sun}(V)] = \frac{hc}{I\lambda q}\Delta J(\lambda,V) , \qquad (4\text{-}6)$$

where I is the irradiation energy of the monochromatic light, q is the elementary charge, h is the Planck's constant, and c is the light velocity. Note that sunlight is used as bias illumination in this EQE evaluation. (4-5) can be then written as

$$\mathrm{CCE}(\lambda,V) = \frac{\mathrm{EQE}(\lambda,V)}{\mathrm{EQE}_{sat}(\lambda)} , \qquad (4\text{-}7)$$

where $\mathrm{EQE}_{sat}(\lambda)$ is the saturated EQE spectrum at reverse bias.

(a) Averaged CCE under sunlight (AM1.5)

J_{dark}: Dark current
J_{sun}: Current under AM1.5
$\Delta J = J_{sun} - J_{dark}$
ΔJ_{sat}: Saturated ΔJ
$\mathrm{CCE} = \Delta J / \Delta J_{sat}$

(b) Monochromatic CCE

J_{sun}: Current under sunlight
J_{mono}: Current under sunlight and weak monochromatic light
$\Delta J = J_{mono} - J_{sun}$
ΔJ_{sat}: Saturated ΔJ
$\mathrm{CCE} = \Delta J / \Delta J_{sat}$
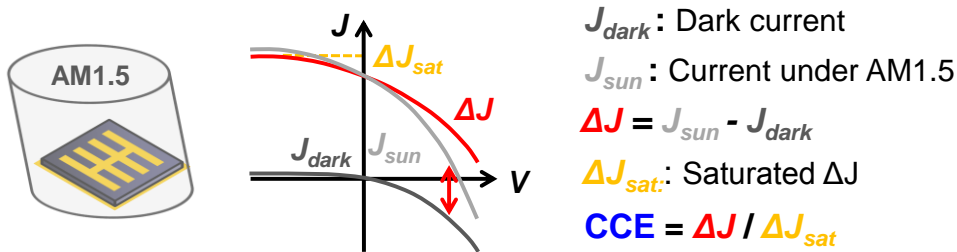
Fig. 4-7   Evaluation procedure of carrier collection efficiency: (a) CCE under AM1.5 illumination, and (b) CCE under monochromatic illumination. (© 2014 IEEE)

Investigation of the bias dependence of the sunlight-induced current $\Delta J(V)$ has been used for solar cell evaluation with a similar concept to $CCE_{AM1.5}$ [97]. In this research, the carrier transport dynamics is more systematically examined by combining wavelength- and bias-dependence of CCE using monochromatic illumination (Fig. 4-8).

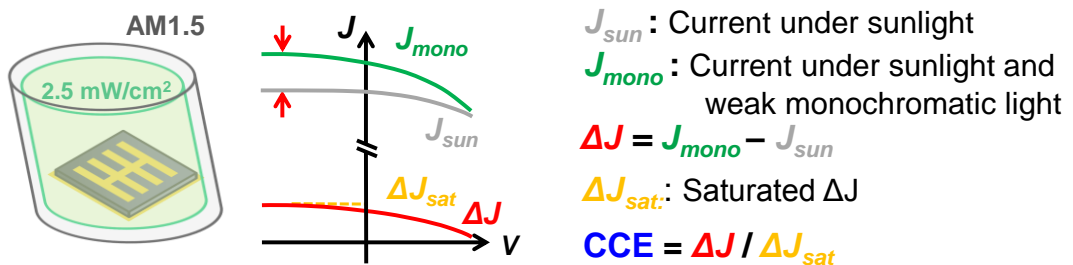In wavelength-dependent evaluation, transport efficiency of the carriers photo-excited in each area of the cell can be examined by changing the illumination wavelength to manipulate the carrier generation distribution. Short wavelength light, in general, has higher absorption coefficient and is thus mostly absorbed in the upper region of the cell above the SL as shown in Fig. 4-8. In this case, CCE is limited to the collection of the carriers which are transported from the top to the bottom. In a P-on-N cell shown in Fig. 4-8, for example, electrons have to pass through the SL region to reach the bottom n-region while there is no blockage for the hole transport to the top contact. The longer the wavelength, the more light is absorbed in the deeper region of the cell, and thus the effects of hole transport to the top region through the SL increases.

In bias-dependent evaluation, applying forward bias weakens the electric field in the depletion region, resulting in larger recombination loss and lower carrier collection efficiency. Combining the wavelength- and bias- dependent measurements, therefore, can examine in detail how efficiently the photo-excited carriers are transported from each area of the cell under operational condition.
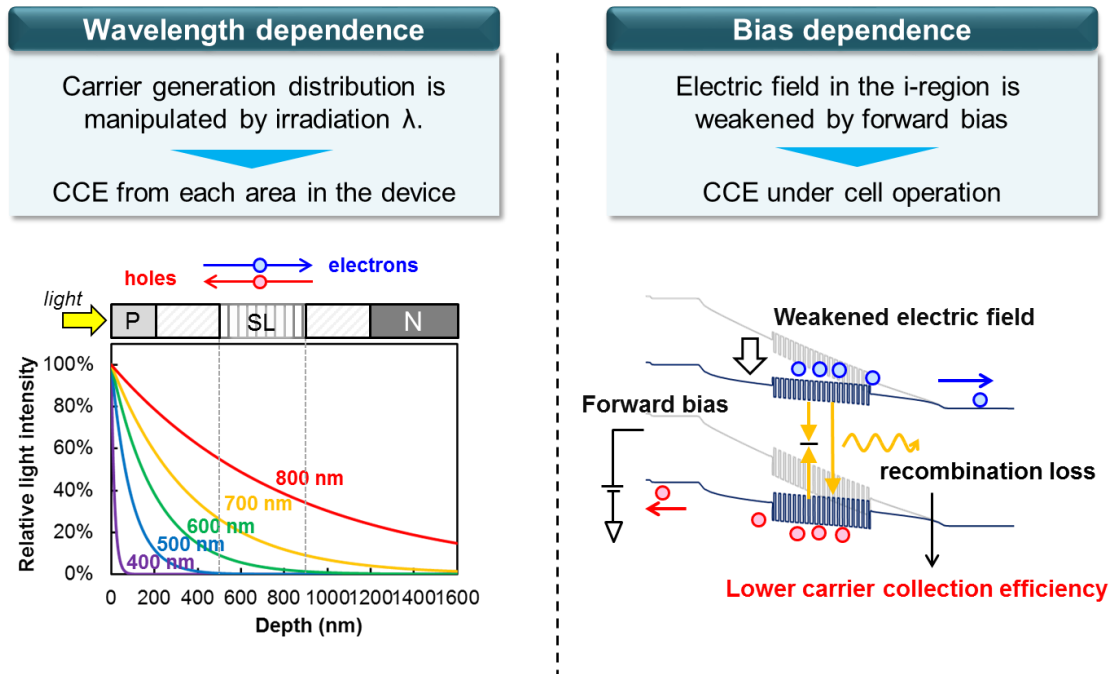

Fig. 4-8   CCE-based solar cell evaluations: (a) Excitation wavelength dependence and (b) Bias dependence.

4.3.1 EQE, IQE, and CCE

In the definition of CCE in the eq. (4-3) and (4-5), the carriers under investigation are those generated in the "active region", not in the entire cell. There are so called "dead-regions" in solar cells such as the near vicinity of the surface or heavily-doped region neighboring the contacts, from which carrier collection is impossible. The other area excluding these dead regions can be regarded as active region, which is basically p-n junction area of the cell.

The difference between QE and CCE is summarized in Fig. 4-9 with major losses in photons and carriers. When light is illuminated on a solar cell, the photons are partially reflected and transmitted (Transmission can be neglected if it is prevented by the back electrode). Regarding the absorbed photons, not all of them generate carriers because they are partly absorbed by free carriers, impurities, metal contacts etc. without exciting electron-hole pairs. In particular, free carrier absorption is fairly large if the substrate is thick and highly-doped. Furthermore, not all the photo-excited carriers can be used, since they are partly generated in the dead regions as mentioned above. Finally the photo-current is obtained by collecting the usable carriers which are generated in the active region, and is reduced by recombination loss if carrier transport is poor.

The EQE and IQE are defined as the ratio of the number of carriers extracted as photocurrent to the number of incident photons and the absorbed photons, respectively. The CCE, on the other hand, is defined as the number of carriers extracted as photocurrent to the number of usable carriers.
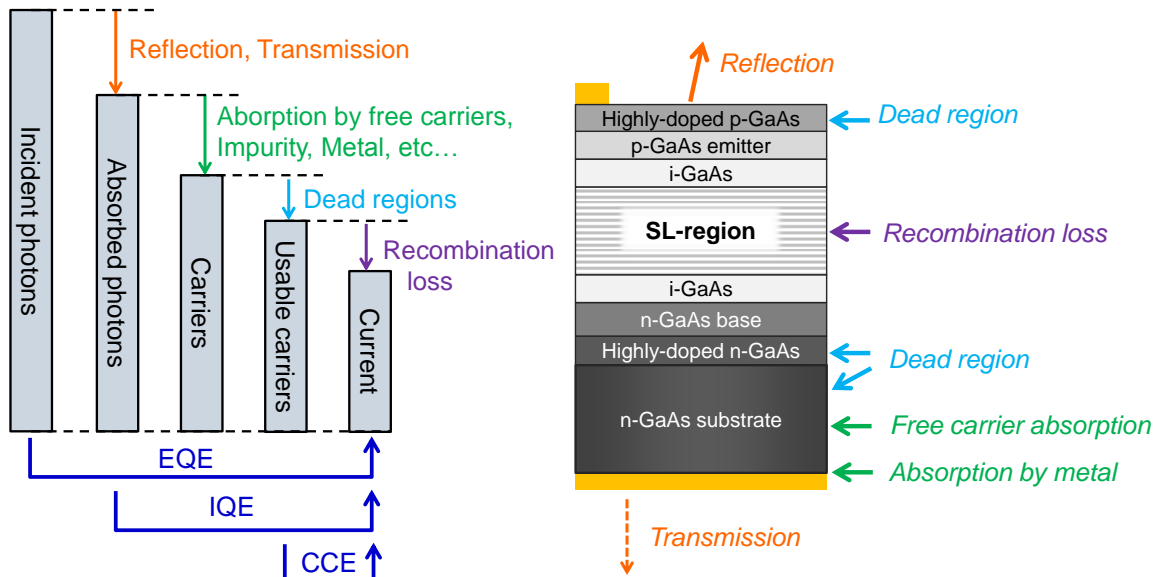

Fig. 4-9   Definition of QE and CCE from the viewpoint of loss of photons and carriers

Note that the expression frequently used in this research "collection of the photo-excited carriers" is not strictly appropriate, and it is used just for descriptive purpose. Although the I-V characteristic of a solar cell can be described as the sum of the dark current and the photo current, it is not true that photo-excited carriers and other carriers are separately responsible for the photo current and the dark current, respectively. All the carriers, whether or not they are photo-generated or injected from the external circuit, equally contribute to either electron or hole concentration at the particular region. Then, the total current is simply measured under steady state condition under which the electric potential and the carrier concentrations at each region are uniquely determined so as to satisfy the Poisson's equation and the current continuity equations including the carrier generation rate due to the illumination. In this sense, 100% CCE does not necessarily mean that the photo-excited carriers themselves are actually collected by the external circuit. In other words, CCE is just a physical quantity which indicates the ratio of the illumination-induced current enhancement to the amount of the photo-excited carriers. Nonetheless, the expression of "collection/transport of the photo-excited carriers" is quite convenient and will be used in the latter chapters as well, because such an interpretation can well explain the experimental data as will be shown later.

4.3.2 Advantages of CCE-based evaluation

Advantages of CCE-based evaluation are:

- Efficiency of carrier transport from each region of the cell can be quantitatively examined by evaluating CCE at different wavelengths and bias voltages. Such properties cannot be directly obtained by widely used characterization measures alone, e.g. I-V, QE at zero bias, V_{oc}, I_{sc}, *FF* and efficiency, which are also affected by other factors unrelated to carrier dynamics inside the cell such as surface reflection, current leak path, and electrode design. For example, with a significant current leak path in the cell due to failure in device processes etc., the diode current-voltage curve is inclined because of the small shunt resistance, resulting in low *FF* and V_{oc}. Since CCE is evaluated by offsetting the current without illumination and normalizing the illumination-induced current component, the results are not affected by the shunt resistance.
- Measurement procedure is simple. Since CCE can be evaluated by measuring QE at various voltages, typical solar simulators can be used.
- It can be applied not only to superlattice solar cells but also to general quantum nano-structured solar cells, where the carrier transport and collection are the major challenges.

4.3.3 Simulation of CCE with inefficient carrier transport

In this section, the concept of CCE analysis is theoretically demonstrated by simulation based on a simple drift-diffusion model for a GaAs p-i-n device illustrated in the Fig. 4-10 (a). To simplify the inefficient carrier transport through a SL or MQW, a bulk region where the carrier mobility is low is incorporated. The low-mobility-region is 600-nm-thick, and is inserted in the middle of a 1000-nm-thick GaAs intrinsic region. The bandgap of the low-mobility region is equal to GaAs for simplification. The top p-GaAs region and the bottom n-GaAs region have doping level of 2×10^{18} and 2×10^{17} cm^{-3} and thickness of 200 and 400 nm, respectively. The device is capped with a 20-nm-thick p-InGaP window layer.

In a simulation based on a drift-diffusion model, the Poisson's equation (2-13) and the current continuity equation (2-14)-(2-15) are self-consistently solved. Semi thermal equilibrium condition at the electrodes is assumed as the boundary condition. Also, the applied voltage is assumed to be equal to the difference between the hole quasi Fermi level at the top surface (p-region) and the electron quasi Fermi level at the bottom surface (n-region). In the intrinsic region, optimistic physical properties are assumed for the i-GaAs: electron mobility of 8500 cm^2/V·s, hole mobility of 400 cm^2/V·s, and nonradiative recombination time constant τ_{NR} of 1000 ns. For the low-mobilty region, τ_{NR} is assumed to be 100 ns, and the carrier mobilities are arbitrary varied. Other physical properties such as effective mass, radiative recombination rate, and light absorption coefficient are assumed to be same as GaAs.

Fig. 4-10 (b) shows simulated CCE under AM1.5 illumination (CCE$_{AM1.5}$) as functions of the applied bias with different carrier mobilities. When ideal mobilities equivalent to those for GaAs are assumed (μ_e =8500 cm^2/V·s, μ_h =400 cm^2/V·s), the degradation of CCE is negligible in the simulated bias range up to 1.0 V. As the mobility is decreased, the carrier transport across the i-region is blocked and extraction of the photo-generated carriers becomes incomplete, resulting in declination of CCE at higher forward bias. For a given mobility in the low-mobility region, CCE is more likely to decrease with lower τ_{NR}. Since exact τ_{NR} for SL or MQW region is not clear, the accuracy of the absolute value of the simulated CCE is not the focus here. However, when τ_{NR} is as low as 100 ns, CCE$_{AM1.5}$ around V_{oc} (0.95 – 1.0 V) remains over 95% even if the carrier mobility in the low-mobility region is lower than GaAs by a factor of 1/100 (μ_e = 85 cm^2/V·s, μ_h = 4 cm^2/V·s).

Fig. 4-10 (c) shows monochromatic CCE (eq. (4-5)) with low electron mobility and high hole mobility (μ_e = 0.03 cm^2/V·s, μ_h = 400 cm^2/V·s) simulated at various monochromatic light wavelengths (500, 600, 700, and 800 nm). With the increase of the forward bias, the CCE at shorter wavelength is more degraded as expected because the slow electron transport is more affective when excitation takes place in the upper region in a P-on-N device. Although longer wavelength light has a longer penetration depth and excites carriers beneath the low-mobility region, CCE at even 800 nm is also severely degraded since the light is mostly absorbed in the upper region of the cell.

Fig. 4-10 (d) shows the simulation results with low hole mobility (μ_e = 8500 cm^2/V·s, μ_h = 0.01 cm^2/V·s). In this case, CCE is limited by the slow hole transport toward the top p-region, and the CCE

is accordingly degraded at longer excitation wavelength. At 500 nm, almost all the light is absorbed above the low-mobility region; 99% of light is absorbed in the top 430-nm-thick GaAs. Since there is no blockage for the photo-excited holes toward the top electrode and the mobility for the electrons that pass through the i-region is very high, the degradation of CCE at forward bias is almost negligible. As the excitation wavelength is longer and more carriers are excited inside or beneath the low-mobility region, CCE showed severer degradation. Since the light is absorbed from the surficial area, however, the reduction of CCE is much suppressed compared to the case of slow electron transport (Fig. 4-10 (c)); at wavelength of 800 nm for example, 40% of the light is absorbed in the 400-nm-thick GaAs above the low-mobility region, and thus CCE remains higher than 60% even at forward bias of 0.8 V.

The simple simulations for bulk p-i-n cells with a low-mobility region clearly shows the strength of CCE-based cell evaluation, with combination of bias- and wavelength-dependent analyses. In the rest of this chapter, the validity of the definition and evaluation procedure of CCE is discussed (section 4.4), and then the effectiveness of CCE-based analysis is experimentally demonstrated (section 4.5).

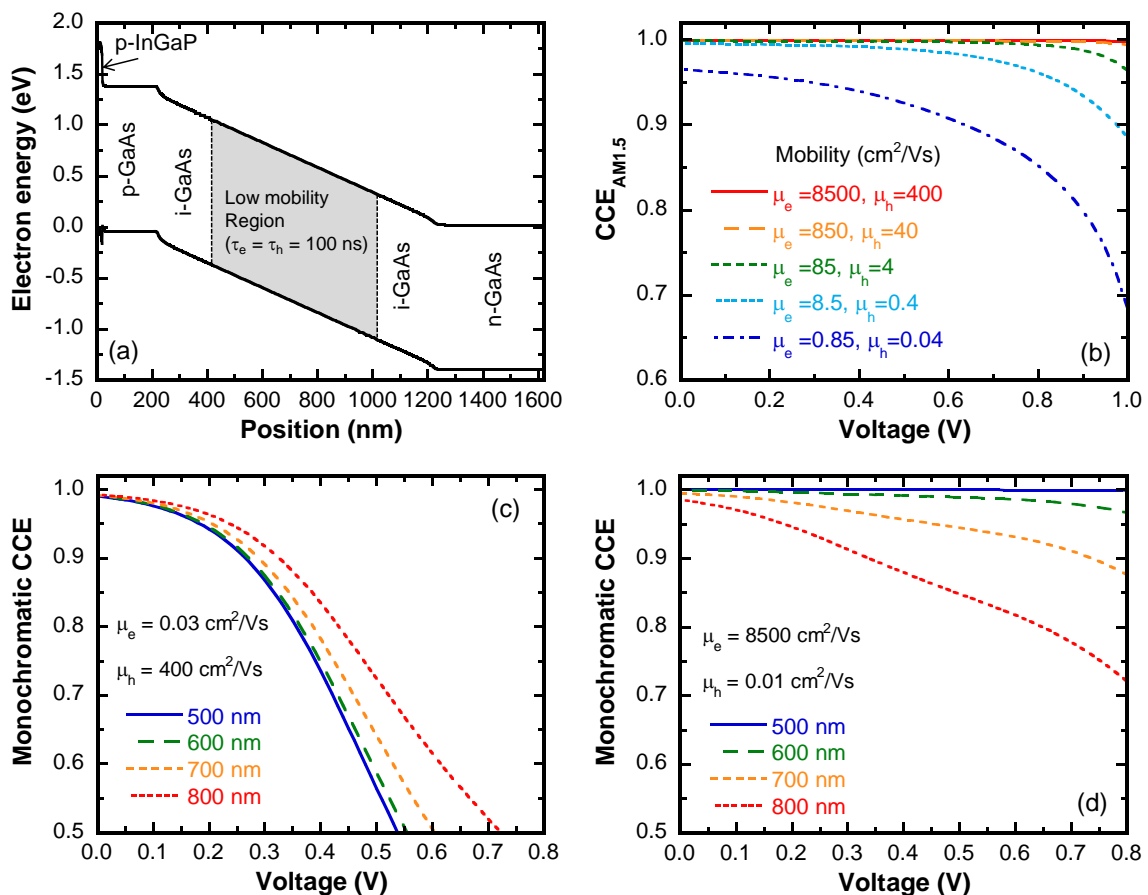Fig. 4-10   Simulation of CCE based on the drift-diffusion model for a P-on-N solar cell device illustrated in (a). To simplify the inefficient carrier transport through a SL or MQW region, a 600-nm-thick bulk region where the carrier mobility is low is incorporated in the center of 1000-nm-thick GaAs i-region. The assumed nonradiative recombination time constant in the low-mobility-region is 100 ns both for electrons and holes.

4.4 Validation of CCE-based analysis

The derivation procedure of CCE explained in the chapter 4.3 is based on four assumptions:

1) The bias dependency of the light absorption and hence carrier generation is negligible.

2) 100% of the carriers are collected when ΔJ is saturated at a sufficient reverse bias.

3) Monochromatic CCE gives the actual efficiency of carrier collection under sunlight. The transport of carriers is not changed by the additional monochromatic illumination.

4) The effects of the series and shunt resistance are negligible.

To use the CCE as an accurate device property, the validity of these assumptions are verified in this section in order to clarify how the CCE should be evaluated for reliable characterization.

4.4.1 Bias dependence of light absorption

The simple estimation of the CCE using eq. (4-3) and (4-5) requires light absorption to be unchanged when the applied bias voltage is varied. This is a reasonable assumption in bulk materials where quantum confinement is negligible. In quantum nanostructures, however, the absorption coefficient depends on overlap of the wave functions for electrons in the conduction band and holes in the valence band, which in general are affected by the electric field. To confirm how the absorption changes under bias, the voltage-dependence of the absorbance in the SL was measured in this section.

■ **Experiments**

(1) A GaAs pin solar cell including 30-period $In_{0.24}Ga_{0.76}As$ (7.5 nm)/$GaAs_{0.67}P_{0.33}$ (11.0 nm) SL in a 1-μm-thick i-region was grown on a double-side polished n-GaAs (0 0 1) substrate by MOVPE. A GaAs cell with 1-μm-thick i-region without SL was also prepared as a reference cell. The cell structure is shown in Fig. 4-11.

(2) 5.5×5.5 mm comb-shaped electrodes were processed both on the back and the front surface so that the light can transmitted the sample through the window area which the contact metal does not shade. For the back contact, Ni (25 nm)/AuGe (350 nm) was deposited by thermal evaporation (SVC-700 TM, Sanyu) and annealed in N_2 ambient at 390 ℃ for 2 min. Ti (20 nm)/Au (300 nm) was then deposited by electron-beam (EB) evaporation (L-045E, Anealva) for the front contact.

(3) The samples were placed on a cupper plate with a 3-mm-diameter hole, which was used as the aperture for the transmission measurement. The back contact was conducted to the cupper plate with silver paste. Au wire bonding was performed for the front contact.

(4) Transmittance of the SL cell and the reference GaAs cell were measured by FTIR changing the

bias voltage from -3.0 V to 0.9 V. The fraction of the effective window area were estimated by comparing the transmittance data under open-circuit conditions between before and after processing the electrodes, in order to correct the absolute values of bias-dependent transmittance.
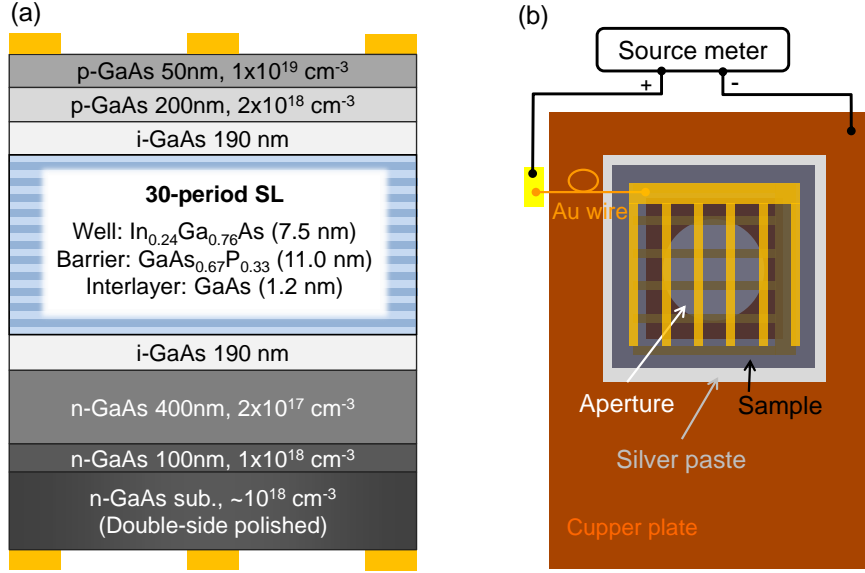
Fig. 4-11   Schematic of sample used for measurement of the bias-dependent absorption in InGaAs/GaAsP SL. (a) Structure of the grown layer, and (b) the sample mounted on a cupper plate with an aperture after processing comb-shaped electrodes.

■ **Results and discussions**

Fig. 4-12 shows calculation formulae for the transmittance *T*, the reflectance *R*, and the absorptance *A* of the light illuminated on a cell grown on a double side polished wafer, derived assuming Fabry-Perot cavity theory.

The absorbance of a SL cell can be written as

$$a = a_{GaAs} + a_{SL}, \tag{4-8}$$

where a_{GaAs} and a_{SL} are absorbance of the GaAs region including the substrate, and the SL-region respectively. By measuring the transmittance of the GaAs reference cell T_{GaAs}, and that of the SL cell T_{SL}, a_{GaAs} and a_{SL} can be calculated as

$$e^{-a_{GaAs}} = \frac{-(1-r_{GaAs})^2 + \sqrt{(1-r_{GaAs})^4 + 4r_{GaAs}^2 T_{GaAs}^2}}{2r_{GaAs}^2 T_{GaAs}}, \tag{4-9}$$

$$e^{-(a_{SL}+a_{GaAs})} = \frac{-(1-r_{GaAs})^2 + \sqrt{(1-r_{GaAs})^4 + 4r_{GaAs}^2 T_{SL}^2}}{2r_{GaAs}^2 T_{SL}}, \tag{4-10}$$

where r_{GaAs} is the reflectivity at the interface between GaAs and the atmosphere, and is determined by the GaAs refractive index.

$$R = \frac{r_1 + r_2(1 - 2r_1)e^{-2a}}{1 - r_1 r_2 e^{-2a}}$$

$$T = \frac{(1 - r_1)(1 - r_2)e^{-a}}{1 - r_1 r_2 e^{-2a}}$$

$$A = \frac{(1 + r_2 e^{-a})(1 - r_1)(1 - e^{-a})}{1 - r_1 r_2 e^{-2a}}$$

R: Reflectance
T: Transmittance
A: Absorptance
r_1: reflectivity (front surface)
r_2: reflectivity (back surface)
a: absorbance
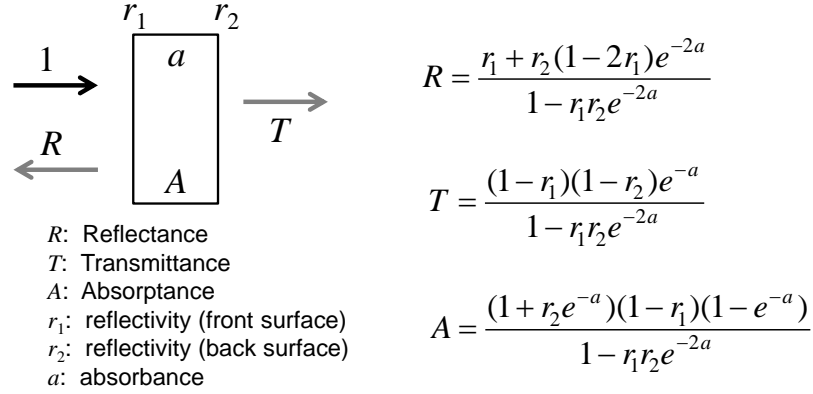
Fig. 4-12   Calculation formulae of transmittance *T*, reflectance *R*, and absorptance *A* of the light illuminated on a cell grown on a double-side polished wafer, assuming Fabry-Perot cavity.
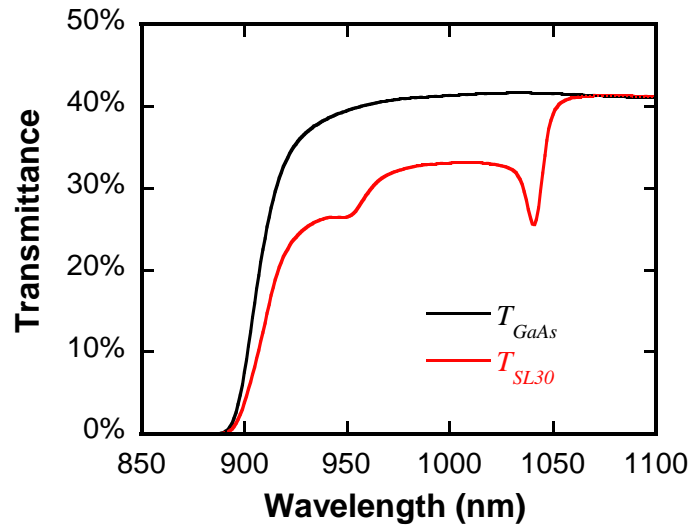
Fig. 4-13   Transmittance spectra of the SL cells and the reference cell under the open circuit condition measured by FTIR.

Fig. 4-13 shows the light transmittance spectra of the SL cells and the GaAs reference cell under the open circuit condition measured by FTIR. Although the band-edge wavelength of GaAs is 860 nm, only 40% light beyond 950 nm was transmitted through the reference cell because of free-carrier absorption in the heavily-doped substrate. The transmittance of the reference cell also showed not abrupt but gradual increase from 900 nm to 930 nm with fairly strong absorption. This is the effects

of Urbach tail of the optical absorption, which is attributed to the atomic vibration in the crystal and hence thermal variation of the bandgap. The SL-cell showed decreased transmittance from 900 nm to 1060 nm owing to additional band-to-band absorption in quantum wells, with clear exciton peaks at 1040 nm and 950 nm.
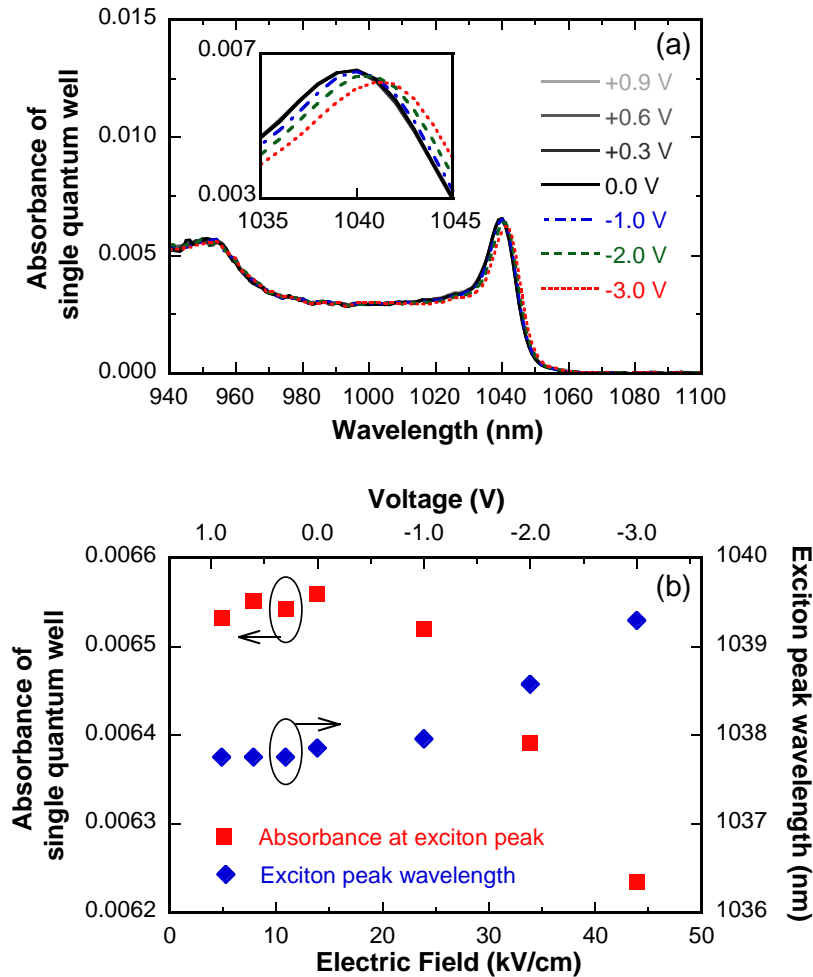
Fig. 4-14 (a) Absorbance spectra of a single quantum well (SQW) in the 1e-1hh transition wavelength range. (b) Bias dependence of the absorbance of SQW at the exciton peak and the exciton peak wavelength. (© 2014 IEEE)

From the transmittance spectrum measured at various bias voltages, the single-path absorbance of GaAs region a_{GaAs} and the SL region a_{SL} at each bias were calculated using the eq. (4-9) and (4-10). Fig. 4-14 shows the absorbance spectrum for a single quantum well, estimated by dividing a_{SL} by the well number of 30. The change in absorbance was negligible at forward bias. At higher reverse bias, however, the exciton peak was slightly lowered and red-shifted. This phenomenon is well known as the quantum confined Stark effect [101], where strong electric field which tilts the band of the quantum wells spatially separates the wave functions of electrons and holes, causing a narrower

effective bandgap and lower excitation probability. This resulted in a 5% difference in absorbance, corresponding to absorption via excitons between 5 kV/cm and 45 kV/cm. On the other hand, the absorbance did not change for varying applied bias from 980 nm to 1010 nm, where the effect of the exciton peak is negligible. For reliable estimation of CCE by simple calculations based on the eq. (4-5), therefore, the evaluation should be carried out at the wavelength range sufficiently far from the exciton peaks, around which additional bias dependent absorption measurement is required for accurate derivation of CCE.

4.4.2 Balance between absorbed photons and collectable carriers

The assumption that saturation of the collected current indicates 100% carrier extraction was validated by investigating the balance between the number of photo-excited carriers that can be collected at a sufficiently large reverse bias and the number of photons absorbed in the active region. It is difficult to estimate the number of collectable carriers generated by photon with energy above the GaAs bandgap (1.42 eV) because excitation also takes place in the dead region. This section, therefore, focuses on the absorption beyond the GaAs bandedge wavelength, where carriers are excited in the SL region which is inside the active p-n junction, and hence extraction of all the photo-generated carriers would be possible.

■ Experiments

(1) The two epitaxial GaAs pin layers with and without 30-period SLs grown in the previous section were used for this study as well. To process them to typical solar cell devices, the Au back contact was deposited on the entire rear surface, and annealed in N_2 ambient at 350 ℃ for 5 min.

(2) After processing the back metal alone, the reflectance of the GaAs reference cell R_{GaAs} was measured by a spectrophotometer, to estimate the reflectivity at the back metal r_{back}.

(3) Ti/Au top electrodes were deposited on the top surface by EB evaporator.

(4) External quantum efficiency (EQE) was measured at reverse bias until the entire spectrum was completely saturated to EQE_{sat} (obtained at -2 V). (High-resolution measurement was performed at Bunkokeiki Co. Ltd.)

(5) The fraction of absorbed photons in the well region with the Au back metal was calculated using a_{SL} and r_{back}, and compared with the EQE_{sat}.

■ Results and discussion

Electric property of solar cells, e.g. current-voltage characteristics and quantum efficiency, are measured after processing back electrodes. Therefore, the value of the reflectivity at the back metal

r_{back} is required for the estimation of the light absorption fraction in a cell under operation. Using the equation in Fig. 4-12, r_{back} can be calculated as

$$r_{back} = \frac{R_{GaAs} - r_{GaAs}}{(1 - 2r_{GaAs} + R_{GaAs} \cdot r_{GaAs})e^{-2a_{GaAs}}} , \qquad (4\text{-}11)$$

where R_{GaAs} is the reflectance of the GaAs reference cell with an Au electrode on the back surface.

Fig. 4-15 (a) shows measured R_{GaAs}, and calculated r_{back}. At wavelength up to 900 nm, R_{GaAs} is mostly determined by the surface reflectivity because almost all the light that comes inside the GaAs is absorbed. R_{GaAs} rose up steeply at approximately 900 nm because the back metal reflects the transmitted light back to the surface. r_{back} was estimated 50% - 60% beyond 930 nm, but its calculated value diverged at wavelength shorter than 930 nm. This is due to the difficulty in accurate estimation of r_{back} with the existence of the Urbach tail of the absorption in GaAs, for which the absorbance rapidly changes with the wavelength. That is, in this particular wavelength range (900 nm – 930 nm), slight measurement error and difference in the measurement resolution between the FTIR spectrometer for the transmittance measurement and the spectrophotometer for the reflectance measurement exponentially influence on the eq. (4-11). Therefore, the calculated value of r_{back} is trustable only in the wavelength range beyond 930 nm, within which the effect of the Urback tail is negligible.

Fig. 4-15   (a) Reflectance of the GaAs reference cell with an Au electrode on the back surface R_{GaAs}, and reflectivity at the back metal r_{back} calculated assuming Fabry-Perot cavity. (b) Cross sectional SEM image of the interface between a GaAs substrate and Au contact which was annealed at 350 ºC for 5 min.

The low reflectivity at the back-side Au metal ($r_{back} \sim$ 50-60%) was probably attributed to absorption loss in the reaction layer at the interface between GaAs and Au as shown in Fig. 4-15 (b), which was formed by thermal annealing at 350 ºC for the purpose of making ohmic contact. Schottky

barrier height between Au and n-GaAs of 0.9 V is reduced by heat treatment, which is accompanied by interface reactions mostly associated with formation of AuGa alloy layer and vaporization of As species [102, 103]. Indeed, by lowering the annealing temperature from 350 ℃ to 290 ℃, R_{GaAs} and the estimated r_{back} at around 1000 nm increased from 51% to 57%, and from 58% to 72%, respectively.

The light absorption fraction in the SL region A_{SL}, i.e. the number of the electron-hole pairs excited inside the wells per irradiated photon, can be expressed as

$$A_{SL} = \frac{(1 + r_{back}e^{-(a_{SL}+2a_{GaAs})})(1 - r_{GaAs})(1 - e^{-a_{SL}})}{1 - r_{GaAs}r_{back}e^{-(2a_{SL}+2a_{GaAs})}}. \tag{4-12}$$

If all the carriers photo-excited in the wells are extracted to the external circuit, A_{SL} should be equal to the external quantum efficiency. Fig. 4-16 shows the saturated EQE spectrum of the SL30 cell and calculated A_{SL} as functions of wavelength. Note that the A_{SL} is plotted beyond 930 nm where the effect of the Urbach tail is negligible. The saturated EQE spectrum well agreed with the absorption fraction spectrum, indicating that the photo-excited carriers can be almost completely extracted by applying a sufficient reverse bias. This is proof that the CCE defined by eq. (4-5) and (4-7) gives an appropriate approximation for the collection efficiency of the carriers photo-generated in the active region of a solar cell.
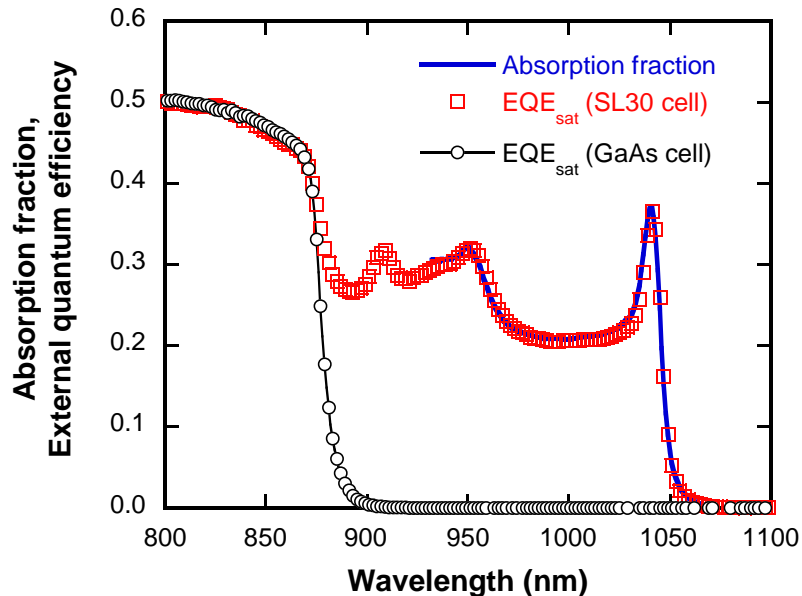

Fig. 4-16   Saturated EQE spectrum (EQE$_{sat}$) and absorption fraction for the SL cell at -2.0 V.

(© 2014 IEEE)

4.4.3 Effect of AM1.5 bias-illumination

As explained earlier, an advantage of evaluation of monochromatic CCE is that it can examine the carrier collection from each region in the cell and thus reveal in detail the bottleneck problem in carrier transport under operational condition. For this reason, this research proposes to use AM1.5 bias-illumination so as to make the situations of the cell at which monochromatic CCE is measured, e.g. carrier density or band-lineup, similar to those under sunlight. In order to argue this advantage, it must be confirmed whether or not the measured monochromatic CCE really reflects the actual carrier transport dynamics in a cell under sunlight illumination. For this investigation, a GaAs pin cell including 100-period $In_{0.26}GaAs$ (7.0 nm) /$GaAsP_{0.40}$ (9.0 nm) was prepared with the same host structure as Fig. 4-11 (a).

If the monochromatic $CCE(\lambda,V)$ gives the collection efficiency of the carriers excited by each wavelength component of AM1.5, the total collection efficiency of the carriers excited by the AM1.5 light can be estimated by averaging the eq. (4-7) over the solar spectrum as

$$\sum_{AM1.5}CCE(\lambda,V) = \frac{\int_0^\infty I_{AM1.5}(\lambda) \cdot QE(\lambda,V)d\lambda}{\int_0^\infty I_{AM1.5}(\lambda) \cdot QE_{sat}(\lambda)d\lambda}, \tag{4-13}$$

where $I_{AM1.5}(\lambda)$ is the photon flux density at wavelength λ in the AM1.5 spectrum, and $QE(\lambda,V)$ is the quantum efficiency measured with monochromatic light at a wavelength λ.

Fig. 4-17 shows a comparison of the measured $CCE_{AM1.5}$ using eq. (4-3) and the calculated results for $\Sigma_{AM1.5}CCE(\lambda,V)$ using eq. (4-13) with the $CCE(\lambda, V)$ under weak monochromatic light with intensity of 2.5 mW/cm^2. In the calculation of $\Sigma_{AM1.5}CCE(\lambda, V)$, $\Delta J(\lambda,V)$ was estimated with and without AM1.5 bias light; an evaluation with bias light is as illustrated in the Fig. 4-7 (b), and the evaluation without bias light can be conducted by simply substituting sunlight with the monochromatic light in Fig. 4-7(a).

Without AM1.5 bias, $\Sigma_{AM1.5}CCE(\lambda,V)$ did not fit the measured $CCE_{AM1.5}(V)$ as seen in Fig. 4-17, and the monochromatic $CCE(\lambda,V)$ was found to be underestimated especially at forward bias. With AM1.5 bias illumination, on the other hand, the calculated $\Sigma_{AM1.5}CCE(\lambda,V)$ well agreed with the actual measured values, indicating that the CCE measured by monochromatic light indeed gives actual transport efficiency of the carriers excited by particular wavelength component of the sunlight. The apparently improved CCE with bias-illumination suggests that the AM1.5 light remarkably enhances carrier transport compared to the case with relatively weak monochromatic light alone. Strong forward bias induces electroluminescence from the SLs, which may exerts a similar effect as the bias illumination to facilitate carrier transport, resulting in a comparable CCE beyond 0.7 V for the cases with and without bias illumination.
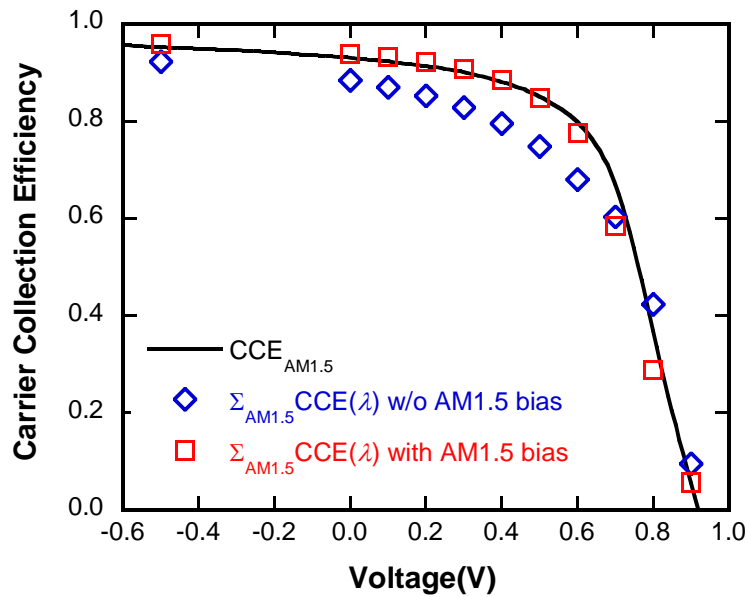
Fig. 4-17　CCE for the SL cell under AM1.5 irradiation. The actual measured CCE$_{AM1.5}$ (solid line), and the calculated $\Sigma_{AM1.5}$CCE(λ,V) with and without AM1.5 bias light are shown for comparison. (© 2014 IEEE)

Possible reasons for the enhanced CCE with bias illumination are:

- Photon-assisted escape

  A carrier in the wells absorbed a photon and is excited to an upper state, either to a discrete level inside the well or the continuum state above the well.

- Band filling effects

  Higher background carrier concentrations under bias illumination may fill the discrete levels in the quantum wells, and thus effective barrier height for the carriers is reduced.

- Passivation of recombination centers.

  The background carriers generated by the bias illumination fill and passivate the recombination centers, making the probability of nonradiative recombination lower.

In order to identify the probable mechanism, we carried out a simple experiment. Fig. 4-18 shows the EQE of the 100-period SL cell with and without AM1.5 bias illumination, and with AM1.5 bias filtered by a silicon substrate to pass only photons with energy below 1.1 eV. Note that the QE was measured with 2.5 mW/cm^2 monochromatic light. The AM1.5 bias increased the overall QE. Since no apparent shift of the exciton peak with the bias illumination was observed, the possibility of band-filling effects, which in general makes the effective bandgap larger, can be eliminated. Besides, the bias light filtered by a Si wafer, which prohibits band-to-band carrier excitation in the cell, did not show apparent QE enhancement despite the presence of a substantial amount of photons with an

energy higher than the band offset between the InGaAs well and GaAsP barrier. This result also rules out the possibility of photon-assisted carrier escape under the bias illumination, which allows photo-generated carriers in the wells to be excited and move over the neighboring barrier more efficiently. Passivation of the recombination centers, therefore, is one of the probable causes of the bias-light-induced CCE enhancement, with reduced non-radiative recombination by the introduction of excessive carriers, as such an effect via impurity doping in quantum dots has been reported [104]. Further investigation is indeed required to clarify the exact mechanics in detail.
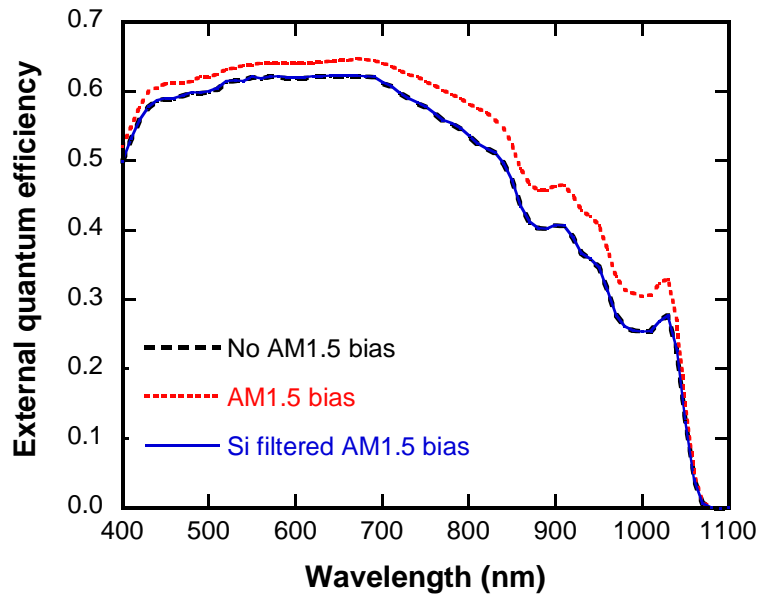
Fig. 4-18　EQE of the SL cell measured at 0 V with and without AM1.5 bias illumination.
(© 2014 IEEE)

It is important to examine in detail how the bias light enhances the transport of carriers in each area in the cell. Fig. 4-19 shows the enhancement factor of the CCE spectrum with the bias illumination, or the ratio of the CCE with bias light to the CCE without it, under various applied bias voltage. At -6.0 V, the CCE with and without bias light were almost equivalent, as described by the unity enhancement factor in the whole spectrum range. At reverse bias between -6 V and -1 V, carrier transport was found to be improved at longer wavelengths, especially beyond the GaAs band edge. This indicates that the probability of electron-hole separation inside wells without recombination is primarily enhanced by the AM1.5 bias light. Forward bias gradually increased the enhancement factor at shorter wavelength from 400 nm to 500 nm, where the light is only absorbed in the top p-region and thus the CCE is dominantly determined by electron transport to the bottom n-region. Applying forward bias lowers the electric field in the i-region, and consequently makes the electron drift transport through the i-region less efficient and weakens the driving force for the electron diffusion from the p-region as well. Therefore, at larger forward bias, AM1.5 bias illumination plays an important role

not only to efficiently separate the electron-hole pairs in wells but also to diffuse the photo-generated electrons to the i-region before they recombine with holes in the p-region.
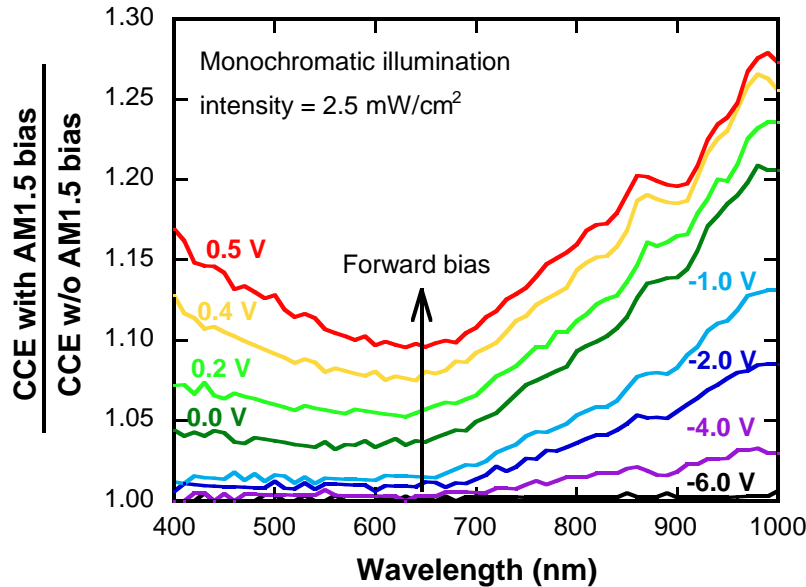
Fig. 4-19   Enhancement factor of the CCE spectrum with AM1.5 bias illumination at a variety of applied bias voltages from -6 V to 0.5 V. (© 2014 IEEE)

In order to estimate the intensity of the bias illumination which is required for substantial CCE enhancement, we carried out CCE measurements with AM1.5 bias illumination weakened by ND filters. Fig. 4-20 shows the CCE enhancement at 0.5 V at various wavelengths as functions of the bias light intensity, or transmittance of the inserted ND filter. Plots at 0% show the results without bias light. The plotted enhancement factors are normalized to the value obtained without the ND filter.

At short wavelengths (400 - 600 nm), only 1% to 10% bias sunlight was found to be effective to enhance CCE, indicating that relatively weak light can suppress recombination in the top p-region to efficiently diffuse the electrons to the i-region where the electric field is present. The longer the measurement wavelength, the stronger bias light was needed to obtain CCE enhancement. At 900 - 1000 nm, at which carriers are excited only in wells, 100% AM1.5 bias illumination was not sufficient to saturate the enhancement. This is reasonable because the most bias sunlight is absorbed in the bulk GaAs region above the SL, and stronger bias illumination is necessary for sufficient light penetration into the SL region. Therefore, carrier collection from the wells is expected to be facilitated even more by operating the SL cell under concentrated light conditions.
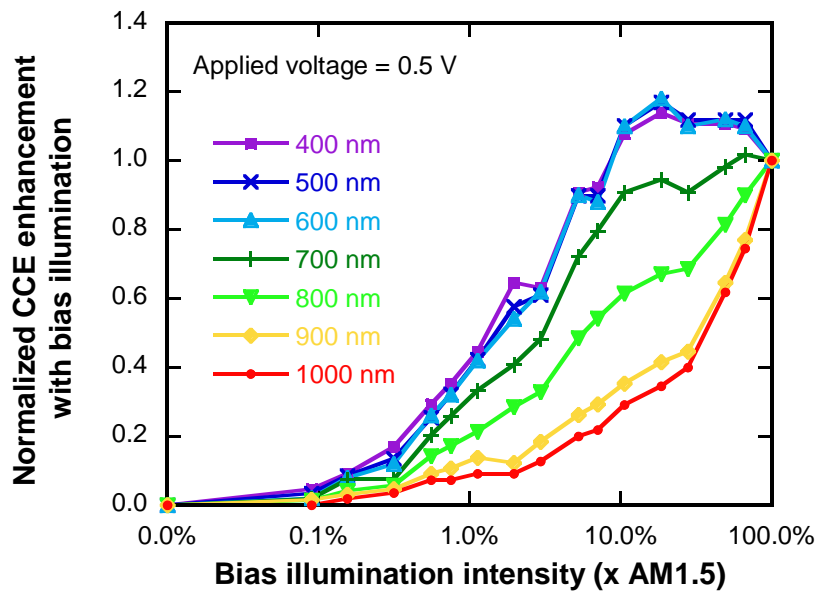
Fig. 4-20   Normalized CCE enhancement at 0.5 V at various wavelengths as a function of the bias light intensity. The plots for each wavelength are normalized to the value obtained without the ND filter. (© 2014 IEEE)

All the above results clearly show that the behavior of photo-excited carriers under weak monochromatic illumination is significantly different from the condition under sunlight irradiation. Therefore, it is more favorable to estimate the collected current ΔJ under bias sunlight to obtain the accurate carrier collection efficiency in solar cells under operation.

4.4.4 Effect of resistance on CCE evaluation

One of the advantages of CCE characterization is that it is less likely to be affected by the diode properties because the CCE is evaluated based on enhancement of the current induced by illumination. Undesired series or shunt resistance lowers the fill factor of the I-V curve even if the carriers in the p-n junction area are perfectly transported. This is the difficulty in direct evaluation of the carrier transport dynamics when we rely on I-V characteristics alone. In the investigation of the CCE, on the other hand, the current before the excitation is offset at an arbitrary bias, and thus the influence of the resistance can be reduced.

A large series resistance, however, leads to underestimation of the CCE because the voltage applied to the p-n junction differs between the conditions with and without illumination and the illumination-induced current enhancement becomes lower than the amount of the extracted photo-excited carriers.

In this section, the effect of a series resistance on the CCE calculation is simulated. Here it is

assumed that the I-V curve of a cell follows a basic equivalent circuit model described as the eq. (4-1). As typical parameters for a single-junction GaAs cell, J_L = 30 mA/cm^2, J_1 = 1.0×10^{-16} mA/cm^2, J_2 = 1.0×10^{-7} mA/cm^2, and R_{sh} = 1.0×10^6 Ωcm^2 were assumed. The CCE was calculated by normalizing the current enhancement induced by AM1.5 illumination. Note that if the I-V curve is described by the eq. (4-1), the carrier collection is always 100% because recombination loss of the photo excited carriers are not considered in the equivalent circuit model.

Fig. 4-21 shows the simulated bias-dependent CCE of such a 100% carrier collection cell with various series resistances R_s. When R_s = 0 Ωcm^2, 100% CCE can be accurately simulated at any bias. With a larger series resistance, however, the CCE is underestimated at forward bias. In typical CCE analysis under cell operation, the forward bias is applied to the maximum power output voltages, which are shown as circles on the plot for each R_s case. The influence of the series resistance is negligible if R_s is lower than 0.01 Ωcm^2. The underestimation can still be suppressed below 0.5% with R_s < 0.1 Ωcm^2. When R_s > 0.1 Ωcm^2, the CCE is significantly miscalculated, resulting in 3% and 10% underestimation with R_s = 1 Ωcm^2 and 10 Ωcm^2 respectively. However, a low series resistance below 10^{-5} Ωcm^2 can be achieved with widely used contact metals such as AuGeNi for n-type GaAs, and AuZn for p-type GaAs [58], and thus sufficiently reliable CCE evaluation is expected to be carried out with the ordinary process. Note that special care must be taken under light-concentrated operation where the effect of a series resistance is far more significant.

A shunt resistance, on the other hand, does not affect the estimation of the CCE if the series resistance is sufficiently small. In contrast to a series resistance, a shunt resistance does not change the voltage applied to the p-n junction either with or without illumination. Therefore, the enhancement in current due to illumination is preserved even if the shunt resistance becomes smaller, meaning that the CCE, derived by the procedure in Fig. 4-7, can be accurately estimated. If we simulate the CCE using the eq. (4-1) with R_s = 0 Ωcm^2, 100% CCE is always obtained regardless of the value of R_{sh}. The effect of the shunt resistance is not negligible when the series resistance is much larger, but the result changes only slightly. For instance, the simulated CCE at maximum power output voltage with R_s = 1.0 Ωcm^2 is 97.6% and 98.0 % with R_{sh} = 10^6 Ωcm^2 and 10^2 Ωcm^2, respectively. If the series resistance is reduced below 10^{-2} Ωcm^2, which can be easily achieved as mentioned above, then the effect of the shunt resistance on the CCE estimation is negligible.
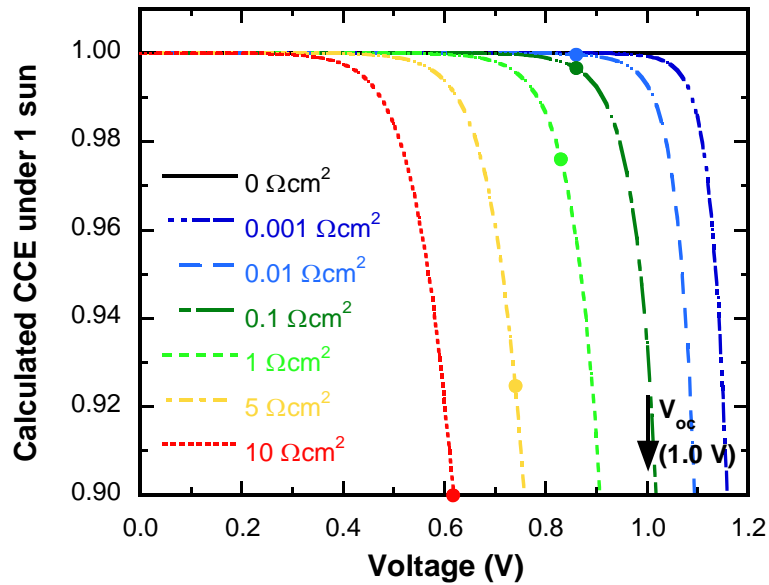
Fig. 4-21   Simulated bias-dependent CCE based on equivalent circuit approximation for a typical GaAs cell under AM1.5 excitation with a variety of series resistance R_s. The maximum power output points are indicated with circles for each plot. The open circuit voltage is 1.0 V, which is independent of the series resistance. (© 2014 IEEE)

4.4.5 Summary of the validity of CCE-based evaluation

In this section, the validity of CCE evaluation illustrated in the Fig. 4-7 have been verified. Here the obtained important insights are briefly summarized.

- Total carriers photo-excited in the active region were proved to be able to be collected at a sufficiently large reverse bias. Therefore, calculation of CCE by normalizing the illumination-induced current enhancement to the saturation value at the reverse is reasonable.

- When the excitation takes place in quantum wells, the absorption around the exciton peak wavelengths changes under strong electric field due to QCSE. Thus, the evaluation should be carried out at wavelength range which is sufficiently far from the exciton peaks.

- Illumination of sunlight was found to significantly change the carrier transport dynamics. With bias sunlight applied during the measurements, therefore, monochromatic CCE gives the reliable value as the efficiency of carrier transport in an actual situation under cell operation.

- Large series resistance leads to underestimation of the CCE because the voltage applied to the p-n junction differs between the conditions with and without illumination. Reliable evaluation is possible with series resistance below 10^{-2} Ωcm², which can be easily obtained with widely used ohmic contacts for GaAs.

4.5 Demonstration of CCE-based analysis

In this section, two demonstrative studies to investigate the carrier transport in SL solar cells using CCE based evaluation will be shown:

(1) Study of compensation doping treatment to show the importance of uniform electric field in the depletion region for efficient carrier transport through the SL.

(2) Study with a 100-period SL with bandgap of 1.2 eV to clarify the underlying challenges in carrier transport for practical application.

4.5.1 Effectiveness of compensation doping

In MOVPE growth of GaAs based materials using widely used metal-organic sources such as TMGa and TBAs, incorporated carbon atoms act as dopants. The main origins of the carbon incorporation has been suggested to be methyl radicals that are produced by pyrolysis of the precursors [105, 79]. They act as either donors or acceptors when incorporated in the Ga or As sites, respectively. The type of the resultant background doping (n-type or p-type) is strongly dependent on growth conditions, e.g. V/III ratio, reactor pressure and growth temperature [105, 106, 107]. For example, it has been reported that the background doping type changes from p-type to n-type with increase of V/III ratio using TMGa and AsH_3 (Fig. 4-22(a)) [108].

In the MOVPE reactor used in this study, p-type background doping is introduced in GaAs under typical growth condition: V/III ratio of 10~20, growth temperature of 610 ℃, reactor pressure of 10 kPa, and growth rate of 10~20 nm/min. Fig. 4-22(b) shows SIMS profiles of a typical SL solar cell grown in this study, from which the carbon concentration in the undoped GaAs region can be estimated 1×10^{16} cm^{-3}. All the incorporated carbon atoms do not necessarily act as acceptors, and the actual background doping level becomes lower than the carbon concentration. Note that the sensitivity coefficient of GaAs was used for the SL region, and thus the absolute values of the atom concentrations in the SL-region may not be accurate.

As will be discussed in detail, the p-type background doping was found to significantly flatten the band lineup in the i-region when its thickness exceeds 1 μm, leading to a weakened electric field in the SL and a severe degradation of carrier transport. This background doping problem is negligible in a typical bulk GaAs pin cell because no band discontinuity exists in the active region, but it is much more influential in quantum-structured solar cells, especially with deep carrier-confining centers. The p-type background doping can be cancelled out by counter-doping with n-type dopants, a technique that is called compensation doping hereafter. In this section the effectiveness of counter n-type doping during the growth of the i-region on the photovoltaic performance of SL cell is discussed.
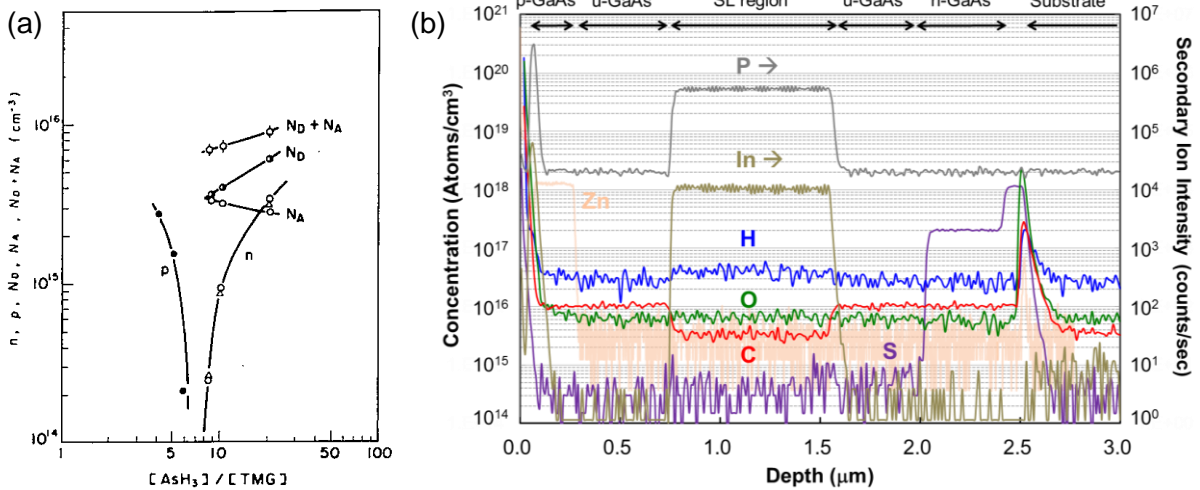
Fig. 4-22   (a) Doping level in undoped GaAs grown using TMGa and AsH$_3$ as a function of V/III ratio [108]. (b) SIMS profiles of a typical SL solar cell. Sensitivity coefficient of GaAs was used for the SL region.

4.5.1.1   Counter doping with sulfur

In order to clarify the growth condition for compensation doping with sulfur, the carrier concentration with various sulfur doping level was clarified by Hall measurement. In experiments, 1.5 μm thick GaAs layers were grown on semi-insulating GaAs (0 0 1) substrates (DOWA) using TMGa and TBAs at growth temperature of 610 °C and reactor pressure of 10 kPa. The partial pressures of Ga and As were 0.513 Pa and 6.59 Pa, respectively, and H$_2$S was supplied at various sulfur to arsenic ratio (P_S/P_{As}) from 0 (undoping) to 4.4×10^{-6}. The doping type and concentration for each sample was measured by Hall measurement to clarify the relation between H$_2$S pressure and the doping level in the epitaxial GaAs layers.
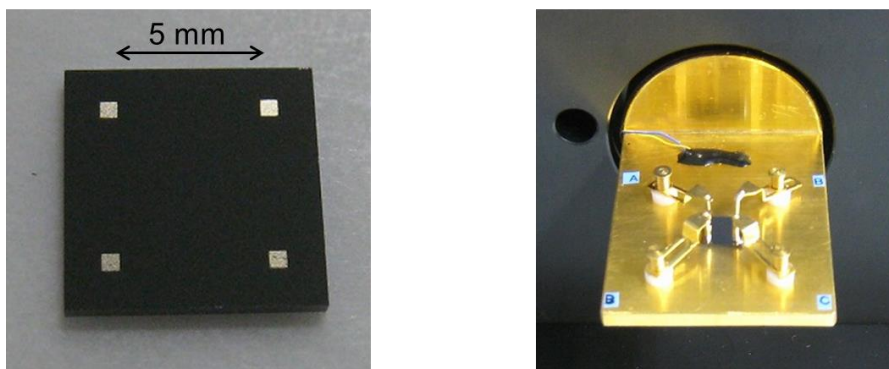
Fig. 4-23   Photos of a sample for Hall measurement.

Fig. 4-24 shows the carrier concentration in the grown GaAs at various sulfur to arsenic ratio in the vapor phase (P_S/P_{As}). The positive and negative values correspond to p-type and n-type, respectively.

The p-type background carrier concentration of the undoped GaAs was estimated approximately 5×10^{15} cm^{-3}, which is reasonable value in light of the incorporated carbon level of 1×10^{16}cm^{-3} estimated by SIMS. Counter doping with sulfur easily inverted the doping type from p-type to n-type. By controlling the injection of H$_2$S to almost the minimum level ($P_S/P_{As} = 4.4 \times 10^{-6}$), the doping concentration was able to be reduced to approximately 5×10^{14} cm^{-3} (n-type).
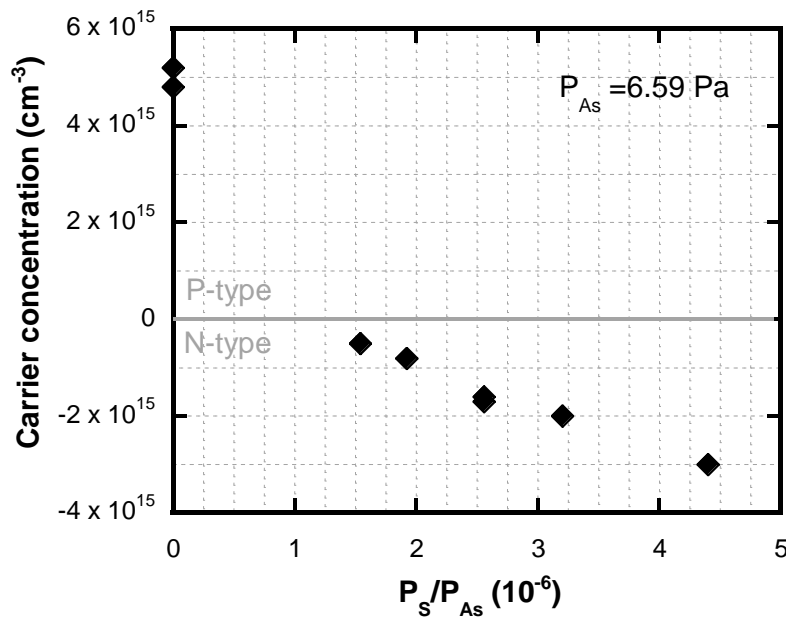
Fig. 4-24   Carrier concentration in GaAs as a function of sulfur to arsenic ratio (P_S/P_{As}) in the vapor phase. The P_{As} was fixed to 6.59 Pa, and only P_S was varied.

4.5.1.2   Investigation of carrier transport

Using the growth condition obtained in Fig. 4-24, the effectiveness of counter n-doing on the photovoltaic performance of SL cell was investigated.

■   Experiments

(1) GaAs pin cells including 20-period In$_{0.25}$Ga$_{0.75}$As (7.0 nm)/GaAs$_{0.66}$P$_{0.34}$ (10.6 nm) SL in the middle of 1000-nm-thick i-region were grown on n-doped GaAs (0 0 1) substrates (Hitach Cable) with doping levels in the i-region of (i) 5×10^{15} cm^{-3} (p-type): undoped, (ii) 3×10^{15} cm^{-3} (n-type): over-doped, and (iii) 5×10^{14} cm^{-3} (n-type): compensation-doped. The SL region was 400-nm-thick in total, including GaAs interlayers inserted between wells and barriers, and was sandwiched

between two 300-nm-thick GaAs spacer layers. A GaAs reference cell with an undoped 1000 nm i-region was also prepared for comparison. Note that H_2S was supplied at a constant partial pressure during growth of the entire i-region since the exact doping level in each layer of the SLs was not well determined. The detailed sample structure is shown in Fig. 4-25

(2) The grown samples were processed into solar cell devices with AuGeNi and Ti/Au electrodes for the n- and p-type contacts, respectively. Ni (20 nm)/AuGe (250 nm) was deposited on the back surface by thermal evaporation and annealed at 390 ºC for 2 min. Ti (20 nm)/Au (250 nm) was then deposited on the front surface by electron-beam (EB) evaporation using a comb-shaped shadow mask. The samples were cleaved to 2.5 mm × 2.5 mm squares with 1.84 mm^2 comb-shaped electrode on the top (Fig. 4-25).

(3) Photovoltaic performance (I-V under AM1.5 and QE) and CCE at various wavelengths were measured in a solar simulator. QE and CCE were measured with 2.5 mW/cm^2 monochromatic light under AM1.5 bias illumination.

(4) To support the CCE-based evaluation, the bias dependence of the PL from the SLs was investigated both in continuous-wave (CW) and time-resolved (TR) analyses. The PL at each voltage was measured by calculating the difference between the spectrum in the dark, or electroluminescence, and the spectrum under CW laser illumination at a wavelength of 532 nm. Illumination intensity was 25 μW, which was sufficiently weak to avoid high excitation effects. In addition, bias-dependent time-resolved PL was measured using a 780-nm pulse laser at a repetition rate of 10 MHz.
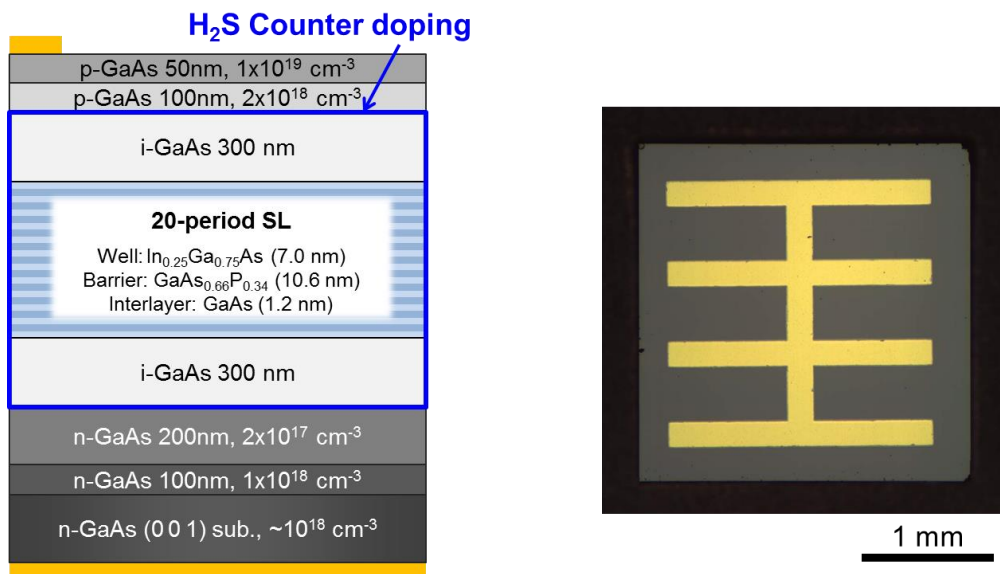
Fig. 4-25   Structure and a photo of a solar cell prepared in this section. The width and the total area of the front contact are 0.2 mm and 1.84 mm^2, respectively

■ **Results and discussion**

Fig. 4-26 shows the band-lineup of the undoped, overdoped, and compensation-doped SL cells simulated at short circuit condition. A p-type background doping of 5×10^{15} cm^{-3} significantly bends the band lineup of the i-region, resulting in a flattened band in the upper part of the i-region. The Over doping at -3×10^{15} cm^{-3} oppositely bends the band of the i-region. Using physical parameters of GaAs, e.g. the dielectric constant and the intrinsic carrier concentration, the thicknesses of the depleted area in the i-region of the undoped cell and the over-doped cell are calculated to be 570 nm and 770 nm, respectively, and thus in both cases 1000 nm thick i-region partly become neutral regions. By compensating the background doping to reduce the carrier concentration by an order of magnitude, the entire i-region is depleted with significant suppression of band flattening effects. The depletion region between an n-GaAs (-5×10^{14} cm^{-3}) and a p-GaAs (2×10^{18} cm^{-3}) can be extended to 1850 nm, which is sufficiently thicker than the 1000 nm i-region in the cell design for this experiments
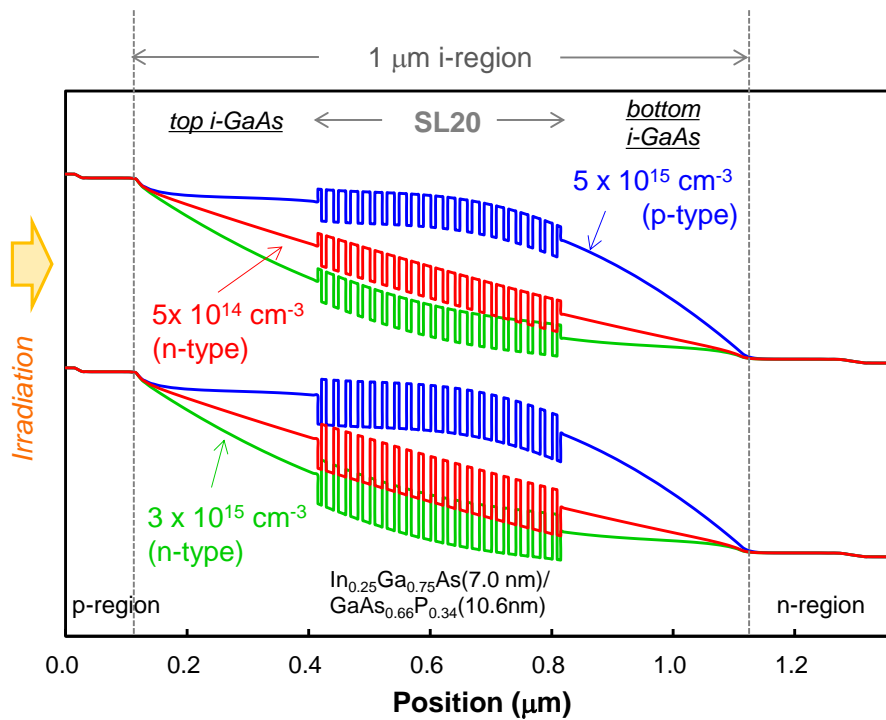
Fig. 4-26   Band lineups under short circuit conditions around the p-i-n regions of the SL cells with different doping levels in the i-region: 5×10^{15} cm^{-3} (p-type): undoped cell, 3×10^{15} cm^{-3} (n-type): over-doped cell, and 5×10^{14} cm^{-3} (n-type): compensation doped cell. Note that the valence band is shown only for heavy holes for simplicity.

In Fig. 4-27, the CCE at various excitation wavelength (400 - 1000 nm) as functions of the applied voltage are plotted for each SL cell. In all the devices, the current enhancement induced by the monochromatic illumination was saturated at around reverse bias of -2 V regardless of the wavelength, and thus the CCE at each bias was obtained by normalizing the QE to the saturation spectrum. Decrease of CCE at higher forward bias is attributed to degradation of carrier transport under weaker electric field. The variation of CCE among the excitation wavelengths indicates different efficiencies of the carrier transport from different areas where the carriers are photo-generated. Since the devices are P-on-N structure and the light was illuminated on the p-side of the cells, CCE at short wavelength is dominantly determined by electron transport from the top to the bottom and the effect of hole transport increases at longer wavelength as mentioned in the Fig. 4-8.

Fig. 4-27 (a) shows the results for the undoped cell with a background doping level of 5×10^{15} cm^{-3} (p-type). The CCE at shorter wavelengths was severely degraded as the voltage increased. Especially around 400–500 nm, only 50% of the carriers were found to be extracted under forward bias of 0.7 V. These results can be well explained by the band lineup of the p-i-n region shown in Fig. 4-26. Due to the flattened band and hence the severely weakened electric field, carriers generated above the SL with short wavelength light are likely to accumulate in the upper part of the i-region and easily recombine before reaching the bottom n-region. Consequently, the collection efficiency for electrons generated in the SL region, wherein a certain electric field exists, is relatively better, as can be seen in the 900–1000 nm plots. However, even within this wavelength range, the CCE values were below 0.8 at 0.7 V because the band lineup in the upper half area of the SL is almost flat even under short circuit conditions.

In contrast to the undoped cell, the band near the bottom n-region is flat in the over doped cell. Therefore, electron transport from the top area is improved by the strong electric field that exists in the upper part of the i-region, but the holes easily accumulate in the bottom part of the i-region in this case. Also, collection of carriers generated in the wells is comparatively difficult because the carriers inside the SL region cannot be driven by the strong electric field that exists in the upper area. As a result, the CCE became worse at longer irradiation wavelengths and a larger applied forward bias as shown in Fig. 4-27 (b).

By compensating the background doping to lower the carrier concentration to the order of 10^{14} cm^{-3}, the electric field becomes almost uniform, independent of the position in the 1-µm-thick i-region. The CCE then exhibited a similar bias dependence regardless of the excitation wavelength, and remained at a very high level at a forward bias as shown in Fig. 4-27 (c).

Comparing Fig. 4-27 (a) and (b), the carrier collection efficiency in the over-doped cell is much higher even at longer wavelengths than in the undoped cell in spite of the relatively high n-type doping concentration in the i-region of 3×10^{15} cm^{-3} and the apparently flattened band lineup in the bottom part of the i-region. This is because light is absorbed from the near-surface region of the device, and most electron-hole pairs are subsequently separated by the strong electric field in the upper part of the i-region in the over-doped cell. It is notable that in the over-doped cell, the CCE at shorter

wavelengths of 400–600 nm remained very high for a strong forward bias of 0.6 V, despite the flattened band in the bottom part of the SLs. This indicates that electrons generated in the upper region by shorter wavelength irradiation can be efficiently transported to the bottom n-region after being rapidly separated from holes, and driven by the strong electric field above the SLs.
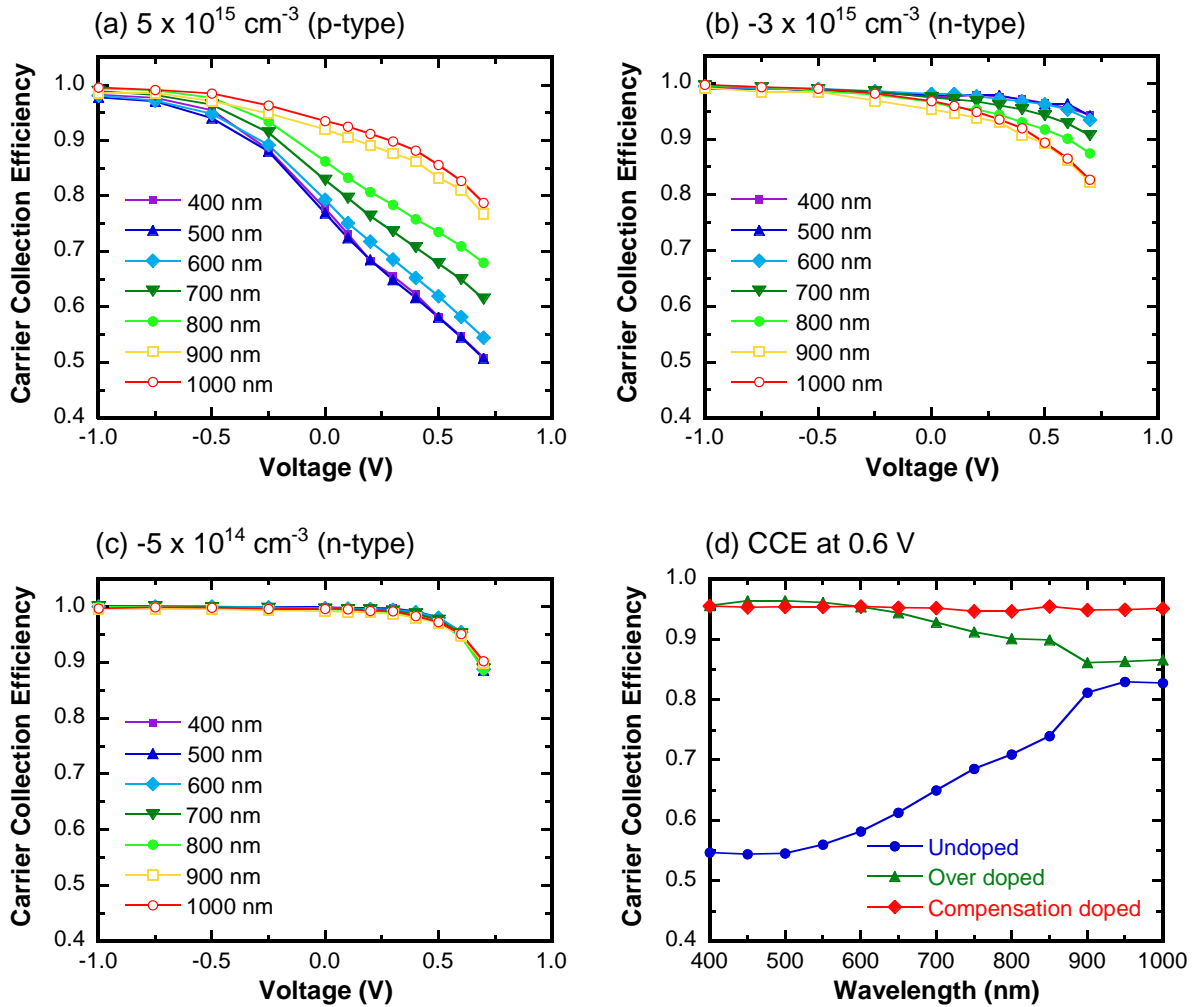

Fig. 4-27 carrier collection efficiency (CCE) for (a) undoped cell (5×10^{15} cm^{-3}, p-type), (b) over-doped cell (-3×10^{15} cm^{-3}, n-type), and (c) compensation-doped cell (-5×10^{14} cm^{-3}, n-type). (d) CCE spectra at the operation voltage of the devices of 0.6 V.

Fig. 4-27 (d) shows the CCE spectra at 0.6 V, which is around the voltage that gives the maximum output power for the cells under investigation. Comparison of the CCE at this bias voltage indicates how severely the quantum structures disturb carrier transport in the devices under operational conditions. Carrier collection under short wavelength light illumination was greatly improved by cancelling out the p-type background doping. Furthermore, the CCE remained over 95% at any wavelength, by lowering the carrier concentration with doping compensation treatment. The CCE at 400–550 nm was higher in the over-doped cell than in the compensation doped cell. This is because the electric field above the SLs is stronger in the over-doped cell and electron-hole pairs generated by short wavelength light are more efficiently separated.

The carrier transport dynamics discussed above resulted in the I-V characteristics and QE at 0 V shown in Fig. 4-28 (a) and (b), respectively. All the three cells showed approximately the same saturated current density at -2.0 V, indicating sufficient carrier collection. These saturated current densities were larger than that for the GaAs reference cell owing to the additional absorption in the wells. The current in the undoped cell started to decrease at approximately -0.5 V as the bias increased, showing a very low fill factor of 0.54, which was much improved to 0.77 using the doping compensation technique. The over-doped cell exhibited a gradual current decrease from -0.3 V to + 0.4 V because of the degraded CCE at longer wavelengths and at forward bias as shown in Fig. 4-27 (b) and (d). The open circuit voltage (V_{oc}) showed absolute enhancement with more efficient carrier transport: 0.831, 0.854, and 0.862 V for the undoped cell, the over-doped cell, and the compensation-doped cell, respectively. V_{oc} can be regarded as the voltage at which the diode current approximately matches the photo-current obtained by the extraction of the photo-excited carriers. The three cells investigated showed almost the same dark current characteristics under forward bias in spite of the significant difference in the band lineup and CCE. The enhancement of V_{oc} by compensation doping, therefore, can be simply explained: the voltage required to match the diode current to the illumination-induced current can be extended because efficient carrier transport increases the amount of collectable photo-excited carriers under forward bias.

Regarding the QE at 0 V, the SL cells showed a response beyond the GaAs absorption edge of 860 nm due to the presence of the SL, from which the effective bandgap was estimated to be 1.2 eV (1030 nm). However, the undoped cell showed a significantly degraded QE below 860 nm, resulting in a lower short circuit current than the GaAs reference cell. The over-doped cell showed almost the same QE from 400 to 650 nm as the reference cell, but showed apparent degradation between 650 and 860 nm because of the lower CCE around the corresponding wavelength range at 0 V. The QE of the compensation doped cell was well matched to that of the reference cell below 860 nm.

Although the I-V and the QE at 0 V show significant difference in the photovoltaic performance among the three cells, the results of these general characterizations alone do not directly clarify the microscopic causes for the poor performance with respect to the carrier behaviors. In contrast, the CCE evaluation based on both wavelength- and bias-dependent analysis clearly reveals the underlying problem in carrier transport, in particular for poor-performance devices.
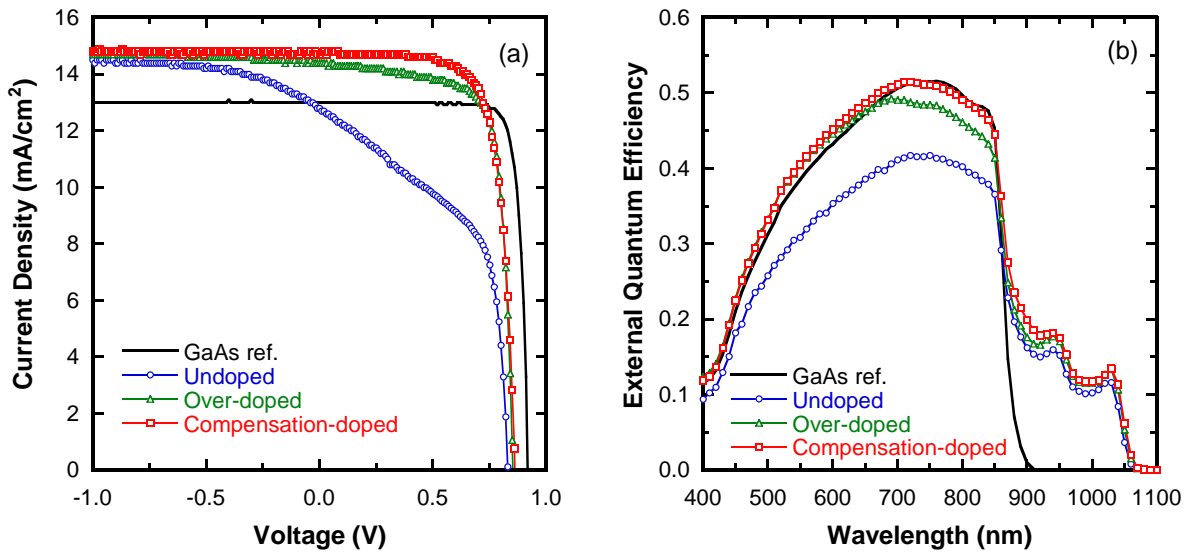
Fig. 4-28   (a) I-V characteristics under AM1.5 illumination and (b) EQE at 0 V of the undoped cell, over-doped cell, and compensation doped cell. The results with the GaAs reference cell are shown together for comparison. Note that the compensation doping treatment was not applied to the reference cell.

As discussed above, the CCE in SL solar cells generally decreases as the applied bias increases because of the weakened electric field in the i-region. The photo-generated carriers not collected by the external circuit would be lost by recombination. Thus, the radiative recombination loss, or PL, is expected to increase with decreasing CCE as the forward bias is applied. As an example, bias-dependent PL spectra of the undoped-cell at an excitation wavelength of 532 nm are shown in Fig. 4-29, from which clear increase of PL intensity at higher forward bias is seen.
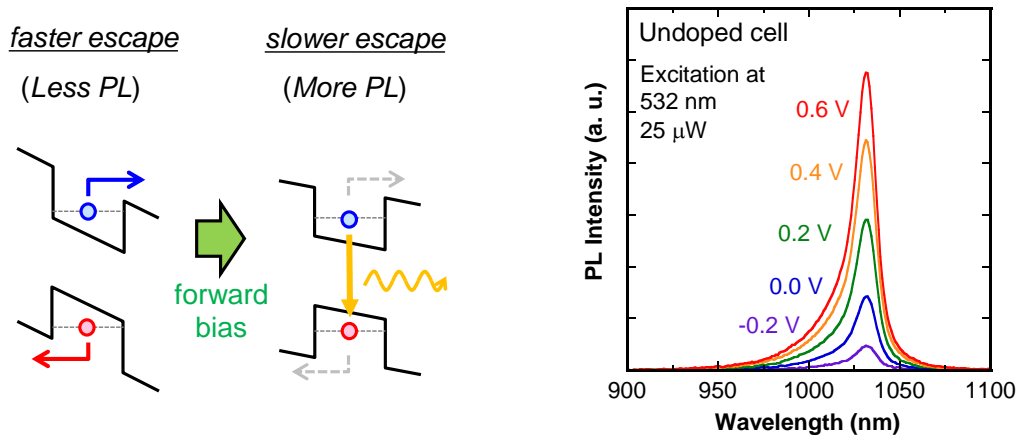
Fig. 4-29   Effects of forward bias in SL solar cells which makes the carrier escape slower and radiative recombination loss larger. Bias dependent PL spectrum of the undoped cell at excitation wavelength of 532 nm and power of 25 μW is shown together as an example.

Fig. 4-30 shows the bias dependence of the integrated PL intensity and the monochromatic CCE at 532 nm for the undoped cell and the compensation doped cell. Note that the PL spectra were obtained by subtracting the electroluminescence in the dark to examine the luminescence via radiative recombination of the photo-generated carriers. In all PL measurements, only one peak at 1030 nm was observed as shown in Fig. 4-29, and no signal appeared around the GaAs band edge wavelength (860 nm). At excitation wavelength of 532 nm, almost all the carriers are generated in the top p-region above the SL, and thus the CCE and PL from the SL are predominantly determined by the electron transport. Therefore, holes are basically not injected to the SL by the illumination, and the PL is attributed to the recombination between the photo-generated electrons and the holes that originally exist inside the SL. Since the radiative recombination rate is determined by the product of the electron and hole concentrations, PL can be obtained when the photo-excited electrons are injected into the SL to make the electron concentration higher.

Note that CCE in this experiment was measured without bias AM1.5 so as to make the carrier dynamics inside the cell similar to the measurement condition of PL, for which bias sunlight was not illuminated. The results of CCE measured under bias light is also shown in the graph for comparison.
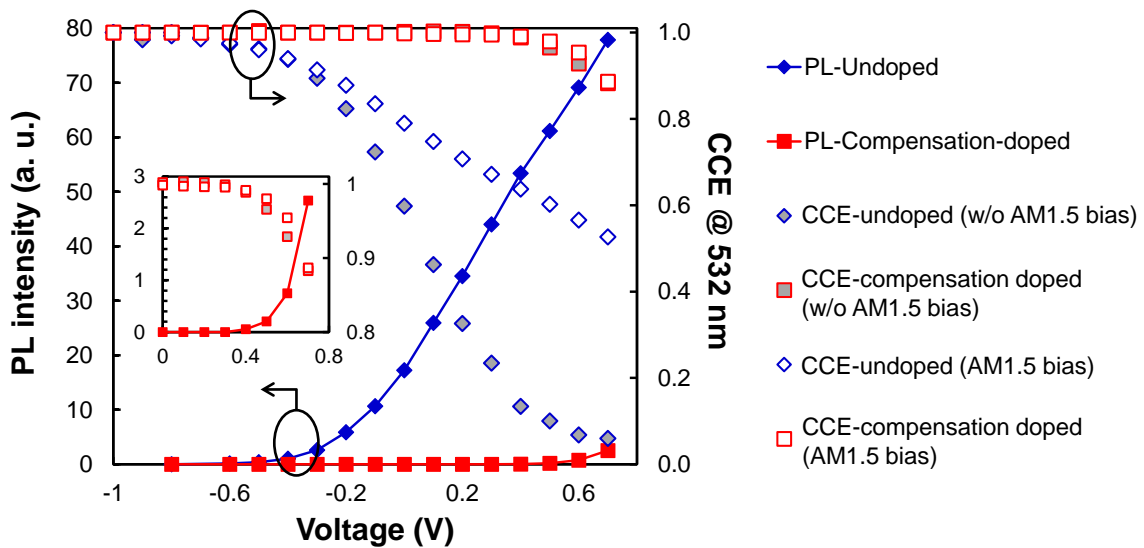
Fig. 4-30 Correlation between the bias-dependent integrated PL intensity and the carrier collection efficiency (CCE) at an excitation wavelength of 532 nm. PL spectra were obtained by subtracting the electroluminescence spectra in the dark at each applied voltage. The blue rhombic plots and red rectangular plots are for the undoped cells and compensation doped cell, respectively. Note that CCE was measured with and without AM1.5 bias light; evaluation without bias light should be more appropriate for the comparison with PL, which was measured in the absence of bias illumination.

As for the undoped cell, CCE started to decrease at approximately -0.4 V. The PL appeared at almost the same bias, and continuously increased as the CCE decreased at a larger bias. Likewise, in the compensation doped cell, the PL appeared at approximately +0.4 V, where degradation of the CCE became apparent, and it rapidly increased in a similar manner to that in which the CCE decreased as the forward bias was further increased. This correlation is clear evidence that CCE degradation indeed leads to radiative recombination loss of the photo-generated carriers.

In the undoped cell, the effects of AM1.5 bias illumination was significant. As discussed in the section 4.4.3, carriers are more likely to be lost in the absence of bias illumination probably due to no passivation of the non-radiative recombination centers. Therefore, CCE showed rapid degradation from reverse voltage with clear PL accordingly observed, and it was only below 0.5 at forward bias. This resulted in extremely low CCE (without bias light) below 0.1 at 0.4 - 0.7 V, indicating that the most photo-excited electrons were lost at an operational voltage. In contrast, the CCE in the compensation doped cell exhibited negligible reduction at reverse bias, and remained over 0.9 at 0.6 V by improving electron transport under strong electric field. Consequently, as estimated from the PL intensity, radiative recombination loss was suppressed by a factor of approximately 1/100 at an operating bias of 0.6 V.

Since the amount of radiative recombination is proportional to the product of the electron and hole concentrations as mentioned above, the decay speed of the photoluminescence after instantaneous excitation with a pulse laser corresponds to the speed at which the carriers disappear from the wells. Therefore, the time constant of the TRPL measurement τ_{PL} is expressed as

$$\frac{1}{\tau_{PL}} = \frac{1}{\tau_R} + \frac{1}{\tau_{NR}} + \frac{1}{\tau_{ES}} \tag{4-14}$$

where τ_R is the radiative recombination time, τ_{NR} is the nonradiative recombination time, and τ_{ES} is the carrier escape time.

Fig. 4-31 (a) shows the results of the TRPL measurements for the undoped cell and the compensation doped cell. In both cases, the PL decay time became longer as the forward bias increased. Under a weaker electric field, in general, carrier escape from the wells becomes slower as illustrated in Fig. 4-29 whereas the nonradiative recombination becomes faster because carriers are less likely to be driven out from the recombination centers. Thus, the τ_{PL} obtained in the present study seems to dominantly reflect the carrier escape time. Comparison of the PL time constant therefore allows us to examine how rapidly photo-excited carriers are transported through the SL region.

Fig. 4-31 (b) shows the bias dependence of the PL time constant estimated from the PL decay curve. The decay curves for the compensation doped cell could be well fitted using a single time constant, whereas the undoped cell showed more than one time constant resulting in long tails in the decay curves. This can be attributed to different carrier escape times, depending on the position of the wells, because the electric field differs in the depth direction due to the bent band lineup. In other words, the carriers in the top part of the SL region have very low escape speeds because of the

flattened band, whereas the carriers in the bottom wells can escape relatively rapidly in the presence of the stronger electric field. In contrast, the electric field distribution in the SL region for the compensation doped cells was almost uniform, resulting in single-exponential decay curves.

As plotted in Fig. 4-31 (b), the PL time constant was much shorter for the compensation doped cell than for the undoped cell at any applied bias: 11‑25 ns and 3 ns at 0 V, and 18‑51 ns and 7 ns at 0.6 V for the undoped and the compensation doped cells, respectively. This result clearly indicates that the compensation doping treatment to manipulate the band lineup enables the photo-generated carriers to escape from the wells much faster, and be transported through the SL region quickly.
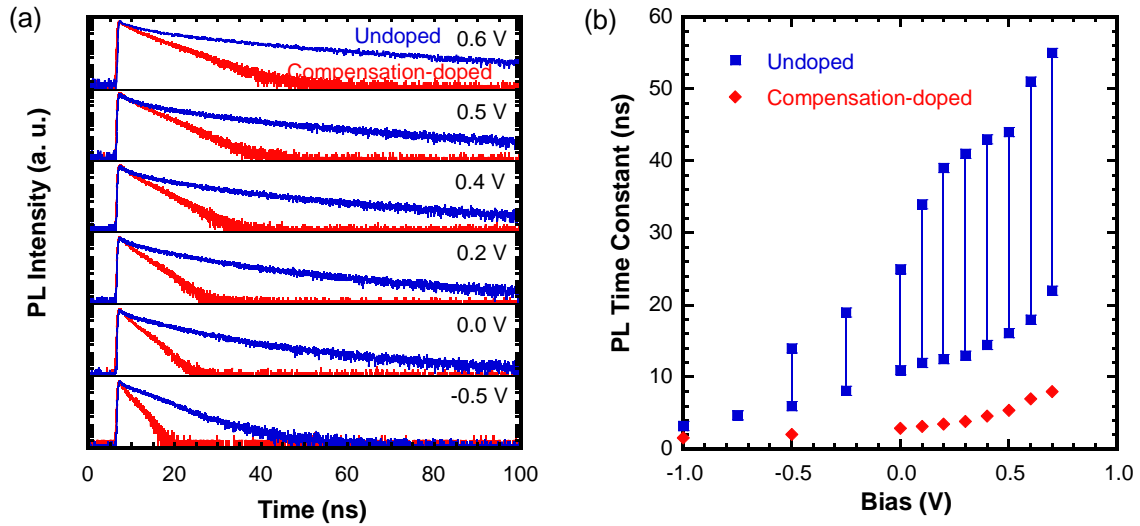
Fig. 4-31 PL decay curves at a variety of applied bias values with the undoped cell and the compensation-doped cell, and (b) PL time constants estimated from the decay curves. The samples were excited at the wavelength of 780 nm and repetition rate of 10 MHz. The PL decay curves with the undoped cell showed multiple time constants whereas those with the compensation doped cell were well fitted with a single time constant. The lines in the plots of the undoped cell indicate the range of the time constant.

4.5.2 Challenges for 1.2 eV bandgap SL solar cells with a large number of periods

For current match in Ge-based triple junction solar cells, the SL to be incorporated should have a band-edge beyond 1000 nm, and a period number of 100 or more. Due to the difficulty in growing high quality SLs with a large number of periods with a high indium content, however, reports related to SL cells that meet such requirements are only few, and most research efforts in this field have introduced SLs with band-edge below 950 nm, or periods up to 70. With extension of the bandedge, the carrier transport becomes more difficult because of the higher potential barriers in the narrow-gap quantum wells. Increasing the SL period number also makes the carrier collection less efficient since each quantum well acts as a carrier trap center.

In this section, the challenges in carrier transport that emerge when such a narrow-gap (1.2 eV) and a large number period (100-period) SL is incorporated are examined by CCE.

■ Experiments

(1) A GaAs pin cell including 100-period $In_{0.25}Ga_{0.75}As$ (7.0 nm)/$GaAs_{0.66}P_{0.34}$ (10.6 nm) SL in the i-region was grown on an n-doped GaAs (0 0 1) substrate (Hitachi Cable). The cell was capped with an InGaP window layer on the top. One period of the SL was 20-nm-thick, including graded interlayers which consisted of GaAs (0.6 nm) and $In_{0.13}GaAs$ (0.6 nm) interlayers inserted between a well and a barrier. The entire SL region was then 2000-nm-thick in total and it was sandwiched between two 100-nm-thick GaAs spacer layers. A GaAs reference cell with 2200 nm i-region was also prepared for comparison. Compensation doping with sulfur was performed for the entire i-region with the same condition mentioned in the previous section to lower the carrier concentration of the GaAs layer to 5×10^{14} cm^{-3}.

(2) *In-situ* reflectance measurement was carried out during the MOVPE of the SL cell to monitor the stability of the SL growth at wavelength of 443 nm. The grown epitaxial layers were characterized by XRD ω-2θ scan around the (0 0 4) diffraction point. The bandgap was confirmed by photoluminescence.

(3) The epitaxial layers were processed into solar cells in a same manner as explained in section 4.5.1.2; AuGeNi back contacts were deposited and annealed prior to the deposition of the Ti/Au front contacts. The heavily-doped p-GaAs top layer was etched in mixed solution of H_2O 35mL / H_2O_2 2.5 mL / $C_6H_8O_7$ 10 g.

(4) Photovoltaic performance (I-V and QE) and CCE were measured in a solar simulator. QE and CCE were measured with 2.5 mW/cm^2 monochromatic light under AM1.5 bias illumination.

Note that a particular bandgap in a SL, which is approximately 1.2 eV in this study, can be achieved by various combinations of composition and thickness for each layer; a thin and deep well, and a thick and shallow well can achieve the same bandgap. Among a various available layer combinations, a very standard SL structure was chosen with moderate indium and phosphorus contents and relatively thick wells and barriers for which the crystal growth is comparatively straightforward as a first step. Therefore, the SL used in this section is designed to prevent tunneling and to allow thermionic escape alone in principle, for the purpose of examining the carrier transport problems that exist in a cell with such a typical SL design.
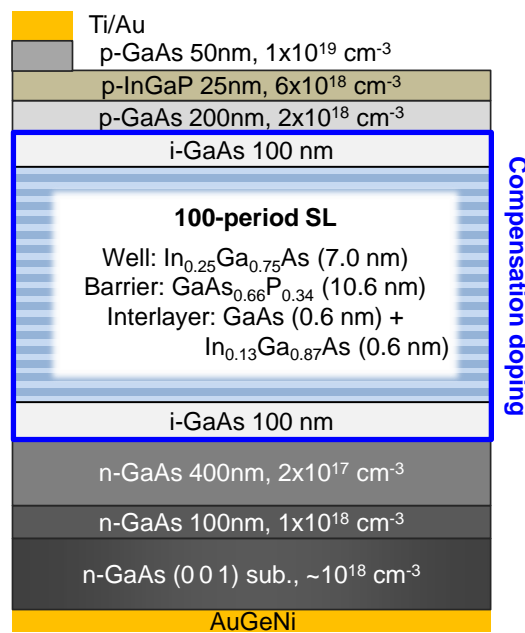
Fig. 4-32   Structure of a GaAs pin cell including 100-period SL

■   **Results and discussion**

Fig. 4-33 shows the time transient DC reflectance and reflectance anisotropy (RA) during the growth of the SL solar cell. The reflectance for the SL oscillates due to the Fabry-Perot interference; it decreases and increases during GaAsP and InGaAs growth, respectively. If the lattice relaxation is negligible and the surface remains flat, the average reflectance remains at a constant value, which is determined by the average refractive index of the SL. Successful growth with good crystal quality and mirror like surface was suggested by the constant average reflectance in the entire SL growth as shown in (a). RA during the SL growth shows periodic signal corresponding to each component layers as indicated in (c) and (d), which shows the RA for two periods in the initial and end part of the SL region, respectively. The signal peaks confirmed from GaAsP to InGaAs are attributed to 2 second

purge with TBAs after the InGaAs growth. Almost the same signals observed in (c) and (d) indicate that the 100 periods in the SL are fairly identical.

The reflectance during the growth of the GaAs spacer layer and the p-GaAs emitter above the SL region showed Fabry-Perot oscillation at the beginning, and was finally recovered to the same level as the GaAs before the SL growth, indicating that apparent crystal degradation due to the SL growth was not confirmed by the reflectance monitoring.
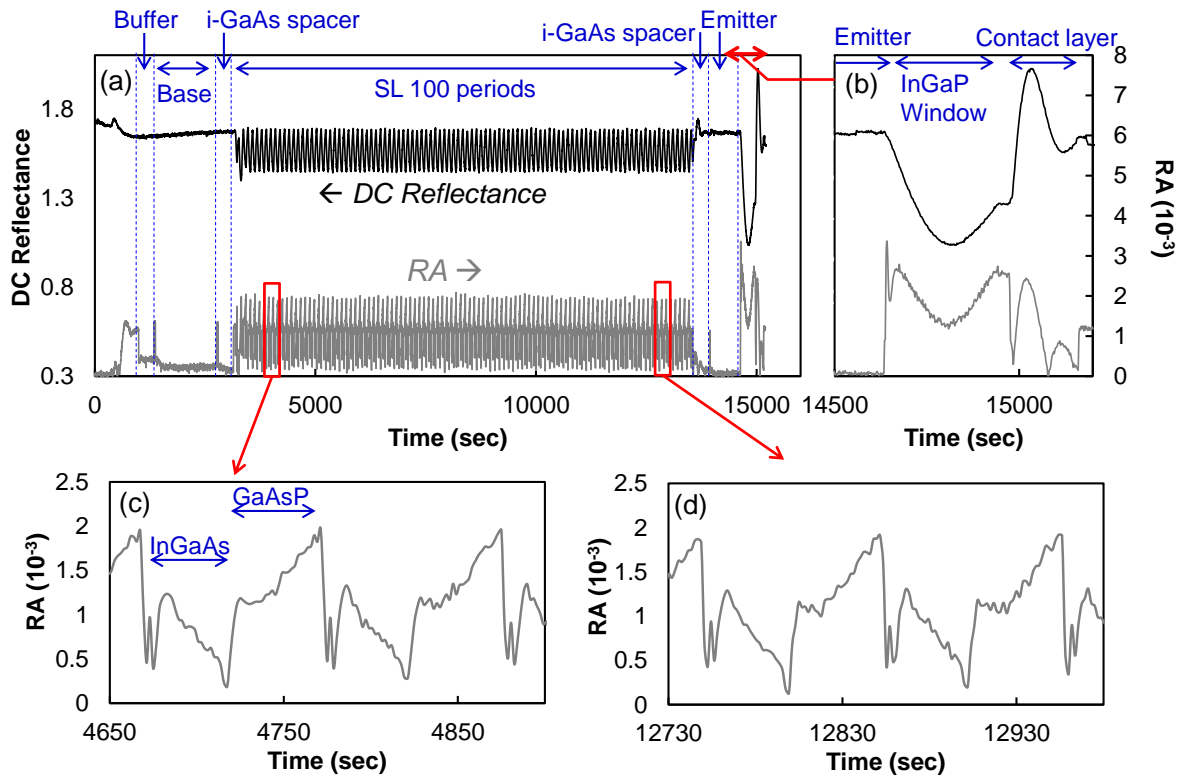
Fig. 4-33 *In-situ* monitored reflectance during growth of a 100-period SL solar cell. (a) DC reflectance and reflectance anisotropy (RA) during the entire growth, (b) a magnified plot from the p-emitter to the p-contact layer, and (c) (d) magnified RA for two period in the initial and the end part of SL growth. Note that the measurement was performed at wavelength of 443 nm.

Fig. 4-34 (a) shows a XRD pattern of the ω-2θ scan recorded around the GaAs (0 0 4) diffraction point of the SL cell. The fringe pattern in the XRD is attributed to the periodic SL structure. The quite sharp and symmetric satellite peaks in the fringe pattern indicate good uniformity of the layer thickness and composition in the 100-period SL.

The target bandgap of 1.20 eV was confirmed in the PL shown in Fig. 4-34 (b). The sharp PL peak and abrupt tail in the longer wavelength side suggest good crystal quality in the SLs.
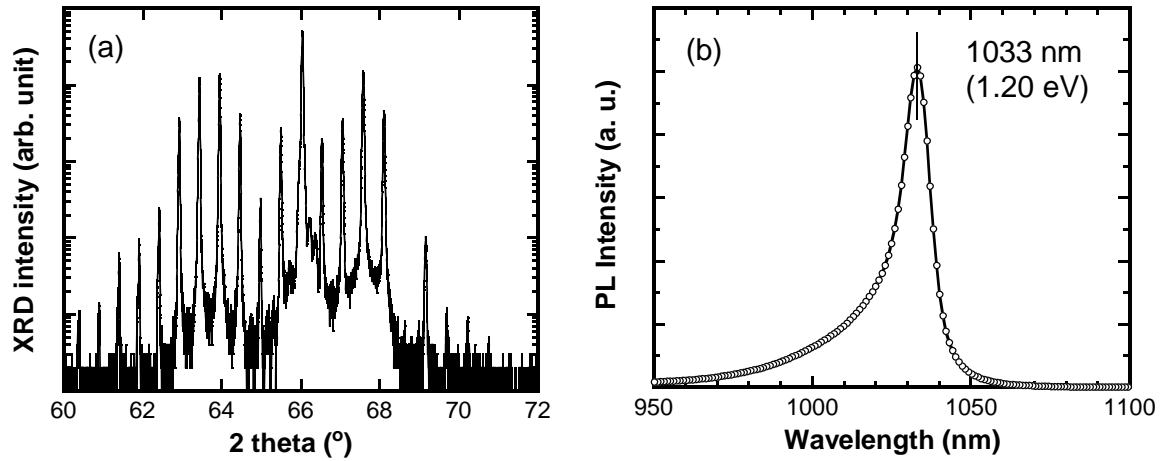
Fig. 4-34 (a) XRD pattern of ω-2θ scan around the (0 0 4) diffraction point and (b) PL spectrum of the 100-period SL cell.

Fig. 4-35 (a) shows the I-V characteristics under AM1.5 illumination of the SL100 cell and the GaAs reference cell. The SL100 cell enhanced the J_{sc} from the reference cell by approximately 3 mA/cm^2, but its degraded V_{oc} and FF resulted in a lower efficiency. The degradation of V_{oc}, however, was only 0.11 V and, which was much smaller than the difference in E_g/q (bandgap over the elementary charge) of 0.22 V (=1.42 eV – 1.20 eV). This phenomenon has been reported in other researches using different SL systems such as AlGaAs/GaAs, InP/InGaAs and GaInP/GaAs [65, 109], which reported that solar cells including SLs exhibited higher V_{oc} than expected for single junction cells which consist of bulk material with the same effective bandgap. This is an important advantage for SL solar cells because efficiency gain can be expected by making the carrier transport efficient and suppressing the degradation of FF.

However, the SL100 cell in Fig. 4-35 showed significant deterioration of FF due to the difficulty of carrier extraction at forward bias through a large number of quantum wells. The I-V showed an apparent slope even at 0 V, and quite high reverse bias of -5 V was necessary to achieve the saturation of the photocurrent and hence total carrier collection. The current of 23.5 mA/cm^2 at the short circuit condition was increased up to 25.3 mA/cm^2 at -5V.

Fig. 4-35 (b) shows EQE at 0 V together with the saturated spectrum obtained at -5 V for the SL100 cell. The saturated spectrum at reverse bias well matched with that of the reference cell in the GaAs absorption wavelength range, and achieved 50% EQE in average beyond the GaAs bandedge. The QE of the SL cell, however, was strongly bias-dependent due to insufficient carrier transport, and exhibited an apparent degradation beyond 650 nm at 0 V. As a result, the EQE for 1e-1hh transition around 1000 nm remained only 32%, which corresponds to 46% IQE.
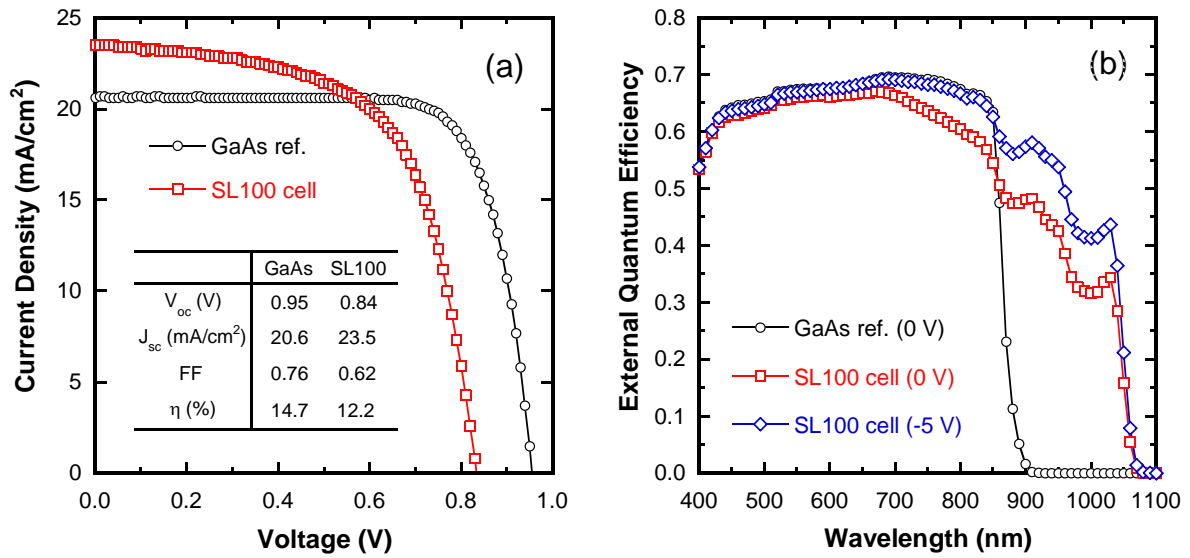
Fig. 4-35   (a) I-V characteristics under AM1.5 illumination and (b) EQE of the SL100 cell and the GaAs reference cell. EQE at -5 V is also plotted for the SL100 cell.

Fig. 4-36 shows wavelength dependent CCE as functions of the applied voltage. CCE was severely degraded at longer wavelength with increase of the forward bias, becoming only 70% and 85% at 0 V and -1 V at 1000 nm. In 400 - 600 nm at which the light is mostly absorbed in the region above the SL, on the other hand, almost 100% CCE was obtained at 0 V, indicating that the electron transport from the top to the bottom was relatively efficient. However, CCE at all wavelengths rapidly decreased beyond 0.5 V, and became only below 60% at 0.7 V regardless of the excitation wavelength.

The total thickness of the i-region was 2.2 µm including a 2-µm-thick SL. The low built-in field in such a thick i-region, leads to high probability of recombination of the electron-hole pairs generated inside the wells before being separated. This explains the specifically degraded CCE beyond 800 nm, at which excitation inside the well becomes dominant. Furthermore, the band-lineup of the 2.2-µm-thick i-region is inevitably bent even with compensation doping treatment to lower the carrier concentration to as low as 5×10^{14} cm^{-3}. Since only slight sulfur doping makes the net doping n-type as mentioned in 4.5.1.1, the band-lineup in the bottom part of the i-region is flattened as illustrated in Fig. 4-37, resulting in the degraded CCE under illumination of longer wavelength light that generate carriers in the deeper region. These results clearly shows the difficulty in achieving good cell performance with more than 100-period SL with typical design. Using barriers thicker than 10 nm, the predominant process of carrier transport is thermionic escape. In order to overcome the problem of insufficient carrier transport through the thick SL, therefore, efficient tunneling transport should be indispensable.

Fig. 4-36   Wavelength dependent CCE of the SL100(1.2 eV) cell as functions of the applied voltage
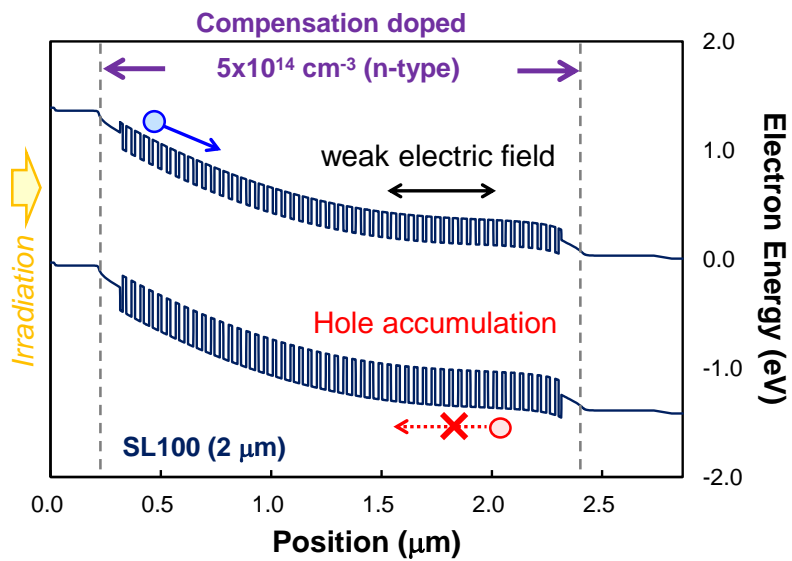
Fig. 4-37   Simulated band-lineup for a GaAs pin cell with a 2-μm-thick SL. To simplify the simulation, 50-period SL with doubled thicknesses for each layer in Fig. 4-32 are incorporated.
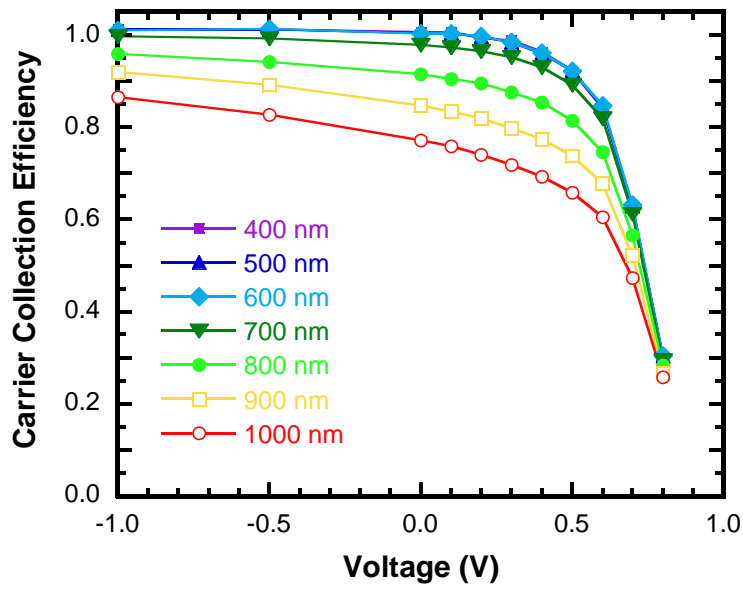
4.6 Summary of chapter 4

In this chapter, carrier collection efficiency (CCE) was defined as a parameter to evaluate the carrier transport in solar cells, and the effects of 1.2 eV bandgap SLs on the photovoltaic performance was investigated.

- The CCE is defined as the fraction of carriers photo-generated in the active p-n junction area of a cell, and can be calculated by normalizing the illumination-induced current enhancement to its saturation value at reverse bias. Combining wavelength- and bias-dependence of CCE, the transport of carriers from each region inside the cell can be examined in detail.

- The derivation procedure of the CCE was comprehensively validated by investigating 1) the bias dependence of the absorption in quantum wells, 2) the balance between the amount of absorbed photons and the amount of collectable carriers, 3) the effect of bias sunlight for monochromatic CCE measurement, and 4) the effects of resistance.

- Effectiveness of compensation doping in the i-region was examined. Unintentional p-type background doping due to carbon incorporation during MOVPE causes undesired bending of the band lineup in the i-region, and was found to severely degrade the carrier transport. By compensating the background doping with sulfur to make the electric field distribution uniform in the i-region, transport of the carriers generated anywhere in the device was greatly improved.

- Challenges in SL cell with a large number of periods was investigated using a standard SL design with moderate indium and phosphorus contents and relatively thick wells and barriers: $In_{0.25}Ga_{0.75}As$ (7.0 nm)/$GaAs_{0.66}P_{0.34}$ (10.6 nm). Incorporation of a 100-period SL makes the total thickness of the i-region over 2 μm, where the carrier transport becomes quite difficult because of the weakened electric field which makes the electron-hole separation insufficient, as well as the inevitably flattened band-lineup even with compensation doping treatment. To overcome this problem, it should be dispensable to make the i-region as thin as possible with efficient light absorption and to facilitate tunneling transport through the barrier layers.

5 Design of SL structure for higher performance

The major challenge in SL or MQW solar cells is the trade-off between light absorption and carrier collection, which is a general problem not only for InGaAs/GaAsP but also other material systems. Sufficient light absorption inside the SL requires a large number of wells to be stacked, which imposes us of more difficulty in extracting carriers through the SL regions because of the weakened electric field in the thickened i-region, in particular with not negligible effects of background doping as revealed in section 4.5.2. Therefore, the SL structure must be appropriately designed for both sufficient light absorption and carrier collection.

In this chapter, the general restriction for the design of InGaAs/GaAsP SL will be first discussed, and then several SL designs used in other researches will be briefly reviewed. On the basis of these backgrounds, this research proposes stepped tunnel superlattice (STSL) as a general SL design principle for higher cell performance. The design criteria for the individual layers in the STSL will be theoretically and experimentally discussed. Consequently, an achievement of absolute photovoltaic efficiency gain using 100-period 1.23 eV bandgap SL will be demonstrated.

5.1 Design of InGaAs/GaAsP SL for efficient carrier transport

5.1.1 Strain balance: a restriction for design of InGaAs/GaAsP SL

InGaAs/GaAsP stain balance SL cannot be arbitrary designed because of the restriction with respect to the epitaxial growth. That is, critical lattice relaxation due to lattice mismatch must be prevented by balancing the compressive strain in the InGaAs layers and the tensile strain in the GaAsP layers. Note that this restriction does not necessarily require exactly zero net strain.

Fig. 5-1 shows the difficulty in designing the InGaAs/GaAsP quantum well structure for efficient carrier transport, which has two mechanisms as introduced in the section 2.2.3: thermionic escape and tunneling escape.

(1) Thermionic escape

For efficient thermionic escape, the potential barrier must be lowered and the electric field should be present because they exponentially affect the escape time constant as indicate in the eq. (2-75). To lower the potential barrier the phosphorus content in the GaAsP must be reduced, but it also requires

the barrier to be thickened to conserve the strain balance condition due to the smaller tensile strain. Consequently, the entire SL region becomes thicker, weakening the built-in field.

The 100-period SL cell fabricated in chapter 4 was designed using $GaAsP_{0.34}$ with bandgap of 1.76 eV, and thus the sum of the barrier heights for the conduction band and the valence band is as large as 0.56 eV. Lowering the phosphorus content, therefore, should be effective to make the thermionic escape more efficient, but it makes the total i-region thicker than 2μm, resulting in much more serious band flattening even with compensation doping treatment.

(2) Tunneling escape

The barriers must be thinner to facilitate efficient tunnel transport, but they cannot be unrestrictedly thinned in light of the strain balance condition. Preservation of the tensile strain accumulation with thinner barriers requires higher a phosphorus content, which makes the crystal growth more difficult. Theoretically, the SL can be infinitely stacked if the thickness of each layer is below the critical thickness and the net strain is well balanced out. In practice, however, partial lattice relaxation tends to gradually occur during formation of the hetero-interfaces between the two oppositely stained layers, eventually resulting in severe crystal degradation [110]. A too high phosphorus content is also detrimental because the barrier height affects the tunneling probability as indicated by the eq. (2-76). If both InGaAs and GaAsP layers are thinned together to conserve strain balance condition, then the bandgap becomes higher due to larger quantum confinement effects.

All the problems summarized above is generally more serious with lower effective bandgap of the SL. It is because narrowing the bandgap requires either deeper wells with higher indium content or thicker wells, both of which enlarge the accumulation of the compressive strain in the InGaAs, thus requiring the GaAsP barriers to be either thickened or with higher phosphorus content for strain balancing.
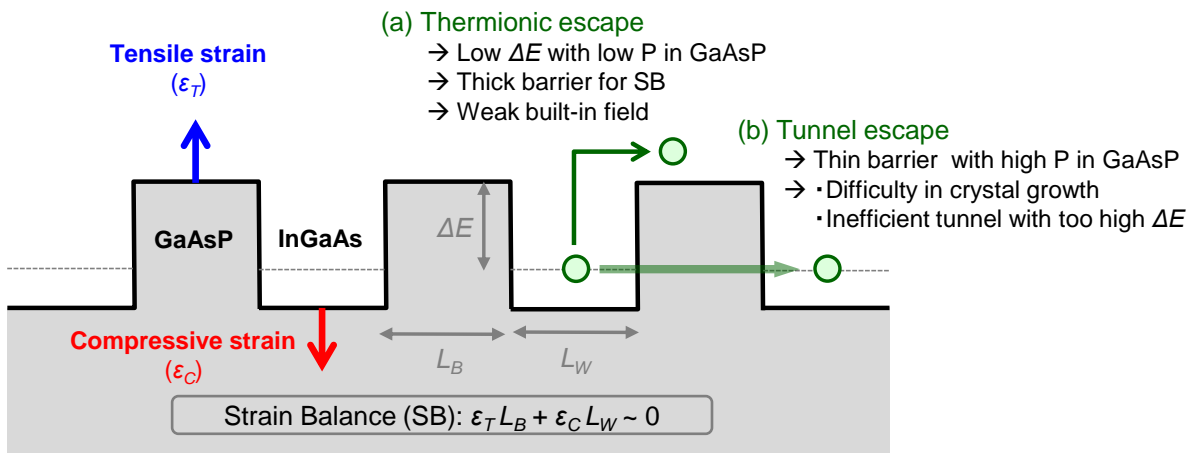

Fig. 5-1   Challenge in design of InGaAs/GaAsP quantum well structure for efficient carrier transport, either via (a) thermionic escape and (b) tunneling escape.

5.1.2 SL design for efficient carrier transport

Various quantum structure have been proposed and investigated for efficient carrier transport in SL solar cells not only with InGaAs/GaAsP system but also with different material combinations. (See Fig. 5-2)

- Stepped potential SL

In a stepped potential SL, the thermionic escape from the wells is assisted by the multiple-stepped potential. Carriers in the ground states can hop out of the well via successive thermionic excitation. This concept was proposed in GaAs/ $In_xGa_{1-x}As$/ $In_yGa_{1-y}As$ ($x < y$) system [111, 112]. In the presence of electric field in such a potentially modulated quantum well, the electrons and the holes that are thermally excited to the upper states move to the opposite step layer regions with their wave functions spatially separated, resulting in lower probability of recombination loss. In InGaAs/GaAsP SL solar cells, strain-neutral GaAs has been used as the step layer [113].

- Tunnel SL

In a tunnel SL, the carriers are transported via efficient tunnel process through thin barriers, for which the mechanism was introduced in the section 2.2.3.2. In InGaAs/GaAsP SL cells, thinning the barriers from 6 to 2 nm has been suggested to be effective to facilitate tunneling by systematic study using low-temperature and time-resolved characterization [114]. Due to the requirement for strain balance condition, however, such tunnel SLs have been mostly demonstrated with band-edge wavelength below 950 nm ($E_g > 1.30$ eV) by using InGaAs layers with small thickness or low indium content [115]. A challenge for tunnel SL is the difficulty in crystal growth with a high phosphorus content to accumulate sufficient tensile strain in thin GaAsP layers [116], which will be also discussed in the section 5.3.2.1.

- Staggered SL

In a staggered SL, the strain balance condition is satisfied in a set of several periods, which is stacked as a unit structure. Thin barriers to facilitate tunneling are inserted between individual InGaAs layers with different well widths. The effective bandgap of the SL is determined by the thickest well with the weakest confinement effect, where the long wavelength light is absorbed. The thin wells are inserted in order to reduce the average compressive strain which have to be compensated by the thin GaAsP. In this structure, carriers tunnel through several thin barriers after being excited in the thickest InGaAs well [117]. This concept can be expanded to resonant tunnel SL as shown in Fig. 5-2, where the carriers in the ground state in the thick well are transported via resonant tunneling to the excited state in the thinner well. In this case, the one period of a staggered SL must be appropriately designed so that the energy levels among the several wells match under the operational condition, namely at the maximum power output voltage. The resonant tunnel SL was proposed with GaAs/GaAsN SL with large conduction band offset [118], and also has been attempted with InGaAs/GaAsP system [119].

Despite the various proposed SL designs, successful demonstration of InGaAs/GaAsP SL cells with band-edge extended beyond 1000 nm, and over 100 periods is yet to be reported to date.

Stepped SL	Tunnel SL	Staggered SL
Successive thermionic escape in stepped potential profile.	Fast tunnel escape through thin barriers.	Resonant tunnel through several wells with different thicknesses.
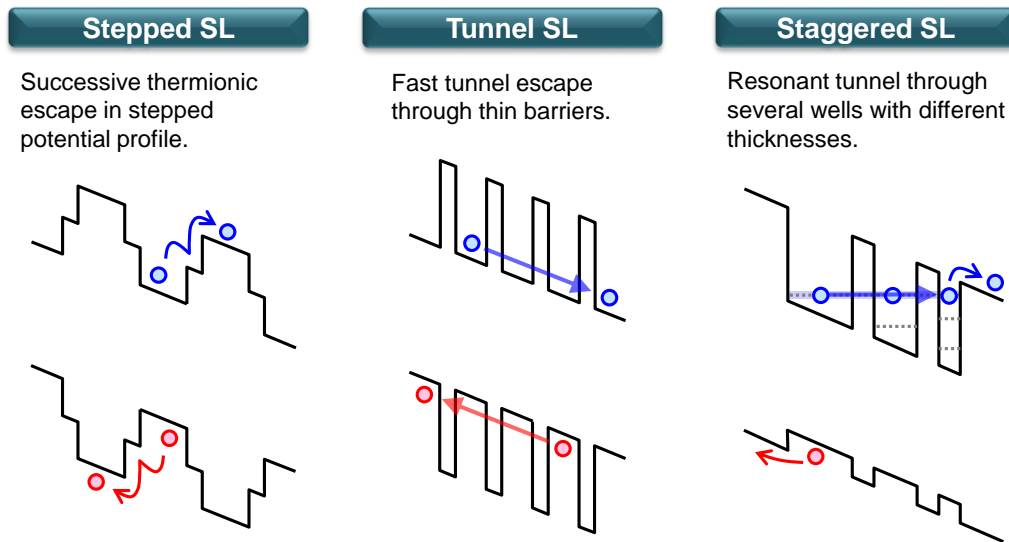
Fig. 5-2   Various types of SL designs for efficient carrier transport proposed in previous researches.

5.2 Stepped tunnel superlattice (STSL)

This research proposes stepped tunnel superlattice (STSL) as a design principle for SL structures that achieve more efficient light absorption and carrier collection while also facilitating successful crystal growth.

The InGaAs/GaAsP quantum wells in general are composed of InGaAs well layers, GaAsP barrier layers, and GaAs interlayers between them. The GaAs interlayers are optional, and the band for a single well has a stepped structure for relatively thick interlayers, whereas it has a rectangular line-up in the absence of interlayers. The proposed design principle in this research can be summarized into the following three points:

1) InGaAs wells should be made thinner and deeper for a given bandgap in order to achieve both a higher absorption coefficient for 1e-1hh transitions, and to reduce the compressive strain accumulation.

2) GaAs interlayers with thicknesses of a few nanometers can effectively extend the absorption edge to longer wavelengths without introducing compressive strain, and can also suppress lattice relaxation during growth.

3) GaAsP barriers should be thinner than 3 nm to facilitate tunneling transport, and their phosphorus content should be minimized while avoiding detrimental lattice relaxation.

In STSL, carriers (electrons and heavy holes) in the InGaAs wells are thermally excited to the upper state and then tunnel through the GaAsP barriers. Since the GaAs interlayers are quite thick, they prevent the carriers in the InGaAs from being transported to the neighboring wells via direct tunneling. It should be noted that for light holes, the valence band is lower in InGaAs than GaAs as will be shown in 5.3.4, and thus the light holes in their ground states can possibly tunnel through the GaAsP barriers directly. However, the heavy hole transport is much less efficient than the light hole transport due to the larger effective mass and the higher potential barrier, and thus extraction of heavy holes should be the major concern that limits the cell performance.

In the rest of this section, the theoretical and experimental grounds for this proposed design principle will be discussed.
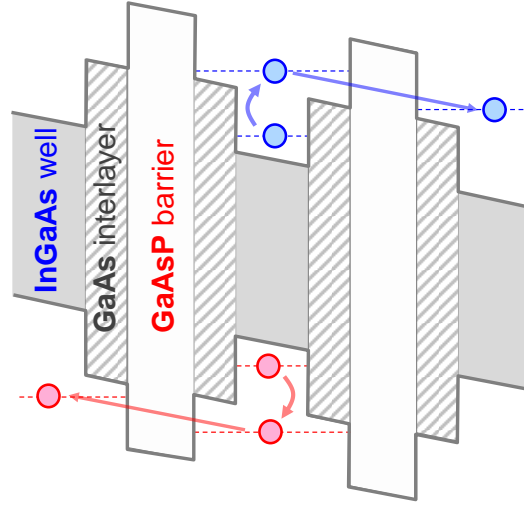
Fig. 5-3   Schematic of stepped tunnel InGaAs/GaAsP superlattice

5.3 Design of InGaAs/GaAsP STSL

5.3.1 InGaAs well design

5.3.1.1   Efficient light absorption in thin wells

Design of InGaAs well region is important since it determines the light absorption in the SL. As derived in the section 2.2.2, The light absorption coefficient due to direct transitions in quantum wells can be written as

$$\alpha_{QW}(E) = \frac{1}{L_W} \cdot \frac{q^2 \hbar |M_0|^2}{m_0^2 \varepsilon_0 cnE} \left(\frac{\mu_r}{\hbar^2}\right) \sum_{n_e,n_h} \Theta(E - E_{\mathrm{QW}}) \left|\left\langle \phi_{\mathrm{e},n_e} \middle| \phi_{\mathrm{h},n_h} \right\rangle\right|^2 [F_{\mathrm{V},n_h}(E) - F_{\mathrm{C},n_e}(E)], \qquad (5\text{-}1)$$

where q is the elementary charge, M_0 is the momentum matrix element, μ_r is the reduced mass of electrons and holes, L_W is the well thickness, m_0 is the electron static mass, ε_0 is the vacuum

permittivity, c is the light velocity, n is the refractive index of the cell material, and Θ is a step function representing the density of states. E_{QW} is the quantized transition energy, which is the sum of the bandgap of the well material and the eigen-energies in the conduction and valence bands. $F_{C,n}$ and $F_{V,n}$ are the distribution functions for each quantum level for electrons and holes, respectively.

Fig. 5-4 shows simulated absorption coefficient for 1.2 eV bandgap bulk $In_{0.16}Ga_{0.84}As$ and $In_xGa_{1-x}As/GaAs_{0.4}P_{0.6}$ single quantum well with different well thicknesses.

For bulk III-V semiconductor, it is known that M_0 can be well approximated as

$$|M_0|^2 = \frac{m_0^2 E_g (E_g + \Delta)}{12 m_e *(E_g + 2\Delta/3)},$$ (5-2)

where Δ is the spin orbit splitting energy, and m_e* is the electron effective mass [120], and this approximation was used for the simulation for the bulk InGaAs and also for the case of quantum well for simplification. To achieve the equal bandgap of 1.2 eV in the quantum well, the well composition was adjusted depending on the well thickness. We also assumed the bandoffset of 0.5, and an approximation that the overlap integral in the eq. (5-1) is 1 ($n_e = n_h$) or 0 ($n_e \neq n_h$). Note that the absorption coefficient simulated in the Fig. 5-4 is only for direct transitions around the Γ point, where parabolic band diagram was assumed.

As can be seen in Fig. 5-4, the absorption coefficient for bulk for is 0 at the band-edge wavelength because of the zero density of states. (In reality, the absorption occurs around the bandgap energy due to the Urbach tail and free carrier absorption as mentioned in the section 4.3.1 and 4.4.1). In a quantum well, in contrast, the absorption coefficient at a specific wavelength is given as a sum for the available transitions, and thus it steeply rises at the band-edge due to finite density of states. As shown in the eq. (5-1), the absorption coefficient for each transition is inversely proportional to L_W. As the well is thickened, therefore, the absorption coefficient for individual transitions are reduced while the number of available transitions increases, resulting in the total absorption coefficient approaching that of the bulk.

The absorption at the lowest energy in InGaAs/GaAsP QWs is attributed to the transition between electrons and holes in their ground states, i.e. 1e-1hh, which must be sufficiently large for complete absorption of photons in the SL. Since the absorption coefficient for each transition is inversely proportional to L_W, the absorbance of one quantum well, which is the product of the well thickness and the absorption coefficient, is preserved for each transition even if the thickness differs. In the entire SL region, consequently, the absorption contribution from the 1e-1hh transitions is determined by the number of wells, regardless of the well thickness.

For a given bandgap, therefore, incorporation of a larger number of thinner wells is a principle strategy in terms of efficient absorption in an i-region, the thickness of which should be minimized for more efficient carrier collection. Note that the wells must be made deeper to preserve the effective bandgap at a longer wavelength because of the stronger quantum confinement effects present in thinner wells.
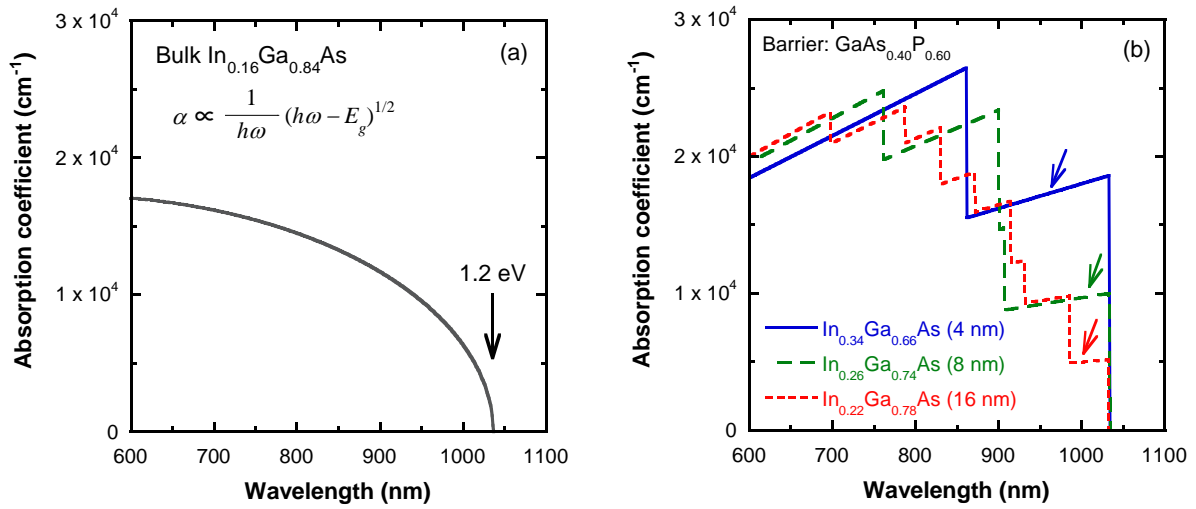
Fig. 5-4   Simulated absorption coefficient for 1.2 eV bandgap (a) $In_{0.16}GaAs$ bulk and (b) an InGaAs/GaAsP single quantum well. The 1e-1hh transition is indicated by the arrows.

5.3.1.2   Accumulation of compressive strain

Thin and deep InGaAs wells also offer advantages with regard to crystal growth. Accumulation of compressive strain per single InGaAs layer is smaller for a thin and deep well with a high indium content than that for a wide and shallow well. Fig. 5-5 shows simulated InGaAs well thickness and accumulated compressive strain per well as functions of indium content for InGaAs/GaAs quantum wells to obtain an equal absorption-edge energy of 1.23 eV. The absorption-edge energy in quantum wells is defined as the sum of the bulk bandgap of the InGaAs layer and the eigen-energies for electrons and heavy holes in their ground states. Therefore, the well thickness necessary to achieve a particular bandgap is uniquely determined for each indium composition.

The accumulated compressive strain per InGaAs layer can be then calculated as the product of the lattice mismatch and the well thickness. By increasing the indium content from 20% to 30%, the necessary well thickness and strain accumulation for the given bandgap of 1.23 eV can be reduced approximately by 1/2 and 1/3, respectively. Smaller accumulation of the compressive strain enables the GaAsP barriers to be thinner or have low phosphorus content to conserve the strain balance condition. However, if the indium content is too high, it may lead to three-dimensional (3D) growth because of the very thin critical thickness [121, 122]. Even within the critical thickness, crystal degradation is more likely to occur during formation of hetero interfaces between GaAs(P) and highly strained InGaAs with higher indium composition.

Therefore, an appropriate indium content level should be chosen to avoid abnormal growth occurring; we choose $In_{0.30}Ga_{0.70}As$ as the well composition because the epitaxial growth is often unsuccessful with indium content higher than 30%. Fig. 5-6 shows a nomarski microscope image for

surface of a 35-period InGaAs/GaAsP SL grown at 610 ºC with indium content of 32%, in which a number of hillocks are observed [123].
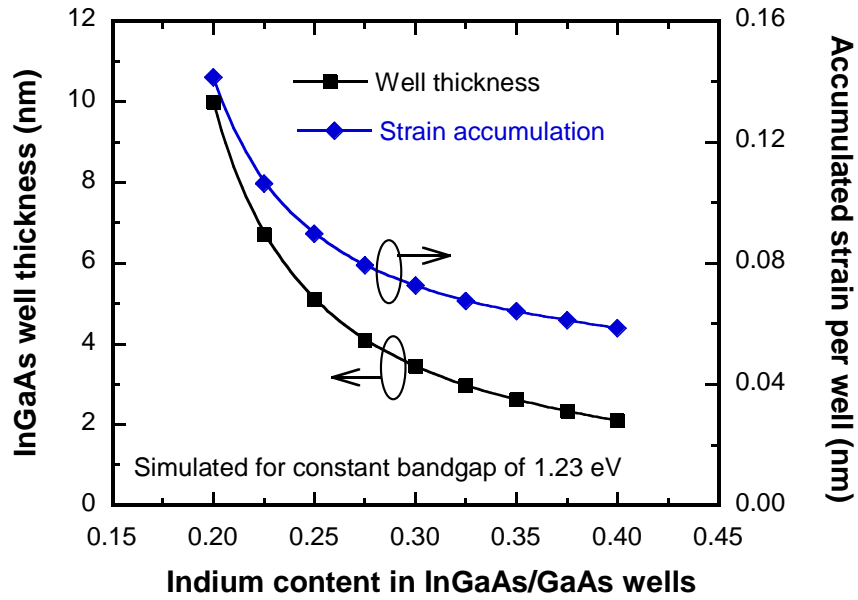
Fig. 5-5 Simulated InGaAs well thickness and accumulated compressive strain per well as a function of indium content for 1.23 eV bandgap InGaAs/GaAs quantum wells. Accumulated strain (nm) is calculated as the product of the lattice mismatch in the InGaAs and the well thickness.
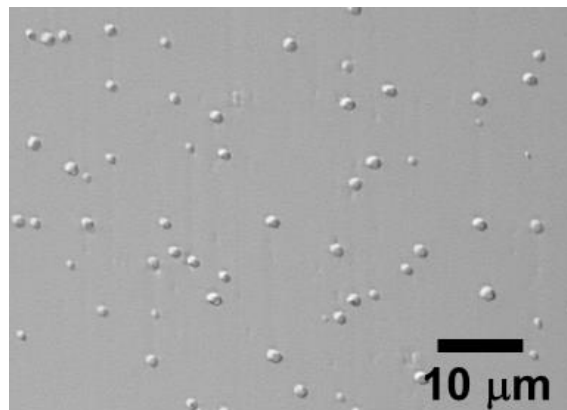
Fig. 5-6 Nomarski microscope image for the surface of 35-period $In_{0.32}Ga_{0.68}As$ (5.2 nm)/$GaAs_{0.79}P_{0.21}$ (17.3 nm) grown on a GaAs (0 0 1) substrate at 610 ºC. The epitaxial layer is capped with GaAs [123].

5.3.2 GaAs interlayer design

5.3.2.1 Suppression of lattice relaxation during hetero interface formation

Insertion of GaAs interlayers that are just a few nanometers thick between the InGaAs wells and the GaAsP barriers is an effective way to improve the crystal quality of the SL, especially those with high indium and phosphorus contents. A strain-neutral interlayer makes the interface less sharp and suppresses the lattice relaxation caused by the abrupt strain change at interfaces [88].

To demonstrate the effects of GaAs interlayers to prevent lattice relaxation during SL composed of highly strained InGaAs or GaAsP, 10-period $In_{0.30}Ga_{0.70}As$ (4.2 nm)/GaAs (x nm)/$GaAs_{0.25}P_{0.75}$ (3.3 nm)/GaAs (x nm) SLs were grown on GaAs (0 0 1) substrates with different interlayer thicknesses (0, 1.12, 1.68, 2.24 nm).

Fig. 5-7 (a) shows time transient of the *in-situ* monitored DC reflectance during SL growth with various thicknesses of the GaAs interlayers. In addition to the oscillations corresponding to the individual periods, the reflectance exhibited a gradual oscillation in average in the first five periods, including a descending trend in the 1st - 3rd period and a subsequent ascending trend in the 4th -5th period. This slow change in the net reflectance is attributed to the net Fabry-Perot oscillation resulted from the difference in refractive index between GaAs and the SL region, and it was clearly observed since the phosphorus content in the GaAsP was quite high.

Without GaAs interlayers, the average reflectance exhibited apparent decrease after the 4-5th period as an indication of crystal degradation. In particular, the growth of InGaAs layers was found to be unsuccessful as suggested by the arrows in the inset in which the reflectance during the InGaAs growth did not keep ascending but it decreased in the latter part of the individual period. In the growth of the subsequent GaAsP layers, the reflectance shortly increased at the beginning, probably due to the recovery of surface smoothness. Yet, the drop of reflectance in the InGaAs layer became larger with the period number, resulting in lower reflectance level for the cap GaAs layer compared to before the SL growth.

Insertion of 1-2 nm thick GaAs interlayers was effective to improve the crystal quality. The degradation of reflectance during InGaAs growth was suppressed with thicker interlayers. With 1.12 and 1.68 nm thick interlayers, the average reflectance still showed a slight degradation beyond the 5th period, but it was completely preserved for 10 periods for the case of 2.24 nm with well recovered reflectance in the GaAs cap layer to a level equivalent to the bottom GaAs layer. These results indicates that the direct growth of a compressively-strained InGaAs layers on a tensely-strained GaAsP layer is difficult, and insertion of GaAs interlayers makes the change of lattice constant and hence the strain at hetero interface smoother, enabling stable growth of the subsequent InGaAs layers.
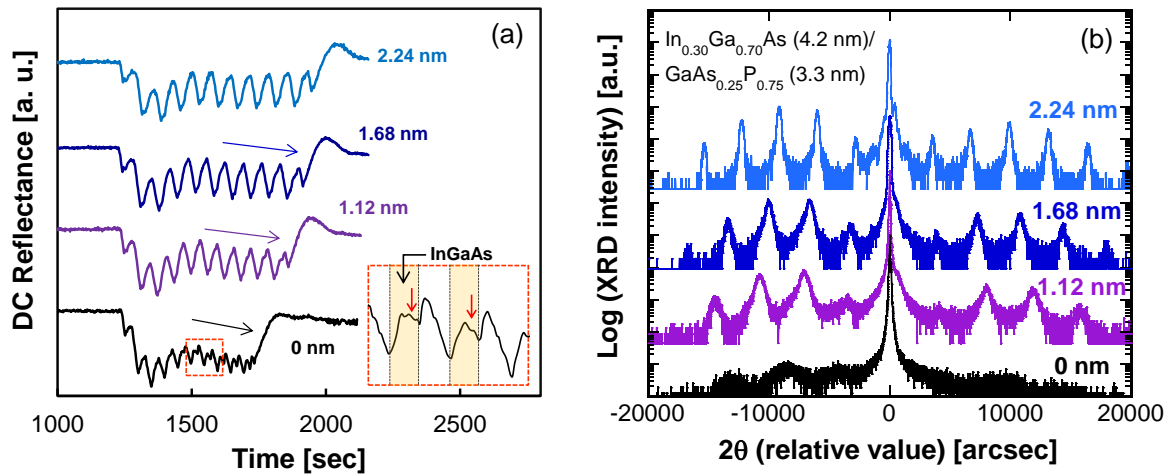
Fig. 5-7   (a) Time transient of DC reflectance during 10-period In$_{0.30}$Ga$_{0.70}$As (4.2 nm)/GaAs /GaAs$_{0.25}$P$_{0.75}$ (3.3 nm)/GaAs SLs with various GaAs thicknesses. A magnified plot for the case without GaAs interlayers is shown in the inset. (b) ω-2θ XRD patterns for the grown 10-period SLs with various GaAs thicknesses recorded around the GaAs (0 0 4) diffraction point.

Fig. 5-7 (b) shows high-resolution XRD patterns for the grown 10-period SLs with different interlayer thicknesses. Without interlayers, no fringe peaks that could be attributed to the superlattice were observed, thus indicating that a periodic structure with controlled layer thicknesses was not formed. In contrast, fringe peaks in the XRD pattern became sharper and stronger when thicker GaAs interlayers were inserted. The full width at half maximum (FWHM) for the second fringe peak at around -7,000 arcsec were 785, 550, and 270 arcsec for interlayer thicknesses of 1.12, 1.68, and 2.24 nm, respectively. The theoretical FWHM without lattice relaxation is 263 arcsec, thus indicating that good crystal quality is obtained with 2.24-nm-thick interlayers.

The unclear and broadened satellite peaks in the fringe patterns with thinner interlayers can be attributed to unstable formation of the hetero interfaces between the two oppositely strained layers, which may lead to partial lattice relaxation and rough interfaces. For this reason, the sufficient interlayer thickness required to achieve acceptable crystal quality strongly depends on the indium or phosphorus content; thicker interlayers should be needed for larger differences in strain between the InGaAs compressive layer and the GaAsP tensile layer. Therefore, the optimum thickness of the interlayer necessary for successful growth should be determined based on the SL structure.

5.3.2.2 Bandgap narrowing effect

GaAs interlayers are also beneficial for reducing the effective bandgap by weakening the quantum confinement effect. While thicker wells alone can reduce the bandgap, they simultaneously increase the accumulated compressive strain. Fig. 5-8 shows the experimentally measured bandgap for $In_{0.30}Ga_{0.70}As$(3.5 nm)/GaAs/$GaAs_{0.50}P_{0.50}$(4.0 nm)/GaAs SLs grown on GaAs substrates with various interlayer thicknesses. Here it can be seen that GaAs layers that are just a few nanometers in thickness successfully reduce the bandgap by 30-40 meV. Importantly, this reduction of the bandgap is attained while conserving the strain balance condition without introducing additional compressive strain.

As shown above, insertion of GaAs interlayers are quite essential in the designing a SL for narrowing the bandgap as well as achieving good crystal quality. A practical way to optimize the well structure is to determine the InGaAs thickness required to achieve the desired bandgap and using the highest indium content possible, which is 30% in this study, with 2- or 3-nm-thick GaAs interlayers. Note that an interlayer that is too thick may thicken the entire SL region without providing any additional benefits in terms of crystal quality improvement and/or bandgap reduction.

It is also important to note that GaAs interlayers that are more than just a few nanometers thick prevent carriers in the InGaAs regions from being transported to the neighboring wells via direct tunneling. This can make it difficult to achieve both high crystal quality and efficient carrier transport. However, by thinning the GaAsP layers sufficiently, carriers in InGaAs wells can be thermally excited to upper states from which they can then tunnel through the GaAsP barriers, as will be shown in the section 5.3.3.
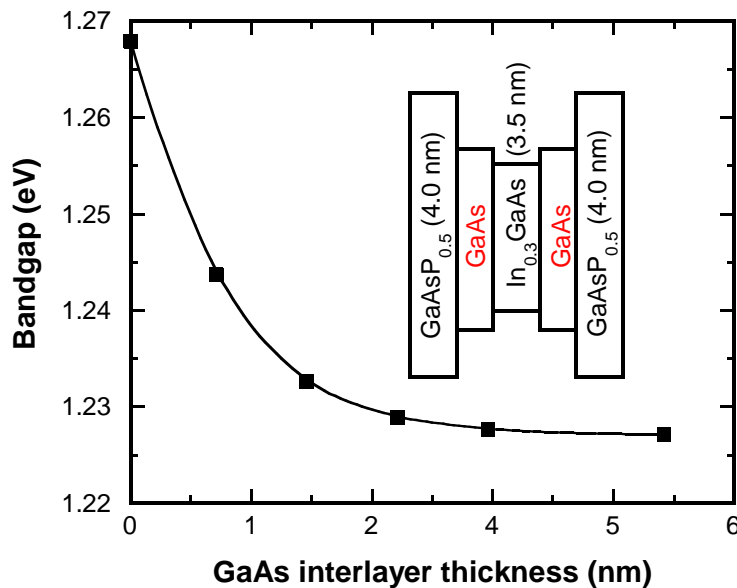
Fig. 5-8 Effective bandgap for $In_{0.30}Ga_{0.70}As$(3.5 nm)/GaAs/$GaAs_{0.50}P_{0.50}$(4.0 nm)/GaAs SLs versus the GaAs interlayer thickness. The bandgap was estimated by PL measurements.

5.3.3 GaAsP barrier design

The GaAsP barrier design has a very significant impact on carrier transport efficiency. The most important requirement is ensuring that tunneling transport through the barrier layers is efficient. However, only a few studies have reported the effects of barrier layers with precisely controlled SL structures on cell performance [114], and the design criteria necessary to sufficiently extract both photo-excited electrons and holes have yet to be well established. Later in this section, experimental investigations into the influence of GaAsP barriers with different widths and heights on the carrier transport dynamics are discussed.

■ **Experiments**

(1) A set of GaAs pin cells including 30-period $In_{0.30}Ga_{0.70}As$(3.5 nm)/GaAs(2.6 nm)/GaAsP /GaAs(2.6 nm) SLs in the i-region were prepared at a variety of barrier thicknesses (2~6 nm) and phosphorus contents (40~60%). The i-region thickness was kept constant at 1000 nm for all the devices by adjusting the thickness of the intrinsic GaAs spacer layers beneath the SL region in order to secure the equal built-in field. Additionally, the thickness of the i-GaAs spacer layer above the SL region was fixed at 200 nm to ensure that the intensity of the incident light penetrating the top of the SL region was equal among the various cells. The epitaxial layers were characterized by XRD-RSM around ($\overline{2}\,\overline{2}\,4$) diffraction point, and PL at excitation wavelength of 532 nm was measured.

(2) After processing top Ti/Au and rear AuGeNi electrodes similarly as the section 4.5.2, bias dependent CCE was measured using both AM1.5 and monochromatic light.
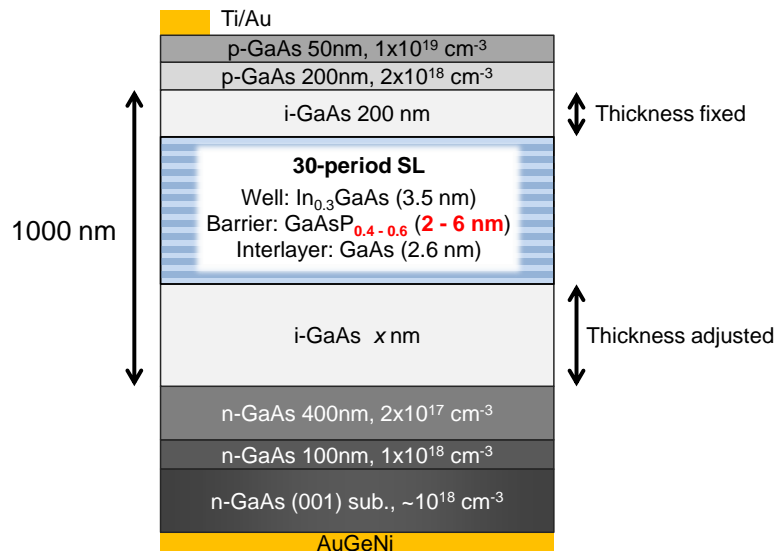
Fig. 5-9   Sample structure for the investigation of GaAsP barriers on carrier transport

5.3.3.1　Effects of barrier thickness

In this experimental study, the composition or the thickness of the GaAsP layer alone were varied while preserving the other layer structures in the SL to examine how the barrier regions affect the carrier transport. For this reason, the strain balance condition was not completely satisfied in all the samples.

For the investigation with different barrier thicknesses (2 - 6 nm), the phosphorus content was fixed at 50%. The strain balance condition was met with 4 nm barriers, and SLs with 2-3 nm and 5-6 nm barriers had compressive and tensile strain accumulation, respectively. Despite the strain unbalance condition for the thick or thin barriers, lattice relaxation resulting from strain accumulation was confirmed to be negligible by the XRD-RSM around the $(\bar{2}\,\bar{2}\,4)$ diffraction point as shown in Fig. 5-10 (a); the fringe peaks attributed to the superlattice were well aligned along the Q_y axis in the reciprocal space for all the SL structures.

The PL peak wavelengths were 1006±1 nm regardless of the barrier thickness as shown in Fig. 5-10 (b), indicating a constant effective bandgap of approximately 1.23 eV with negligible effects of coupling for the ground states, which generally red-shift and broaden the PL peak due to the overlap of the wave functions among the neighboring wells [114]. In the SL structure used in this study, the distances between the two adjacent well were as thick as 7.2 – 11.2 nm, which was sufficient to prevent the wave functions to be coupled. This was also confirmed with the almost equivalent FWHM of the PL peaks for all the samples: 16.3, 15.4, 15.9, 16.2, and 15.2 nm for 2, 3, 4, 5, and 6 nm thick barriers, respectively

Fig. 5-10　(a) XRD-RSM recorded around $(\bar{2}\,\bar{2}\,4)$ diffraction points for 2-nm and 6-nm thick barrier samples, and (b) PL spectra under open circuit condition obtained for different barrier thicknesses. The barrier composition was GaAsP$_{0.5}$ for all the SLs

Fig. 5-11 (a) shows the carrier collection efficiency under AM1.5 illumination ($CCE_{AM1.5}$) as a function of the voltage for various (2~6 nm) GaAsP barrier thicknesses, and with a fixed phosphorus composition of 50%. As the barrier thickens, carrier transport becomes dom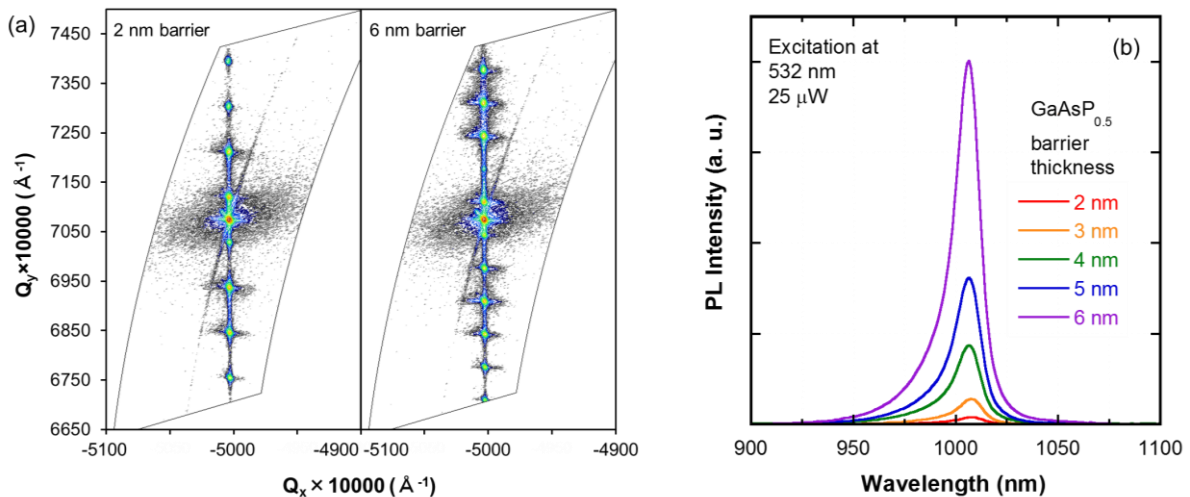inated by slow thermionic escape, which lowers the CCE below 100%, even under short circuit conditions for 5 and 6 nm barriers. This effect appeared more significantly at forward bias with a weak electric field in the i-region, and the 4 nm barrier sample also showed gradual CCE degradation. Regarding the I-V characteristics, poor carrier collection primarily affected the fill factor (FF), which were 0.75 and 0.79 for 6 and 2 nm, respectively. No significant bias dependence of the $CCE_{AM1.5}$ was found for barriers thinner than 3 nm, thus indicating sufficient facilitation of tunneling transport. The $CCE_{AM1.5}$ at the maximum power output voltage of 0.81 V for the GaAs reference cell, 0.73 V for the 3-nm barrier cell, and 0.76 V for the 6-nm barrier cell, were 98%, 97%, and 87%, respectively. As a result, carrier transport in the 3-nm barrier cell was found to be as efficient as that in the GaAs bulk reference cell.

Considering that fast carrier escape suppresses photoluminescence as discussed in the section 4.5.1, more efficient carrier transport through thinner barriers were also suggested by the PL intensity in the Fig. 5-10 (b), which was consistently lower with smaller thicknesses for the GaAsP layers.

In order to determine the mechanism of the enhanced CCE with thinner barriers in greater detail, the monochromatic CCE was examined at 500, 700, and 950 nm with the 3- and 6-nm barrier cells, as shown in Fig. 5-11 (b). Because of the high absorption coefficient, 500-nm light is absorbed only in the top p-region, and thus the obtained CCE is solely determined by electron transport through the SL region. At 700 nm, approximately 40% of the light reaches the SL region, partially exciting carriers in the wells. Therefore, the CCE at 700 nm includes the dynamics of electron-hole separation inside the wells, and the efficiency of hole transport through the SL to the top p-region. Since 950-nm light is only absorbed in the InGaAs wells, the CCE selectively shows the probability of carrier escape from the SL region. Note that excitation at 950 nm only generates electrons and heavy holes in their ground states because only 1e-1hh transitions are possible at this wavelength.

At a forward bias of 0.7 V, the CCE was degraded at longer wavelengths for the 6-nm barrier, and had values of 97%, 89%, and 77% at 500, 700, and 950 nm, respectively. This indicates that the transport of heavy holes which are photo-generated inside the wells is more likely to be blocked by thick barriers. This conclusion is reasonable because heavy holes in GaAs-based materials have effective masses that are approximately ten times larger than that of electrons, and the thermionic escape rate for heavy holes from a well is much lower than that for electrons. In addition, a larger effective mass lowers the confinement energy in a quantum well, and since the ground state of a heavy hole is located close to the bottom of the well, the potential barrier for heavy holes is higher. At 500 nm, the CCEs for the 3- and 6-nm barrier cells were comparable, thus indicating extremely fast electron thermionic escape. On the other hand, the 3-nm barrier cells showed an almost equivalent CCE bias dependence, regardless of the excitation wavelength, with a CCE of 97% at 0.7 V. This is clear evidence that heavy hole transport can be sufficiently enhanced by tunneling with GaAsP barriers as thin as 3 nm.
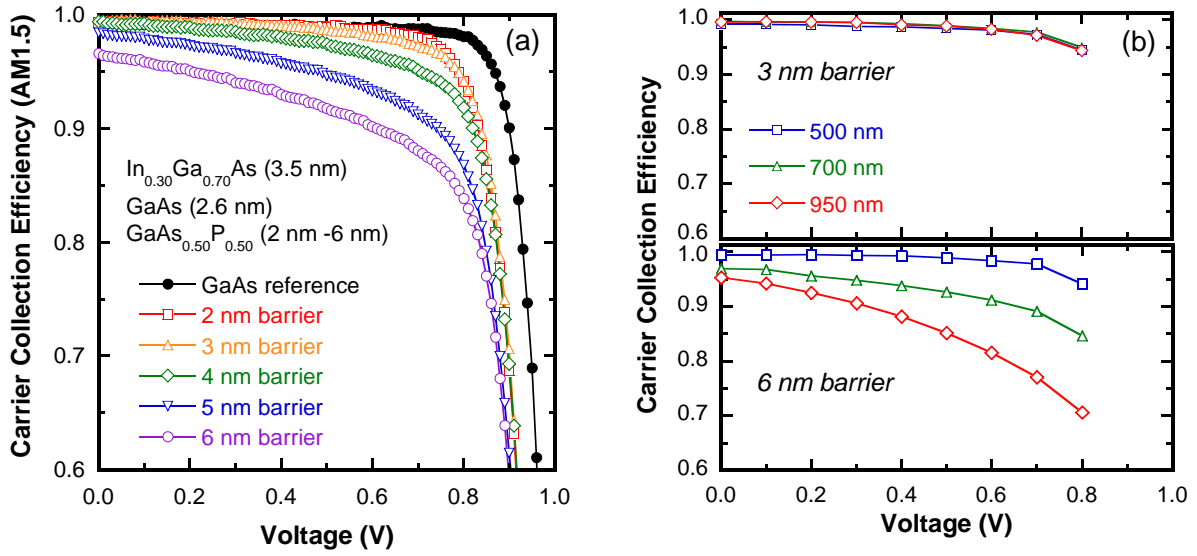
Fig. 5-11   Effects of GaAsP barrier thickness on carrier transport in 30-period $In_{0.30}Ga_{0.70}As$(3.5 nm)/GaAs(2.6 nm)/$GaAs_{0.50}P_{0.50}$ SL cells. (a) CCE under AM1.5 as function of applied bias with various barrier thicknesses from 2 to 6 nm. Data for GaAs reference cell is shown for comparison. (b) Monochromatic CCE for 2- and 6-nm barriers at excitation wavelengths of 500, 700, and 950 nm.

5.3.3.2   Effects of barrier height

Although the tunneling probability is primarily determined by the barrier thickness, the height of the potential barrier is another important factor that affects the tunneling probability as seen in the eq. (2-76).

For the investigation with different barrier heights, the phosphorus content in the GaAsP layers was varied from 40% to 60% while the thickness was fixed at 3 nm. All the SL structures were compressively strained, with values for the net strain in the SL was larger with lower phosphorus contents: 931 ppm and 2764 ppm for the cases of 60% and 40% phosphorus, respectively. Similarly to the previous section, the XRD-RSM around the $(\bar{2}\,\bar{2}\,4)$ diffraction point showed vertically aligned satellite peaks for the SL at the equal Q_x for the GaAs substrates for both 40% and 60% phosphorus cases (Fig. 5-12(a)), thus meaning that the lattice relaxation in the SL resulting from the strain accumulation or unstable hetero-interface formation especially for higher phosphorus content was not apparently confirmed.

An equal bandgap of 1.23 eV for the set of samples was also confirmed by PL with an equal peak wavelength of 1007 nm as shown in Fig. 5-12 (b). Sharp spectra with small variation in FWHM of 15.5 ± 1 nm suggested that the crystal quality was similarly good and that the difference in the roughness of the hetero interface was negligible.
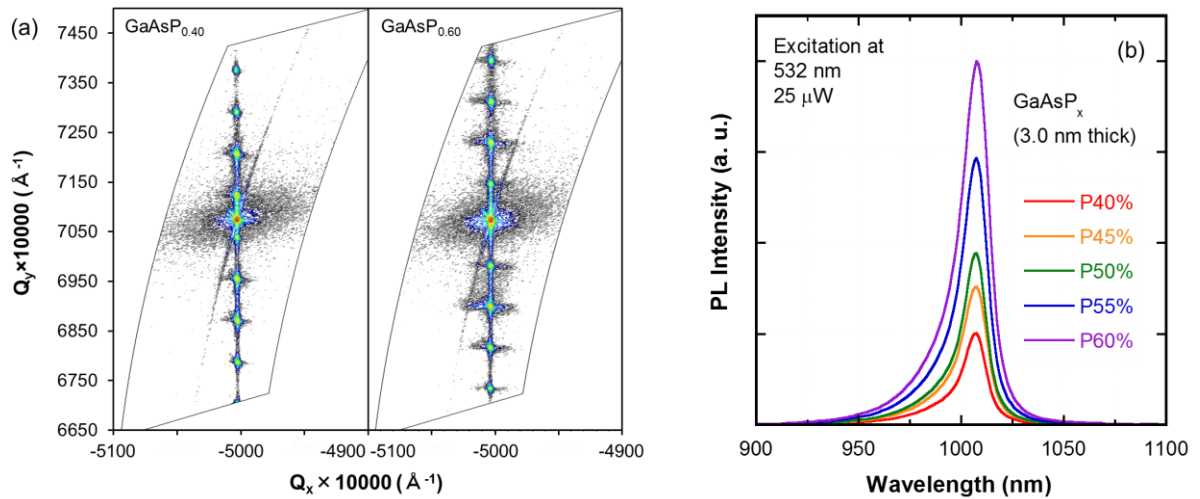
Fig. 5-12 (a) XRD-RSM recorded around $(\bar{2}\,\bar{2}\,4)$ diffraction points for barrier composition of GaAsP$_{0.4}$ and GaAsP$_{0.6}$, and (b) PL spectra under open circuit condition obtained for different phosphorus contents in the barriers. The barrier was 3 nm thick for all the SLs.

Fig. 5-13 (a) shows the CCE$_{AM1.5}$ with various phosphorus contents (40~60%). As can be seen, a very high CCE of approximately 99% was obtained at 0 V regardless of the barrier height (or the phosphorus content) because tunneling transport is well facilitated through 3 nm thick barriers. However, due to the lower tunneling probability through higher potential barriers, the CCE for samples with higher phosphorus contents decreased drastically as the forward bias increased, resulting in a CCE of 95% and 98% at 0.7 V for a phosphorous content of 60% and 40%, respectively. This effect was also confirmed with the tendency of the PL intensity in the Fig. 5-12(b), which was continuously higher with higher phosphorus contents.

As indicated in the graph, increasing the phosphorus content from 40% to 60% increased the difference in the bandgap at the Γ point between GaAs and GaAsP by approximately 0.2 eV, but the effect of the barrier height on the carrier transport is much smaller than that of the barrier width because tunneling is far more efficient than thermionic processes. Therefore, the influence of the barrier height difference on the J-V characteristics was very small for the five devices, and included a slight *FF* degradation from 0.801 with 40% phosphorus to 0.789 with 60% phosphorus, and no apparent change in J_{sc} or V_{oc}. The degradation in cell performance with higher barriers, however, should be more apparent when over 100 wells are incorporated, and reducing the phosphorus content in the barriers becomes more important as the well number increases.

A CCE investigation under monochromatic illumination conditions was also carried out to determine how higher barriers block carrier transport. Fig. 5-13 (b) shows the CCE for SL cells with 40% and 60% phosphorus at various excitation wavelengths. Here, it can be seen that the CCE with 40% phosphorus showed a similar bias-dependence regardless of the illumination wavelength with a value over 98% at 0.7 V, thus indicating equivalent transport efficiency for electrons and holes. On the

other hand, at longer wavelengths, obvious degradation was observed for 60% phosphorus, with a CCE of 98%, 96%, and 95% at 500, 700, and 950 nm, respectively, at the forward bias of 0.7 V. This clearly indicates that the escape of heavy holes is blocked by higher barriers. This is partly because the effective mass of a heavy hole is much larger than that of an electron as previously mentioned. Moreover, the higher phosphorus content in GaAsP generally leads to a larger band offset for the valence band than the conduction band, and hence creates higher potential barriers and a lower tunneling probability for heavy holes.

The above investigation into carrier behavior in various GaAsP layer structures led us to the principle design criteria that barriers should be no more than 3-nm thick, and that they should have as low a phosphorus content as possible without introducing detrimental lattice relaxation. Although direct tunneling between the ground states in InGaAs wells is prevented when GaAs interlayers that are just a few nanometers thick are inserted on both sides of GaAsP barriers, facilitating tunneling between the excited states was found to be a remarkably effective way of enhancing the carrier transport for the entire device, and this could be accomplished by reducing the barrier thickness to 3 nm and limiting the phosphorus content to 0.4.
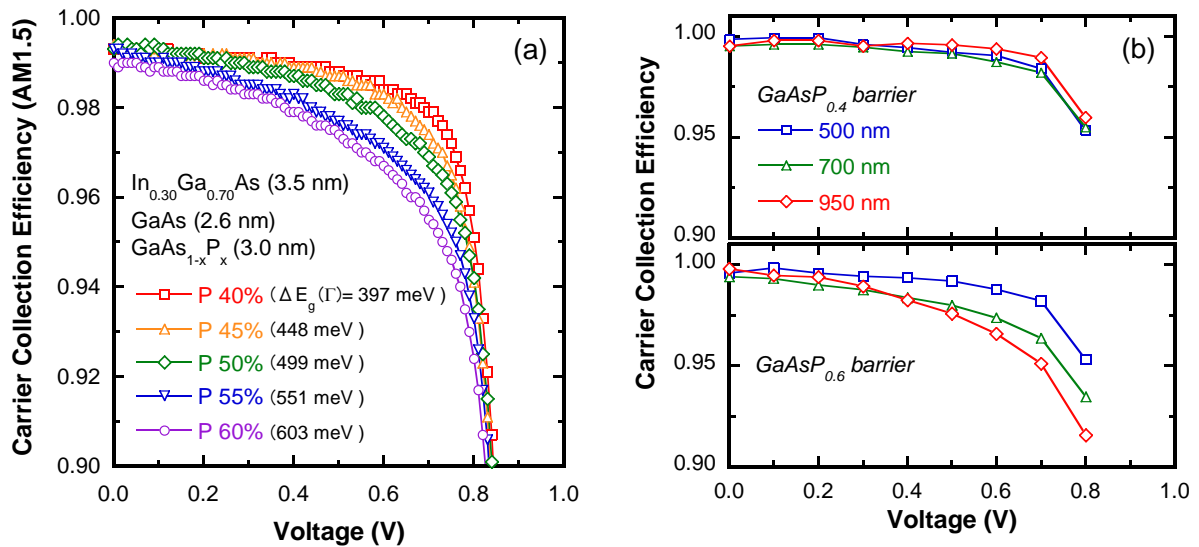
Fig. 5-13   Effects of GaAsP barrier composition on carrier transport in 30-period $In_{0.30}Ga_{0.70}As$(3.5 nm)/GaAs(2.6 nm)/GaAsP(3.0 nm) MQW cells. (a) CCE under AM1.5 as function of applied bias with various phosphorus contents from 40 to 60%. Bandgap difference at the Γ-point between GaAs and GaAsP is shown as $\Delta E_g(\Gamma)$. (b) Monochromatic CCE with 40 and 60% phosphorus at excitation wavelength of 500, 700, and 950 nm.

5.3.4 Carrier transport mechanism in STSL

In STSL, the photo-excited carriers in the InGaAs wells are excited to the upper states and are transported via tunneling through the GaAsP layers, which was experimentally confirmed by thinning the GaAsP barriers in the section 5.3.3.

Fig. 5-14 shows wave functions for each eigen-state in a $GaAs_{0.60}P_{0.40}$/GaAs (2.7 nm)/$In_{0.30}Ga_{0.70}As$ (3.5 nm)/GaAs (2.7 nm)/$GaAs_{0.60}P_{0.40}$ single quantum well simulated using physical properties summarized in ref. [124]. The bandoffset ($\Delta E_C/(\Delta E_C+\Delta E_V)$) at hetero interfaces in InGaAsP system has not been exactly known due to the variation depending on the measurement methods, but it has been suggested that the bandoffset without strain is in the range of 0.75 – 0.85 for InGaAs/GaAs [125, 124], and 0.45–0.60 for GaAsP/GaAs [126, 124]. For the simulation in this section, bandoffsets without strain are assumed to be 0.80 for InGaAs/GaAs, and 0.55 for GaAs/GaAsP.

In a single quantum well (SQW), electrons, heavy holes, and light holes have two, six, and two eigen-states, respectively. Electrons and heavy holes possesses excited states above the GaAs interlayers, in which the potential barrier thickness for the carriers are only the thickness of the GaAsP layers. Therefore, thinning the barriers in the MQW system can indeed enhance the tunnel probability among the excited states. For light holes, on the other hand, the valence band of InGaAs is lower than that of GaAs due to the strain-induced band deformation [125, 127, 128], and thus the light holes in the ground states can directly tunnel through the GaAsP barriers.

As increasing the well number (N), each discrete energy level in a SQW is split to form a miniband. Fig. 5-14 shows the formed minibands with 3.0-nm-thick $GaAsP_{0.4}$ barrier as a function of N, which was calculated by transfer matrix method explained in the section 2.2.1.2. Flat-band condition is assumed here for simplicity. The miniband energy width is rapidly increased from $N = 1$ to $N = 5$, and is almost saturated beyond with $N > 10$.
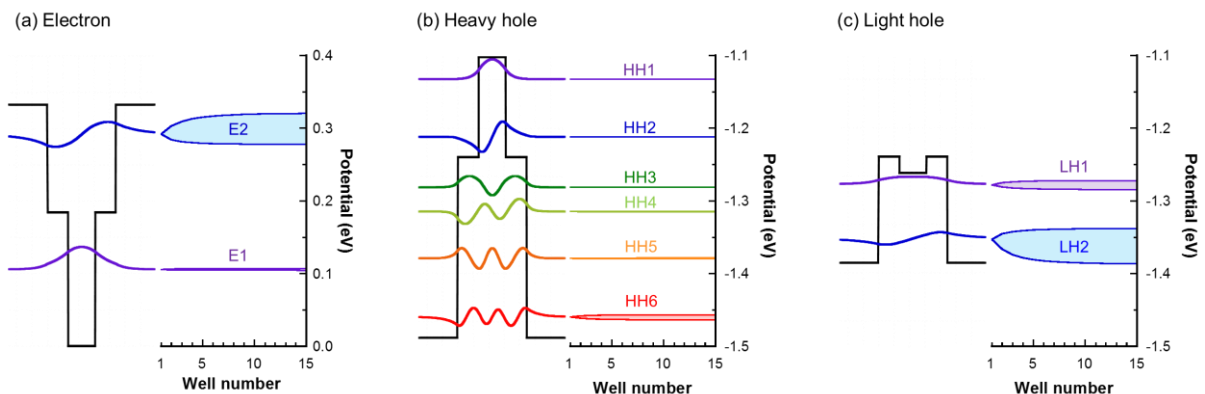
Fig. 5-14   Eigen states for (a) electrons, (b) heavy holes, and (c) light holes in a $GaAs_{0.60}P_{0.40}$/GaAs (2.7 nm)/$In_{0.30}Ga_{0.70}As$(3.5 nm)/GaAs(2.7 nm)/$GaAs_{0.60}P_{0.40}$ single quantum well. Minibands formed due to energy splitting are shown for each level versus the well number for the case with 3.0-nm-thick barriers. The potential is defined zero at the bottom of the conduction band of the InGaAs well.

Fig. 5-15 shows the miniband energy width for each discrete level in a 15-period SL as functions of the thickness of GaAsP$_{0.40}$ barriers. As can be seen, upper excited states have wider energy split, and the miniband become wider with thinner barriers due to the larger coupling of the wave functions; the miniband width for the second states for the electrons and light holes are 6.5 meV (E2), 7.9 meV (LH2) with 8-nm-thick GaAsP, and 42.7 meV (E2) and 48.5 meV (LH2) with 3-nm-thick GaAsP. For heavy holes, the miniband width is only 7.0 meV with 3-nm GaAsP even for the sixth states (HH6) due to the large effective mass.
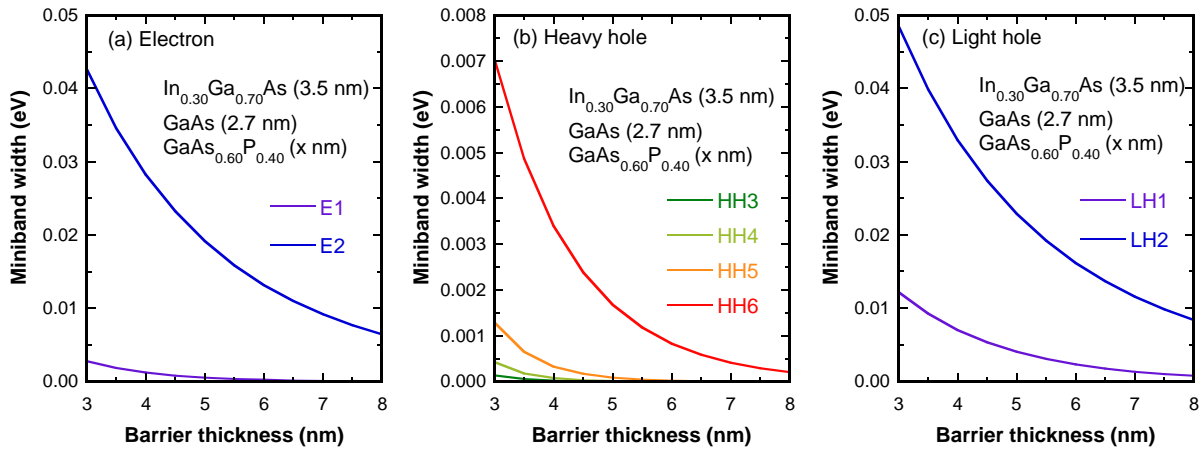
Fig. 5-15   Miniband energy width calculated for each eigen-state as functions of the GaAsP barrier thickness for 15-period In$_{0.30}$Ga$_{0.70}$As (3.5 nm)/GaAs (2.7 nm)/GaAs$_{0.60}$P$_{0.40}$ (*x* nm)/ GaAs (2.7 nm) SL. The miniband energy width for HH1 and HH2 are $<1.0\times10^{-6}$ eV.

The improved CCE with thinner barriers shown in the section 5.3.3.1 should be attributed to either higher tunneling probability described by the eq. (2-76) and hence faster sequential tunneling through the SL, or efficient resonant tunneling that is possible within the minibands. Since the SL is included in the i-region in actual solar cell devices, the miniband energy width must be sufficiently larger than the potential change due to the electric field if tunneling through the miniband occurs. Fig. 5-16 shows the miniband energy widths as functions of the period number in a flat-band SL with 3.0-nm-thick GaAsP$_{0.4}$ barriers, through which the carrier transport was found to be quite efficient (Fig. 5-11), together with the potential changes corresponding to the SL thickness in real devices. Under short circuit condition, for instance, the built-in field in a p-i-n cell is 1.35 mV/nm in 1000 nm i-region, and thus the potential change for one-period, which is 11.8 nm in thickness, is 16 meV. In this case, the potential change through the SL is much larger than the miniband width calculated for the flat band condition, indicating that the miniband breaks up into series of localized states in the actual cells. For heavy holes, in particular, the energy splitting is quite small because of the little coupling of the wave functions, though the Fig. 5-11(b) clearly revealed that their tunneling transport was greatly enhanced by using thinner barriers. Applying forward bias weakens the electric field, and assists miniband formation. If this happens and keeps the minibands formed, CCE should be improved at sufficiently

high forward bias, though such a feature was not observed in the Fig. 5-11 and Fig. 5-13. For these reasons, the enhanced carrier transport in STSL with thin GaAsP layers should be attributed to faster sequential tunneling rather than formation of minibands.
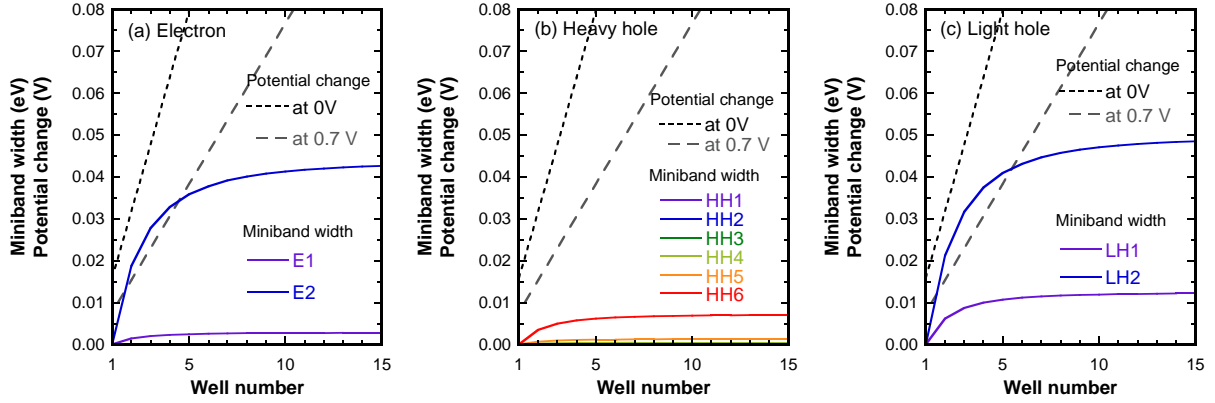
Fig. 5-16   Miniband width (flat band condition) in In$_{0.30}$Ga$_{0.70}$As(3.5 nm)/GaAs(2.7 nm)/GaAs$_{0.60}$P$_{0.40}$ (3.0 nm)/GaAs(2.7 nm) MQW as function of well number. The potential change within the MQW region for the corresponding period number under electric field in actual cells are shown together.

5.4 Performance of the optimized STSL

In this section, the effectiveness of the proposed SL structure on the photovoltaic performance is examined by structure optimization based on the design principle discussed in the section 5.3. The aim of this section is twofold: 1) to demonstrate an advantage of using a STSL structure compared to typical SL for a given bandgap, and 2) to achieve an enhancement in cell performance by incorporating 100-period SL with a bandedge extended beyond 1000 nm.

■ **Experiments**

(1) GaAs pin epitaxial layers including two types of SLs were grown on n-type GaAs (0 0 1) substrates by MOVPE at 610 ºC and 10 kPa: 100-period In$_{0.30}$Ga$_{0.70}$As(3.5 nm)/ GaAs(2.7 nm)/ GaAs$_{0.60}$P$_{0.40}$ (3.0 nm)/GaAs(2.7 nm) stepped tunnel (ST) SL as the optimized structure, or 70-period In$_{0.22}$Ga$_{0.78}$As(7.5 nm)/GaAs(0.6 nm)/GaAs$_{0.60}$P$_{0.40}$(8.0 nm) SL as a typical SL structure with rectangular shaped potential barriers. The detailed structures are summarized in the Fig. 5-17. The overall SL regions in both cells were equally 1180 nm in thickness, and were incorporated at the center of 1380-nm-thick i-region. 100-nm-thick intrinsic GaAs spacer layers were inserted at the top and the bottom of the SLs. A GaAs bulk cell with a 1380-nm-thick i-region without SLs was also prepared as a reference cell. Note that compensation doping with sulfur was applied for the entire i-region under a same condition used in the section 4.5.1.

111

(3) *In-situ* reflectance measurement was carried out during MOVPE at wavelength of 443 nm. The grown epitaxial layers were characterized by *ex-situ* XRD ω-2θ scan around the ($0\,0\,4$) diffraction point. The absorbance spectra were also measured by FTIR spectroscopy.

(4) Au (500 nm) bottom contact was deposited by EB evaporation and annealed at 330 °C for 5 min in N_2 ambient prior to the deposition of Ti (20 nm)/Au(300 nm) top contact. The heavily doped p-GaAs on the top of the aperture area was removed by etching.

(5) Photovoltaic performance (I-V under AM1.5 and QE) and CCE at various wavelengths were measured in a solar simulator. QE and CCE were measured with 2.5 mW/cm² monochromatic light under AM1.5 bias illumination.

For the 70-period typical SL cell, which is called typical-SL70 cell hereafter, the band-lineup of the SL was designed to be conventional rectangular potential profile with very thin GaAs interlayers. The GaAsP layer were relatively thick (8 nm) in order to prohibit tunneling transport so that the carriers in the InGaAs wells have to be thermally transported over the barriers. For the 100-period STSL cell, which is called STSL100 cell hereafter, the GaAsP barrier had thickness of 3 nm and phosphorus content of 0.4 in order to facilitate tunnel transport. For this reason, the entire STSL was compressively strained in average at 2620 ppm at the growth temperature whereas the strain balance condition was almost completely satisfied at net strain of 50 ppm for the typical SL. Moreover, the InGaAs wells in STSL was thinned to 3.0 nm with higher indium content for higher absorption coefficient for the transition between the ground states. Note that the bandgap for both structure was equally 1.23 eV as shown later, and the phosphorus content was also equally 0.4 for fair comparison.

	STSL (100-period)	Typical SL (70-period)
Well	$In_{0.30}Ga_{0.70}As$ (3.5 nm) E_g = 1.10 eV $\Delta a/a$ = 2.13%	$In_{0.22}Ga_{0.78}As$ (7.5 nm) E_g = 1.18 eV $\Delta a/a$ = 1.78%
Barrier	$GaAs_{0.60}P_{0.40}$ (3.0 nm) E_g = 1.91 eV $\Delta a/a$ = -1.45%	$GaAs_{0.60}P_{0.40}$ (8.0 nm) E_g = 1.91 eV $\Delta a/a$ = -1.45%
Interlayer	GaAs (2.7 nm) E_g = 1.42 eV $\Delta a/a$ = 0%	GaAs (0.6 nm) E_g = 1.42 eV $\Delta a/a$ = 0%

Layer structure (left panel):

Ti/Au
p-GaAs 50nm, 1×10^{19} cm⁻³
p-InGaP 25nm, 6×10^{18} cm⁻³
p-GaAs 100nm, 2×10^{18} cm⁻³
i-GaAs 100 nm
SL-region (1180 nm)
100-period STSL
70-period Typical SL
(1180 nm i-GaAs for a reference cell)
i-GaAs 100 nm
n-GaAs 400nm, 2×10^{17} cm⁻³
n-GaAs 100nm, 1×10^{18} cm⁻³
n-GaAs (001) sub., $\sim10^{18}$ cm⁻³
Au

Fig. 5-17   GaAs pin solar cells including either 100-period STSL or 70-period typical SL.

■ **Results and discussion**

Fig. 5-18 shows the time transient DC reflectance and RA during the MOVPE of the STSL100-cell at wavelength of 443 nm. In spite of the severer risks for stable growth of STSL structure, such as the strain-unbalance condition with intentionally thinned GaAsP layers and the quite high indium content in the InGaAs and hence large difference in the lattice constant, the *in-situ* monitored reflectance suggested good crystal quality and uniformity of the 100-period SL; the average reflectance remained constant for the entire growth as can be seen in (a), and the periodic RA signal corresponding to each component layer was perfectly preserved as shown in (b) and (c). The time transient reflectance was also very stable for the growth of typical-SL70 cell, for which the growth should be less severe because of the well compensated strain and the lower indium content.
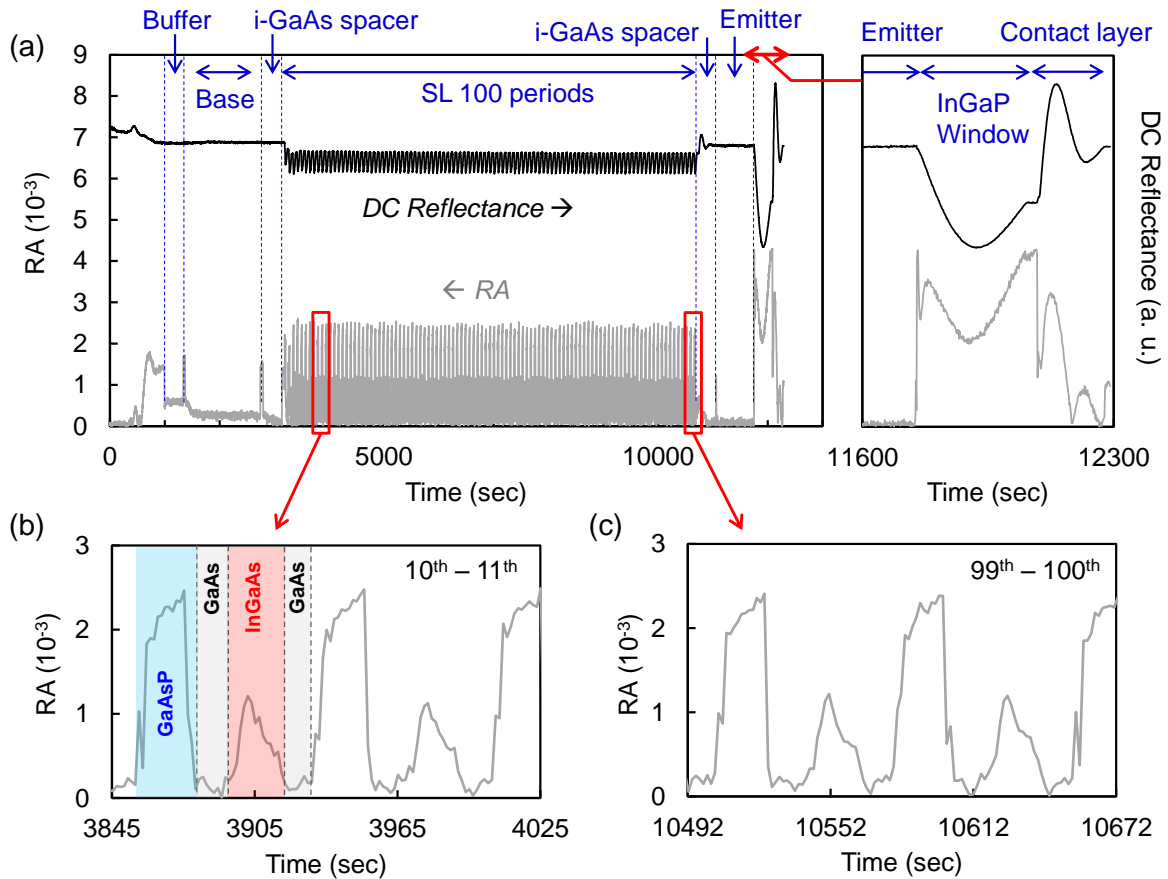
Fig. 5-18 *In-situ* monitored reflectance during growth of a 100-period STSL solar cell. (a) DC reflectance and reflectance anisotropy (RA) during the entire growth, with a magnified plot from the p-emitter to the p-contact layer, and (b) (c) magnified RA for two periods in the initial (10th -11th period) and the end part (99th -100th) of SL growth. Note that the measurement was performed at wavelength of 443 nm.

Fig. 5-19 shows XRD patterns for the two SL cells under investigation. The net compressive strain in the STSL structure of 2720 ppm was confirmed by the zeroth peak of the fringe pattern shifted from the GaAs substrate peak, whereas the zeroth peak for the typical SL was completely matched with the substrate peak. Despite the strain unbalance condition, the XRD pattern for the STSL100 cell exhibited very sharp satellite peaks, which were attributed to a high crystal quality and uniformity with flat interfaces. Typical-SL70 cells also showed sharp fringe patterns in spite of their relatively thin (0.6 nm) GaAs interlayers. This was the result of the low indium content in the wells, and hence the smaller difference in strain between the InGaAs and GaAsP layers. For both cells, the fringe peak positions and their relative intensities agreed quite well with the theoretical curve taking account of the designed structure, thus indicating that the SL regions were uniformly grown as designed in terms of the composition and the thickness of each layer.
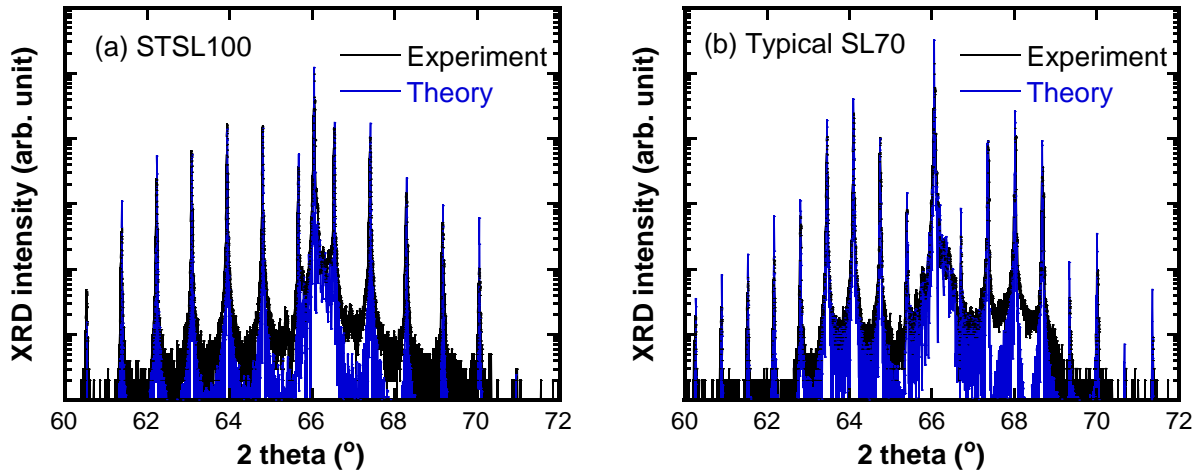
Fig. 5-19   XRD 2θ-ω pattern for typical MQW70 cell and optimized MQW100 cell around the (004) diffraction peak. Theoretical curves for the designed cell structures are also shown.

Fig. 5-20 shows the absorbance of the SL A_{SL} beyond the GaAs band edge measured by Fourier transform infrared spectroscopy (FTIR) before processing the surface and back contacts. A_{SL} was calculated as

$$A_{SL} = -\ln\left(\frac{T_{sample}}{T_{reference}}\right) \tag{5-3}$$

where T_{sample} and $T_{reference}$ were the transmittance of the cells with the SL and the GaAs reference cell, respectively. Note that the absorbance values in the figure include the effects of multiple reflections

inside the cells since single side polished wafers were used, and do not represent the single path absorbance discussed in the section 4.4.1.

The exciton peak wavelength was confirmed to be equally 1008 nm for both SL structures. This corresponds to the effective bandgap of 1.23eV, which is within the target range for InGaAs/GaAsP SL for middle cell material of Ge-based triple junction solar cells.

The STSL100 cell showed approximately 100/70 times larger absorbance in the 1e-1hh transition wavelength range than the typical MQW70 cell, as theoretically expected from eq. (5-3), thus proving that the absorbance is determined not by the well thickness, but by the number of wells. The total thickness of the well region, i.e., the product of the InGaAs layer thickness and the period number, were 350 and 525 nm for the STSL100 and typical SL70 cells, respectively. This means that the STSL structure can absorb more light with a smaller total thickness of the well region than the typical SL structure composed of thicker wells with a lower indium content. Therefore, incorporating a larger number of thinner wells is now an experimentally confirmed strategy leading to increased light absorption with a limited total well thickness.

Fig. 5-20   Absorbance of STSL100 and typical-SL70 measured by FTIR before depositing contacts on back surface. Absorbance 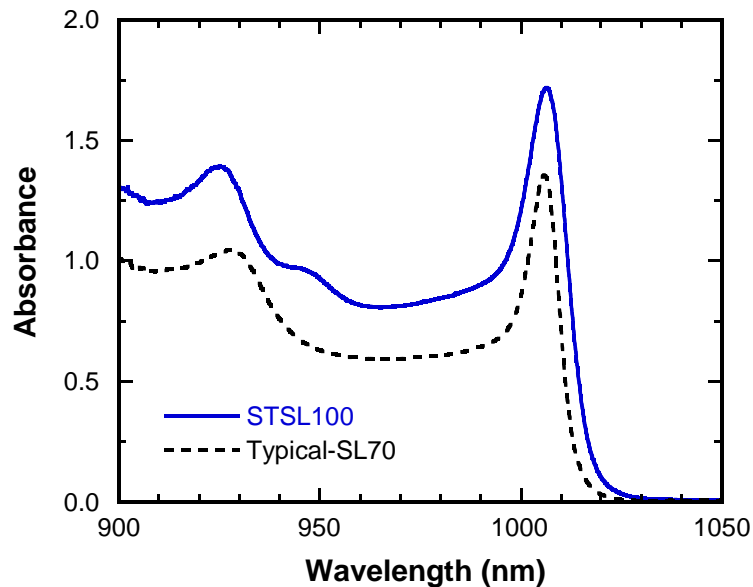of the GaAs reference cell without a SL was used for the background spectrum. Note that the absorbance includes the effects of multiple reflections inside the cells.

Fig. 5-21 (a) shows the I-V curves for the two SL cells and the GaAs reference cell under standard AM1.5 illumination, and the I-V properties including J_{sc}, V_{oc}, *FF*, and efficiency are summarized in Table 5-1. The typical SL70 cell showed a larger J_{sc} of 23.3 mA/cm^2 than the GaAs reference cell (20.9 mA/cm^2) due to the infrared response of the SL. V_{oc} was reduced from 0.96 to 0.88 V, but the drop in qV_{oc} (0.08 eV) was much smaller than the difference in band edge energy (0.19 eV) between GaAs and the SL. However, poor carrier transport (due to the lack of tunneling) caused a visible slope in the I-V curve, even at 0 V, resulting in a small FF of 0.75. Accordingly, the AM1.5 efficiency was lower for the typical SL70 cell (15.3%) than the GaAs cell (15.9%). Along with an increased well number, the STSL100 cell showed an even larger J_{sc} of 25.0 mA/cm^2, which was 1.2 times higher than the GaAs reference cell. The J_{sc} enhancement was as large as 4.1 mA/cm^2 without an ARC. The V_{oc} for the optimized-cell was 0.85 V with an approximately 0.03 V drop when compared to the typical-SL70 cell, which may be attributed to slight lattice relaxation caused by the accumulated compressive strain. The V_{oc} drop from the GaAs reference cell was 0.11 V, which was still less than the difference between their effective bandgaps. Furthermore, the STSL100 cell did not show an apparent slope in the J-V curve at 0 V, due to the efficient tunneling made possible by the 3-nm-thick barriers. As a result, the STSL100 cell exhibited a higher FF of 0.76 than the typical-SL70 cell and a higher AM1.5 efficiency of 16.2% without an ARC, which is 0.3% higher than that for the GaAs reference cell.

Fig. 5-21 (b) shows the I-V characteristics under AM1.5, filtered using a 665 nm long-pass filter (FGL665S, THORLABS), which is a more practical performance in a situation where SL cells are operated as middle cells beneath InGaP top cells in triple junction devices. Note that FGL665S transmits approximately 90% of the light beyond 665 nm. Filtering the light slightly lowered the V_{oc} for all the cell because of the reduced photocurrent. The degradations in V_{oc} due to the SL incorporation were 0.07 V and 0.10 V for the typical-SL and STSL, respectively, and both of them were more or less same as the case of full AM1.5 illumination. Cutting off the short wavelength illumination increases the fraction of the light beyond the GaAs band edge in the incident light, and consequently leads to relatively better performance for the cells with SLs. The short-circuit currents for the typical-SL70 and the STSL100 cells were increased by 25% and 44%, respectively, from the GaAs reference, resulting in an efficiency enhancement for the SL cells by a factor of 1.06 and 1.22, respectively. However, the typical-SL70 cell showed a significantly degraded FF due to the insertion of the filter, from 0.75 to 0.71, because of the less efficient extraction of carriers excited at longer wavelength illumination and hence more rapid decrease of the photo-current with the forward bias. For the STSL100 cell, on the other hand, such degradation in FF was suppressed, primarily due to the improved heavy hole transport through thin barriers. As a result, compared with the reference cell, the maximum power output current J_{max} was enhanced by 38% for the STSL cell, whereas it was limited to only 13% with the typical SLs. J_{max} for the STSL100 cell was 10.7 mA/cm^2 under the filtered illumination. Considering the transmittance of the filter and the reflectance of the cell, this value

corresponds to 17.0 mA/cm^2 in expectation with ARC, which is the target current density for a current matched triple junction cell with an InGaP top cell as introduced in the chapter 1.
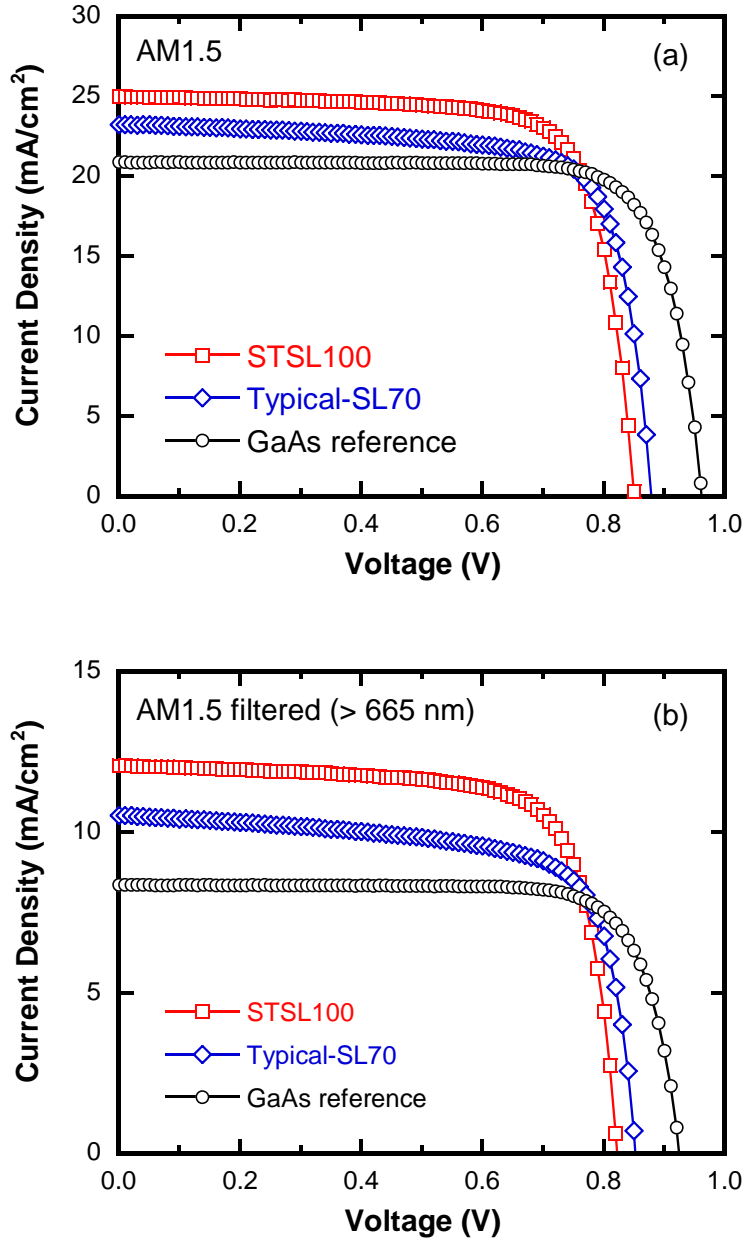
Fig. 5-21 I-V characteristics of the STSL100 cell and the typical SL70 cell under (a) standard AM1.5 illumination and (b) AM1.5 filtered by a 665 nm long-pass filter (FGL665S, THORLABS)

Table 5-1   I-V parameters for the fabricated PV devices (w/o ARC). Data in the right column were obtained with AM1.5 cut-off by a long-pass filter (FGL665S, THORLABS), which transmits approximately 90% of light beyond 665 nm. Note that the efficiency under the filtered AM1.5 was calculated with a filtered incident illumination energy of 514 W/m^2.

	AM1.5				AM1.5 filtered (> 665 nm)			
	J_{sc}(mA/cm^2)	V_{oc} (V)	*FF*	Efficiency	J_{sc}(mA/cm^2)	V_{oc} (V)	*FF*	Efficiency
STSL100	25.0	0.850	0.761	16.2%	12.1	0.823	0.746	14.4%
Typical-SL70	23.3	0.879	0.751	15.3%	10.5	0.853	0.716	12.5%
GaAs ref.	20.9	0.962	0.792	15.9%	8.4	0.925	0.784	11.8%

Fig. 5-22 shows the internal quantum efficiency (IQE) at 0 V. As can be seen, both SL structures extended the band edge beyond 1000 nm. However, the typical SL70 cell had an IQE of only 50% beyond the GaAs band edge. It also showed degraded response from 650 to 850 nm compared to the GaAs reference cell because of the poor carrier collection. In contrast, the STSL100 cell had an IQE of over 70% for almost the entire SL absorption wavelength range, with the response spectrum perfectly matched to the reference cell from 400 to 850 nm.
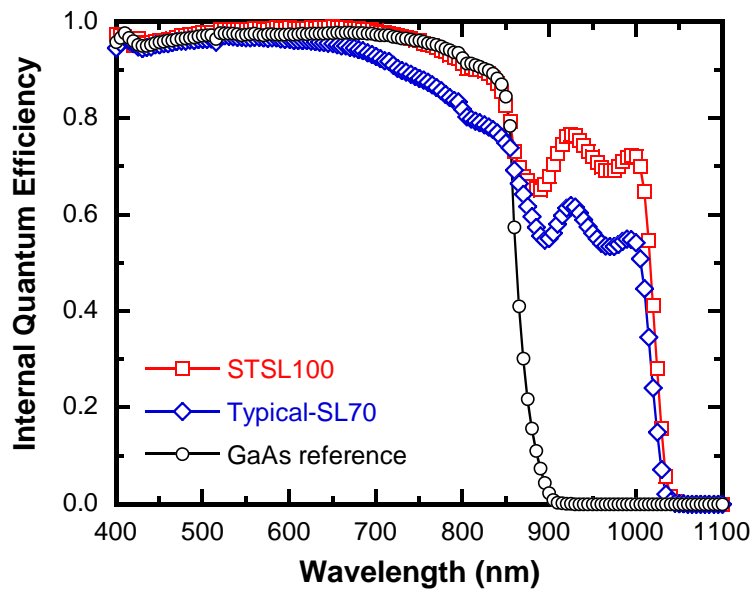
Fig. 5-22   Internal quantum efficiency (IQE) at 0 V for the STSL100 cell, the typical SL70 cell, and the GaAs reference cell
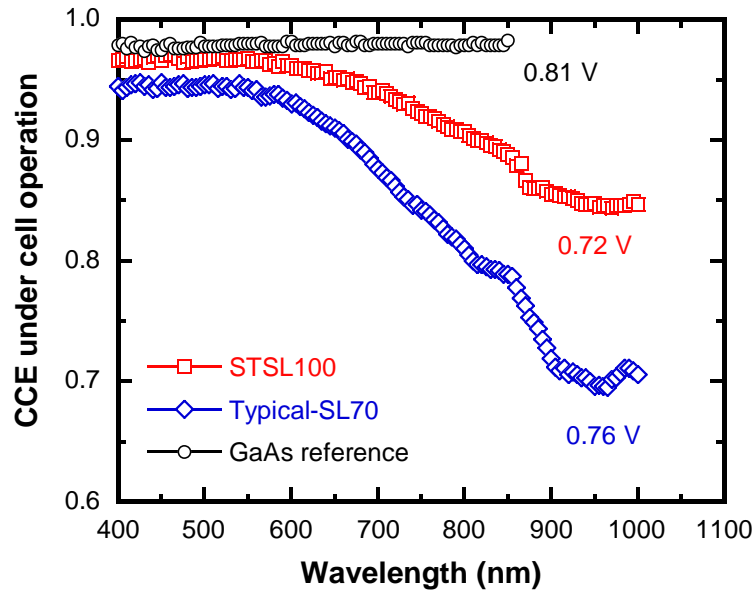
Fig. 5-23   Carrier collection efficiency spectra at maximum power output voltages (V_{max}) for the STSL100 cell, the typical-SL70 cell, and the GaAs reference cell. The values for V_{max} of each cell are shown together with the corresponding plots

Evaluation of the carrier collection efficiency at the operation voltage, CCE(V_{max}), is important in terms of practical application. Fig. 5-23 shows a comparison of CCE spectra at the maximum output voltages, which were 0.72, 0.76 and 0.81 V for the STSL100 cell, typical-SL70 cell, and the GaAs reference cell, respectively. These spectra can be divided into three wavelength ranges based on the region where the photons are absorbed in the cells: (i) 400 - 550 nm, (ii) 550 - 850 nm, and (iii) 850 - 1000 nm.

(i) 400 – 500 nm

Photons are absorbed in the upper area above the SL region, and thus the CCE is solely determined by electron transport through the i-region. Within this short wavelength range, the typical-SL70 cell had a high CCE of 94% despite the lack of quick tunneling transport, because electron thermal escape is efficient. In the STSL100 cell, the CCE was further improved to approximately 97%, which was comparable to the value of 98% obtained for the GaAs reference cell, indicating that a 100-period quantum well structure does not block electron transport.

(ii) 550 – 850 nm

Photons can reach the SL region as well as the upper GaAs region. If the light penetration to the SL is shallow, the CCE is primarily determined by electron transport because most carriers are generated in the upper GaAs. As the wavelength becomes longer, the fraction of carriers generated in

the wells increases, and the effect of hole transport across the i-region becomes larger. The typical-SL70 cell showed a severely degraded CCE at longer wavelengths, indicating poor transport of heavy holes. The STSL100 cell also exhibited a gradual CCE reduction at longer wavelengths, but it was strongly suppressed due to tunneling transport. The CCE for the GaAs reference remained above 98%, regardless of the excitation wavelength, because of highly efficient transport resulting from the absence of a carrier trapping structure. The effect of slow transport of heavy holes in the typical-SL70 cell was apparent even at 0 V, and is reflected in the degraded QE from 650 to 850 nm in Fig. 5-22. Heavy hole transport in the STSL100 cell, on the other hand, was still efficient at 0 V, resulting in almost an equivalent QE in the GaAs absorption wavelength range.

(iii) 850 – 1000 nm

Carriers are photo-excited only in the wells and the CCE is determined by the efficiency of heavy hole transport. Therefore, the CCE for the typical-SL70 cell with thick barriers was further degraded to approximately 70%, while the STSL100 cell showed a significantly improved CCE of 85%.

As shown above, we have now experimentally demonstrated the advantages of STSL for photovoltaic performance for a given SL bandgap, i.e. both efficient light absorption and efficient carrier collection, by designing thin well and barrier layers and few-nm-thick interlayers rather than using typical thick quantum wells with a rectangular band profile. The expected value for the J_{max} of 17.0 mA/cm^2 with 100-period SL with bandgap of 1.23 eV suggests a promising potential for using such a SL for the middle cell material in the Ge-based triple junction solar cells.

5.5 Summary of Chapter 5

In chis chapter, a stepped tunnel superlattice (STSL) was proposed as a general design principle for quantum well structure that overcomes the major challenges faced by InGaAs/GaAsP SL solar cells, specifically, the trade-off between light absorption and carrier collection as well as the difficulty in crystal growth of a high-quality SL consisting of strained layers.

- The essential strategies for structural optimization are as follows:
  1) InGaAs wells should be thinner and deeper for a given bandgap to achieve both a higher absorption coefficient for 1e-1hh transitions and lower compressive strain accumulation.
  2) GaAs interlayers with thicknesses of a few nanometers are effective for extending the absorption edge to longer wavelengths without additional compressive strain, and for suppressing lattice relaxation during growth.
  3) GaAsP barriers should be thinner than 3 nm to facilitate tunneling transport, and their phosphorus content should be minimized while avoiding detrimental lattice relaxation.

- For designing the GaAsP layers, the influences of the barrier structure on the carrier transport were systematically investigated in terms of the CCE with various widths (2~6 nm) and phosphorus contents (40~60%). The transport of heavy holes was found to be the bottleneck, especially in the thermionic escape processes, and making the barriers as thin as 3 nm was found to be an essential criterion for sufficiently facilitating tunneling transport.

- Efficient light absorption using thinner and deeper wells, i.e. more absorption with a thinner total thickness of the InGaAs region, was experimentally demonstrated.

- After optimization of a SL structure with the absorption-edge energy of 1.23 eV, a cell with a 100-period $In_{0.30}Ga_{0.70}As$(3.5 nm)/GaAs(2.7 nm)/$GaAs_{0.60}P_{0.40}$(3.0 nm)/GaAs(2.7 nm) SL achieved significantly improved performance, showing a 16.2% AM1.5 efficiency without an ARC, an IQE of 70% (0 V) and a CCE of 85% (V_{max}) at wavelengths beyond the GaAs band edge. Compared to the GaAs control cell, the STSL100 cell showed an absolute gain in AM1.5 efficiency, and achieved a 1.22 times higher efficiency with 38% enhancement of the maximum-power-output current under AM1.5 cut-off by 665 nm long-pass filter, indicating a strong potential for introduction into Ge-based 3J tandem devices.

6   MOVPE of SLs on vicinal substrates

For practical application of an InGaAs/GaAsP SL for Ge-based triple junction solar cells, the epitaxial layers are required to be grown on vicinal substrates for two reasons: 1) to avoid formation of anti-phase domains in the III-V layers on the Ge substrate, and 2) to prevent ordering of InGaP layer in MOVPE (if InGaP is used for the top cell material). In most researches and demonstration of III-V solar cells on Ge, (0 0 1) substrates that are 6° offoriented toward either [1 1 1] or [1 0 1] direction are used [52, 129, 130, 131].

Growth of InGaAs/GaAsP SLs on vicinal substrates, however, is much more difficult than on exact oriented substrates. In this chapter, the challenges of the SL growth on misoriented substrates are briefly overviewed at first. To overcome the problems, low-temperature MOVPE of SL using triethylgallium will be proposed and developed, aiming at successful implementation of the designed STSL (Chap. 5) onto vicinal substrates.

6.1   Crystal growth of III-V on vicinal substrates

6.1.1   Anti-phase domain

Crystal growth of III-V compounds on Ge substrates is not straightforward because of formation of anti-phase domain (APD), which is a region where the arrangement of the group-III and group-V atoms are opposite to the surrounding crystal, and is a general problem in epitaxy of a polar material on a nonpolar material [132, 133]. APD is suggested to be formed at single steps as shown in the Fig. 6-1, where the compounds crystal is disordered by one atomic layer with formation of bonds between same group atoms, e.g. Ga-Ga and As-As, which becomes the boundary between the two phases with opposite polarity: anti-phase boundary (APB). APBs in the epilayer act as deep-level nonradiative recombination centers [134, 135, 136], and thus growth of APD-free crystal is a vital requirement to minimize the energy loss for high efficiency solar cells.

Even in an exact oriented substrate, single steps cannot be completely eliminated even if the wafer surface is sufficiently polished. When polar compounds are grown on such an exact-oriented non-polar substrate, the formed APD at such single steps becomes larger as epitaxy is continued. To terminate the expansion of APD, vicinal substrates are widely used to for self-annihilation of APDs; the two APBs from neighboring single steps are fused together and terminate the APD region. Using vicinal substrates, APD-free III-V compounds on Ge substrates have been demonstrated [137].
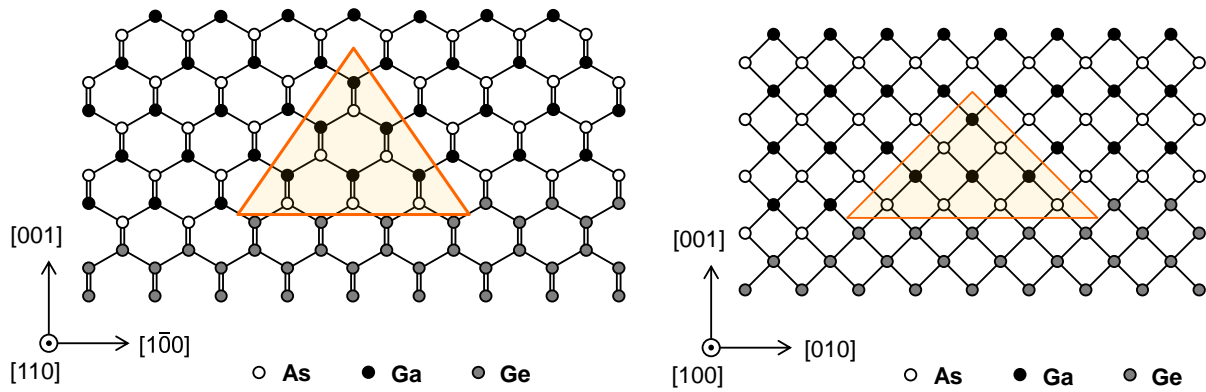
Fig. 6-1   Self-annihilation of anti-phase domain (APD) in GaAs grown on vicinal Ge substrates. The triangle areas represent APD.

6.1.2 Ordering in InGaP

InGaP grown on GaAs with orientation of (0 0 1), has been reported to form CuPt ordered structure with alternating In-rich and Ga-rich {1 1 1} monolayers as shown in Fig. 6-2 (a) [138, 139], and it is often observed with spots in electron diffraction pattern representing additional {½ ½ ½} diffraction (Fig. 6-2 (b)) [140]. The bandgap of the ordered InGaP is decreased from disordered InGaP where the Ga and In atoms are randomly aligned. The ordering in InGaP does not take place significantly in MBE and is a specific problem for MOVPE [141]. The mechanism for the CuPt ordering has not been completely elucidated yet, but it is suggested to be related to formation of (2×4) surface reconstruction, and its degree is strongly dependent on growth rate, V/III ratio, doping level, and substrate misorientation angle [142]. In order to prevent the ordering, use of substrates offoriented toward [1 1 0] direction is effective as shown in the Fig. 6-2 (c). Therefore, offcut direction for the vicinal Ge substrates for tandem solar cells with InGaP top cells would be desired to be [1 1 0], or [1 1 1]; the other misorientation direction can be chosen with other top cell materials.

Fig. 6-2   (a) Structure model for naturally formed ordering in InGaP [139], (b) [1 1 0] pole electron diffraction pattern for ordered InGaP [140], and (c) degree of the order in InGaP vs substrate misorientation angle [142].

6.1.3 Step bunching in strained SLs on vicinal substrates

For the reasons above, InGaAs/GaAsP SLs are required to be grown on vicinal substrates for the application into InGaP/SL/Ge triple-junction solar cells. However, it has been reported that when such a SL composed of strained layers is grown on vicinal substrates, the component layers are likely to b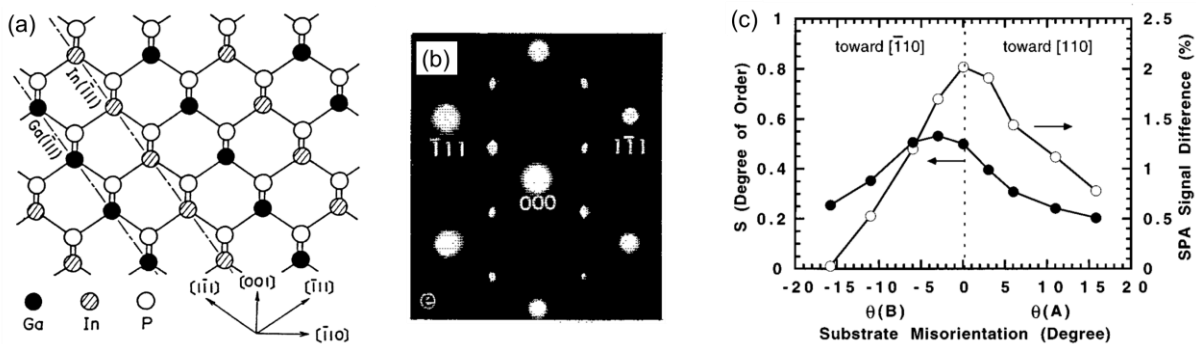e undulated due to formation of step bunching [143, 144]. Some universal phenomena with respect to the thickness modulation in SLs have been revealed by several systematic studies using various substrate misorientations and lattice mismatches in the individual layers; 1) the modulation amplitudes are larger with higher strain, and they increase as the deposition proceeds [143], 2) the resultant layer undulation exhibits lateral periodicity toward the offcut direction [144, 145]. Severe layer undulation on vicinal substrates with large step bunching easily causes lattice relaxation and hence degrades the crystal quality (Fig. 6-3 for example).
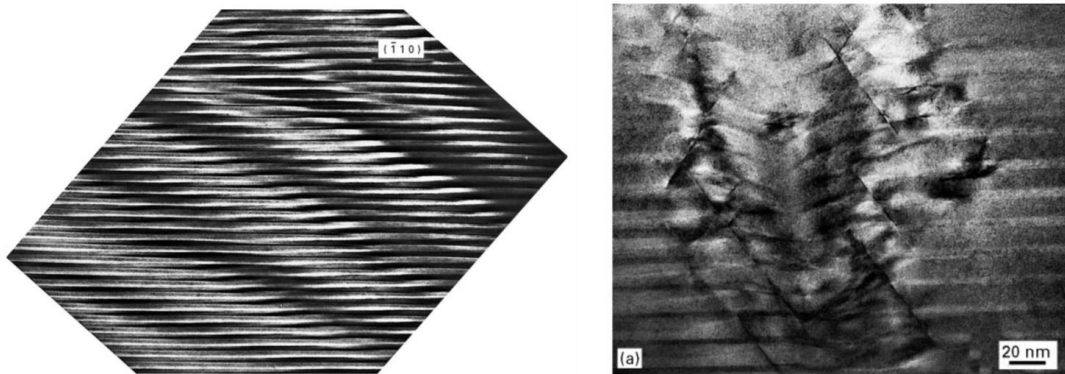
Fig. 6-3   (left) Thickness modulation in symmetrically strained InGaAs/GaAsP SL on a GaAs (0 0 1) substrate 2°-off toward [0 1 0] direction. (right) Severe distortion in layer growth of SL [143]

The exact mechanism for the formation of step bunching is not fully elucidated yet, but a possible origin has been suggested to be multi-terrace migration of the cation adatoms [146]. As in the schematic diagram is shown in Fig. 6-4 (a), an adatom encountering a terrace has four allowed processes: single-terrace and multi-terrace migration either in descending or ascending directions. In single-terrace migration, the adatom attaches to the step edges, whereas in the multi-terrace migration, the adatom crosses over the steps and can migrate to another terrace. A simulation study based on the model illustrated in Fig. 6-4 (a) revealed that step bunching develops rapidly when the multi-terrace migration occurs with a net adatom flow toward the descending direction [146], a possible explanation for the layer undulation in SLs on vicinal substrates (Fig. 6-4(b)).

In general, multi-terrace migration becomes predominant at higher growth temperature because of the longer diffusion length the adatoms [147]. Therefore, lowering the temperature is expected to suppress the formation of step bunching by shortening the atom migration length.
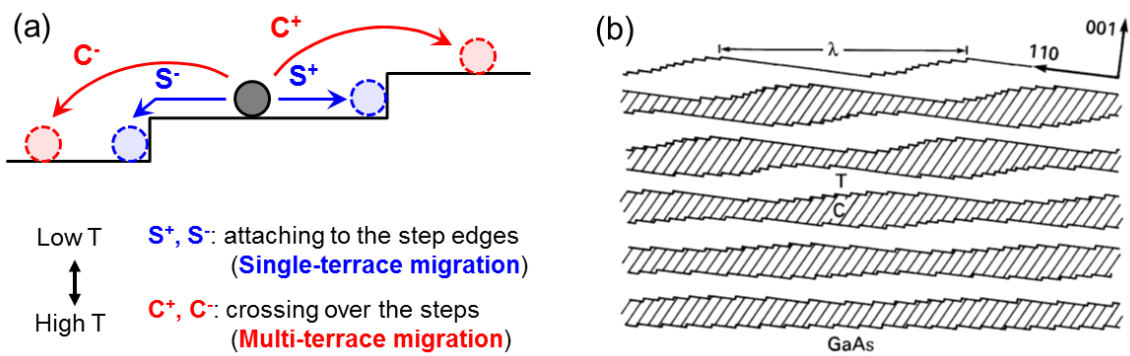
Fig. 6-4   (a) Schematic diagram of single-terrace and multi-terrace migration that are allowed of an adatom on a terrace [146]. (b) Layer undulation in a SL on a vicinal substrate attributed to step bunching evolution [143].

6.2 Low temperature MOVPE with triethylgallium (TEGa)

Although low temperature growth is expected to make the SL growth on vicinal substrates stable and hence to prevent lattice relaxation by suppressing step bunching formation as explained above, too low growth temperature may lead to several drawbacks such as low crystal quality due to insufficient atom migration on a terrace surface and high background impurity levels. In a typical MOVPE for GaAs-based materials, trimethylgallium (TMGa) is the most widely used gallium precursor, and it has been used in this study as well so far. Here in this chapter, triethylgallium (TEGa) is used for the growth of SLs on vicinal substrates in order to overcome these problems associated with low-temperature MOVPE (LT-MOVPE). The aim for using TEGa instead of TMGa is twofold: (1) improvement of the crystal quality of the SL owing to stable mass-transport limited growth with efficient pyrolysis of TEGa, and (2) prevention of carbon incorporation by suppressing formation of methyl radicals. These two advantages of TEGa to TMGa will be discussed in the rest of this section, and they will be experimentally demonstrated in the section 6.3 and 6.4.

6.2.1 Mass transport limited growth

Growth processes in MOVPE involve a number of reactions. Metal-organic precursors injected in the reactor are firstly decomposed by chemical reactions while diffusing in the boundary layer from the gas flow region to the substrate. The adatoms produced by the pyrolysis then attaches to the crystal surface, repeat adsorption, surface migration, and desorption, and finally are incorporated in the crystal through surface reactions. The slowest process, therefore, predominantly determine the deposition rate for crystal growth in MOVPE.

Thermal decomposition and chemical reaction of precursors in the vapor phase strongly depend on the ambient gas. In H_2 ambient, TMGa is pyrolysed with hemolytic fission of Ga-CH$_3$ bonds [79]:

$$Ga(CH_3)_3 \quad \rightarrow \quad Ga(CH_3)_2 + CH_3 \qquad\qquad (6\text{-}1)$$

$$Ga(CH_3)_2 \quad \rightarrow \quad Ga(CH_3) + CH_3 \qquad\qquad (6\text{-}2)$$
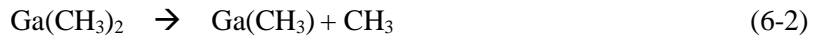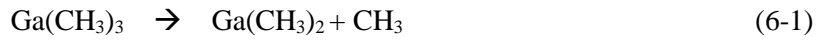
The third Ga-CH$_3$ bond remains and thus mono-methyl gallium (MMGa, GaCH$_3$) is believed to be the main surface species [148]. During growth of GaAs, Ga is incorporated to As-terminated crystal surface with desorption of CH$_3$ to the vapor phase. For typical MOVPE, V/III ratio is chosen to be sufficiently high, and thus the growth rate is determined by the injection concentration and the incorporation rate of the group-III sources.

Fig. 6-5 shows the growth rates of GaAs as functions of the growth temperature using different Ga sources and AsH$_3$ [149]. Using TMGa, the growth rate is almost independent at 800 - 600 ℃. This is because the diffusion of the source molecules to the substrate surface is the limiting process; the growth in this temperature range is called mass transport limited growth. In this growth regime, the surface reaction is sufficiently faster than the mass diffusion, and thus the Ga species delivered to the crystal surface are efficiently incorporated. Therefore, the growth rate is linearly proportional to the partial pressure of TMGa.

At higher than the mass transport limited regime, the desorption process becomes predominant. That is, the fraction of the source molecules on the crystal surface that are desorbed without being incorporated becomes larger at higher temperature, resulting in a lower growth rate. In addition, higher temperature of the whole reactor makes material deposition on the inner wall surface significant, and thus causes lower growth rate due to less amount of source molecules that reach the substrates.
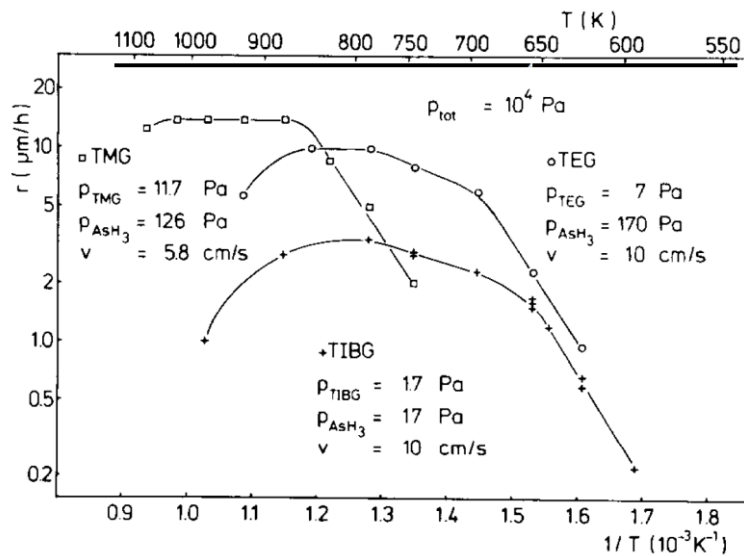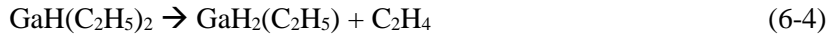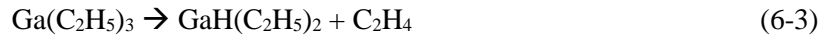

Fig. 6-5 Temperature dependence of GaAs growth rate using TMGa, TEGa, TIBGa as the gallium source. AsH$_3$ is used for the arsenic precursor [149].

At lower temperature than the mass-transport limited regime, on the other hand, the growth is kinetically limited; precursor decomposition in the gas phase, kinetic movement of the source molecules, and the surface reactions associated with atom incorporation become slower at lower temperature to limit the growth rate. In this regime, the growth rate is not linearly proportional to the partial pressure of the group-III sources. Using TMGa, in particular, desorption of CH_3 produced in (6-1) and (6-2) is less efficient at lower temperature, and thus they tend to bond to incorporated Ga atoms on the surface, preventing further adsorption of metal-organic compounds and blocking the diffusion of adatoms. Therefore, the growth becomes limited by surface reaction below 600 ℃.

Mass transport limited regime is favored in MOVPE because high purity and crystal quality can be obtained owing to rapid adatom incorporation, whereas growth at kinetically governed regime tends to become unstable due to insufficient atom migration and incomplete surface reaction that induce impurity incorporation [150]. Also, small temperature dependence of the growth rate in the mass transport limited regime can improve the uniformity of the epilayer over the substrate.

On the other hand, TEGa is known to be decomposed by β-elimination reaction in H_2 as

$$Ga(C_2H_5)_3 \rightarrow GaH(C_2H_5)_2 + C_2H_4 \tag{6-3}$$

$$GaH(C_2H_5)_2 \rightarrow GaH_2(C_2H_5) + C_2H_4 \tag{6-4}$$

$$GaH_2(C_2H_5) \rightarrow GaH_3 + C_2H_4 \tag{6-5}$$

which occur much more efficiently than TMGa [79]. The resultant species on the crystal surface is highly reactive GaH_3, and thus low temperature growth is possible [148]. Furthermore, since C_2H_4 produced by the pyrolysis process are subsequently desorbed, the incorporated Ga atoms are be immediately covered by As, resulting in efficient surface reaction. Therefore, the temperature range for the mass transport limited regime can be lowered than the case with TMGa by approximately 100 ℃.

6.2.2 Carbon incorporation

As already discussed in the section 4.5.1, carbon background doping is a quite detrimental problem in SL solar cells. The origin of carbon incorporation in GaAs growth has been suggested to be methyl radicals produced by decomposition of TMGa in (6-1) and (6-2) [79]. Intrinsic carbon level is influenced by various growth conditions, e.g. V/III ratio [105, 107], reactor pressure [106], substrate orientation [151], and growth temperature [105, 107]. Removal of methyl radicals from the surface is generally less efficient at lower temperature, resulting in higher carbon doping level. In many cases, higher V/III ratio reduces the intrinsic accepter concentration because it prevents carbon incorporation to As sites. At too low temperature, however, increase of V/III ratio cannot effectively suppress the carbon incorporation since the almost entire surface is covered by methyl groups [105].

Use of TEGa, on the other hand, does not produce methyl radicals in the decomposition reaction as can be seen in (6-3) - (6-5), and thus can prevent carbon incorporation in principle even at low temperature [152, 153].

6.3 Improvement in crystal quality and uniformity of SL

InGaAs/GaAsP SLs on vicinal substrates are expected to be grown more stably and uniformly at lower temperature with suppression of step bunching formation, and thus use of TEGa should be superior to TMGa in terms of efficient kinetics. Here in this section, the effect of growth temperature and Ga precursor on the structural uniformity of SLs and resultant difference in their optical properties are investigated. The misorientation angle of all the vicinal substrates used in this study is 6°, which has been widely used for Ge-based triple junction photovoltaic devices.

■ **Experiments**

(1) $In_{0.30}Ga_{0.70}As$ (3.5 nm)/GaAs (2.7 nm)/$GaAs_{0.60}P_{0.40}$ (5.0 nm)/GaAs (2.7 nm) SL was grown on GaAs substrates with orientation (0 0 1) 6°-off towards [1 0 1] direction at a reactor pressure of 10 kPa. This SL structure is same the optimized one demonstrated in the section 5.4 except for the 5-nm-thick GaAsP. Due to the thickened barriers, the strain balance condition is exactly satisfied in this experiment, in order to eliminate the effects of strain accumulation on the growth stability. The growth temperature was varied from 610 °C to 520 °C for growth with TMGa, and it was lowered to 510 °C for the growth with TEGa. The composition and the thickness for each layer were identified by XRD 2θ-ω scans for samples grown on exact-oriented substrates. During growth of SL, the reactor was purged with group-V sources for 2 seconds before starting and after stopping the injection of group-III sources. InGaAs layer and its neighboring GaAs interlayers on the top and the bottom were grown continuously without purging by group-V source in between.

(2) DC reflectance and RA were *in-situ* measured during growth of 100-period SLs at a wavelength of 443 nm for monitoring the stability of the growth and uniformity of individual layers. Severe crystal degradation was identified by decrease of the average reflectance during SL growth, and morphological change in SL due to step bunching was detected by comparing the periodic signals of RA.

(3) XRD-RSM was measured around (0 0 4) diffraction point for the 50-period SLs grown under each condition to investigate the SL structure in detail, and it was compared with the direct observation of cross sectional scanning transmission electron microscopy (STEM). Note that the incident X-ray for XRD measurement was directed toward $[\bar{1}\,0\,0]$, which is parallel to the offcut direction of the substrates.

(4) PL and FTIR were performed for 50-period SLs at room temperature to further characterize the luminescence and absorption properties. PL was measured at an excitation intensity of 25 μW at wavelength of 532 nm.

■ Results and discussions

In order to grow the same SL structure at different temperatures, adjustment of the growth condition such as growth time and ratios of partial pressures were necessary. Using TMGa for example, lowering the growth temperature from 610 ℃ to 520 ℃ led to lower growth rate due to kinetically limited growth and less phosphorus incorporation in GaAsP at the same vapor phase content. The growth rate was especially decreased for $GaAsP_{0.4}$ region at lower temperature compared to GaAs and InGaAs. In contrast to GaAsP, the change in the composition of InGaAs with temperature decrease was only slight. Therefore, the growth parameters for each temperature was adjusted to ensure the equal thickness and composition of the component layers as can be seen in the almost identical XRD-patterns for 10-period SLs grown on exact oriented substrates in the Fig. 6-6.
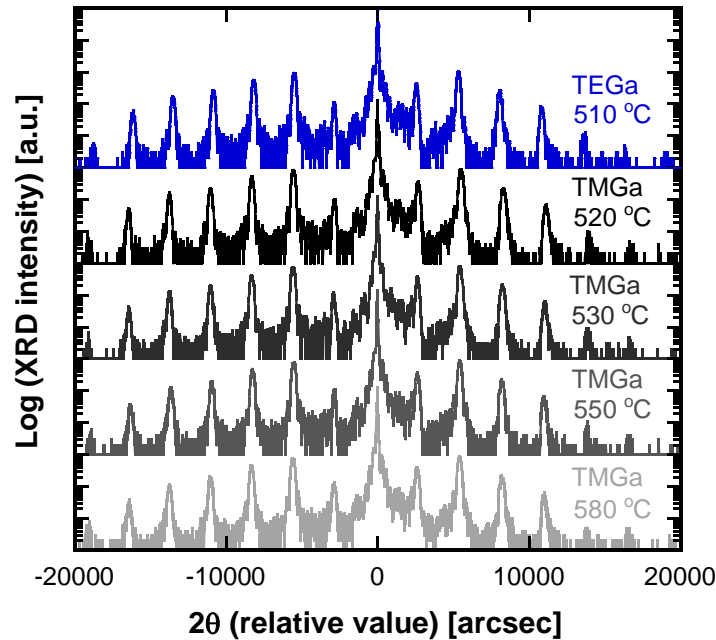
Fig. 6-6   Patterns of XRD 2θ-ω scan around (0 0 4) diffraction point for 10-period $In_{0.30}Ga_{0.70}As$ (3.5 nm)/GaAs(2.7 nm)/$GaAs_{0.60}P_{0.40}$(5.0 nm)/GaAs (2.7 nm) SLs grown on exact oriented GaAs (0 0 1) substrates. Samples were grown using TMGa (580 – 520 ℃) or TEGa (510 ℃).

Fig. 6-7 shows the time transient of DC reflectance during the growth of a 10-period SL grown at 610 ℃ with TMGa, 100-period SLs grown at 580 - 520 ℃ with TMGa, and 100-period SLs grown at 510 ℃ with TEGa. The growth rate at lower temperature using TMGa was lower as mentioned above, resulting in longer growth time for the growth of 100-period SLs. As already discussed in the section 4.5.2 and 5.4, the reflectance during SL growth oscillates due to the Fabry-Pérot interference, and the average reflectance remains constant if the lattice relaxation is negligible and the surface remains flat. Critical lattice relaxation and hence crystal degradation, therefore, was assumed to happen when the average reflectance started to drop as indicated with arrows in the graph.

At growth temperature of 610 °C, the average reflectance started to drop from the beginning, and even a 10-period SL could not be stably grown. At 580 °C, the average reflectance started to gradually decrease after approximately the 50th period, indicating severe lattice relaxation due to formation of large step bunching. Milky surface was obtained after the growth of a 100-period SL, and small hillocks covering the surface were confirmed by nomarski microscopy. Lowering the temperature to 550 °C was effective to suppress the severe crystal deterioration, and 100-period SLs were stably grown at 550 °C and 530 °C without degradation in the average reflectance. At 520 °C, however, the reflectance gradually decreased after the 70th period. This indicates that crystal degradation occurred at too low temperature as mentioned earlier, due to insufficient migration of adatoms or unstable incorporation of adatoms in the presence of adsorbates covering the surface. Use of TEGa, in contrast, enabled a 100-period SL to be successfully grown with mirror-like surface at even lower temperature of 510 °C, proving that TEGa is much more suitable for stable growth of SLs at low temperature. Although TMIn was used as the indium precursor and thus methyl radicals on the surface might not be completely eliminated, only the exchange of TMGa with TEGa was found to be effective to improve the crystal quality at low temperature.
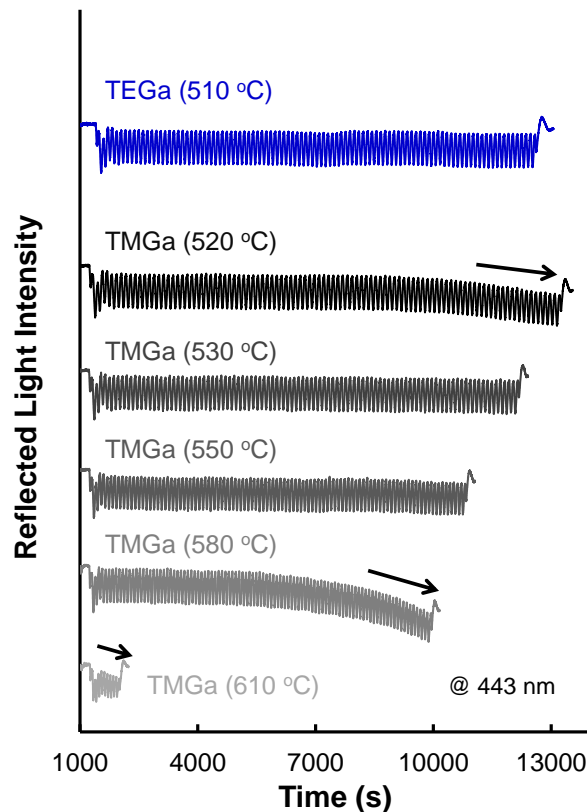

Fig. 6-7 *In-situ* monitored DC reflectance at wavelength of 443 nm during growth of SLs at different temperatures and gallium sources. 10-period SL was grown at 610 °C, and 100-period SLs were grown at other temperatures. SLs were capped with 50 nm thick GaAs. Apparent decrease of reflectance due to crystal degradation is indicated with arrows.

Fig. 6-8 shows time transient of reflectance anisotropy (RA) around the 10th and 100th period of SLs grown at 550 ℃ and 530 ℃ with TMGa, and at 510 ℃ with TEGa. Periodic RA was obtained corresponding to each component layer as indicated in the plots for the 10th-11th period. At 550 ℃, the RA value as a whole gradually increased while the relative changes among the component layers were unchanged. At this stage, the average reflectance did not show an apparent degradation. This gives an indication of larger surface anisotropy due to the formation of step-bunching and hence thickness modulation in the lateral direction. The RA at 550 ℃ slowly changed during the growth of the first 50-period SLs, and showed accelerated change in the signal shape during the latter 50-period growth, while it monotonically increased from the beginning at the temperature of 580 ℃. This indicates that the step-bunching rapidly became more significant in the latter part of the growth while the stacking of SL was relatively stable and uniform at the beginning. A similar trend has been observation in another literature, which reports that formation of step-bunching starts after deposition of certain thickness of SLs, and that the period for the onset of apparent layer undulation is dependent on growth condition and lattice mismatch [143].

At 530 ℃, the change of RA signal between the 10th and the 100th period was much smaller, indicating that the formation of step-bunching can be suppressed by lowering the temperature. The periodic RA did not show an apparent change until approximately the 80th-period. However, it started to gradually change in the end part of the SL especially during the growth of the InGaAs-GaAs region, for which a slight increase in RA can be seen in the comparison between the plots for the 10th and the 100th period, indicating that the lateral uniformity of the grown SL is still not complete. At further lower temperature of 520 ℃ with TMGa, the periodic RA signal was well preserved until the 70th period, but it rapidly rose up with the decrease of the average DC reflectance shown in Fig. 6-7. At this stage, RA was no longer periodic, and thus the signal for each component layer was not well distinguished. Such severe crystal degradation below 530 ℃, therefore, suggests the difficulty of SLs growth on vicinal substrates with TMGa to achieve both good crystal quality and uniformity.

In the growth using TEGa at 510 ℃, on the other hand, the RA for 10th-period SL was perfectly preserved even at the 100th-period, indicating that very uniform SLs were grown with negligible formation of step-bunching. This is an experimental proof for more stable and well-controlled SL growth using TEGa at even lower temperature than for TMGa. The very dissimilar signal shape of RA for a set of SL between the growth with TMGa and TEGa suggests quite different dynamics for SLs growth with different Ga sources, e.g. surface reconstruction or the kinetics of adsorption and desorption.

All of the 100-period SLs in Fig. 6-8 were successfully grown without an apparent drop in average DC reflectance, but RA showed significant difference. This gives us an insight that RA, which is more sensitive to surface morphology and kinetics processes, is a better *in-situ* characterization method to examine the uniformity of SLs.
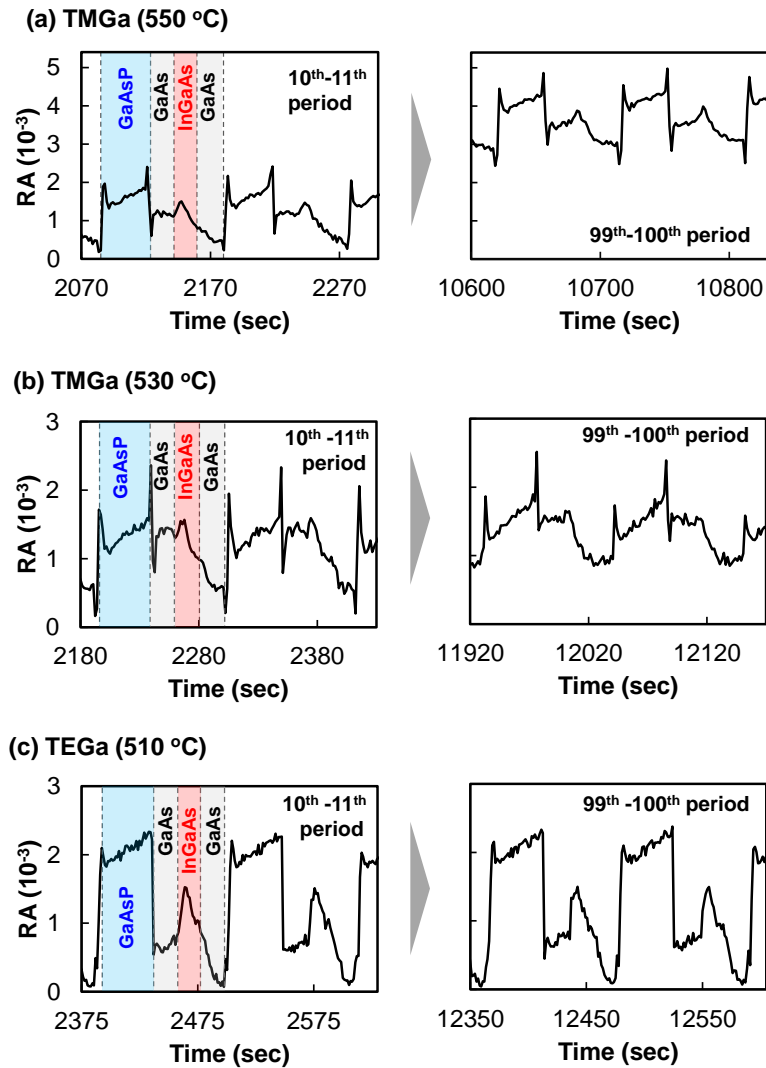
Fig. 6-8   Time transient reflectance anisotropy (RA) for the 10th-11th and the 99th-100th period of SL growth. Periodic signals corresponding to each layer of SL were obtained as indicated in the 10th-11th plots. Measurement was performed at wavelength of 443 nm.

Layer undulation due to step bunching on vicinal substrates forms laterally periodic structure toward the offcut direction. An example can be seen in the cross sectional STEM image for a SL grown at 580 ºC in Fig. 6-9 (a), which shows a wavy layer stack with their crests aligned along a particular direction that is inclined from the growth direction. Therefore, a superlattice with periodic step bunching grown on vicinal substrates have 2-dimentional periodicity, in both vertical and lateral directions. The detailed structure of such an undulated SL, e.g. lateral and vertical periodicity as well as the angle of the inclination for the corrugated structure, can be analyzed by XRD-RSM [144, 145], since the reciprocal space map is basically the two dimensional Fourier transform of the real space.
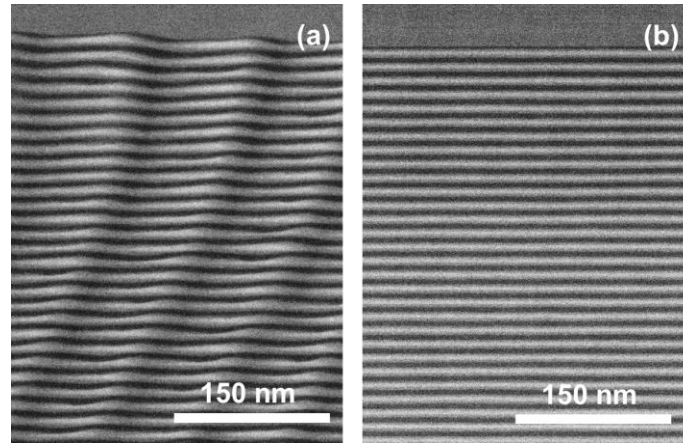
Fig. 6-9   HAADF-STEM images for the upper part of 50-period SLs on 6o-off substrates grown (a) at 580 ºC with TMGa and (b) at 510 ºC with TEGa. The SLs were capped with GaAs.

Fig. 6-10 shows XRD-RSM around the (0 0 4) diffraction point for 50-period SLs grown at different temperatures and Ga precursors. HAADF-STEM images for the top five period SLs with GaAs cap-layers on the top are shown together. The X-ray diffraction was observed in the plane which is parallel to the miscut direction of the substrate so that the RSM can capture lateral periodicity of undulation which is also along the miscut direction. Samples grown at 580 ºC and 550 ºC with TMGa showed two-dimensional XRD fringe patterns around the substrate peak. Superlattice periodicity in the vertical direction can be derived from the interval of the satellite-peaks along the solid line in the plots for 580 ºC, which is inclined from the Q_y axis by the offcut angle of 6º. From the interval of the fringe-peaks along the dotted line, on the other hand, lateral periodicity can be estimated [144].

The estimated vertical periodicity was 14.2 nm for SL grown with TMGa at 580-530 ºC and 13.8 nm for the growth with TEGa at 510 ºC, both of which were close to the designed superlattice period. The reason for the slightly higher growth rate with TMGa is not clear yet, but maybe due to different incorporation rate of Ga species at the step edges. The periodicities of the in-plane thickness undulation for 580 ºC and 550 ºC were estimated as 84 nm and 47 nm, respectively, indicating smaller step-bunching and hence smaller in-place undulation at lower growth temperature. These values well matched with the periodicity of the layer corrugation directly observed by STEM shown in Fig. 6-9(a).

The origin of the layer undulation was clarified to be step-bunching formed during InGaAs growth as seen in the magnified STEM image for the top 5-period SLs for the temperature of 580 ºC in Fig. 6-10, which showed clear three-dimensionally grown InGaAs regions with extended (0 0 1) terraces. Formation of step bunching in InGaAs induced unstable growth of the upper layers, resulting in very rough interfaces between GaAs and GaAsP layers. It should be also noted that the GaAs layers on the InGaAs are more likely to be deposited on the bunched-steps region rather than on the (0 0 1) plane, probably because Ga species tend to be incorporated in step edges. This leads to relatively thin GaAs interlayers between InGaAs and GaAsP on (0 0 1) plane and may bring about more difficulty in

formation of the hetero interfaces as discussed in the section 5.3.2. At 550 °C the three-dimensionally grown InGaAs region with step bunching became smaller than at 580 °C, resulting in shorter lateral periodicity and smaller layer corrugation in the entire SL. Step-bunching was significantly suppressed by lowering the temperature to 530 °C, and three-dimensional growth of InGaAs was not confirmed in the STEM image. Consequently XRD peaks attributed to lateral periodicity disappeared and fringe patterns were obtained only along the vertical direction. Roughness of each layer was reduced and the interfaces became smoother and clearer. Nevertheless, the layer undulation was not completely eliminated, and as a result, fringe spots in RSM attributed to SLs structures were still broad.

By lowering the growth temperature to 510 °C using TEGa, step-bunching was further suppressed, resulting in an extremely uniform SL with very flat interfaces as seen in the STEM images in Fig. 6-9(b) and Fig. 6-10, and the fringe spots in the XRD-RSM became much smaller. Comparing with the SL grown at 530 °C with TMGa, the FWHM of the fringe spot around $(Q_x \times 10000, Q_y \times 10000) = (-15, 6940)$ in the ω direction was reduced from 40.6 sec to 33.9 arcsec. The broad tail around this fringe peak was also remarkably suppressed, with the diffraction intensity at ω of 200 arcsec (relative from the peak ω) reduced by a factor of 1/20.
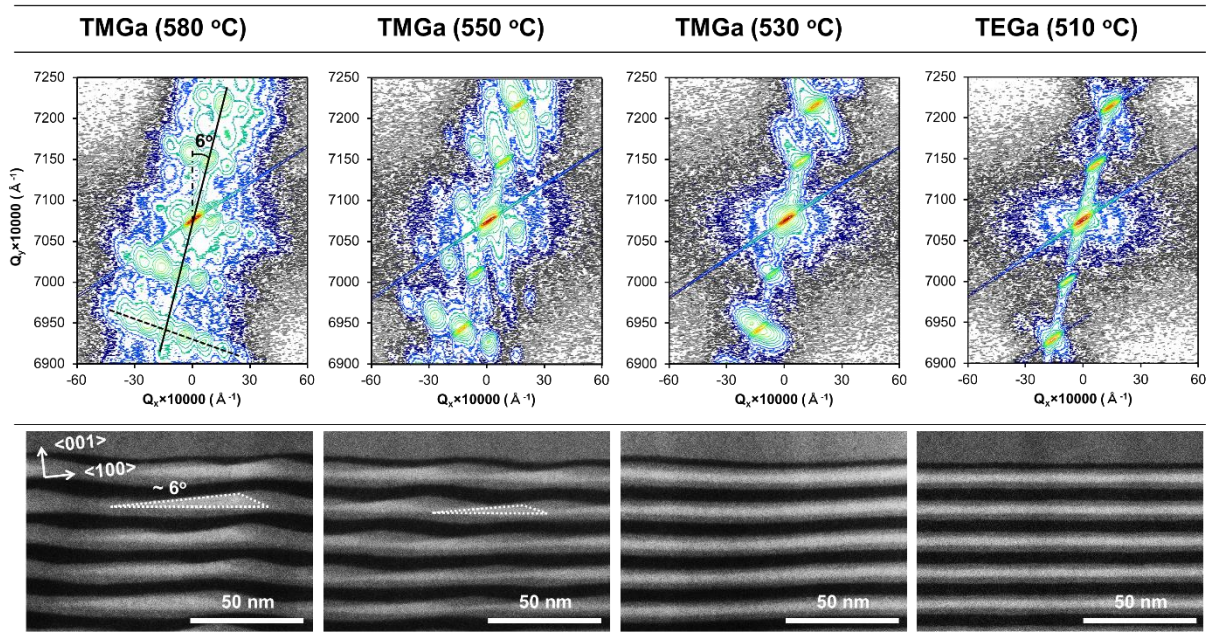
Fig. 6-10   XRD-RSM around (0 0 4) diffraction point recorded for 50-period SLs grown on 6°-off GaAs substrates at different temperatures using TMGa or TEGa. Incident X-ray was directed toward the off-cut direction of the substrates. Magnified HAADF-STEM images for the top 5-period SLs including the GaAs cap layers are shown together. Bright and dark regions in STEM images correspond to InGaAs and GaAsP layers, respectively. Three-dimensional growth of InGaAs regions with expanded (0 0 1) terraces and bunched steps were confirmed at 580 and 550 °C as indicated with dotted triangles, which would be the origin of periodic layer undulation.

Fig. 6-11 shows photoluminescence spectra of the 50-period SLs grown at different temperatures, in comparison with a SL grown on an exact-oriented substrate. Layer undulation formed at high growth temperature locally weakens the quantum confinement in the InGaAs well regions, resulting in a lower effective bandgap. Because of this, PL peak was red-shifted at high growth temperatures; the PL peak wavelengths for each growth temperature using TMGa were 1042, 1036, and 1026 nm for 580, 550, and 530 °C, respectively. Moreover, non-uniform quantum confinement and hence spatial variation in bandgap in the undulated SLs broadened the PL spectra, resulting in larger FWHM at higher growth temperature: 64.9, 62.4, and 46.6 nm at 580, 550, 530 °C, respectively. The SL grown using TEGa at 510 °C showed a much sharper PL spectrum than the ones using TMGa with peak wavelength of 1013 nm and FWHM of 18.4 nm. The almost equivalent PL spectrum to that on an exact-oriented substrate indicates that the SL on vicinal substrate were very uniform.
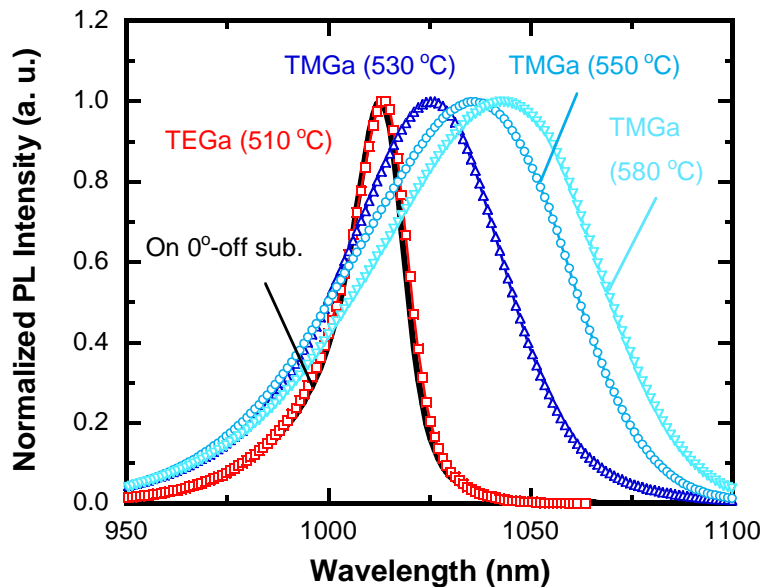
Fig. 6-11   Normalized room-temperature photoluminescence spectra of 50-period SLs grown on vicinal substrates at different growth temperatures using TMGa or TEGa. Samples were excited at wavelength of 532 nm and power of 25 µW. A spectrum for a 50-period SL grown on an exact-oriented substrate using TEGa is shown together for comparison.

Fig. 6-12 shows absorbance spectra of 50-period SLs grown under different conditions, which were measured by FTIR using GaAs substrates as the reference sample in a similar manner as the eq. (5-3). Absorbance of one-dimensional SLs generally shows a step-like spectrum representing the available quantum states as derived in the section 2.2.2 and as also shown in the Fig. 5-20. At 550 and 580 °C using TMGa, however, the quantum energy levels were indistinguishable with gradually decreasing absorbance toward longer wavelength due to non-uniform thickness of the quantum wells. Relatively low absorbance for the SL grown at 580 °C is probably attributed to poor coverage of the

InGaAs region with step bunching as shown in Fig. 6-10; the SL structure was far from layer-by-layer quantum wells as designed, but rather laterally aligned quantum wires with periodic intervals. Therefore, the areas between the wires are either absent of InGaAs layers or covered by extremely thin InGaAs where long-wavelength light cannot be absorbed. Clear stepped spectrum was obtained for the SL grown at 530 °C, in which three-dimensional InGaAs growth was much suppressed, but still it showed a long absorbance tail near the absorption-edge with no clear exciton peaks. In contrast, use of TEGa to lower the temperature to 510 °C significantly enhanced the absorbance of the SL around 1000 nm including a sharp exciton peak. Lower intensity of the exciton peak compared with the spectrum for the SL on an exact-oriented substrate indicates that slight roughness exists on an atomic scale including the original steps on the vicinal substrates. Nevertheless, the rise of the absorbance at the absorption edge was as steep as the SL on an exact-oriented substrate, indicating that the lateral distribution of the bandgap is sufficiently uniform.
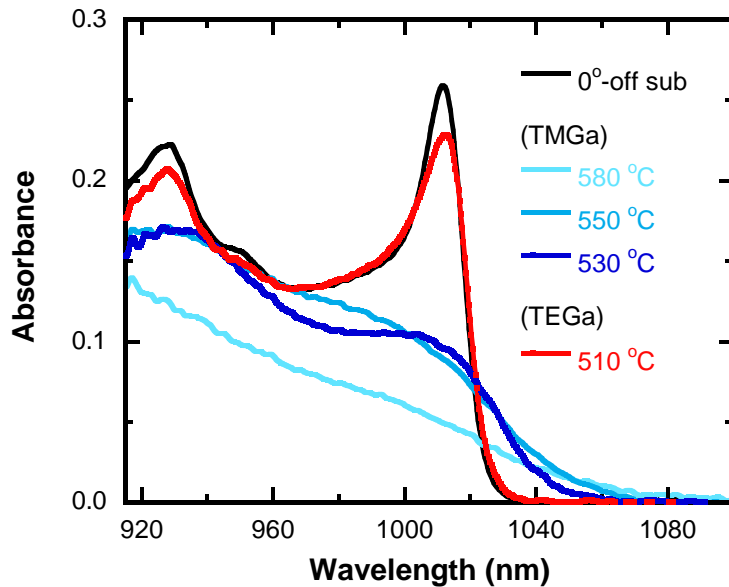
Fig. 6-12   Absorbance spectra of 50-period SLs on 6°-off substrates measured by FTIR for different growth temperatures and gallium sources. Absorbance of a GaAs substrate was used for the background spectrum.

6.3.1 Growth of STSL on vicinal substrates

The results for high-temperature growth of SLs on vicinal substrates shown above clearly indicated that crystal degradation easily occurs when large step bunching is formed even if the net strain is well balanced out. As discussed in the chapter 5, however, GaAsP barrier layers have to be thinner than 3 nm to facilitate efficient tunnel transport, and thus compressively stained STSL with thin barriers was proposed as an optimized structure, which may lead to more difficulty in stacking a

SL with a large number period. In this subsection, SLs with the optimized structure used in the section 5.4, i.e. $In_{0.30}Ga_{0.70}As$ (3.5 nm)/GaAs (2.7 nm)/$GaAs_{0.60}P_{0.40}$ (3.0 nm)/GaAs (2.7 nm) were grown on vicinal GaAs substrates with orientation (0 0 1) 6° offoriented toward [1 0 1] direction.

Fig. 6-13(a) shows the time transient DC reflectance at wavelength of 443 nm for 50-period SL growth using TMGa at 530 °C and TEGa at 510 °C. Using TMGa, the reflectance started to gradually decrease from approximately the 20th period indicating crystal degradation due to lattice relaxation, though a 100-period SL was stably grown without decrease in reflectance with 5-nm-thick barriers. This suggests the difficulty in low-temperature growth of SL using TMGa under strain-unbalanced condition because growth with TMGa is unstable kinetic-limited regime below 600 °C. The apparent degradation in crystal quality and severely distorted SL structure was also confirmed by XRD-RSM around the (0 0 4) diffraction point shown in Fig. 6-13(b). In comparison with a strain-balanced SL with 5-nm-thick GaAsP layers grown at the same temperature of 530 °C using TMGa, for which the RSM is shown in Fig. 6-10, much broader tails are seen around the satellite peaks for the SL and the GaAs (0 0 4) diffraction peak, as an indication of rougher interfaces of the stacked layers as well as inhomogeneity in the bulk GaAs layer on the top due to lattice relaxation during SL growth.

For the SL grown with TEGa at 510 °C, in contrast, a 50-period SL was successfully grown without drop in the average DC reflectance. RA showed no apparent change in the periodic signal for the entire SL region, indicating that 50-period layers were quite identically grown even under strain unbalance condition. The fringe pattern in the XRD-RSM was much sharper than the SL grown with TMGa owing to remarkable improvement in the uniformity and crystal quality of the SL. Furthermore, the satellite peaks for the SL were as abrupt as the case of strain balance condition, indicating that the formation of layer undulation was sufficiently suppressed with thinned GaAsP layers.

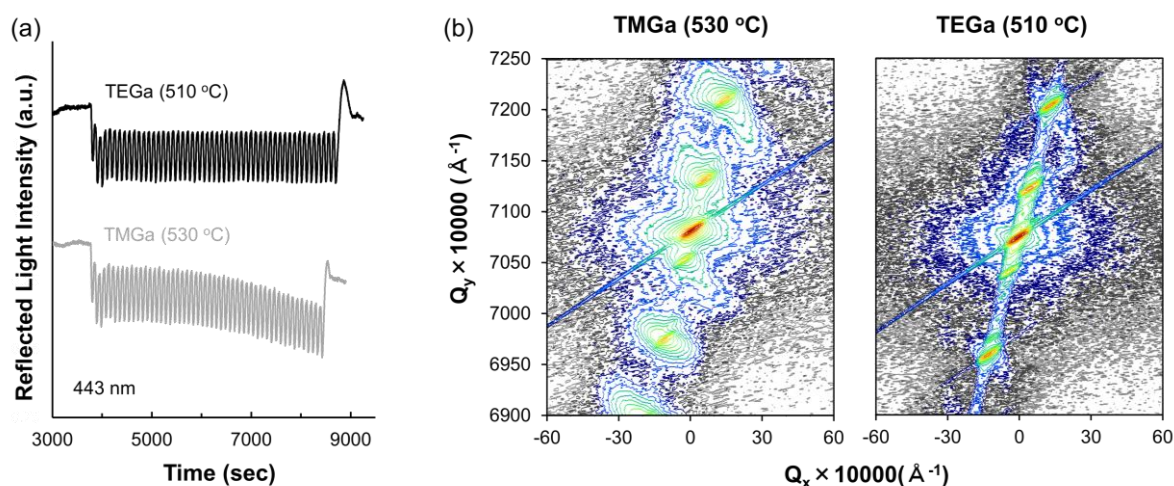Fig. 6-13 (a) *In-situ* monitored DC reflectance at wavelength of 443 nm during growth of 50-period $In_{0.3}Ga_{0.7}As$ (3.5 nm)/GaAs (2.7 nm)/$GaAs_{0.6}P_{0.4}$ (3.0 nm)/GaAs (2.7 nm) SLs on 6°-off GaAs (0 0 1) substrates using TMGa at 530 °C and TEGa at 510 °C. (b) XRD-RSM around (0 0 4) diffraction point recorded for 50-period SLs. Incident X-ray was directed toward the off-cut direction of the substrates.

6.4 Suppression of carbon incorporation

Another problem for using TMGa as the gallium source for LT-MOVPE is that the carbon incorporation and resultant p-type background doping level becomes higher at lower growth temperature because of the less efficient removal of methyl groups from the crystal surface. Therefore, prevention of carrier transport due to the bent band-lineup, which was shown in the section 4.5.1, becomes more serious for low temperature grown SL solar cells. Therefore, compensation doping treatment with n-type dopants to recover the built-in field should be very effective to solve this problem. On the other hand, Carbon incorporation in the SL-region is expected to be suppressed by substituting TMGa with TEGa as mentioned earlier owing to its β-elimination pyrolysis, which does not produce methyl radicals.

Here in this section, the effects of counter sulfur doping with TMGa and growth using TEGa on the photovoltaic performance of InGaAs/GaAsP SL cell grown at low temperature are investigated and discussed.

■ **Experiments**

(1) GaAs pin solar cells including 50-period $In_{0.30}Ga_{0.70}As$ (3.2 - 3.5 nm)/GaAs (2.7 nm)/$GaAs_{0.60}P_{0.40}$ (5.0 nm) /GaAs (2.7 nm) SLs were grown on GaAs substrates with orientation (0 0 1) 6°-off towards [1 0 1] direction at a reactor pressure of 10 kPa. The device structure is shown in Fig. 6-14. 200-nm-thick top p-emitter and 400-nm-thick bottom n-base were grown using TMGa at 610 °C, and the SLs were grown using either TMGa or TEGa. The SL-region was approximately 690-nm-thick in total and was sandwiched between two 100-nm-thick GaAs spacer layers, which were grown at 610 °C for the half 50-nm-thick region, and at low temperature for the other half region. A GaAs reference cell with an undoped 900 nm i-region, which was grown at 610 °C using TMGa, was also prepared for comparison. The growth temperatures for the SLs were 530 °C and 520 °C for TMGa and TEGa, respectively. The reason for the higher temperature with TMGa is that the crystal was found to be degraded below 530 °C as shown earlier. The thickness of InGaAs wells were 3.2 nm and 3.5 nm for the cells grown with TMGa and TEGa, respectively, so that they had an equal absorption-edge wavelength of 1025 nm; the SL grown with TMGa at 530 °C were more likely to be undulated to result in red-shift of the absorption edge as shown in the Fig. 6-12. The net strains in the SLs grown with TMGa and TEGa were -336 ppm and 134 ppm, respectively, both of which well satisfied the strain-balance condition.

(2) During SL growth with TMGa, the i-region was doped with sulfur using H_2S at various vapor-phase concentrations to compensate the p-type background doping due to carbon incorporation. The H_2S to TBAs ratio (S/As) was varied among 0 (undoping), 5.0×10^{-5}, 6.3×10^{-5}, 6.6×10^{-5}, 7.5×10^{-5}, and 1.0×10^{-4}. Note that these S/As values are for the growth of InGaAs layers and the adjacent GaAs interlayers. H_2S was supplied at a constant partial pressure during growth

of the entire i-region while the partial pressure of As was reduced for GaAsP layers. Therefore, the actual S/As for GaAsP growth was higher than these values. S-doping was also performed for the growth using TEGa at S/As of 0 (undoped) and 1.7×10^{-6}, which is with the minimum injection of H_2S in the used MOVPE system.

(3) All the grown samples were processed into solar cell devices with AuGeNi and TiAu contacts deposited on the back and the front side, respectively, in a similar manner as the section 4.5.2. Photovoltaic properties were measured using standard AM1.5 illumination for current-voltage measurement. The QE and CCE was measured with 2.5 mW/cm^2 monochromatic light under AM1.5 bias illumination.
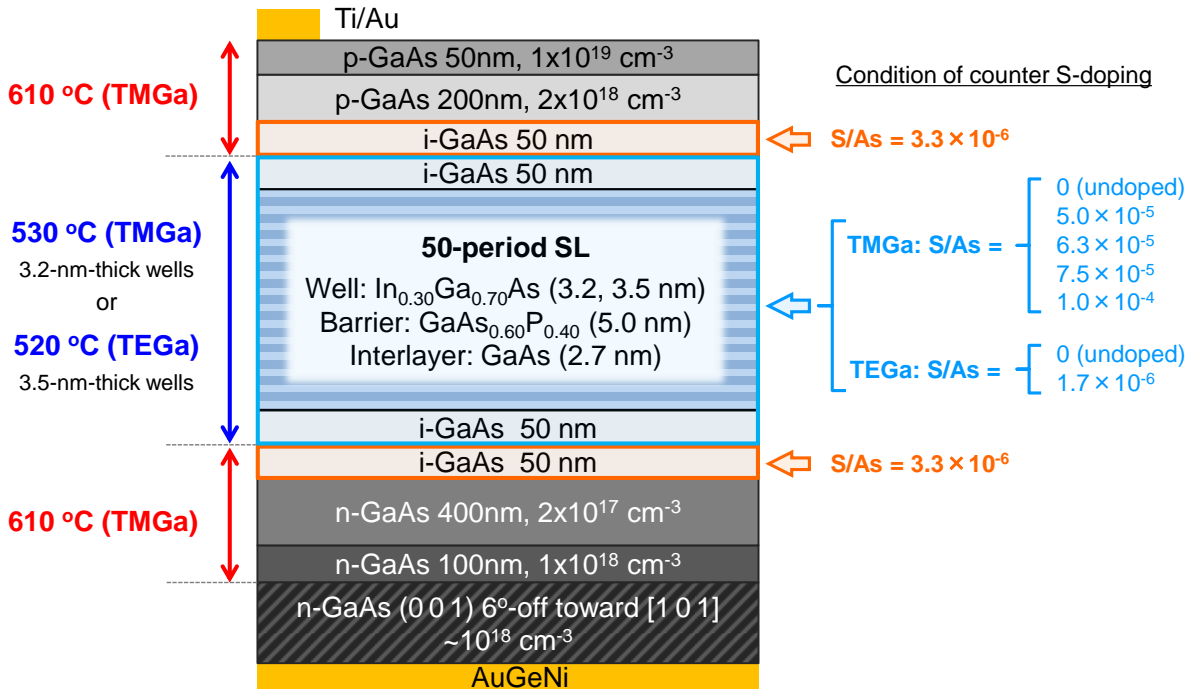
Fig. 6-14 Schematic of the samples prepared for this section. Growth temperatures and conditions of counter sulfur doping for the growth with TMGa and TEGa are shown together.

6.4.1 Compensation doping for low-temperature growth with TMGa

The p-type background doping level in GaAs grown at 530 °C with TMGa was estimated to be approximately 1×10^{17} cm^{-3} by Hall measurement. This value is much higher than 5×10^{15} cm^{-3}, which was obtained for the growth at 610 °C in the section 4.5.1, and thus the effect of band-bending and resultant blocking of carrier transport should become far more severe.

Fig. 6-15 shows band-lineups under short circuit conditions around the p-i-n regions of the cells

with different doping levels in the i-region including 690-nm-thick InGaAs/GaAsP SL region. Note that the SL structure in the band-lineup is not stepped shaped potential but typical rectangular profile for simplifying the calculation. The p-type background doping in the i-region at 1×10^{17} cm^{-3} significantly flattens the band of almost entire region of the SL. To cancel out this background hole concentration, therefore, counter sulfur doping has to be performed at an equivalent level in the order of 10^{17} cm^{-3}, which in turn carries risks for excessive n-doping to oppositely bend the band-lineup as depicted in the Fig. 6-15(c). The electric field in the 900-nm-thick i-region becomes uniform with suppression of background carrier concentration to the order of 10^{14} cm^{-3} as earlier demonstrated in the chapter 4.5.1.
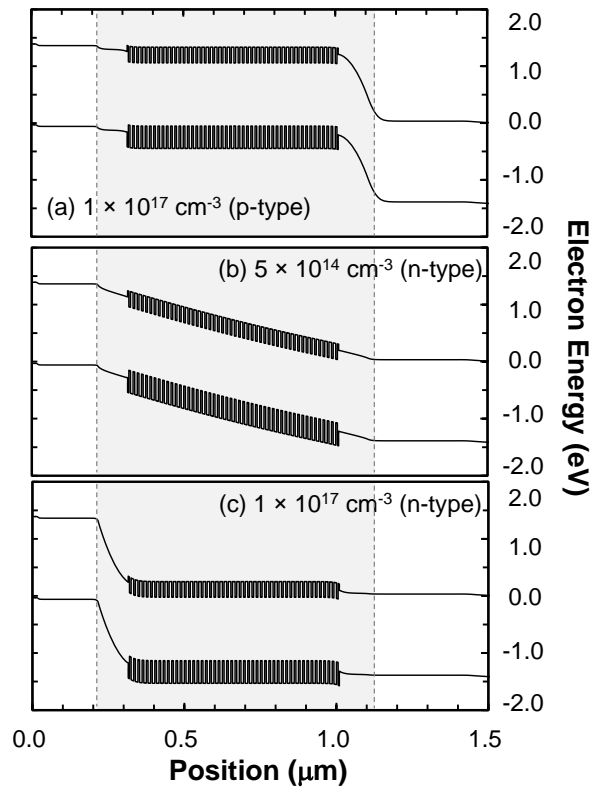
Fig. 6-15   Band-lineups under short circuit conditions around the p-i-n regions of the cells with different doping levels in the i-region including 690-nm-thick InGaAs/GaAsP SL region: (a) 1×10^{17} cm^{-3} (p-type), (b) 5×10^{14} cm^{-3} (n-type), and (c)1×10^{17} cm^{-3} (n-type). The valence band is shown only for heavy holes for simplification. Note that the p-sides of the cells were illuminated in the experiment.

Fig. 6-16 shows the external QE (EQE) at 0 V of the 50-period SL cells grown using TMGa with various S doping levels. The cell grown without S-doping, which is called undoped SL(TMGa)-cell hereafter, exhibited very low QE over the entire spectrum. Although slight signal was obtained from

600 to 850 nm, almost no output was confirmed in 400-600 nm and beyond 850 nm, indicating that most photo-excited carriers were lost via recombination. The reason for the extremely insufficient charge extraction is that the band-lineup of the i-region is severely flattened by the high p-type background doping at a low growth temperature for the SL as depicted in Fig. 6-15 (a), where the structure becomes p-p-n rather than p-i-n, and thus the weakened built-in field from the top p-region to the SL makes the carrier transport less efficient. When electron-hole pairs are photo-generated above the SL, electrons have to pass through the 50-period SL to the bottom-n-region while there is no blockage for the hole transport to the top contact. Therefore, electron transport limits the photocurrent under excitation by shorter wavelength light, which has higher absorption coefficient and is mostly absorbed in the upper region of the cell. Electrons photo-generated above the SL by such short wavelength light easily accumulate in the upper area of the i-region due to the absence of electric field and subsequently recombine before reaching the bottom n-region, resulting in almost negligible QE. The similar phenomenon was discussed in the section 4.5.1 for high-temperature grown SL cell on exact-oriented substrates, but the degradation in QE at short wavelength was far more obvious for low temperature grown sample as expected. Light with wavelength beyond 850 nm, on the other hand, are only absorbed in InGaAs in the SL regions. In this case, the electrons and holes generated inside the SL cannot be separated in the absence of electric field, producing no current output. In 600 - 850 nm, light can penetrate through the SL and partly excite carriers in the bottom GaAs spacer layer beneath the SL. Strong electric field in this region drifts the photo-excited holes and enable them to be transported to the top p-region through the SL while electrons can be easily collected to the n-region through no block layers. For this reason slight EQE were obtained in this wavelength range though the absolute values were quite low (< 0.1).

As sulfur was doped in the i-region to cancel out the p-type background doping, QE was accordingly improved owing to the recovered built-in field in the SL. Supply of sulfur at S/As up to 5.0×10^{-5}, which corresponds to S-doping of approximately 5×10^{16} cm^{-3} in GaAs, did not apparently change the QE spectrum from the undoped cell. At S/As of 6.3×10^{-5}, QE showed substantial enhancement in the entire wavelength range. Spectrum response in the short wavelength region (400 - 600 nm) and long wavelength region (850 - 1000 nm), which was not obtained in the undoped cell, indicates that the depletion region was expanded and the electric field existed in the SL-region. Low QE especially at short wavelength, however, indicates that the i-region was still strongly p-doped as a whole with bent band-lineup in the upper part of the SL.

S-doping at S/As of 6.6×10^{-5} significantly enhanced the QE with a nearly equivalent spectrum to the reference cell in the GaAs absorption wavelength range. Compensation doping condition, under which the n-type sulfur doping well balances out the p-type carbon background doping, was almost satisfied. In this case, the electric field in the i-region is uniform as shown in the band-lineup in Fig. 6-15(b), and it makes both electron and hole transport efficient regardless of the region where excitation takes place. Note that the variation of doping level as a function of In or P content in GaAs was not investigated exactly, and the compensation doping condition mentioned here does not

necessarily mean that the background doping is well compensated in every layer, but rather it means that the net doping level in the SL is cancelled out in average.

S-doping over the compensation doping condition makes the device structure p-n-n as shown in Fig. 2(c) with a flattened band in the bottom i-region. In this case, photo-excited carriers easily accumulate and recombine when they are generated in the deep area of the i-region by long wavelength light. The transport of electrons excited by short wavelength light from the top region, on the other hand, is relatively efficient with drift force due to the strong electric field that exists in the upper part of the i-region. Therefore, excessive-doping at S/As of 7.5×10^{-5} degraded the QE at longer wavelength while preserving the high QE in 400 – 600 nm. S-doping at S/As of 1.0×10^{-4} further bent the band-lineup, resulting in lower QE at longer wavelength. Almost completely flattened band in the SL was indicated by no spectral response beyond the GaAs band-edge. Nevertheless, almost the same QE at 400 – 500 nm as the reference cell suggests that photo-excited electrons can be quite efficiently transported once they are accelerated by the electric field that exists beneath the p-region even though the electric field in the 50-period SL is only slight. In this sense, electric field in the i-region should be designed to be present in the upper area rather than the bottom area since carriers are generally photo-excited from the upper region of the cell.
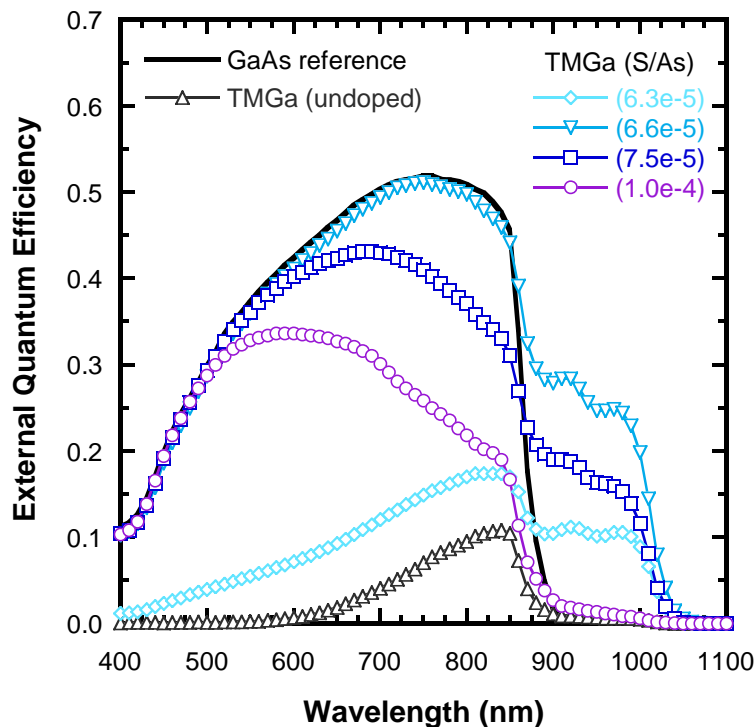
Fig. 6-16   EQE of GaAs p-on-n cells including 50-period SLs grown using TMGa at 530 °C with sulfur doping at various S/As ratios. Spectrum for a GaAs reference cell is shown together.

Fig. 6-17 (a) shows I-V characteristics under AM1.5 illumination for the cells grown at different S/As ratios. S-doping significantly enhanced the photocurrent by making the carrier transport efficient. The compensation-doped cell at S/As of 6.6×10^{-5} showed higher current density than the GaAs reference cell by extracting the carriers that were additionally excited in the SL. Other SL cells which did not satisfy the compensation doping condition exhibited lower current than the reference cell, and the photocurrent were not recovered even at reverse bias up to -3 V. As shown in the Fig. 4-28, applying a strong reverse bias in an undoped cell could recover the current to a level equivalent to a compensation-doped cell if the background carrier concentration was as low as 5×10^{15} cm^{-3}. For the low-temperature grown samples, however, the depletion region did not expand to the entire SL-region as illustrated in Fig. 6-15 (a) and (c) because of the too high background doping. Therefore, applying reverse bias only strengthens the electric field within the narrow depletion region, and cannot improve the transport efficiency of the carriers photo-excited in the neutral regions. In other words, in a p-p-n structure with insufficient S-doping, there existed a dead zone above the depletion region where photo-excited carriers can never be collected even at strong reverse bias. The zone beneath the depletion region was similarly dead in a p-n-n structure with excessive S-doping.
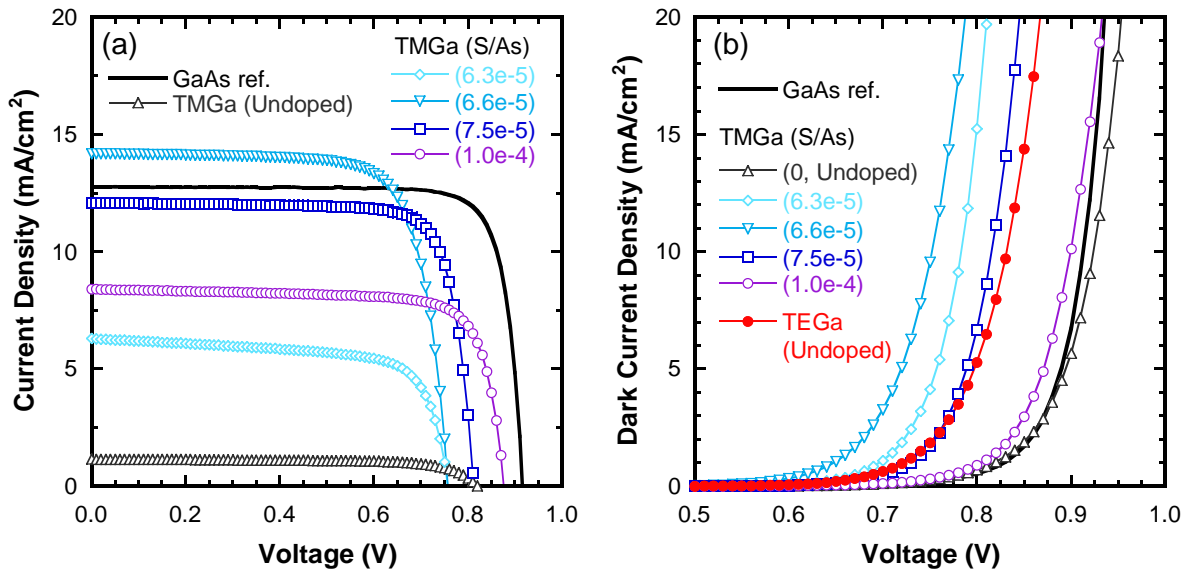
Fig. 6-17   (a) I-V characteristics under AM1.5 illumination and (b) dark current density of GaAs p-on-n cells including 50-period SLs grown using TMGa at 530 °C with sulfur doping at various S/As ratios. Dark current for the SL cell grown with TEGa without S-doping is shown together.

In Fig. 6-18, the open circuit voltage (V_{oc}) and the short circuit current (J_{sc}) for SL cells grown with TMGa are plotted as functions of S/As ratio, with additional data for S/As of 5.0×10^{-5}. J_{sc} and V_{oc} values for the GaAs reference cell are clarified together with arrows on the *y*-axes. As sulfur doping

concentration increased, V_{oc} became lower and recorded the minimum under the compensation doping condition (S/As = 6.6×10^{-5}), and then became higher again with excessive S-doping. In the simplest equivalent circuit model, V_{oc} can be regarded as the voltage at which the dark current approximately matches the photo-current obtained by the extraction of the photo-excited carriers. Therefore, larger dark current reduces V_{oc} in principle. For a diode including a SL in the i-region, the main contributing process for the dark current is non-radiative recombination in quantum wells, which is dominant in the depletion region where the electron concentration and the hole concentration are comparable. Fig. 6-17 (b) shows the dark current around the V_{oc} for each photovoltaic device. In the undoped SL(TMGa)-cell and the excessively doped cell with S/As of 1.0×10^{-4}, the depletion regions are much narrower than the entire thickness of the SL-region, and the quasi-Fermi levels in the SL-region cannot be split. Therefore, recombination in the SL does not take place efficiently, and consequently, the dark current remains low at forward bias. As the depletion region is expanded to the entire SL-region with counter sulfur doping closer to the carbon background level, the dark current increases due to the recombination in the i-region. This explains why the V_{oc} takes the minimum under compensation doping condition. Needless to say, lower photocurrent also decreases V_{oc} even if the dark current is small. In comparison between the cells doped at S/As of 6.3×10^{-5} (insufficient doping) and 6.6×10^{-5} (compensation doping), for example, the former device showed a smaller J_{sc} due to the thicker dead region above the SL while its dark current was lower because of the narrower depletion region, resulting in similar V_{oc} obtained by the two cells.
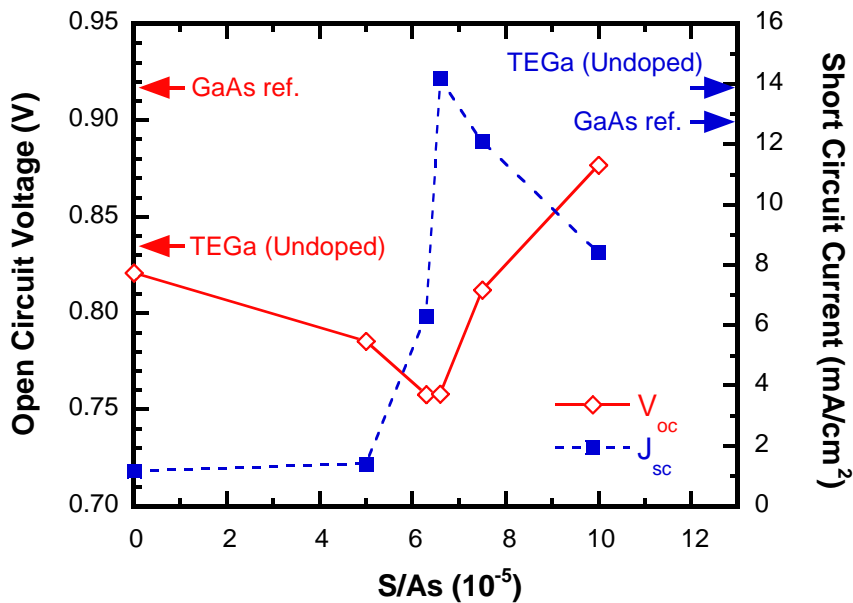
Fig. 6-18   Short circuit current (J_{sc}) and open circuit voltage (V_{oc}) of SL-cells grown with TMGa under AM1.5 illumination as functions of S/As ratio.

6.4.2 Low temperature grown SL cell using TEGa

Use of TEGa as the gallium source is expected to reduce the background carbon incorporation in SL by suppressing CH_3 production. Fig. 6-19 shows carbon profiles in the 50-period SL cells grown either TMGa or TEGa, which were obtained by SIMS measurement. Using TMGa, the measured carbon concentration in the SL grown at 530 ℃ was as high as 2×10^{18} cm^{-3} while it was below the detection limit of 4×10^{15} cm^{-3} for the bulk GaAs region grown at 610 ℃. A reason for the large mismatch between the carbon level in the SL measured by SIMS and the p-type carrier concentration measured by Hall measurement is that the atom concentration in the Fig. 6-19 was calculated by using sensitivity coefficient of GaAs for the entire depth. Although the absolute value of the carbon profile should not be accurate for this reason, it is obvious that the carbon incorporation becomes far more significant by lowering the temperature from 610 ℃ to 530 ℃ using TMGa. By using TEGa for the SL growth at even lower temperature of 520 ℃, the carbon level was greatly suppressed to below the detection limit.
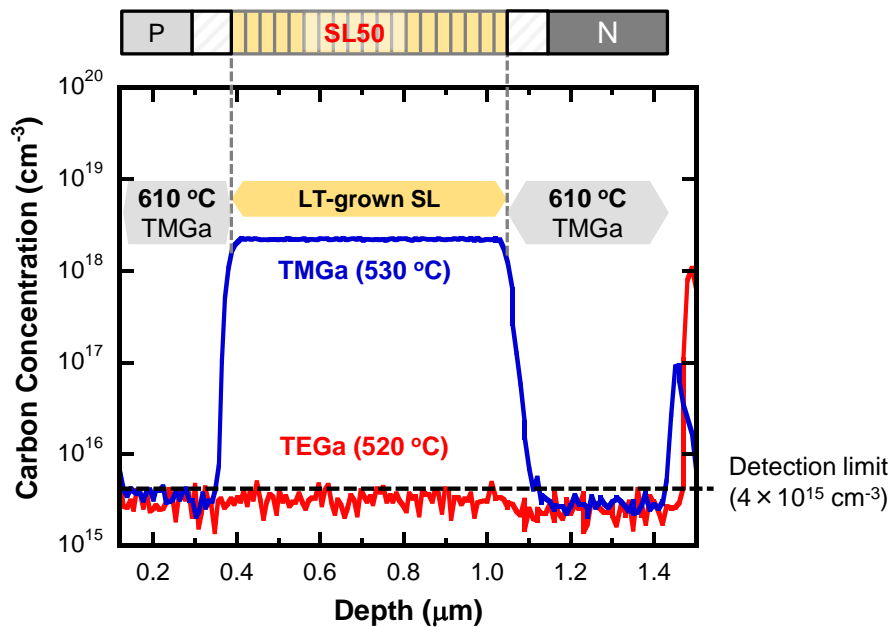
Fig. 6-19   Carbon profiles in GaAs pin cells including 50-period SLs grown at low temperature with either TMGa or TEGa measured by SIMS. The atom concentration was calculated using the sensitivity coefficient for GaAs.

Fig. 6-20 shows I-V characteristics and QE of the SL cells grown using TEGa with/without sulfur doping, which are called sulfur-doped/undoped SL(TEGa)-cell hereafter, respectively. Just substituting TMGa with TEGa significantly improved the photovoltaic properties of the undoped-SL devices, in

particular enhancing the J_{sc} from 1.2 mA/cm^2 to 13.8 mA/cm^2. Compared to the compensation-doped SL(TMGa)-cell, V_{oc} was substantially higher while J_{sc} became slightly lower as indicated by arrows on the *y*-axis in the Fig. 6-18, and the resultant AM1.5 efficiency was improved from 8.1% to 8.4%. The more abrupt QE edge for the SL(TEGa)-cell was due to the suppressed layer undulation in the SLs and hence steeper absorption edge. The photo-current of undoped SL(TEGa)-cell was saturated to an equivalent level to the compensation-doped SL(TMGa)-cell approximately at -1 V. As forward bias was applied, however, the photo-current gradually decreased, showing an apparent slope at 0 V in the I-V curve. This resulted in a lower FF in SL(TEGa)-cell than in the compensation-doped SL(TMGa)-cell.
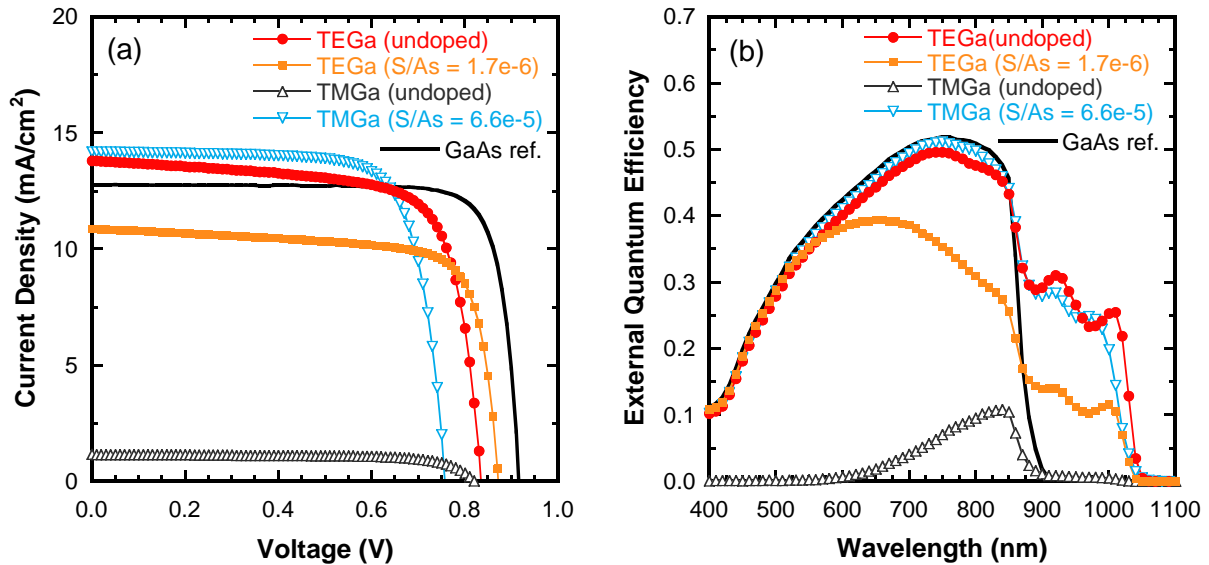
Fig. 6-20　(a) I-V characteristics undr AM1.5 illumination and (b) EQE spectra for 50-period SL cells in comparison between growth with TEGa and TMGa. For the case of TMGa, results for the undoped cell and the compensation doped cells are shown.

Gradual decrease in photo-current and hence degraded FF in the undoped SL(TEGa) cell indicates insufficient carrier collection at forward voltage. To inspect the underlying problem in carrier transport, CCE was examined by normalizing EQE to the saturated spectrum at reverse bias. Both compensation-doped SL(TMGa)-cell and undoped SL(TEGa)-cell showed saturation of QE at reverse bias with good agreement in spectra with the reference cell in the GaAs absorption wavelength range, indicating that both SL-regions were well-depleted and that 100% carriers were collected at reverse bias. Note that reliable estimation of CCE was impossible for the other devices since the band flattening effect narrowed the active region and the QE did not show recovery at reverse bias with much lower value than the reference cell. Fig. 6-21 shows CCE spectra at 0.6 V for the

compensation-doped SL(TMGa)-cell, the undoped SL(TEGa)-cell, and the GaAs reference cell. While the reference cell could extract almost all the carriers with high CCE over 99%, the two SL-cells showed degraded CCE, meaning that the photo-generated carriers were partly lost via recombination at forward bias. Nevertheless, the compensation-doped SL(TMGa)-cell showed CCE over 95% in the entire spectrum, indicating quite efficient carrier transport through the 50-period SL. On the other hand, the CCE of SL(TEGa)-cell showed apparent deterioration at shorter wavelength, becoming below 90% at 400-500 nm while remaining over 95% beyond the GaAs band-edge. This indicated that both electrons and holes were efficiently transported when excitation takes place in the SL, but the transport of electrons generated in the top p-region is less efficient, a result suggesting that the background doping of the i-region is p-type as discussed above. Although the reason for the incomplete removal of p-type background doping even with substitution of TMGa with TEGa is unknown exactly, a possible origin is TMIn as the indium source, which produces methyl radicals during its decomposition in the vapor phase. Nonetheless, the background carrier level in SL(TEGa)-cell was sufficiently reduced to deplete the entire i-region so that the carriers were well collected at reverse bias, while in the undoped SL(TMGa)-cell, most part of the i-region became a neutral p-region and acted as a dead-region.
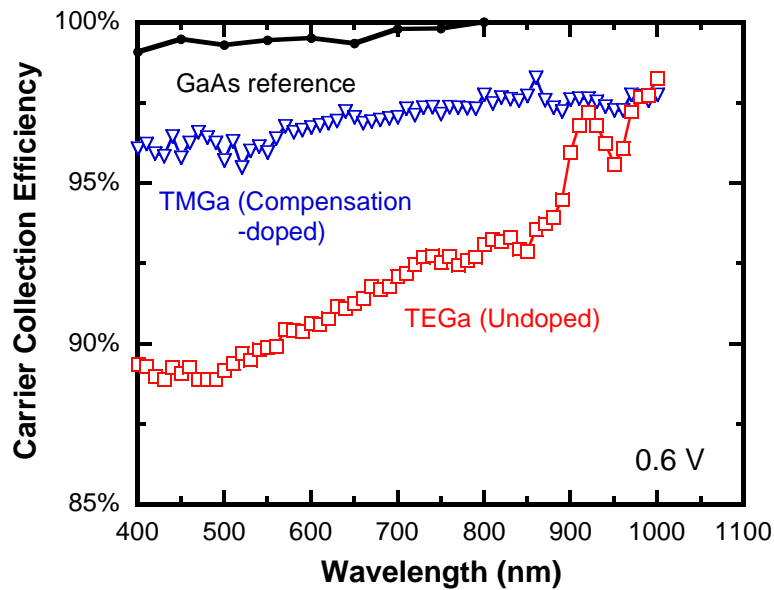
Fig. 6-21 Carrier Collection Efficiency (CCE) spectrum at 0.6 V evaluated for compensation-doped SL(TMGa)-cell, undoped SL(TEGa)-cell, and the GaAs reference cell. CCE was calculated by normalizing the bias dependent QE to the saturation spectrum at reverse bias.

The higher V_{oc} obtained by the undoped SL(TEGa)-cell compared to the compensation-doped SL(TMGa)-cell was not due to the band-flattening effect, i.e., decrease of dark current by the slight

p-type background as discussed earlier, but it would be attributed to better crystal quality brought about by the use of TEGa. Indeed, the SL(TEGa)-cell exhibited an even lower dark-current than other cells grown with TMGa in which the depletion regions were much narrower, e.g. S-doped SL(TMGa)-cell at S/As of 6.3×10^{-5} cm^{-3} where the sulfur doping was insufficient to cancel out the p-type background doping (see Fig. 6-17 (b)). The probable reason for the enhancement of V_{oc}, therefore, is suppression of the dark current owing to reduction of the density of defects that act as recombination centers by using TEGa, which enables stable mass-transport limited growth even at low temperature below 550 ^{o}C.

As so far discussed, it is now clear that simply substituting TMGa with TEGa for low-temperature MOVPE of InGaAs/GaAsP SLs can significantly enhance the cell performance by suppressing carbon background doping to make the photocurrent extraction efficient as well as improving the crystal quality to reduce the dark current. In order to further improve the cell performance of the undoped SL(TEGa)-cell, it is necessary to suppress the degradation of FF due to the reduced CCE at forward bias by making the carrier transport efficient, in particular considering that the period number of the SL used in the section is only 50, and that it is desired to be more increased for practical application. However, compensation doping treatment in the SL(TEGa)-cell was found to be not straightforward for this aim because the background carbon level is so low as shown in the Fig. 6-19 that only slight injection of sulfur makes the i-region strongly n-type doped.

The I-V under AM1.5 illumination and EQE of the sulfur-doped SL(TEGa) cell, for which H$_2$S was supplied for the i-region at S/As of 1.7×10^{-6} are shown together in Fig. 6-20. Although the sulfur was injected at minimum controllable level with partial pressure of 1.0×10^{-5} Pa, the photovoltaic performance was severely deteriorated compared to the undoped cell. The obvious degradation of QE at longer wavelength is a clear indication of excessive n-doping and hence flattened band-lineup for the bottom part of the i-region. Narrowing of the depletion region with thick dead zone expanded from the bottom n-region was also indicated by the unsaturated photo-current at reverse bias up to -3 V as well as the larger V_{oc} resulted from reduction of diode current compared to the case without sulfur doping.

All the results above led us conclude that an appropriate design of the SL structure alone should be more realistic approach to improve the carrier transport rather than performing compensation doping for the case of growth using TEGa. The devices used in this section were prepared under strain balance condition with 5-nm-thick barriers, and thus further enhancement in cell performance is surely expected by thinning the barriers below 3 nm. As already seen in Fig. 6-13, use of TEGa has been proved to be advantageous for growing high quality SLs under strain unbalance condition owing to the stable growth regime at low temperature. Implementation of STSL with thin barriers by using low temperature growth of TEGa, therefore, should be a reasonable pathway to achieve high efficiency SL solar cells on vicinal substrates.

6.5 Summary of chapter 6

In this chapter, low temperature MOVPE of InGaAs/GaAsP SLs on vicinal substrate was developed using TEGa, aiming at practical implementation of SLs into Ge based multi-junction solar cells. Below is the summary of this chapter.

- SLs grown on vicinal substrates tend to be undulated due to formation of step bunching. Lowering the growth temperature to shorten the diffusion length of the adatom is effective to suppress the layer undulation, but too low temperature may lead to detrimental effects such as low crystal quality ad high impurity incorporation.

- Using TMGa as the gallium source, lattice relaxation due to large step-bunching formation was significantly prevented by lowering the growth temperature, and 100-period SLs were stably grown at 550-530 $^\circ$C. At lower temperature than 530 $^\circ$C, however, crystal degradation apparently occurred because of insufficient atom migration on the crystal surface, and thus the layer undulation could not be completely eliminated.

- The use of TEGa enabled 100-period SLs to be successfully grown at even lower temperature of 510 $^\circ$C owing to its efficient pyrolysis and hence mass transport limited growth. An extremely uniform SL with negligible formation of step bunching was confirmed by *in-situ* reflectance monitoring, *ex-situ* XRD, TEM, PL, and FTIR.

- Growth of compressively stepped-tunnel SL with thin GaAsP layers was found to be difficult using TMGa because of unstable kinetically-limited regime, but was made successful using TEGa.

- P-type background carbon doping level in the SL grown at 530 $^\circ$C with TMGa was found to be very high ($\sim 10^{17}$ cm^{-3} in bulk GaAs), and compensation doping with sulfur for efficient carrier transport required extremely precise control of the doping level. Furthermore, degradation of V_{oc} attributed to low crystal quality due to kinetically limited growth at 530 $^\circ$C was inevitable.

- Substitution of TMGa with TEGa reduced the carbon incorporation to below the detection limit of SIMS measurement, owing to its β-elimination reaction that does not produce methyl radicals. As a result, higher photovoltaic performance than the compensation-doped SL cell grown with TMGa was achieved without performing sulfur doping, in particular with enhancement in V_{oc} attributed to higher crystal quality.

7   Implementation of SL into N-on-P cells

In this chapter, an InGaAs/GaAsP SL solar cell with required photovoltaic properties for practical application for Ge-based tandem cells is demonstrated, on the basis of the proposed design principle for the quantum structure as well as the established growth technology on vicinal substrates in the previous sections. As mentioned in the chapter 1, the aimed target is to achieve higher N-on-P type cell performance than a GaAs reference cell, by incorporating a 100-period SL with bandedge extended beyond 1000 nm on 6°-off substrate. Toward this target, the effect of growth temperature and the layer undulation of the SL structure on the photovoltaic performance will be discussed in section 7.1, and then 100-period SL will be incorporated in an N-on-P type cell based on the optimization of the growth temperature.

7.1 Temperature optimization for SL growth using TEGa

As shown in the section 6.1, use of TEGa instead of TMGa enables low-temperature MOVPE of high-quality SL on vicinal substrates, in particular achieving extremely uniform layer deposition as well as preventing the incorporation of carbon impurity. Although the suppression of carbon incorporation and hence low background doping level is quite essential for SL solar cells, the structural uniformity of the SL does not necessarily mean that it is beneficial for the photovoltaic performance.

Probable advantages and disadvantages for uniform SLs grown at low temperature and undulated SLs grown at high temperatures are summarized in the Fig. 7-1.

(1) Uniform SL grown at low temperature
- The growth is stable and well controlled because the individual periods of the SL are identical. Too low temperature, however, degrade the crystal due to insufficient migration of the adatoms on the terrace surface.
- The light absorption is efficient because the InGaAs well regions can cover the entire surface by layer-by-layer deposition. The uniform SL structure makes the excitonic absorption peak sharper and the absorption edge steeper.
- Carriers are transported in a manner proposed in chapter 5; thermally excited carriers in the upper state in the well tunnel through the GaAsP barrier layers, for which the thickness is uniform in the

lateral direction.

- Lower growth temperature is more likely to induce crystal defects that act as nonradiative recombination centers due to shorter atom migration length on the crystal surface. This may lead to higher probability for recombination loss of the photo-excited carriers.

(2) Undulated SL grown at high temperature

- Formation of too large step bunching cause lattice relaxation and hence severe crystal degradation. Even with moderate layer undulation, the amplitude of the thickness modulation becomes larger with the stack of SL, thus leading to higher risks for lattice distortion for growth of a large number periods.
- Poor in-plane coverage of the three-dimensionally grown InGaAs region decreases the light absorption beyond the GaAs band-edge. The lateral thickness variation broadens the exciton peak and makes the absorption edge red-shifted and less abrupt.
- Unless lattice relaxation is induced by formation of too large step bunching, higher growth temperature makes the kinetic reactions on the surface faster and more complete and thus reduces crystal defects.
- Lateral thickness variation for the GaAsP layers may enhance tunnel transport of the carriers through thin barrier regions

Because of these potential trade-offs, the effect of growth temperature and structural uniformity of the SL on the photovoltaic performance of InGaAs/GaAsP SL solar cells on vicinal substrates must be investigated.
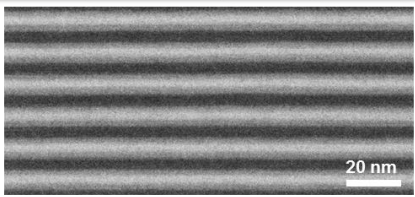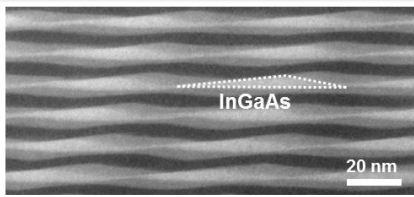
	Uniform SL at low T		Undulated SL at high T	
Growth	🙂	Well controlled, stable growth (if migration is sufficient)	☹️	Lattice relaxation at too high temperature
Light absorption	🙂	High absorbance in layer-by-layer grown InGaAs regions	☹️	Poor coverage of InGaAs wells (3D growth with bunched steps)
Carrier transport	☹️	Recombination loss due to high defect density	🙂	Tunnel transport through thin barrier regions

Fig. 7-1   Advantages and disadvantages of a uniform SL grown at low temperature and an undulated SL grown at high temperature in terms of photovoltaic application.

■ **Experiments**

(1) GaAs pin solar cells including 50-period $In_{0.30}Ga_{0.70}As$ (3.4 nm)/GaAs (2.7 nm)/$GaAs_{0.60}P_{0.40}$ (3.0 nm) /GaAs (2.7 nm) SLs were grown on GaAs substrates with orientation (0 0 1) 6°-off towards [1 1 1] direction at a reactor pressure of 10 kPa. The device structure is shown in Fig. 7-2. The top p-emitter and the bottom n-base were grown using TMGa at 610 °C, and the SL regions were grown using TEGa at various temperatures (490, 500, 510, 520, 530, 550 °C). Because of the thin GaAsP barrier layers to facilitate tunnel transport, the net compressive strain of the SL was 2560 ppm. Note that the counter doping with sulfur was not performed during the low-temperature growth for the SL-region. A GaAs reference cell with an 800 nm i-region, which was grown at 610 °C using TMGa, was also prepared for comparison.

(2) *In-situ* reflectance measurement was carried out during MOVPE at wavelength of 443 nm. The structural uniformity of the grown SL was evaluated by *ex-situ* XRD-RSM around (004) diffraction point and FTIR.

(3) All the grown samples were processed into solar cell devices with Au and Ti/Au contacts deposited on the back and the front side, respectively. The back Au electrodes were annealed at 330 °C for 5 min in N_2 ambient prior to the deposition of the top electrode. The highly-doped p-GaAs layers above the InGaP window layers were removed by wet etching. Photovoltaic properties were measured using filtered AM1.5 (> 665 nm) for current-voltage measurement to evaluate middle cell performance (assuming cell operation beneath InGaP top cells). The QE was measured with 2.5 mW/cm^2 monochromatic light under AM1.5 bias illumination.
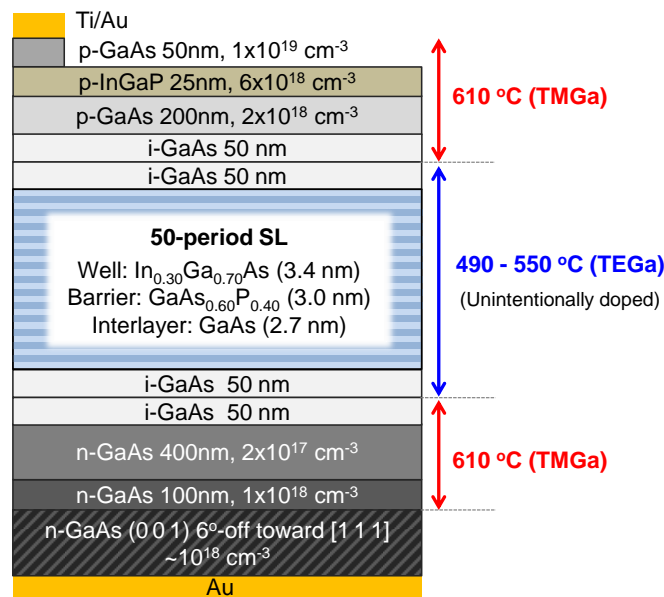
Fig. 7-2   Schematic of P-on-N GaAs solar cells with incorporation of 50-period SLs grown at different temperatures.

7.1.1 Thickness modulation in SL grown with TEGa

Fig. 7-3 shows the time transient DC reflectance during growth of 50-period SLs at various temperatures (490 – 550 °C). Critical lattice relaxation and hence crystal degradation was assumed to occur with decrease of the average reflectance as indicated with arrows in the graph. The longer growth time for 50-period at lower temperature is due to lower growth rate for the same SL structure. The reduction of the growth rate, however, was only 5% from 530 °C to 510 °C, and thus the temperature dependence is much smaller than the case with TMGa for low temperature growth as seen in Fig. 6-7; using TMGa, the growth rate was reduced by 24% from 530 °C to 510 °C in the kinetically-governed regime. This is because the surface reaction is much faster at low temperature with TEGa and thus the growth is mostly mass transport limited regime, owing to its efficient pyrolysis and absence of alkyl-groups adsorbates on the surface. When the temperature was lowered from 510 °C to 490 °C, however, the growth rate was further reduced by 8% with larger temperature dependence, indicating that the effect of slower surface reactions gradually became apparent even using TEGa.
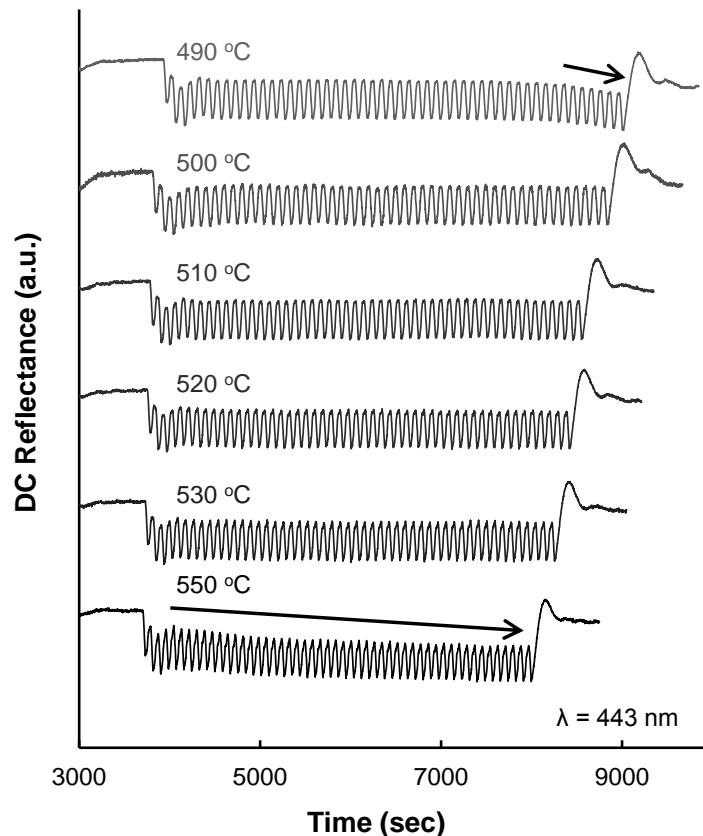
Fig. 7-3 *In-situ* monitored DC reflectance at wavelength of 443 nm during growth of 50-period SL regions at different temperatures. Apparent decrease of reflectance due to crystal degradation is indicated with arrows.

As can be seen in Fig. 7-3, SL growth at 550 ºC was not successful with the declining average reflectance due to the lattice relaxation induced by formation of too large step bunching at too high temperature. By lowering the temperature to suppress multi-terrace migration of the adatoms and thus to prevent formation of step bunching, 50-period SLs were stably grown at 530-500 ºC without apparent degradation in the reflectance. At even lower temperature of 490 ºC, however, the reflectance gradually decreased after the 40th period. This indicates the epitaxial crystal was deteriorated at too low temperature due to insufficient migration of adatoms as mentioned earlier, resulting in a quite narrow temperature range for successful growth of SLs on vicinal substrate using TEGa as well as TMGa. Although the results in the Fig. 7-3 should not be simply compared to Fig. 6-7 because the misorientation direction of the substrates is different between these cases, the temperature range for stable SL growth on 6º-off substrates seems lower for TEGa than for TMGa.

Fig. 7-4 shows XRD-RSM around (0 0 4) diffraction points recorded for the SLs grown at various temperatures. At 550 ºC, fringe pattern that could be attributed to SL structure was not observed, thus indicating that a periodic layer structure with controlled layer thicknesses was not formed due to the severe lattice relaxation. The decreasing reflectance from the beginning of the growth suggests that the layer stack was not coherent from the very initial stage of the growth of the 50-period SL.

By lowering the temperature to 530 ºC, a clear fringe pattern was obtained owing to the well-controlled periodic SL structure. The two dimensional fringe pattern was less clear at lower temperature because of the suppressed step bunching formation as can be seen in Fig. 7-4 (b)-(d). Accordingly, the peak intervals along the dotted line became wider at lower temperature with smaller periodicity for the thickness modulation: 65, 53, and 44 nm at 530, 520, and 510 ºC, respectively. The satellite spots aside the main fringe pattern became slight at 510 ºC but clearly observed, whereas they were completely diminished on a substrate misofforiented toward [1 0 1] direction as shown in Fig. 6-13. This would be attributed to the slight difference in the migration rate for crossing over the steps between the two different offcut directions: [1 0 1] and [1 1 1].

At 500 ºC, XRD peaks attributed to lateral periodicity completely disappeared and fringe patterns were obtained only along the vertical direction, indicating extremely uniform layer-by-layer SL structure. Therefore, the difference in the growth temperature to completely eliminate layer undulation between the two offcut directions was approximately 10 ºC, and thus the effect of offcut direction on the formation of step-bunching was found to be not so significant.

At further lower temperature of 490℃, however, severe distortion of the SL structure was confirmed by the broadened peaks around $(Q_x \times 10000, Q_y \times 10000) = (15, 7210)$ and $(5, 7125)$, as also suggested by the clear reflectance decrease during growth of the last 10-period.
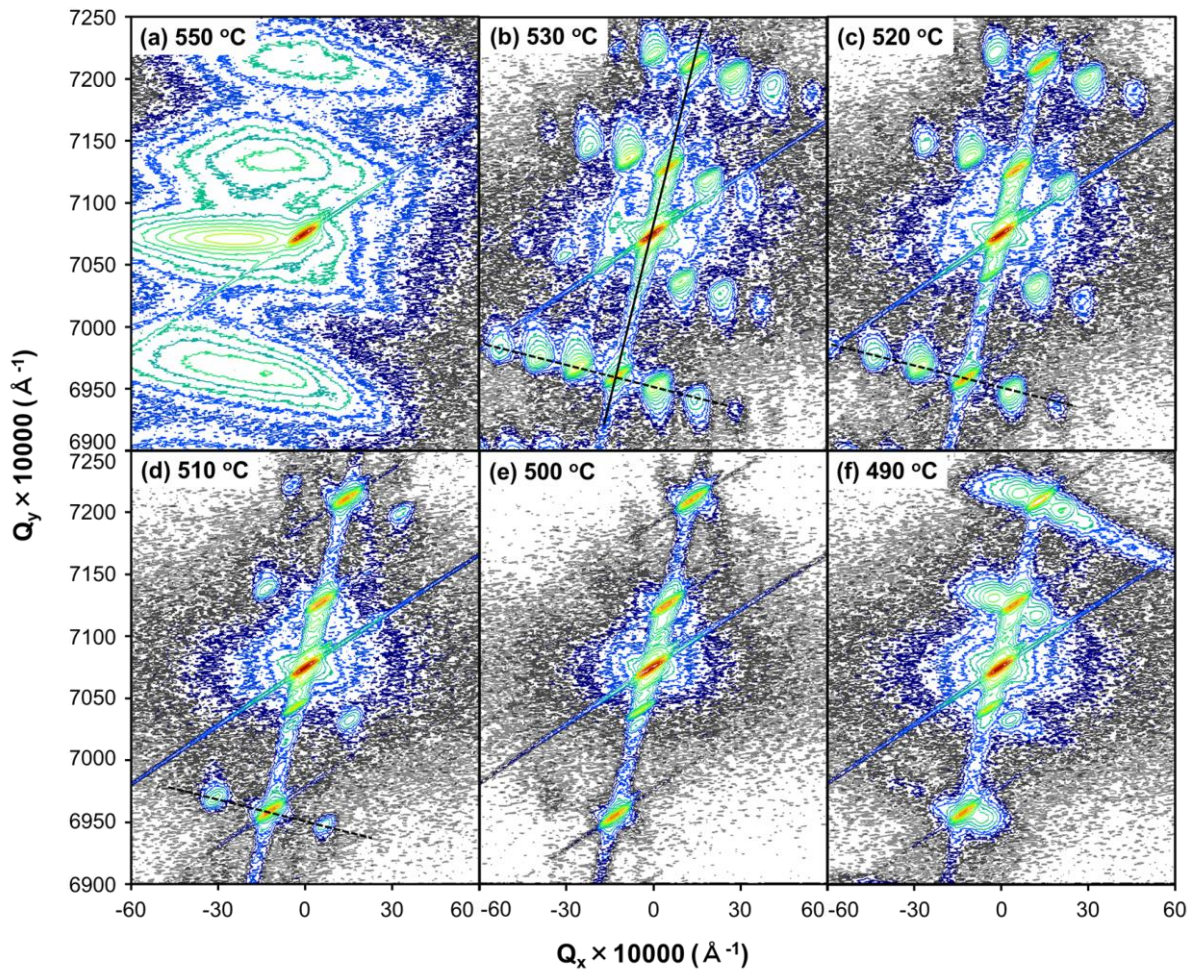
Fig. 7-4   XRD-RSM around the GaAs (004) diffraction point recorded for 50-period $In_{0.30}Ga_{0.70}As$ (3.4 nm)/GaAs (2.7 nm)/$GaAs_{0.60}P_{0.40}$ (3.0 nm)/GaAs (2.7 nm) SL solar cells at different temperatures: (a) 550 ℃, (b) 530 ℃, (c) 520 ℃, (d) 510 ℃, (e) 500 ℃, and (f) 490 ℃. The incident X-ray was directed toward the offcut direction of the substrates.

7.1.2 Effects of thickness modulation of SL on PV performance

Such large structural difference in the SL significantly influenced the photovoltaic properties, e.g. short circuit current density (J_{sc}), open circuit voltage (V_{oc}), fill factor (FF), and efficiency, all of which are summarized in the Fig. 3 as functions of the growth temperature. Note that the illuminated AM1.5 light was filtered by a long pass filter with cut off wavelength of 665 nm, and thus the efficiency was calculated using the filtered illumination power density of 514 W/m^2. Except for the result for 550 ℃, at which significant lattice relaxation degraded all the cell properties, the J_{sc} showed maximum at 510 ℃ whereas the V_{oc} and FF showed continuous improvement at higher temperature. The reason for each trend will be discussed hereafter.

155
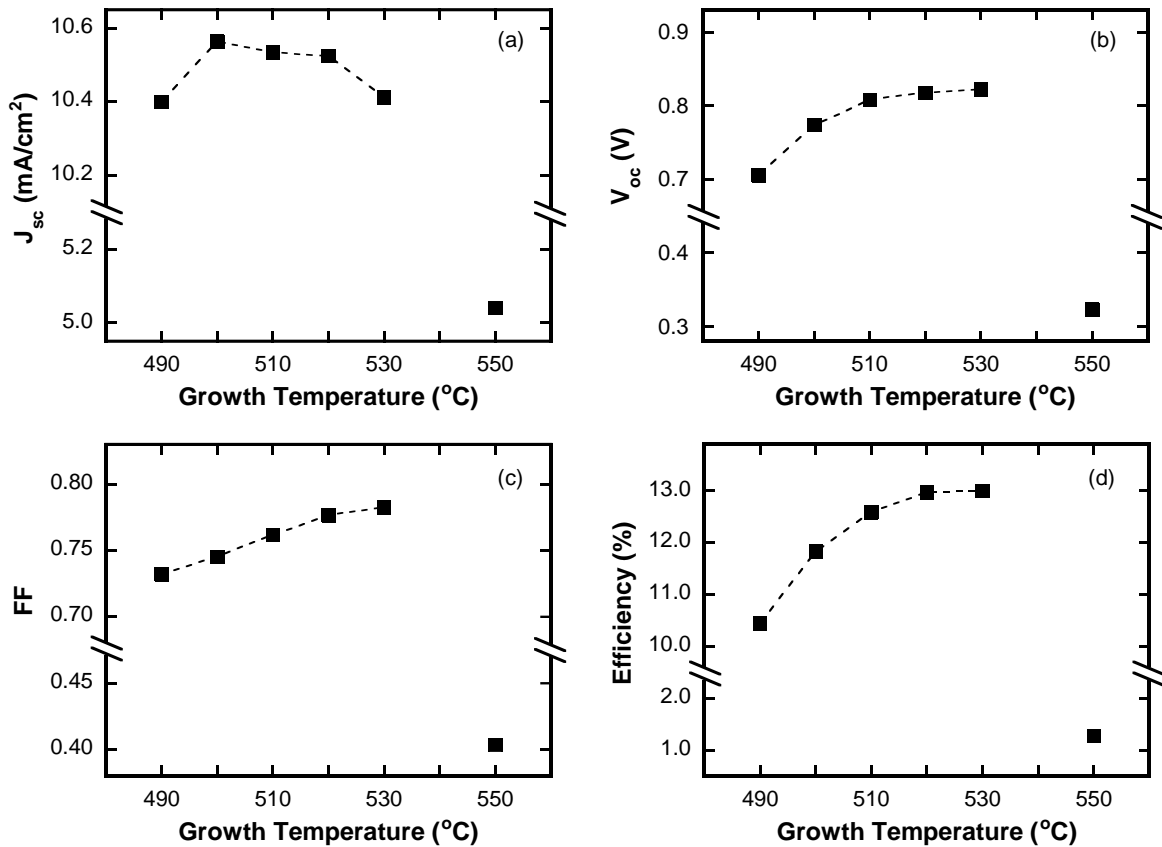
Fig. 7-5   Photovoltaic properties of the fabricated solar cells as functions of the growth temperature for the SL region. The cells were illuminated with AM1.5 filtered by a long pass filter (FGL665S, Thorlabs), which transmits approximately 90% of light beyond 665 nm. The efficiency was calculated with a filtered incident illumination energy of 514 W/m^2.

J_{sc} is determined by absorption of light and collection of the photo-excited carriers at 0 V. Fig. 7-6 shows the absorbance spectra beyond the GaAs band edge for the 50-period SLs grown at different temperatures. At 500 °C, a typical stepped spectrum representing the available quantum states was obtained with a sharp exciton peak for the 1e-1hh transition, owing to the very uniform multiple quantum wells with controlled thickness for the component layers. The trend in absorbance spectrum with respect to the growth temperature was similar to the case of TMGa shown in Fig. 6-12. As the SL was more undulated at higher growth temperature, the quantum energy levels became indistinguishable due to non-uniform thickness of the well regions, resulting in declining absorption tails with red-shifted spectrum edges: 1016, 1022, 1042, 1053, and 1065 nm for 500, 510, 520, 530, and 550 °C, respectively. Although obvious lateral undulation was confirmed by XRD-RSM for the growth at 510 °C, the absorbance spectrum showed a clear exciton peak, suggesting that the structural nonuniformity was slight. Nevertheless, the lower and broadened exciton peak compared to the case for 500 °C indicates non-negligible interface roughness. At 520 °C, the clear lateral thickness

modulation contributed additional light absorption in 1020 - 1050 nm, though it reduced the absorption in 970 – 1010 nm with extinction of the exciton peak around 1000 nm. Increase of the temperature to 530 ℃ further enlarged the amplitude of the thickness modulation, resulting in significant reduction of the absorbance in 950-1030 nm due to lower in-plane coverage of the thick InGaAs region as mentioned earlier. Increasing the temperature to 550 ℃ led to further lower absorbance, of which the spectrum continuously decreased toward the longer wavelength with no features attributed to the discrete quantum states.

As the absorption beyond the GaAs bandedge was reduced at higher temperature due to lower in-plane coverage of the InGaAs region, the J_{sc} accordingly became lower as can be seen in Fig. 7-5(a): 10.56, 10.53, 10.52, 10.41 mA/cm^2 at 500, 510, 520, and 530 ℃, respectively. For the case of 550 ℃, the significant recombination loss of the photo-excited carrier in the poor-quality crystals in addition to the low absorbance resulted in much degraded J_{sc} of 5.04 mA/cm^2.

The absorption edge for the SL grown at 490 ℃ was broader than at 500 ℃ with a less sharp exciton peak, in spite of the lower growth temperature. This should be attributed to the roughened interfaces due to the insufficient atomic migration at too low temperature as indicated by broadened satellite spots observed in the XRD-RSM. Although the absorbance spectrum remained almost equivalent to that for 510 ℃, the resultant J_{sc} for 490 ℃ (10.40 mA/cm^2) was apparently lower, meaning that the photo-excited carriers could not be sufficiently collected under short circuit condition due to the deteriorated crystal quality; the current density was recovered to 10.54 mA/cm^2 by applying reverse bias of -1 V. Consequently, the J_{sc} was the highest for the growth temperature of 500 ℃, at which the grown SL was the most uniform and thus the light absorption was the largest.
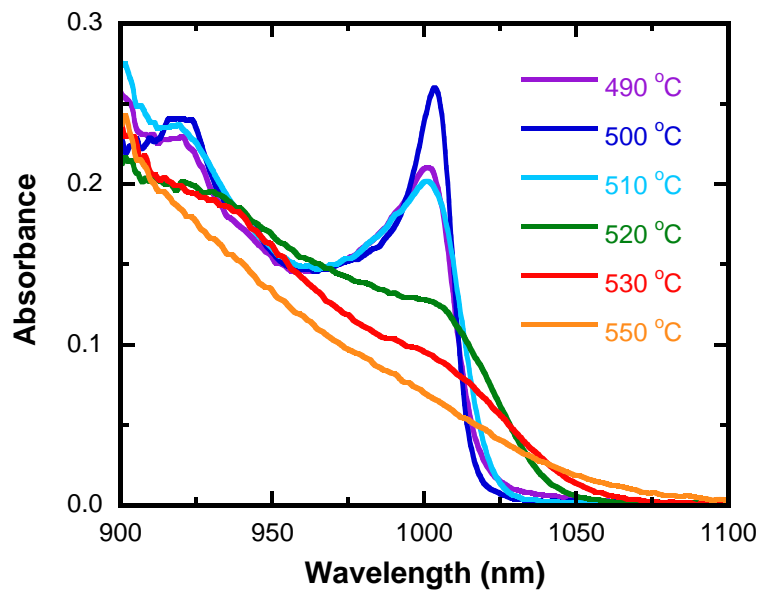
Fig. 7-6   Absorbance spectra of 50-period SLs on 6°-off substrates measured by FTIR for different growth temperatures. Absorbance of a GaAs substrate was used for the background spectrum.
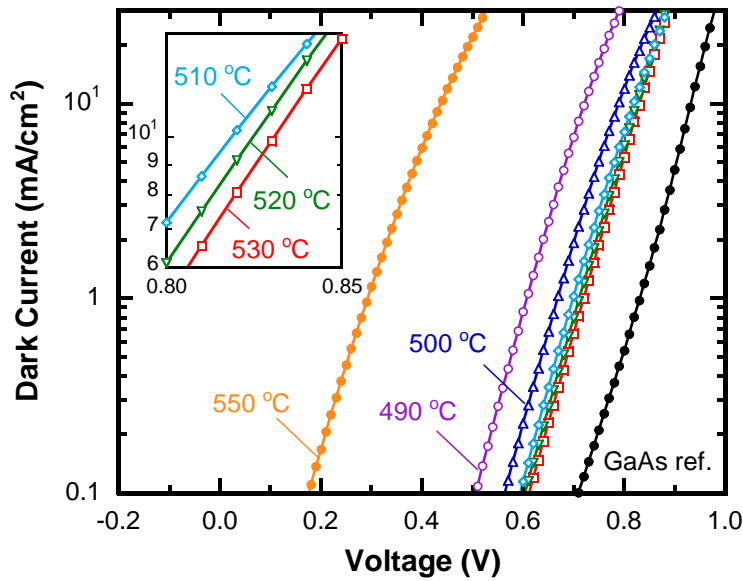
Fig. 7-7 Dark currents of the fabricated cells for different growth temperatures for the SL regions. Magnified plots around the V_{oc} for 510 – 530 °C are shown in the inset.

As has been discussed in the section 6.4, a most influential characteristic that determines V_{oc} is dark current; larger dark current reduces V_{oc} in principle. Fig. 7-7 shows the dark current of the SL cells for different growth temperatures. Note that the dark currents are plotted up to only 30 mA/cm^2 in the graph in order to focus on the correlation between the dark current and the V_{oc}. The SL cell grown at 550 °C showed extremely large dark current since the whole 50-period SL region was severely relaxed and thus high-density nonradiative recombination centers should be introduced. Similarly the cell grown at 490 °C exhibited comparatively high dark current because of the apparent crystal degradation as discussed above.

In the temperature range of 500 – 530 °C, at which the reflectance for the 50-period SL did not show apparent decrease, the dark current was higher at lower growth temperature. This is probably because the crystal defects are more likely to be introduced at lower temperature due to inefficient atom migration on the terrace surfaces, although the corrugation of the individual layers can be well suppressed. This result, therefore, gives us an important insight that the structural uniformity for the SL does not necessarily represent better crystal quality. In other words, unless critical lattice relaxation is induced by formation of too large step bunching as was seen for the growth at 550 °C, higher temperature should be favored for growth of high quality crystals owing to more complete surface reactions. In the temperature range of 490 – 510 °C, the influence of the kinetic processes on the growth rate became gradually apparent as discussed in the Fig. 7-3, and thus the degradation in the V_{oc} at lower temperature was significant: 0.706, 0.774, and 0.808 V for 490, 500, and 510 °C. At higher temperature of 520 – 530 °C, on the other hand, the growth regime was more mass-transport-governed

as indicated by the weaker temperature dependence of the growth rate, resulting in smaller difference in crystal quality and hence V_{oc}: 0.818 and 0.822 V at 520 and 530 °C, respectively. As a result, the V_{oc} showed continuous increase toward higher temperature from 490 to 530 °C with saturation around 530 °C, and severely dropped to 0.323 V at 550 °C due to crystal degradation with large step bunching.

In SL solar cells, *FF* is a good characteristic that indicates how efficiently carriers are collected under operational condition. If the carrier transport through the SL is inefficient, then the slope of the I-V curve becomes larger at higher forward bias due to weakened electric field in the i-region, resulting in lower FF. Fig. 7-8 shows the bias dependent CCE under filtered AM1.5 illumination of the SL cells grown at 490 – 530 °C, in which the illumination-induced current enhancement was all saturated at -1 V. As for the SL cell grown at 550 °C, CCE could not be evaluated since the current enhancement was not saturated at reverse bias due to the too much degraded crystal quality.

Although all the cells recorded high CCE over 98% under shot circuit condition, the superiority for higher temperature was obviously observed at forward bias. The probable reason is twofold. First, the crystal quality is improved at higher growth temperature as already mentioned with respect to the reduced dark current; the crystal defects where the photo-excited carriers are likely to be lost should be reduced. For this reason, the cell grown at the 490 °C, which exhibited clear crystal degradation in the time-transient reflectance and the XRD-RSM, showed particularly low CCE at 0 V. This resulted in significant reduction in J_{sc} in comparison with the cases of 500-530 °C as shown in Fig. 7-5 (c). Second, the larger thickness modulation at higher growth temperature forms the region where GaAsP barriers are thin, through which the tunnel transport of the carriers is more efficient. The GaAsP is designed to be 3.0-nm-thick, but substantial improvement in CCE through the STSL-region was clearly observed by thinning the barriers from 4 to 2 nm in the Fig. 5-11.

In order to investigate whether the undulated layers enhance tunnel transport, CCE for the case of 530 °C was further compared between a cell grown on an exact-oriented substrate and the one grown on a misoriented substrate; the layer thickness is uniform in the former cell whereas it has large lateral variation in the latter cell. Since both SLs were grown at the same temperature, the crystal quality with respect to the defect density should be equal or possibly lower on a vicinal substrate because the growth is more unstable due to formation of step-bunching. The result of CCE for the cell on the exact-oriented substrate is shown together in the Fig. 7-8. Comparison of the bias dependence of CCE between the two cells clearly revealed that the carrier transport was efficient for the SL cell on the vicinal substrate; CCE over 99% was preserved up to 0.6 V on a vicinal substrate whereas it showed continuous declination on a just-oriented substrate. This suggests that the tunnel transport of the carriers is indeed enhanced in thickness-modulated SLs on vicinal substrates. Compared to the SL-cell grown at 500 °C on a vicinal substrate, the SL cell grown on the exact-oriented substrate at 530 °C showed almost equivalent CCE up to 0.4 V, indicating similar carrier transport behavior through the layer-by-layer SLs with uniform thickness. The SL-cell grown at 500 °C, however, showed more rapid degradation of CCE beyond 0.4 V, which is probably attributed to lower crystal quality due to the lower growth temperature.

CCE at the maximum power output voltage (V_{max}) is an important property that represents how the solar cell performs well under operation in terms carrier transport, and it primarily affects *FF* in the I-V characteristics. V_{max} for the SL cells were higher at higher growth temperature: 0.57, 0.63, 0.67, 0.68, and 0.69 V for 490, 500, 510, 520, and 530 °C, respectively, and thus the electric field in the i-region at V_{max} was weaker at higher temperature. Nevertheless, the CCE at V_{max} was improved at higher temperature because of the two reasons mentioned above, resulting in higher *FF*; the CCE at V_{max} were 93.6%, 95.2%, 96.5%, 97.8%, and 98.1%, and the resultant *FF* were 0.732, 0.745, 0.762, 0.777, and 0.783 for 490, 500, 510, 520, and 530 °C, respectively. The *FF* for 550 °C was severely degraded to 0.404 because of deterioration of the crystal quality.
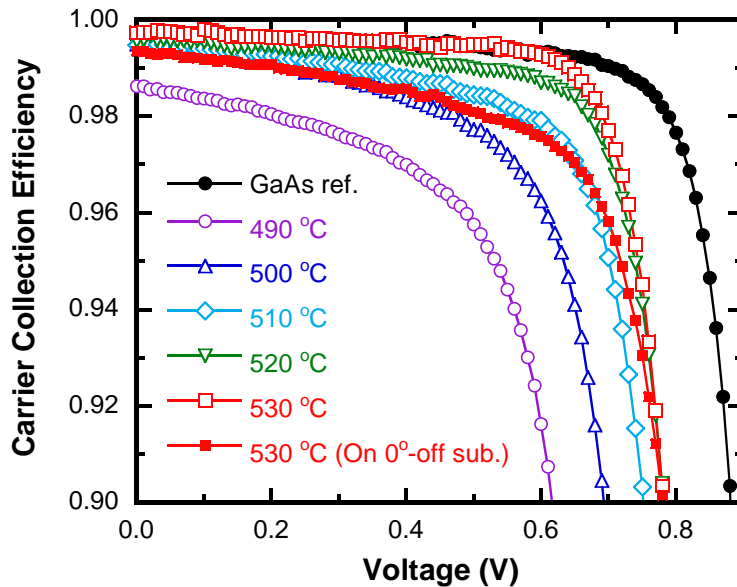
Fig. 7-8 Bias dependence of the carrier collection efficiency (CCE) under filtered AM1.5 illumination (> 665 nm) for the GaAs reference cell, and the SL cells for different growth temperatures for the SL regions. For 530 °C, a result of a SL cell grown on an exact oriented substrate is shown together for comparison.

As experimentally revealed above, SL solar cells grown on vicinal substrates has a tradeoff among the photovoltaic properties; lower growth temperature to enable layer-by-layer growth of more uniform SLs can improve the in-plane coverage of the InGaAs region and hence J_{sc}, whereas higher growth temperature enhances V_{oc} and *FF* owing to better crystal quality as well as more efficient tunnel transport through thickness-modulated barriers. As a result, the energy conversion efficiency was improved with the temperature from 490 to 510 °C and recorded a maximum of approximately 13.0% at 520-530 °C. Further increase of the growth temperature to 550 °C degraded all the photovoltaic parameters, and consequently dropped the efficiency to 1.3%.

7.2 N-on-P structure solar cell with 100-period SL

In typical Ge-based multi-junction solar cells, N-on-P structure is favorably chosen rather than P-on-N type. Therefore, the InGaAs/GaAsP SL cell should be N-on-P structure for practical application. Toward this aim, a GaAs nip cell with incorporation of 100-period SL was fabricated here, based on the temperature optimization carried out in the previous section.

■ **Experiments**

(1) An N-on-P GaAs solar cell including a 100-period $In_{0.30}Ga_{0.70}As$ (3.4 nm)/GaAs (2.7 nm)/$GaAs_{0.60}P_{0.40}$ (2.5 nm)/GaAs (2.7 nm) SL was grown on a p-type GaAs substrate with orientation (0 0 1) 6º-off towards [1 1 1] direction at a reactor pressure of 10 kPa. The device structure is shown in Fig. 7-9. The top n-emitter and the bottom p-base were grown using TMGa at 610 ºC, and the SL region were grown using TEGa at the optimized temperature of 520 ºC. Since sufficient light absorption beyond the GaAs absorption-edge is essential, 520 ºC was chosen for the SL growth rather than 530 ºC, though both temperature resulted in similar efficiency as shown in Fig. 7-5. Considering that the carrier transport in the SL grown at 520 ºC was slightly less efficient than at 530 ºC due to the smaller thickness modulation, the GaAsP barrier layers were further thinned to 2.5 nm. Note that the counter doping with sulfur was not performed during the low-temperature growth for the SL-region. A GaAs reference cell with an 1330 nm i-region, which was grown at 610 ºC using TMGa, was also prepared for comparison.

(2) *In-situ* reflectance measurement was carried out during MOVPE at wavelength of 443 nm. The periodic layer structure of the grown SL was evaluated by *ex-situ* XRD-RSM around (0 0 4) diffraction point.

(3) The epitaxial layers were processed into solar cell devices with Ag (8 nm)/Au (350 nm) and Au (500 nm) contacts on the back and the front side, respectively. The Ag/Au rear electrodes were deposited by thermal evaporation and the Au front electrodes were deposited by EB-evaporation. Annealing was not performed for the metal. The highly-doped n-GaAs layers above the InGaP window layers were removed by wet etching ($NH_3 : H_2O_2 : H_2O = 1 : 1 : 100$).

(4) Photovoltaic properties were measured using filtered AM1.5 (>665 nm) for current-voltage measurement to evaluate middle cell performance. The QE and CCE was measured with 2.5 mW/cm^2 monochromatic light under AM1.5 bias illumination.
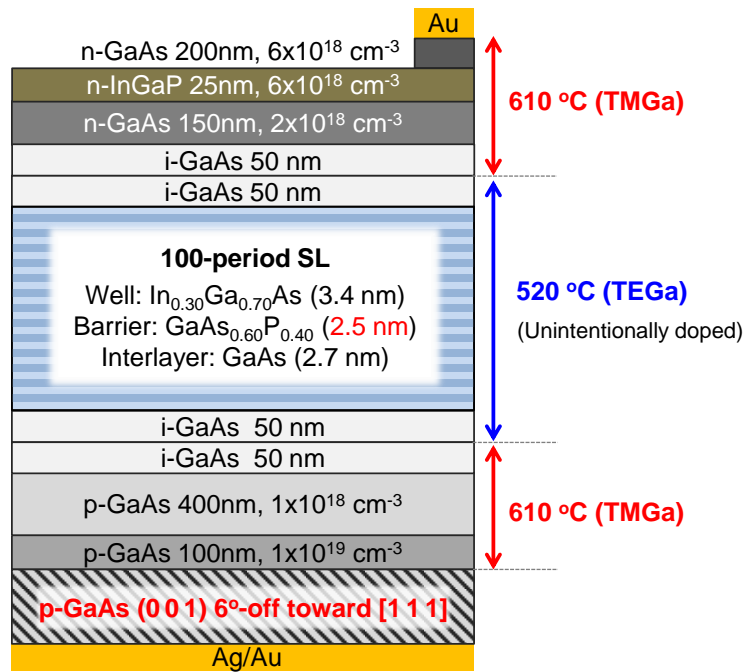
Fig. 7-9   Structure of an N-on-P GaAs solar cell with 100-period InGaAs/GaAsP SL on a 6°-offoriented substrate

■ **Results and discussion**

Because of the further smaller thickness of the GaAsP barriers of 2.5 nm and larger period number of 100 than the series samples prepared in the previous section, the SL structure in Fig. 7-9 was far more challenging. Nevertheless, the stability of the growth of the SL-region and the resultant thickness-modulated SL structure was good as shown in the Fig. 7-10. The average DC reflectance during the SL growth at 520 °C was completely preserved for the entire 100 periods, indicating no apparent crystal degradation was brought about even for the growth of such a thick SL with large net compressive strain (3300 ppm).

The XRD-RSM around $(0\,0\,4)$ diffraction point for the SL100-cell showed a quite similar feature of the fringe pattern as the 50-period SL grown at the same temperature of 520 °C with 3.0-nm-thick GaAsP layers, for which the RSM is shown in the Fig. 7-4(c). Except for the shift of the entire fringe pattern to -Q_y direction due to the smaller GaAsP thickness of 2.5 nm for the SL100 cell, the distribution and the intensity of the satellite peaks that represent the periodic lateral thickness modulation, which are aligned aside the main fringe pattern, were almost unchanged. The estimated lateral periodicity was 54 nm, which well agreed with 53 nm obtained for the 50-period SL. This suggests that the formation of layer undulation and the resultant modulation amplitude are not significantly affected by slight change in the GaAs P layer thickness nor the period number from 50 to 100.
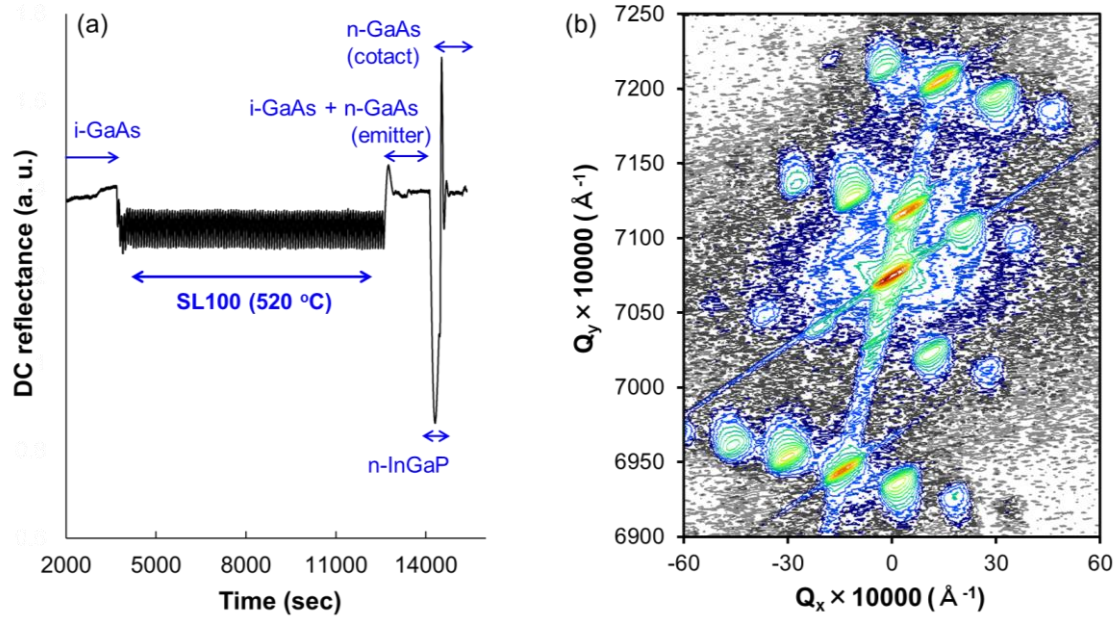
Fig. 7-10 (a) Time transient DC reflectance for the 100-period SL and the upper layers in the SL100-cell. (b) XRD-RSM around (0 0 4) diffraction point for the SL100-cell.

Fig. 7-11 shows the I-V characteristics under filtered AM1.5 illumination (> 665 nm) and the IQE of the SL100-cell and the GaAs reference cell, and their photovoltaic properties are summarized in the Table 7-1. Note that an anti-reflection coating was not applied, and the reflection was approximately 30% in the entire wavelength range. IQE was thus obtained by dividing the EQE by the reflectance spectra. By incorporating the SL, the band-edge wavelength was extended to approximately 1025 nm, which corresponds to a target bandgap of 1.21 eV. Since the SL was undulated at the growth temperature of 520 °C, the QE spectrum showed a long tail near the absorption edge with absence of clear exciton peaks. Nevertheless, the SL100 cell achieved 60-70% IQE in 850 - 1000 nm. The carrier transport through the SL was sufficient at 0 V, and thus almost equivalent QE to the reference cell was obtained in the GaAs absorption wavelength range, in which mismatch of the spectrum is often observed with poor carrier collection as was seen in Fig. 4-35 and Fig. 5-22. Consequently, the SL100 cell showed 1.38 times higher J_{sc} than the GaAs cell.

V_{oc} of the SL100 cell was substantially lower than that of the reference cell due to additional recombination current in the quantum wells. The difference in V_{oc} of 0.126 V, however, was much smaller than the difference in E_g/q (bandgap over elementary charge) of 0.21 V (1.42 V – 1.21 V), a phenomenon which was also observed for P-on-N type SL solar cells (Fig. 5-21). The V_{oc} under full AM1.5 illumination without the long pass filter were 0.826 and 0.944 V for the SL100-cell and the GaAs cell, respectively. It is often suggested that a single-junction soar cell can be generally regarded as a high-performance device if the bandgap-voltage offset ($W_{oc} = E_g/q - V_{oc}$) under 1 sun illumination is below 0.4 V [154]. The W_{oc} of 0.38 V for the SL100 cell, therefore, indicates the competitive

potential of InGaAs/GaAsP SL cells to a high-performance single junction device composed of the same bandgap materials. The comparatively low V_{oc} for the GaAs reference cell is attributed to the large light reflection without ARC, incomplete absorption in only 400-nm-thick p-GaAs base, and significant surface recombination due to unoptimized InGaP window layer as can be seen in the dropped QE in the short wavelength region in Fig. 7-11(b). Optimization of the host n-i-p structure, therefore, is expected to further enhance the V_{oc} of the SL cell as well.
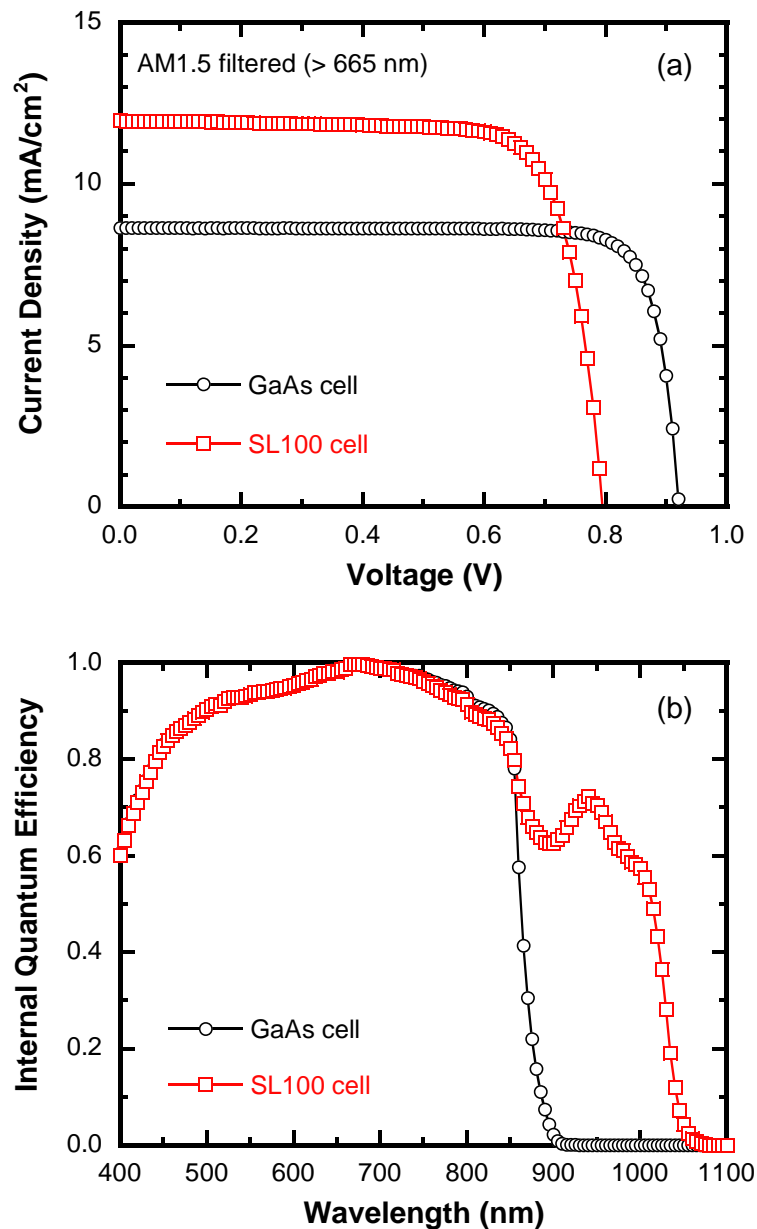

Fig. 7-11 (a) I-V characteristics under filtered AM1.5 illumination (>665 nm) and (b) internal quantum efficiency of the N-on-P architecture 100-period SL solar cell and the GaAs reference cell.

Table 7-1 I-V parameters for the fabricated N-on-P solar cells (w/o ARC) under AM1.5 illumination cut-off by a 665 nm long-pass filter (FGL665S, THORLABS).

	AM1.5 filtered (>665 nm)					
	J_{sc} (mA/cm^2)	J_{max} (mA/cm^2)	V_{oc} (V)	V_{max} (V)	*FF*	Efficiency
SL100 cell	11.96	11.14	0.795	0.66	0.773	14.3%
GaAs cell	8.64	8.19	0.921	0.81	0.834	12.9%

As discussed in the section 5.4, a bottleneck with respect to the carrier transport in InGaAs/GaAsP SL solar cells is the collection of heavy holes, which have a large effective mass and a low mobility and thus are likely to limit the photocurrent. One of the difficulties in achieving high performance in N-on-P structure, therefore, is longer transport distance for such heavy holes to the bottom p-region through the SL-region, since the light is absorbed from the surficial area of the cell. In spite of this challenge, the SL100-cell showed almost flat I-V curve up to 0.6 V owing to efficient tunnel transport through thin barriers.

Fig. 7-12 shows CCE spectrum at V_{max} for the SL100 cell and the reference cell. The SL100 cell showed clear wavelength dependence in CCE whereas it was over 99% at V_{max} over the spectrum for GaAs reference cell owing to the almost complete carrier collection. At wavelength of below 550 nm, the light is mostly absorbed in the top-n-region due to the high absorption coefficient. The direction of the electron and hole transport is opposite between P-on-N and N-on-P cells. In an N-on-P cell, when electron-hole pairs are photo-generated above the SL, the holes have to pass through the entire 100-period SL to the bottom-p-region while there is no blockage for the electron transport to the top contact. Therefore, the hole transport limits the photocurrent under excitation by shorter wavelength light. However, the SL100-cell recorded very high CCE over 98%, and thus the collection of the heavy holes was found to be sufficient even under operational forward bias in spite of the large effective mass. This indicates the tunnel transport of heavy holes was quite efficient through the 2.5-nm-thick GaAsP barrier layers, which was also laterally undulated to form even thinner regions.

In the wavelength range between 550 and 850 nm, the light can reach the SL-region and partly excite carriers inside the InGaAs wells. As the wavelength becomes longer, the effect of electron transport across the i-region becomes larger because more excitation takes place in the SL. Beyond 850 nm, carriers are photo-excited only in the SL-region and thus the efficiency of electron transport is the most influential on the CCE.

SL100-cell showed a gradually degraded CCE at longer wavelengths, clearly indicating poor electron transport. The probable reason for the inefficient transport of electrons, which have much higher mobility than heavy holes, is the band-bending effect due to background carbon doping. According to the results discussed in the section 6.4.2, the background doping in the InGaAs/GaAsP SL grown using TEGa at 520 °C was suggested to be slightly p-type, and thus the band lineup of bottom part of the i-region becomes slightly flattened in an N-on-P cell. In this case, the electric field

in the i-region is weakened near the p-region while it is strengthened near the top n-region. When excitation takes place in the deeper region of the cell, therefore, the electron transport toward the n-region becomes less efficient under smaller drift force, resulting in lower CCE under longer wavelength illumination. In Fig. 6-21, the inefficient electron transport from the p-side due to the p-type background doping in the SL(TEGa)-cell was quite apparent with 900-nm-thick i-region. Since the i-region in the N-on-P SL100-cell is further thicker (1330 nm), the effect of band-bending should be even more serious. Nevertheless, use of sufficiently thin GaAsP barrier layers (2.5 nm) enabled the CCE beyond the GaAs absorption edge to remain at very high value over 95% at V_{max}. The high CCE at 400 - 550 nm in spite of the weakened electric field in the bottom part of the i-region, suggests that photo-excited holes can be quite efficiently transported once they are accelerated by the strong electric field that exists beneath the n-region; a similar result for the electron transport in P-on-N cell was observed in the section 6.4.

Consequently, SL100 cell achieved 1.11 times higher energy conversion efficiency than the GaAs reference cell with 36% enhancement in the maximum power output current. Considering 10% absorption loss in the long-pass filter and approximately 30% reflection, the expected J_{max} as a middle cell beneath the InGaP top cell with AR coating is 17.4 mA/cm^2, achieving the target current density for the current-matched InGaP/SL/Ge triple junction solar cells.

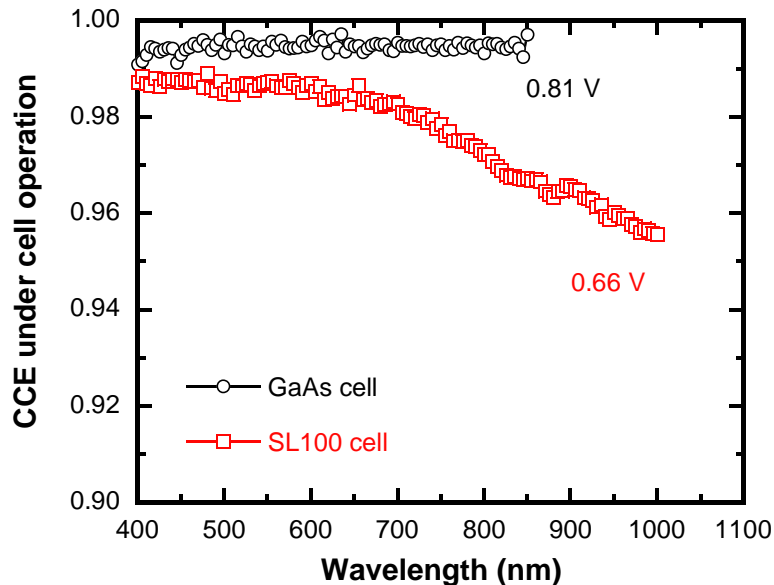Fig. 7-12   Wavelength dependent carrier collection efficiency at maximum power output voltages (V_{max}) of the N-on-P SL100 cell and the GaAs reference cell. The value of V_{max} for each cell is shown together.

7.3 Summary of chapter 7

In this chapter, the designed STSL (chapter 5) was implemented into an N-on-P solar cell on a vicinal substrate with the developed growth technique using TEGa (chapter 6). On the basis of further optimization of the growth temperature for SL on vicinal substrate with TEGa, incorporation of a 100-period thickness-modulated SL successfully achieved enhanced the N-on-P type middle cell performance.

- Effects of growth temperature (490 – 550 °C) in MOVPE with TEGa and layer undulation on the photovoltaic performance were investigated with 50-period $In_{0.30}Ga_{0.70}As$ (3.4 nm)/GaAs (2.7 nm)/$GaAs_{0.60}P_{0.40}$ (3.0 nm)/GaAs (2.7 nm) SLs.

- Suppression of step bunching formation and hence more structural uniformity of the SL at lower growth temperature were confirmed by XRD-RSM, but the crystal quality was degraded at 490 °C due to insufficient atom migration on the surface. 50-period SLs were stably grown at 500 – 530 °C with occurrence of larger thickness modulation at higher temperature. The entire SL was severely deteriorated at even higher temperature of 550 °C due to lattice relaxation induced by too large step bunching, resulting in a small temperature range for stable growth of SLs on vicinal substrates.

- Larger layer undulation of the SL significantly reduced the light absorbance due to poorer in-plane coverage of the InGaAs well region, resulting in lower J_{sc}. The V_{oc}, on the other hand, was enhanced by increasing the temperature with reduction of the dark current owing to the higher crystal quality. The layer undulation of the SL was also found to enable more efficient tunnel transport through the thin GaAsP barrier regions, and thus to improve the CCE and the *FF*. Due to this trade-off relation, the highest efficiency was achieved at 520-530 °C.

- Based on the temperature optimization, an N-on-P type 100-period $In_{0.3}GaAs$ (3.4 nm)/GaAs (2.7 nm)/$GaAsP_{0.4}$ (2.5 nm)/GaAs (2.7 nm) SL cell with bandgap of 1.21 eV was grown on a 6°-off substrate at 520 °C. Sufficiently thin GaAsP barriers to facilitate tunnel transport enabled CCE to remain over 95% under operational condition. Consequently, the SL100-cell achieved 1.11 times higher efficiency with 36% current enhancement as middle cell performance than a GaAs reference cell. Targeted J_{max} as a middle cell of 17 mA/cm^2 was also achieved as an expected value (17.4 mA/cm^2) with AR coating.

8 Conclusion

8.1 Overview of this research

III-V based multi-junction solar cells for terrestrial application under concentrated sunlight are promising concepts to overcome the current challenges for solar photovoltaics: "high power generation cost" and "low energy conversion efficiency". InGaP (1.85 eV)/(In)GaAs (1.42 eV)/Ge (0.67 eV) has been the conventional material combination for Ge-based triple junction solar cells, but the current mismatch due to the wide bandgap of the middle cell has been limiting the device performance. This research aims at development of narrow-gap InGaAs/GaAsP superlattice (SL) for Ge-based tandem solar cells, which has been accomplished through characterization of carrier transport in SL cell, design of suitable quantum structure, and establishment of metal-organic vapor phase epitaxy (MOVPE) technology. The aimed target is to achieve higher N-on-P type middle cell performance than a GaAs cell, by incorporating a 100-period SL with bandedge wavelength extended beyond 1000 nm on a 6°-off vicinal substrate.

In chapter 2 and 3, related fundamental theories and the experimental equipment used in this research were introduced, respectively.

In chapter 4, carrier collection efficiency (CCE) was defined as a parameter to evaluate the carrier transport in solar cells, and the challenge of SL cells in terms of carrier transport was investigated. The CCE is defined as the fraction of carriers photo-generated in the active p-n junction area of a cell, and can be calculated by normalizing the illumination-induced current enhancement to its saturation value at reverse bias. Combining wavelength- and bias-dependence of CCE, the transport of carriers from each region inside the cell can be examined in detail. The derivation procedure of the CCE was comprehensively validated by investigating 1) the bias dependence of the absorption in quantum wells, 2) the balance between the amount of absorbed photons and the amount of collectable carriers, 3) the effect of bias sunlight for monochromatic CCE measurement, and 4) the effects of resistance.

To demonstrate the advantages of CCE-based analyses, effectiveness of compensation doping in the i-region was examined. Unintentional p-type background doping due to carbon incorporation during MOVPE causes undesired bending of the band lineup in the i-region, and was found to severely degrade the carrier transport. By compensating the background doping with sulfur to make the electric field uniform in the i-region, transport of the carriers generated anywhere in the device was greatly improved. Furthermore, the challenges in carrier transport for a SL cell with a large period number

was clarified based on CCE-analyses, in particular for a standard SL design with moderate indium and phosphorus contents (1.2 – 1.7% strain) and relatively thick wells and barriers (> 7 nm); incorporation of a large number of quantum wells significantly thickens the i-region, and thus the carrier transport becomes quite difficult due to the weakened built-in field as well as the inevitably flattened band even with compensation doping.

In chapter 5, stepped tunnel superlattice (STSL) was proposed as a general design principle for quantum well structure that overcomes the major challenges faced by InGaAs/GaAsP SL solar cells, specifically, the trade-off between light absorption and carrier collection as well as the difficulty in crystal growth of a high-quality SL consisting of strained layers. The essential strategies for structural design are: 1) InGaAs wells should be thinner and deeper for a given bandgap for higher absorption coefficient and lower compressive strain accumulation, 2) GaAs interlayers with thicknesses of a few nanometers are effective for extending the absorption edge to longer wavelengths without additional compressive strain, and for suppressing lattice relaxation during growth, and 3) GaAsP barriers should be thinner than 3 nm to facilitate tunneling transport, and their phosphorus content should be minimized while avoiding detrimental lattice relaxation. For structural optimization of the STSL, the influences of GaAsP barriers on the carrier transport in terms of the CCE was systematically investigated. As a result, a P-on-N cell with 100-period $In_{0.30}Ga_{0.70}As$ (3.5 nm)/GaAs (2.7 nm)/ $GaAs_{0.60}P_{0.40}$ (3.0 nm)/GaAs (2.7 nm) STSL achieved significantly improved middle cell performance compared to a GaAs control cell, indicating promising potential of the designed SL structure for practical application.

In chapter 6, low temperature MOVPE of InGaAs/GaAsP SLs on vicinal substrates was developed using TEGa, aiming at implementation of the designed SL into Ge based multi-junction solar cells. SLs grown on vicinal substrates tend to be undulated due to formation of step bunching. Lowering the growth temperature to shorten the diffusion length of the adatom is effective to suppress the layer undulation, but too low temperature may lead to detrimental effects such as low crystal quality and high impurity incorporation. Using TMGa as the gallium source, lattice relaxation due to large step-bunching formation was significantly prevented by lowering the growth temperature, but severe crystal degradation apparently occurred below 530 °C because of insufficient atom migration on the crystal surface. The use of TEGa enabled 100-period SLs to be successfully grown at even lower temperature of 510 °C owing to the fast surface reaction as well as the efficient pyrolysis, resulted in an extremely uniform SL with negligible formation of step bunching. P-type background carbon doping level in the SL grown at 530 °C with TMGa was found to be very high ($\sim 10^{17}$ cm^{-3} in bulk GaAs), and compensation doping with sulfur for efficient carrier transport required extremely precise control of the doping level. Substitution of TMGa with TEGa reduced the carbon incorporation owing to its β-elimination reaction that does not produce methyl radicals, and higher photovoltaic performance than the compensation-doped SL cell grown with TMGa was achieved without performing sulfur doping. Furthermore, growth of compressively-strained STSL with thin GaAsP layers was found to be difficult using TMGa because of unstable kinetically-limited regime, but was

made successful using TEGa.

In chapter 7, optimally-designed 100-period STSL was implemented into an N-on-P solar cell on a vicinal substrate with the developed growth technique using TEGa. In order for the optimization of SL growth in term of photovoltaic performance, the effects of growth temperature (490-550 ºC) and layer undulation were investigated. Larger layer undulation of the SL significantly reduced the light absorbance due to poorer in-plane coverage of the InGaAs well region, resulting in lower J_{sc}. The V_{oc}, on the other hand, was enhanced by increasing the temperature with reduction of the dark current owing to the higher crystal quality. The layer undulation of the SL was also found to enable more efficient tunnel transport through the thin GaAsP barrier regions, and thus to improve the CCE and the FF.

Based on the temperature optimization, an N-on-P type 100-period $In_{0.30}Ga_{0.70}As$ (3.4 nm)/GaAs (2.7 nm)/$GaAs_{0.60}P_{0.40}$ (2.5 nm)/GaAs (2.7 nm) SL cell with a bandgap of 1.21 eV was grown on a 6º-off substrate at 520 ºC. Sufficiently thin GaAsP barriers to facilitate tunnel transport enabled CCE to remain over 95% under operational condition. Consequently, the SL100-cell achieved 1.11 times higher efficiency with 36% current enhancement as middle cell performance than a GaAs reference cell. Targeted J_{max} as a middle cell of 17 mA/cm^2 was also achieved as an expected value (17.4 mA/cm^2) with AR coating.

8.2 Conclusions

- This research aims at development of InGaAs/GaAsP superlattice solar cells for current-matched Ge-based triple-junction solar cells.

- Carrier collection efficiency (CCE) was defined as a parameter to evaluate the carrier transport in solar cells, and its measurement procedure has been established.

- The advantages of CCE-based analyses were experimentally demonstrated, and the challenges of InGaAs/GaAsP SL solar cells in terms of carrier transport were well clarified.

- Stepped tunnel superlattice (STSL) was proposed as a general design principle for higher photovoltaic performance as well as more successful crystal growth of the SL.

- Low temperature MOVPE of high-quality InGaAs/GaAsP SLs on vicinal substrate was developed using triethylgallium (TEGa).

- Higher middle cell performance with an InGaAs/GaAsP SL than a GaAs reference cell has been achieved by meeting the aimed targets in Table 1-1.

    - ✧ Incorporation of a 100-period SL with a bandgap of 1.21 eV
    - ✧ Maximum power output-current of 17.4 mA/cm^2 (expected with anti-reflection coating)
    - ✧ N-on-P type cell on 6°-off vicinal (0 0 1) substrate

Appendix A: SL/Ge dual junction solar cell

As a step forward the application of InGaAs/GaAsP SLs developed in this research into Ge-based multi-junction solar cells, a SL/Ge dual junction cell was fabricated, and here its preliminary results are shown.

The structure of SL/Ge cell is shown in the Fig. A(a). An N-on-P GaAs cell including a 100-period SL demonstrated in the section 7.2 was grown on a Ge substrate template by MOVPE. A GaAs/Ge reference cell without SL was also fabricated. The Ge template, which was prepared at Fraunhofer ISE, consisted of a Ge bottom cell with a nucleation layer, a GaAs buffer layer, a tunnel junction, and a GaAs highly p-doped layer on the top. Since GaAs has a lattice constant slightly smaller than Ge by 0.08 %, $In_{0.01}Ga_{0.99}As$ is widely used as the epilayer for exact lattice matching. Note that GaAs was used as the host material for the trial fabrication here, but the *in-situ* monitored reflectance in MOVPE did not show apparent degradation neither during the GaAs nor the 100-period SL growth, showing almost an almost equivalent time transient as Fig. 7-10(a). Fig. A(b) shows XRD-RSM around the $(0\,0\,4)$ diffraction point after the growth. The two dimensional satellite pattern attributed to the SL was almost same as Fig. 7-10(b), indicating that a similar thickness-modulated SL structure was obtained on a Ge substrate. However, the surface of the regrown sample was not completely mirror-like and several white spots were observed probably because of the incomplete removal of particles in the template cleaning. The grown samples were processed into photovoltaic devices with Ag (100 nm)/Au (350 nm) back electrodes and AuGe (350 nm) top electrodes. The devices were separated into 3 × 3 mm cells by dry etching. The top n-GaAs contact layer was finally removed by wet etching.

Fig. A (c) and (d) shows the I-V characteristics under filtered AM1.5 illumination (> 665 nm) and the EQE spectra, respectively. I-V measurements with insertion of a 665 nm long pass filter give the performances of the SL/Ge or GaAs/Ge tandem cells operated beneath InGaP top cells. The V_{oc} of SL/Ge and GaAs/Ge cells were 0.981 and 1.111 V, respectively, both of which were higher than V_{oc} of single junction devices on GaAs substrates (Table 7-1) by approximately 0.19 V. This voltage enhancement, however, is smaller than a typical V_{oc} of Ge cell (0.25V), and thus crystal degradation might be caused by the regrowth process. Nevertheless, the V_{oc} difference between the SL/Ge and the GaAs/Ge cell of 0.13 V was similar to the case of single junction cells, and thus the growth of the 100-period SL itself on a Ge substrate should be successful. Although the absolute values of the J_{sc} for both cells, which were limited by the top SL or GaAs cells, were slightly smaller than the single-junction devices, the SL/Ge cell achieved 1.33 times higher J_{sc} than GaAs/Ge reference cell; the enhancement factor was comparable to the case of single-junction. As a result, the dual-junction cell efficiency was enhanced by a factor of 1.12 by incorporating a 100-period SL.

The QE spectrum for the SL or GaAs subcells were measured under white bias light filtered by a

silicon substrate, and those for the Ge subcells were measured under white bias light filtered by a band pass filter (400 – 1000 nm). Despite the quite similar fringe pattern in the XRD-RSM between the SLs grown on a GaAs and a Ge substrate, the shapes of the QE spectra in 870 – 1050 nm, which are attributed to the absorption in the SL-region were slightly different (in comparison between Fig. A(d) and Fig. 7-11(b)). The exact reason for this is yet to be clarified, and further investigation of the structural and optical properties of the SL on Ge is necessary. Nevertheless, the entire EQE spectra of the SL cell on a GaAs substrate was well preserved even on a Ge substrate with an almost equivalent spectrum obtained in the GaAs absorption wavelength range to that of the reference cell.

The demonstration of SL/Ge cell shown here strongly indicates a promising potential of InGaAs/GaAsP SL for Ge-based multi-junction solar cells, and more progress such as implementation of InGaP or AlGaAs top cell, and single growth of SL cell from nucleation on Ge substrates would further develop this concept toward practical application.
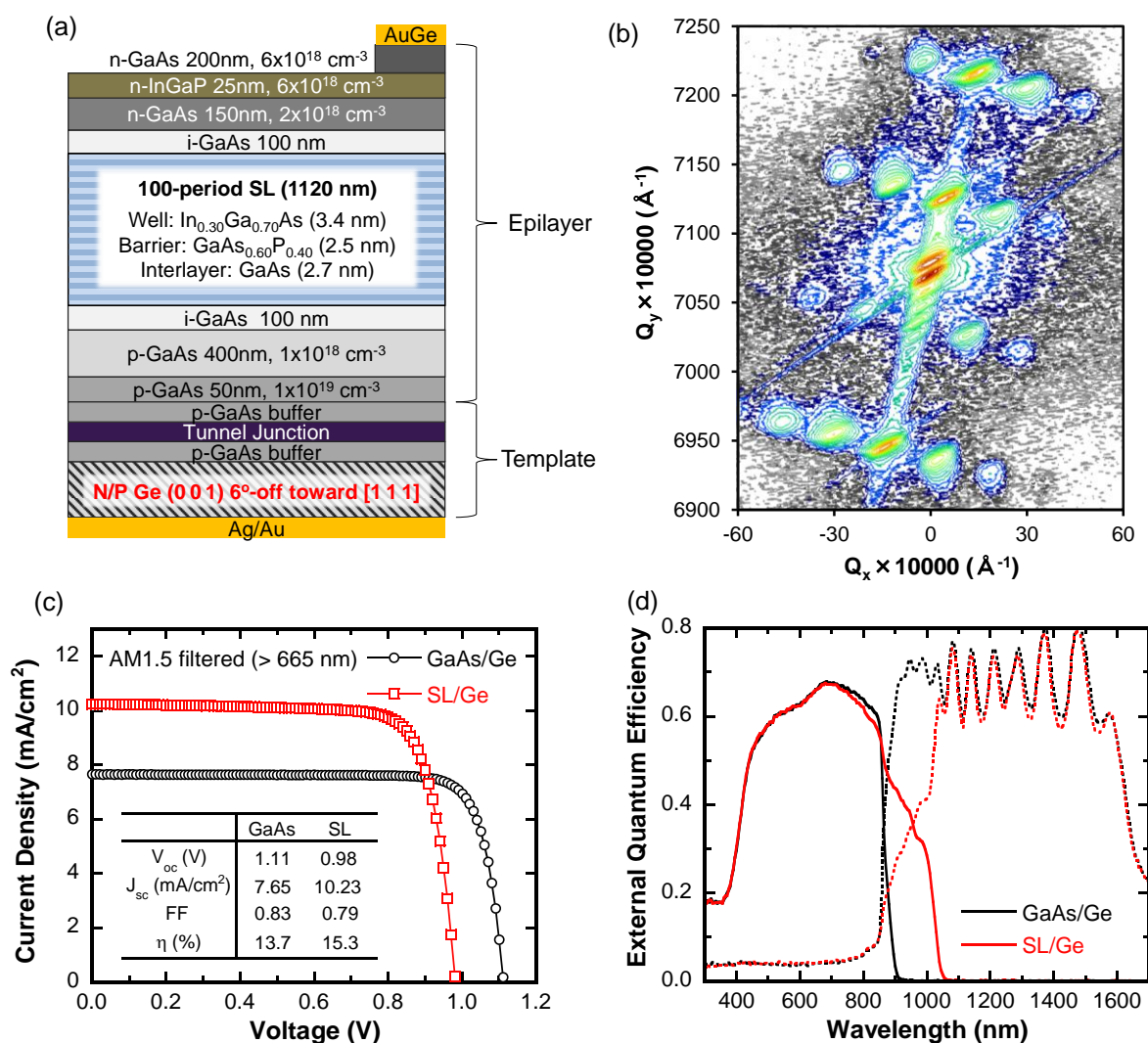

Fig. A (a) Structure of SL/Ge dual junction cell, (b) XRD-RSM of the SL/Ge cell around the (004) diffraction point, (c) I-V under filtered AM1.5 (> 665 nm) an (d) EQE of SL/Ge and GaAs/Ge cells.

Appendix B: Correspondence between sections and publications

The contents in the chapters or sections listed below have been partly published in the corresponding articles.

Section 4.3 - 4.4:

H. Fujii, K. Toprasertpong, K. Watanabe, and M. Sugiyama, "Evaluation of Carrier Collection Efficiency in Multiple Quantum Well Solar Cells", *IEEE Journal of Photovoltaics*, **4** (2014) 237-243.

Section 4.5.1

H. Fujii, Y. Wang, K. Watanabe, M. Sugiyama, and Y. Nakano, "Compensation doping in InGaAs/GaAsP multiple quantum well solar cells for efficient carrier transport and improved cell performance", *Journal of Applied Physics*, **114** (2013) 103101.

Chapter 5

H. Fujii, K. Toprasertpong, Y. Wang, K. Watanabe, M. Sugiyama, Y. Nakano, "100-period, 1.23-eV bandgap InGaAs/GaAsP quantum wells for high-efficiency GaAs solar cells: toward current-matched Ge-based tandem cells", *Progress in Photovoltaics: Research and Applications*, **22** (2014) 784-795.

Section 6.3

H. Fujii, H. Sodabanlu, M. Sugiyama, and Y. Nakano, "Low-temperature MOVPE using TEGa for suppressed layer undulation in InGaAs/GaAsP superlattice on vicinal substrates", *Journal of Crystal Growth*, http://dx.doi.org/10.1016/j.jcrysgro.2014.10.043 (in press).

Section 6.4

H. Fujii, K. Toprasertpong, H. Sodabanlu, K. Watanabe, M. Sugiyama, and Y. Nakano, "InGaAs/GaAsP superlattice solar cells with reduced carbon impurity grown by low-temperature metal-organic vapor phase epitaxy using triethylgallium", *Journal of Applied Physics* **116** (2014) 203101.

Chapter 7

H. Fujii, T. Kato, K. Toprasertpong, H. Sodabanlu, K. Watanabe, M. Sugiyama, and Y. Nakano, "Thickness-modulated InGaAs/GaAsP superlattice solar cells on vicinal substrates", *Journal of Applied Physics* (under review).

References

[1] US, EIA, "International Energy Statistics," [Online]. Available: http://www.eia.gov/cfapps/ipdbproject/IEDIndex3.cfm.

[2] British Petroleum, "BP Statistical Review of Wourld Energy, June 2014," 2014.

[3] METI Japan, "Yearbook of mineral resourcces and petroleum products statistics," 2013.

[4] World Bank, "World Development Indicators," [Online]. Available: http://data.worldbank.org/data-catalog/world-development-indicators.

[5] NEA, "URANIUM 2009," 2009.

[6] M. Konagai, "Present Status and Future Prospects of Silicon Thin-Film Solar Cells," *Jpn. J. Appl. Phys.,* vol. 50, p. 030001, 2011.

[7] DOE, US, "$1/W Photovoltaic Systems," 2010.

[8] EPIA, "Solar Photovoltaics Competing in the Energy Sector on the Road to Competitiveness," EPIA, 2011.

[9] NREL, "Research Cell Efficiency Records," [Online]. Available: http://www.nrel.gov/rredc/.

[10] J. Zhao, A. Wang and M. A. Green, "24.5% Efficiency Silicon PERT Cells on MCZ Substrates and 24.7% Efficiency PERL Cells on FZ Substrates," *Prog. Photovolt: Res. Appl.,* vol. 1999, pp. 471-474, 1999.

[11] J. Nakamura, N. Asano, T. Hieda, C. Okamoto, T. Ohnishi, M. Kobayashi, H. Tadokoro, R. Suganuma, Y. Matsumoto, H. Katayama, K. Higashi, T. Kamikawa, K. Kimoto, M. Harada, T. Sakai, H. Shigeta, T. Kuniyoshi, K. Tsujino, L. Zou, N. Koide and K. Nakamura, "Development of Heterojunction Back Contact Si Solar Cells," *Proc. 29th European PV Solar Energy Conference and Exhibition,* pp. 373-375, 2014.

[12] K. Masuko, M. Shigematsu, T. Hashiguchi, D. Fujishima, M. Kai, N. Yoshimura, T. Yamaguchi, Y. Ichihashi, T. Yamanishi, T. Takahama, M. Taguchi, E. Maruyama and S. Okamoto, "Achievement of more than 25% conversion efficiency with crystalline silicon heterojunction solar cell," *J. Photovoltaics,* vol. 4, pp. 1433-1435, 2014.

[13] "Sunpower," [Online]. Available: http://us.sunpower.com/.

[14] D. L. Staebler and C. R. Wronski, "Reversible conductivity changes in dischargeproduced amorphous Si," *Appl. Phys. Lett.,* vol. 31, pp. 292-294, 1977.

[15] B. Yan, G. Yue, J. Yang and S. Guha, "Correlation of Current Mismatch and Fill Factor in Amorphous and Nanocrystalline Silicon Based High Efficiency Multi-Junction Solar Cells," *Proc. 33th Photovoltaic Specialist Conference,* pp. 1-6, 2008.

[16] M. Powalla, P. Jackson, D. Hariskos, S. Paetel, W. Witte, R. Würz, E. Lotter,, R. Menner and W. Wischmann, "CIGS Thin-Film Solar Cells with an Improved Efficiency of 20.8%," in *29th European PV Solar Energy Conference and Exhibition*, Amsterdam, 2014.

[17] First Solar, [Online]. Available: http://www.firstsolar.com/.

[18] M. A. Green, K. Emery, Y. Hishikawa, W. Warta and E. D. Dunlop, "Solar cell efficiency tables (version 43)," *Prog. Photovolt: Res. Appl.,* vol. 22, pp. 1-9, 2014.

[19] T. N. Tibbits, P. Beutel, M. Grave, C. Karcher, E. Oliva, G. Siefer, A. Wekkeli, M. Schachtner, F. Dimroth, A. W. Bett, R. Krause, M. Piccin, N. Blanc, M. M. Rico, C. Arena, E. Guiot, C. Charles-Alfred, C. Drazek, F. Janin, L. Farrugia, B. Hoarau, J. Wasselin, A. Tauzin, T. Signamarcheix, T. Hannappel, K. Schwarzburg and A. Dobrich, "New efficiency frontiers with wafer-bonded multi-junction solar cells," in *29th European PV Solar Energy Conference and Exhibition*, Amsterdam, 2014.

[20] R. R. King, D. Bhusari, D. Larrabee, X. -Q. Liu, E. Rehder, K. Edmondson, H. Cotal, R. K. Jones, J. H. Ermer, C. M. Fetzer, D. C. Law and N. H. Karam, "Solar cell generations over 40% efficiency," *Progress in Photovoltaics: Research and Applications,* vol. 20, pp. 801-815, 2012.

[21] NREL, "Solar Spectra," [Online]. Available: http://rredc.nrel.gov/solar/spectra/.

[22] C. H. Henry, "Limiting efficiencies of ideal single and multiple energy gap terrestrial solar cells," *J. Appl. Phys,* vol. 51, pp. 4494-4500, 1980.

[23] P. Würfel, Physics of Solar Cells: From Basic Principles to Advanced Concepts, WILEY-VCH, 2009.

[24] W. Shockley and H. J. Queisser, "Detailed Banalnce Limit of Efficiency of p-n Junction Solar Cells," *J. Appl. Phys.,* vol. 32, pp. 510-519, 1961.

[25] A. Luque and A. Martí, "Increasing the Efficiency of Ideal Solar Cells by Photon Induced Transitions at Intermediate Levels," *Phys. Rev. Lett.,* vol. 78, pp. 5014-5017, 1997.

[26] A. Martí, N. López, E. Antolín, E. Cánovas, C. Stanley, C. Farmer, L. Cuadra and A. Luque, "Novel semiconductor solar cell structures: The quantum dot intermediate band solar cell," *Thin Solid Films,* Vols. 511-512, pp. 638-644, 2006.

[27] N. López, L. A. Reichertz, K. M. Yu, K. Campman and W. Walukiewicz, "Engineering the Electronic Band Structure for Multiband Solar Cells," *Phys. Rev. Lett.,* vol. 106, p. 028701, 2011.

[28] A. Martí, C. Tablero, E. Antolín, A. Luque, R. P. Campion, S. V. Novikov and C. T. Foxon, "Potential of Mn doped In1−xGaxN for implementing intermediate band solar cells," *Sol. Energy Mater. Sol. Cells,* vol. 93, pp. 641-644, 2009.

[29] A. J. Nozik, "Multiple exciton generation in semiconductor quantum dots," *Chem. Phys. Lett,* vol. 457, pp. 3-11, 2008.

[30] O. E. Semonin, J. M. Luther, S. Choi, H. Y. Chen, J. Gao, A. J. Nozik and M. C. Beard, "Peak External Photocurrent Quantum Efficiency Exceeding 100% via MEG in a Quantum Dot Solar Cell,"

Science, vol. 334, pp. 1530-1533, 2011.

[31] R. T. Ross and A. J. Nozik, "Efficiency of hotcarrier solar energy converters," *J. Appl. Phys,* vol. 53, pp. 3813-3818, 1982.

[32] G. J. Conibeer, C. W. Jiang, D. König, S. Shrestha, T. Walsh and M. A. Green, "Selective energy contacts for hot carrier solar cells," *Thin Solid Film,* vol. 516, pp. 6968-6973, 2008.

[33] S. Seyrling, S. Calnan, S. Bücheler, J. Hüpkes, S. Wenger, D. Brémaud, H. Zogg and A. N. Tiwari, "CuIn1-xGaxSe2 photovoltaic devices for tandem solar cell application," *Thin Solid Films,* vol. 517, pp. 2411-2414, 2009.

[34] S. Kang, R. Sharma, J. K. Sim and C. R. Lee, "Band gap engineering of tandem structured CIGS compound absorption layer fabricated by sputtering and selenization," *J. Alloys Compounds,* vol. 563, pp. 207-215, 2013.

[35] A. Banerjee, T. Su, D. Beglau, G. Pietka, F. S. Liu, S. Almutawalli, J. Yang and S. Guha, "High-Efficiency, Multijunction nc-Si:H-Based Solar Cells at High Deposition Rate," *J. Photovoltaics,* vol. 2, pp. 99-103, 2012.

[36] T. Matsui, H. Jia, M. Kondo, K. Mizuno, S. Tsuruga, S. Sakai and Y. Takeuchi, "Application of Microcrystalline Si1-xGex Infrared Absorbers in Triple Junction Solar Cells," in *IEEE 35th Photovoltaics Specialist Conference*, 2010.

[37] M. Yamaguchi, T. Takamoto and K. Araki, "Present and Future of Super High Efficiency Multi-Junction Solar Cells," *Proc. SPIE,* vol. 6889, p. 688906, 2008.

[38] T. Takamoto, M. Kaneiwa, M. Imaizumi and M. Yamaguchi, "InGaP/GaAs-based Multijunction Solar Cells," *Prog. Photovolt: Res. Appl.,* vol. 13, pp. 495-511, 2005.

[39] C. Algora, I. Rey-Stolle, I. García, B. Galiana, M. Baudrit, P. Espinet, E. Barrigón , J. R. González, "III-V Multijunction Solar Cells for Ultra-high Concentration Photovoltaics," *Proc. 34th Photovoltaic Specialist Conference,* pp. 001571-001575, 2009.

[40] M. Bosi and C. Pelosi, "The Potential of III-V Semiconductors as Terrestrial Photovoltaic Devices," *Prog. Photovolt: Res. Appl,* vol. 15, pp. 51-68, 2007.

[41] S. Sato, T. Ohshima and M. Imaizumi, "Modeling of degradation behavior of InGaP/GaAs/Ge triple-junction space," *J. Appl. Phys.,* vol. 105, p. 044504, 2009.

[42] N. H. Karam, R. R. King, M. Haddad, J. H. Ermer, H. Yoon, H. L. Cotal, R. Sudharsanan, J. W. Eldredge, K. Edmondson, D. E. Joslin, D. D. Krut, M. Takahashi, W. Nishikawa, M. Gillanders, J. Granata, P. Hebert, B. T. Cavicchi and D. Lillington, "Recent developments in high-effciency Ga0.5In0.5P/GaAs/Ge dual- and triple-junction solar cells: steps to next-generation PV cells," *Sol. Energy Mater. Sol. Cells,* vol. 66, pp. 453-466, 2001.

[43] R. R. King, D. C. Law, K. M. Edmondson, C. M. Fetzer, G. S. Kinsey, H. Yoon, R. A. Sherif and N. H. Karam, "40% efficient metamorphic GaInP/GaInAs/Ge multijunction solar cells," *Appl. Phys.*

Lett., vol. 90, p. 183516, 2007.

[44] D. J. Friedman, J. F. Geisz, S. R. Kurtz and J. M. Olson, "1-eV solar cells with GaInNAs active layer," *J. Cryst. Growth,* vol. 195, pp. 409-415, 1998.

[45] K. Volz, D. Lackner and I. Néimeth, "Optimization of annealing conditions of (GaIn)(NAs) for solar cell applications," *J. Cryst. Growth,* vol. 310, p. 2222, 2008.

[46] Y. Ohshita, H. Suzuki, N. Kojima, T. Tanaka, T. Honda, M. Inagaki and M. Yamaguchi, "Novel material for super high efficiency multi-junction solar cells," *J. Cryst. Growth,* vol. 318, p. 328, 2011.

[47] W. Li, M. Pessa and J. Likonen, "Lattice parameter in GaNAs epilayers on GaAs: Deviation from Vegard's law," *Appl. Phys. Lett,* vol. 78, pp. 2864-2866, 2001.

[48] A. Ohmae, N. Matsumoto and Y. Okada, "Growth of GaInNAs by atomichydrogen-assisted RF-MBE," *J. Cryst. Growth,* vol. 251, pp. 412-416, 2003.

[49] Y. K. Shimizu, S. Niki and Y. Okada, "Fabrication of homojunction GaInNAs solar cells by atomic hydrogen-assisted molecular beam epitaxy," *Sol. Energy Mater. Sol. Cells,* vol. 93, pp. 1120-1123, 2009.

[50] D. B. Jackrel, S. R. Bank, H. B. Yuen, M. A. Wistey and J. S. Harris, Jr, "Dilute nitride GaInNAs and GaInNAsSb solar cells by molecular beam epitaxy," *J. Appl. Phys,* vol. 101, p. 114916, 2007.

[51] M. Wiemer , V. Sabnis and H. Yuen, "43.5% efficient lattice matched solar cells," *Proc. SPIE,* vol. 8108, p. 810804, 2011.

[52] W. Guter, J. Schöne, S. P. Philipps, M. Steiner, G. Siefer, A. Wekkeli, E. Welser, E. Oliva, A. W. Bett and F. Dimroth, "Current-matched triple-junction solar cell reaching 41.1% conversion efficiency under concentrated sunlight," *Appl. Phys. Lett,* vol. 94, p. 223504, 2009.

[53] C. M. Fetzer, R. R. King, P. C. Colter, K. M. Edmondson, D. C. Law, A. P. Stavrides, H. Yoon, J. H. Ermer, M. J. Romero and N. H. Karam, "High-efficiency metamorphic GaInP/GaInAs/Ge solar cells grown by MOVPE," *J. Cryst. Growth,* vol. 261, pp. 341-348, 2004.

[54] S. M. Bedair, T. Katsuyama, P. K. Chiang, N. A. El-Masry, M. Tischler and M. Timmons, "GaAsP-GaInAsSb Superlattice: A New Structure for Electronic Devices," *J. Cryst. Growth,* vol. 68, pp. 477-482, 1984.

[55] S. M. Bedair, T. Katsuyama, M. Timmons and M. A. Tischler, "A new GaAsP-InGaAs strained-layer superlattice light-emitting diode," *IEEE Electron Device Lett.,* Vols. EDL-5, pp. 45-47, 1984.

[56] H. Hatakeyama, T. Anan, T. Akagawa, K. Fukutsu, N. Suzuki, K. Tokutome and M. Tsuji, "Highly Reliable High-Speed 1.1-um-Range VCSELs With InGaAs/GaAsP-MQWs," *IEEE J. Quantum Electron.,* vol. 46, pp. 890-897, 2010.

[57] N. Tansu and L. J. Mawst, "High-performance strain-compensated InGaAs-GaAsP-GaAs (λ=1.17 μm) quantum well diode lasers," *IEEE Photonics Technology Letters,* vol. 13, pp. 179-181, 2001.

[58] K. Bacher, S. Massie and M. Seaford, "Molecular beam epitaxy of strain-compensated

InGaAs/GaAsP quantum-well intersubband photodetectors," *J. Cryst. Growth,* Vols. 175-176, pp. 977-982, 1997.

[59] J. E. Cunningham, K. W. Goossen, M. Williams and W. Y. Jan, "Pseudomorphic InGaAs‑GaAsP quantum well modulators on GaAs," *Appl. Phys. Lett.,* vol. 60, pp. 727-729, 1992.

[60] N. J. Ekins-Daukes, J. M. Barnes, K. W. J. Barnham, J. P. Connolly, M. Mazzer, J. C. Clark, R. Grey, G. Hill, M. A. Pate and J. S. Roberts, "Strained and strain-balanced quantum well devices for high-efficiency tandem solar cells," *Sol. Energy Mater. Sol. Cells,* vol. 68, pp. 71-87, 2001.

[61] N. J. Ekins-Daukes, D. B. Bushnell, J. P. Connolly, K. W. J. Barnham, M. Mazzer, J. S. Roberts, G. Hill and R. Airey, "Strain-balanced quantum well solar cells," *Physica E,* vol. 14, pp. 132-135, 2002.

[62] H. Sodabanlu, S. Ma, K. Watanabe, M. Sugiyama and N. Yoshiaki, "Impact of Strain Accumulation on InGaAs/GaAsP Multiple Quantum Wells Solar Cells: Direct Correlation between in-situ strain measurement and cell performance," *Jpn. J. Appl. Phys.,* vol. 51, p. 10ND16, 2011.

[63] B. Browne, J. Lacey, T. Tibbits, G. Bacchin, T. C. Wu, J. Q. Liu, X. Chen, V. Rees, J. Tsai and J. G. Werthen, "Triple-Junction Quantum-Well Solar Cells in Commercial Production," *AIP Conf. Proc.,* vol. 1556, pp. 3-5, 2013.

[64] K. W. J. Barnham, "A new approach to high-efficiency multi-band-gap solar cells," *J. Appl. Phys,* vol. 67, pp. 3490-3493, 1990.

[65] N. G. Anderson and S. J. Wojtczuk, "Open-circuit voltage characteristics of InP-based quantum well solar cells," *J. Appl. Phys.,* vol. 79, pp. 1973-1978, 1996.

[66] M. Sugiyama, Y. Wang, H. Fujii, H. Sodabanlu, K. Watanabe and Y. Nakano, "A quantum-well superlattice solar cell for enhanced current output and minimized drop in open-circuit voltage under sunlight concentration," *J. Phys. D: Appl. Phys.,* vol. 46, p. 024001, 2013.

[67] G. L. Araujo, *Proc. 12th EUPVSEC,* p. 1481, 1994.

[68] J. Nelson, J. Barnes, N. Ekins-Daukes, B. Kluftinger, E. Tsui and K. Barnham, "Observation of suppressed radiative recombination in single quantum well p-i-n photodiodes," *J. Appl. Phys.,* vol. 82, pp. 6240-6246, 1997.

[69] K. W. J. Barnham, I. Ballard, J. G. Connolly, N. Ekins-Daukes, B. G. Kluftinger, J. Nelson and C. Rohr, "Recent results on quantum well solar cells," *J. Mater. Sci: Mater. Electron,* vol. 11, pp. 531-536, 2000.

[70] N. J. Ekins-Daukes, K. W. J. Barnham, J. P. Connolly, J. S. Roberts, J. C. Clark, G. Hill and M. Mazzer, "Strain-balanced GaAsP/InGaAs quantum well solar cells," *Appl. Phys. Lett.,* vol. 75, pp. 4195-4197, 1999.

[71] P. Würfel, "The Chemical Potential of Radiation," *Solid State Phys.,* vol. 15, pp. 3967-3985, 1982.

[72] J. Nelson, The Physics of Solar Cells, Imperial Collage Press, 2003.

[73] G. L. Araújo and A. Martí, "Absolute limiting efficiencies for photovoltaic energy conversion," *Solar*

Energy Materials & Solar Cells, vol. 33, pp. 213-240, 1994.

[74] F. D. Pollak, "Modulation spectroscopy under uniaxial stress," *Surface Science,* vol. 37, pp. 863-895, 1973.

[75] S. L. Chuang, Physics of Optoelectronic Devices, John Wiley &Song, Inc, 1995.

[76] M. Nakayama, Optical property of semiconductor, Corona Publishing, 2013.

[77] H. Schneider and K. v. Klitzing, "Thermionic emission and Gaussian transport of holes in a GaAs/AlxGa1-xAs multiple-quantum-well structure," *Phys. Rev. B,* vol. 38, pp. 6160-6165, 1988.

[78] O. Y. Raisky, W. B. Wang, R. R. Alfano, C. L. Reynolds, Jr and V. Swaminathan, "Investigation of photoluminescence and photocurrent in InGaAsP/InP strained multiple quantum well heterostructures," *J. Appl. Phys.,* vol. 81, p. 394, 1997.

[79] G. B. Stringfellow, Organometallic Vapor-Phase Epitaxy - Theory and Practice, Academic Press, 1999.

[80] Y. Wang, R. Onitsuka, M. Deura, W. Yu, M. Sugiyama and Y. Nakano, "In situ reflectance monitoring for the MOVPE of strain-balanced InGaAs/GaAsP quantum-wells," *Journal of Crystal Growth,* vol. 312, pp. 1364-1369, 2010.

[81] I. Kamiya, D. E. Aspnes, H. Tanaka, L. T. Florez, J. P. Harbison and R. Bhat, "Surface science at atmospheric pressure: Reconstructions on (001) GaAs in organometallic chemical vapor deposition," *Physical Review Letters,* vol. 68, pp. 627-630, 1992.

[82] W. Richter and J. F. McGlip, "Optical in situ Surface Control during MOVPE and MBE Growth," *Phil. Trans. R. Soc. Lond. A,* vol. 344, pp. 453-467, 1993.

[83] F. Reinhardt, J. Jonsson, M. Zorn, W. Richter, K. Ploska, J. Rumberg and P. Kurpas, "Monolayer growth oscillations and surface structure of GaAs(001) during metalorganic vapor phase epitaxy growth," *J. Vac. Sci. Technol. B,* vol. 12, pp. 2541-2546, 1994.

[84] F. Reinhardt, W. Richter, A. B. Müller, D. Gutsche and P. Kurpas, "GaAs surface control during metalorganic vapor phase epitaxy by reflectance anisotropy spectroscopy," *J. Vac. Sci. Technol. B,* vol. 11, pp. 1427-1430, 1993.

[85] C. Krahmer, M. Philippens, M. Schubert and K. Streubel, "MOVPE growth investigations of doping and ordering in AlGaAs and GaInP with reflectance anisotropy spectroscopy," *J. Cryst. Growth,* vol. 298, pp. 18-22, 2007.

[86] M. Zorn and M. Weyers, "Comprehensive study of (Al)GaAs Si-doping using reflectance anisotropy spectroscopy in metal-organic vapour-phase epitaxy," *J. Phys. D: Appl. Phys.,* vol. 40, pp. 878-882, 2007.

[87] M. Zorn, J. Jönsson, A. Krost, W. Richter, J. T. Zettler, K. Ploska and F. Reinhardt, "In-situ reflectance anisotropy studies of ternary III—V surfaces and growth of heterostructures," *J. Cryst. Growth,* vol. 145, pp. 53-60, 1994.

[88] H. Fujii, Y. Wang, K. Watanabe, M. Sugiyama and Y. Nakano, "Suppressed lattice relaxation during InGaAs/GaAsP MQW growth with INGaAs and GaAs unltra-thin interlayers," *J. Cryst. Growth,* vol. 352, pp. 239-244, 2012.

[89] T. C. Wen and W. I. Lee, "Influence of Barrier Growth Temperature on the Properties of InGaN/GaN Quantum Well," *Jpn. J. Appl. Phys,* vol. 40, pp. 5302-5303, 2001.

[90] D. B. Bushnell, T. N. D. Tibbits, K. W. J. Barnham, J. P. Connolly, M. Mazzer, N. J. Ekins-Daukes, J. S. Roberts, G. Hill and R. Airey, "Effect of well number on the performance of quantum-well solar cells," *J. Appl. Phys.,* vol. 97, p. 124908, 2005.

[91] M. C. Lynch, I. M. Ballard, D. B. Bushnell, J. P. Connolly, D. C. Johnson, T. N. D. Tibbits, K. W. J. Barnham, N. J. Ekins-Daukes, J. S. Roberts, G. Hill, R. Airey and M. Mazzer, "Spectral response and I-V characteristics of large well number multi quantum well solar cells," *J. Mater. Sci.,* vol. 40, pp. 1445-1449, 2005.

[92] I. Serdiukova, C. Monier, M. F. Vilela and A. Freundlich, "Critical built-in electric field for an optimum carrier collection in multiquantum well p-i-n diodes," *Appl. Phys. Lett.,* vol. 74, pp. 2812-2814, 1999.

[93] A. Alemu, J. A. H. Coaquira and A. Freundlich, "Dependence of device performance on carrier escape sequence in multi-quantum-well p-i-n solar cells," *J. Appl. Phys.,* vol. 99, p. 084506, 2006.

[94] A. Alemu and A. Freundlich, "Thermionic Escape Study in p-i-n InP/InAs53P47 Multi-Quantum Well Solar Cell," *Proc. of 34th Photocoltaic Specialist Conference, Philadelphia,* pp. 001374-001376, 2009.

[95] O. Y. Raisky, W. B. Wang and R. R. Alfano, "Carrier screening effects in photoluminescence spectra of InGaAsP/InP multiple quantum well photovoltaic structures," *Appl. Phys. Lett.,* vol. 79, pp. 430-432, 2001.

[96] J. Nelson, M. Paxman, K. W. J. Barnham, J. S. Roberts and C. Button, "Steady-State Carrier Escape from Single Quantum Wells," *IEEE J. Quantum Electron.,* vol. 29, pp. 1460-1468, 1993.

[97] J. Barnes, E. S. M. Tsui, K. W. J. Barnham, S. C. McFarlane, C. Button and J. S. Roberts, "Steady state photocurrent and photoluminescence from single quantum wells as a function of temperature and bias," *J. Appl. Phys.,* vol. 81, pp. 892-900, 1997.

[98] A. Zachariou, J. Barnes, K. W. J. Barnham, J. Nelson, E. S. M. Tsui, J. Epler and M. Pate, "A carrier escape study from InP/InGaAs single quantum well solar cells," *J. Appl. Phys,* vol. 83, pp. 877-881, 1998.

[99] F. A. Lindholm, J. G. Fossum and E. L. Burgess, "Application of the superposition principle to solar-cell analysis," *IEEE Trans. Electron Devices,* Vols. ED-26, pp. 165-171, 1979.

[100] M. Eron and A. Rothwarf, "Effects of a voltage-dependent light-generated current on solar cell measurements: CuInSe2/Cd(Zn)S," *Appl. Phys. Lett,* vol. 44, pp. 131-133, 1984.

[101] D. Miller, D. S. Chemla, T. C. Damen, A. C. Gossard, W. Wiegmann, T. H. Wood and C. A. Burrus, "Band-edge electroabsorption in quantum well structures: The quantum-confined stark effect," *Phys. Rev. Lett.,* vol. 53, pp. 2173-2176, 1984.

[102] T. Yoshiie, C. L. Bauer and A. G. Milnes, "Interfacial reactions between gold thin films and GaAs substrates," *Thin Solid Films,* vol. 111, pp. 149-166, 1984.

[103] S. J. Pearton, Processing of Wide band Gap Semiconductors, William Andrew, 2001.

[104] T. Kita, R. Hasegawa and T. Inoue, "Suppression of nonradiative recombination process in directly Si-doped InAs/GaAs quantum dots," *J. Appl. Phys.,* vol. 110, p. 103511, 2011.

[105] M. Pristovsek, B. Han, J. T. Zettler and W. Richter, "In situ investigation of GaAs (001) intrinsic carbon p-doping in metal-organic vapor phase epitaxy," *J. Cryst. Growth,* vol. 221, pp. 149-155, 2000.

[106] S. Takagishi and H. Mori, "Effect of Operating Pressure on the Properties of GaAs Grown by Low-Pressure MOCVD," *Jpn. J. Appl. Phys.,* vol. 22, pp. L795-L797, 1983.

[107] M. Longo, R. Magnanini, A. Parisini, L. Tarricone, A. Carbognani, C. Bocchi and E. Gombia, "Controlled intrinsic carbon doping in MOVPE-grown GaAs layers by using TMGa and TBAs," *J. Cryst. Growth,* vol. 248, pp. 119-123, 2003.

[108] T. Nakanisi, "The Growth and Characterization of High Quality MOVPE GaAs AND GaAlAs," *J. Cryst. Growth,* vol. 68, pp. 282-294, 1984.

[109] K. Barnham, J. Connolly, P. Griffin, G. Haarpaintner, J. Nelson, E. Tsui, A. Zachariou and J. Osborne, "Voltage enhancement in quantum well solar cells," *J. Appl. Phys.,* vol. 80, pp. 1201-1206, 1996.

[110] H. Fujii, Y. Wang, K. Watanabe, M. Sugiyama and Y. Nakano, "Suppressed lattice relaxation during InGaAs/GaAsP MQW growth with InGaAs and GaAs ultra-thin interlayers," *J. Cryst. Growth,* vol. 352, pp. 239-244, 2012.

[111] Y. Okada, S. Seki, T. Takeda and M. Kawabe, "Control of dark currents in multi-quantum well solar cells fabricated by atomic H-assisted molecular beam epitaxy," *J. Cryst. Growth,* Vols. 237-239, pp. 1515-1518, 2002.

[112] Y. Okada, N. Shiotsuka and T. Takeda, "Potentially modulated multi-quantum wells for high-efficiency solar cell applications," *Sol. Energy Mater. Sol. Cells,* vol. 85, pp. 143-152, 2005.

[113] Y. Wen, Y. Wang, K. Watanabe, M. Sugiyama and Y. Nakano, "Effect of GaAs Step Layer Thickness in InGaAs/GaAsP Stepped Quantum-Well Solar Cell," *IEEE J. Photovoltaics,* vol. 3, pp. 289-294, 2013.

[114] K. Toprasertpong, H. Fujii, Y. Wang, K. Watanabe, M. Sugiyama and Y. Nakano, "Carrier Escape Time and Temperature-Dependent Carrier Collection Efficiency of Tunneling-Enhanced Multiple Quantum Well Solar Cells," *IEEE J. Photovoltaics,* vol. 4, pp. 607-613, 2013.

[115] Y. Wang, Y. Wen, H. sodabanlu, K. Watanabe, M. Sugiyama and Y. Nakano, "A Superlattice Solar Cell With Enhanced Short-Circuit Current and Minimized Drop in Open-Circuit Voltage," *IEEE J. Photovoltaics,* vol. 2, pp. 387-392, 2012.

[116] J. P. Samberg, C. Z. Carlin, G. K. Bradshaw, P. C. Colter and S. M. Bedair, "J. Electron. Mater.," *Growth and Characterization of InxGa1−xAs/GaAs1−yPy Strained-Layer Superlattices with High Values of y (~80%),* vol. 42, pp. 912-917, 2013.

[117] P. C. Colter, C. Z. Carlin, J. P. Samberg, G. K. Bradshaw and S. M. Bedair, "Staggered InGaAs/GaAsP strained layer superlattices for use in optical devices," *Phys. Status Solidi A,* vol. 208, pp. 2884-2888, 2011.

[118] A. Alemu and A. Freundlich, "Resonant thermotunneling design for high-performance single-junction quantum-well solar cells," *IEEE J. Photovoltaics,* vol. 2, pp. 256-260, 2012.

[119] S. J. Ma, H. Sodabanlu, Y. P. Wang, K. Watanabe, M. Sugiyama and Y. Nakano, "InGaAs/GaAsP asymmetric quantum wells for enhancing carrier escape through resonant tunneling," *Proc. 38th IEEE Photovoltaic Specialists Conference,* pp. 001908 - 001910, 2012.

[120] T. S. Moss and T. D. Hawkins, "Infrared absorption in gallium arsenide," *Infrared Physics,* vol. 1, p. 111, 1961.

[121] H. H. Tan, P. Lever and C. Jagadish, "Growth of highly strained InGaAs quantum wells on GaAs substrates - effect of growth rate," *J. Cryst. Growth,* vol. 274, pp. 85-89, 2005.

[122] J. G. Cederberg, "Self-assembled quantum dot formation during the growth of In0.4Ga0.6As on GaAs(0 0 1) by metal-organic vapor phase epitaxy: The role of In segregation," *J. Cryst. Growth,* vol. 307, pp. 44-50, 2007.

[123] K. Toprasertpong, H. Fujii, M. Führer, D. Alonso-Álvarez, D. J. Farrell, K. Watanabe, Y. Okada, N. J. Ekins-Daukes, M. Sugiyama and Y. Nakano, "Absorption Threshold Extended to 1.15 eV Using InGaAs/GaAsP Quantum Wells for over-50%-Efficient Lattice-Matched Quad-Junction Solar Cells," in *29th European PV Solar Energy Conference and Exhibition*, Amsterdam, 2014.

[124] I. Vurgaftman, J. R. Meyer and L. R. Ram-Mohan, "Band parameters for III–V compound semiconductors and their alloys," *J. Appl. Phys.,* vol. 89, pp. 5815-5875, 2001.

[125] D. J. Arent, K. Deneffe, C. Van Hoof, J. De Boeck and G. Borghs, "Strain effects and band offsets in GaAs/InGaAs strained layered quantum structures," *J. Appl. Phys.,* vol. 66, pp. 1739-1747, 1989.

[126] L. Malikova, F. H. Pollak, O. Gorea and A. Korotcov, "Modulation Spectroscopy Study of a Strained Layer GaAs/GaAsP Multiple Quantum Well Structure," *J. Electron. Mater.,* vol. 29, pp. 1346-1350, 2000.

[127] E. S. Koteles, "Determining energyband offsets in quantum wells using only spectroscopic data," *J. Appl. Phys.,* vol. 73, pp. 8480-8484, 1993.

[128] W. Z. Shen, W. G. Tang, S. C. Shen, S. M. Wang and T. Andersson, "Absorption spectroscopy studies

of strained InGaAs/GaAs singlequantum wells," *Appl. Phys. Lett.,* vol. 65, p. 2728, 1994.

[129] B. Galiana, I. Rey-Stolle, I. Beinik, C. Algora, C. Teichert, J. M. Molina-Aldareguia and P. Tejedor, "Characterization of antiphase domains on GaAs grown on Ge substrates by conductive atomic force microscopy for photovoltaic applications," *Sol. Energy. Mater. Sol. Cells,* vol. 95, pp. 1949-1954, 2011.

[130] S. K. Agarwal, R. Tyagi, M. Singh and R. K. Jain, "Effect of growth parameters on the MOVPE of GaAs/Ge for solar cell applications," *Sol. Energy. Mater. Sol. Cells,* vol. 59, pp. 19-26, 1999.

[131] P. H. Wu, Y. K. Su, I. L. Chen, S. F. Chen, C. H. Chiou, S. H. Guo, J. T. Hsu and W. R. Chen, "Research of surface morphology in Ga(In)As epilayers on Ge grown by MOVPE for multi-junction solar cells," *J. Cryst. Growth,* vol. 298, pp. 767-771, 2007.

[132] H. Kroemer, "Polar on Nonpolar Epitaxy," *J. Cryst. Growth,* vol. 81, pp. 193-204, 1987.

[133] Y. Li and L. J. Giling, "A closer study on the self-annihilation of antiphase boundaries in GaAs epilayers," *J. Cryst. Growth,* vol. 163, pp. 203-211, 1996.

[134] D. B. Holt, "Antiphase boundaries in semiconducting compounds," *J. Cryst. Growth,* vol. 30, pp. 1297-1308, 1969.

[135] P. M. Petroff, "Nucleation and growth of GaAs on Ge and the structure of antiphase boundaries," *J. Vac. Sci. Technol. B,* vol. 4, pp. 874-877, 1986.

[136] S. N. G. Chu, S. Nakahara, S. J. Pearton, T. Boone and S. M. Vernon, "Antiphase domains in GaAs grown by metalorganic chemical vapor deposition on silicon‐on‐insulator," *J. Appl. Phys.,* vol. 64, pp. 2981-2989, 1988.

[137] L. Lazzarini, L. Nasi, G. Salviati, C. Z. Fregonara, C. Z. Li, L. J. Giling, C. Hardingham and D. B. Holt, "Antiphase disorder in GaAs/Ge heterostructures for solar cells," *Micron,* vol. 31, pp. 217-222, 2001.

[138] O. Ueda, M. Takikawa, J. Komeno and I. Umebu, "Atomic structure of ordered InGaP crystals grown on (001) GaAs substrates by metalorganic chamical vapor deposition," *Jpn. J. Appl. Phys.,* vol. 26, pp. L1824-L1827, 1987.

[139] T. Suzuki, A. Gomyo, S. Iijima, K. Kobayashi, S. Kawata, I. Hino and T. Yuasa, "Band-gap energy anomaly and sublattice ordering in GaInP and AlGaInP grown by metalorganic vapor phase epitaxy," *Jpn. J. Appl. Phys.,* vol. 27, pp. 2098-2106, 1988.

[140] L. C. Su, I. H. Ho and G. B. Stringfellow, "Effects of substrate misorientation and growth rate on ordering in GaInP," *J. Appl. Phys.,* vol. 75, pp. 5135-5141, 1994.

[141] N. Liu, C. K. Shih, J. Geisz, A. Mascarenhas and J. M. Olson, "Alloy ordering in GaInP alloys: A cross-sectional scanning tunneling microscopy study," *Appl. Phys. Lett.,* vol. 73, pp. 1979-1981, 1998.

[142] H. Murata, S. H. Lee, I. H. Ho and G. B. Stringfellow, "Correlation between surface structure and

ordering in GaInP," *J. Vac. Sci. Technol. B,* vol. 14, pp. 3013-3018, 1996.

[143] N. Y. Jin-Phillipp, F. Phillipp, T. Marschner and W. Stolz, "Thickness modulation in symmetrically strained III–V semiconductor superlattices grown by MOVPE," *J. Mater. Sci. Mater. Electron.,* vol. 8, pp. 289-299, 1997.

[144] C. Giannini, L. Tapfer, Y. Zhuang, L. D. Caro, T. Marschner and W. Stolz, "Structural ordering and interface morphology in symmetrically strained (GaIn)As/Ga(PAs) superlattices grown on off-oriented GaAs (100)," *Phys. Rev. B,* vol. 55, pp. 5276-5283, 1997.

[145] C. Giannini, T. Baumbach, D. Lübbert, R. Felici, L. Tapfer, T. Marschner, W. Stolz, N. Y. Jin-Phillipp and F. Phillipp, "Strain-driven transition from stepped interfaces to regularly spaced macrosteps in (GaIn)As/Ga(PAs) symmetrically strained superlattices," *Phys. Rev. B,* vol. 61, pp. 2173-2179, 2000.

[146] S. A. Chalmers, J. Y. Tsao and A. C. Gossard, "Terrace width evolution during stepflow growth with multiterrace adatom," *J. Appl. Phys.,* vol. 73, pp. 7351-7357, 1993.

[147] S. V. Ghaisas and S. D. Sarma, "Surface diffusion length under kinetic growth conditions," *Phys. Rev. B,* vol. 46, pp. 7308-7311, 1992.

[148] M. Pristovsek, M. Zorn and M. Weyers, "In situ study of GaAs growth mechanisms using tri-methyl gallium and tri-ethyl gallium precursors in metal-organic vapour phasee pitaxy," *J. Cryst. Growth,* vol. 262, pp. 78-83, 2004.

[149] C. Plass, H. Heinecke, O. Kayser, H. Lüth and P. Balk, "A Comparative Study of Ga(CH3)3, Ga(C2H5)3 and Ga(C4H9)3 in the Low Pressure MOCVD of GaAs," *J. Cryst. Growth,* vol. 88, pp. 455-464, 1988.

[150] H. Sakaguchi, T. Mishima, T. Meguro and Y. Fujiwara, "Low-temperature growth of GaAs with high quality by metalorganic vapor phase epitaxy," *J. Phys. Conf. Ser.,* vol. 165, pp. 012024_1-012024_4, 2009.

[151] M. Kondo and T. Tanahashi, "Dependence of carbon incorporation on crystallographic orientation during metalorganic vapor phase epitaxy of GaAs and AlGaAs," *J. Cryst. Growth,* pp. 390-396, 1994.

[152] N. Kobayashi and T. Makimoto, "Reduced carbon contamination in OMVPE grown GaAs and AlGaAs," *Jpn. J. Appl. Phys.,* vol. 24, pp. L824-L826, 1985.

[153] T. F. Kuech and R. Potemski, "Reduction of background doping in metalorganic vapor phase epitaxy of GaAs using triethylgallium at low reactor pressure," *Appl. Phys. Lett.,* vol. 47, pp. 821-823, 1985.

[154] R. R. King, D. Bhusari, A. Boca, D. Larrabee, X. Q. Liu, W. Hong, C. M. Fetzer, D. C. Law and N. H. Karam, "Band gap-voltage offset and energy production in next-generation multijunction solar cells," *Prog. Photovolt. Res. Appl.,* vol. 19, pp. 797-812, 2011.

Publication list

(1) Journal Papers

First author

[1] <u>H. Fujii</u>, Y. Wang, K. Watanabe, M. Sugiyama, and Y. Nakano, "Suppressed lattice relaxation during InGaAs/GaAsP MQW growth with InGaAs and GaAs ultra-thin interlayers", *Journal of Crystal Growth,* **352** (2012) 239-244.

[2] <u>H. Fujii,</u> K. Watanabe, M. Sugiyama, and Y. Nakano, "Effect of Quantum Well on the Efficiency of Carrier Collection in InGaAs/GaAsP Multiple Quantum Well Solar Cells", *Japanese Journal of Applied Physics*, **51** (2012) 10ND04.

[3] <u>H. Fujii</u>, Y. Wang, K. Watanabe, M. Sugiyama, and Y. Nakano, "High-Aspect Ratio Structures for Efficient Light Absorption and Carrier Transport in InGaAs/GaAsP Multiple Quantum-Well Solar Cells", *IEEE Journal of Photovoltaics*, **3** (2013) 859-867.

[4] <u>H. Fujii</u>, Y. Wang, K. Watanabe, M. Sugiyama, and Y. Nakano, "Compensation doping in InGaAs/GaAsP multiple quantum well solar cells for efficient carrier transport and improved cell performance", *Journal of Applied Physics*, **114** (2013) 103101.

[5] <u>H. Fujii</u>, K. Toprasertpong, K. Watanabe, and M. Sugiyama, "Evaluation of Carrier Collection Efficiency in Multiple Quantum Well Solar Cells", *IEEE Journal of Photovoltaics*, **4** (2014) 237-243.

[6] <u>H. Fujii</u>, K. Toprasertpong, Y. Wang, K. Watanabe, M. Sugiyama, Y. Nakano, "100-period, 1.23-eV bandgap InGaAs/GaAsP quantum wells for high-efficiency GaAs solar cells: toward current-matched Ge-based tandem cells", *Progress in Photovoltaics: Research and Applications*, **22** (2014) 784-795.

[7] <u>H. Fujii</u>, H. Sodabanlu, M. Sugiyama, and Y. Nakano, "Low-temperature MOVPE using TEGa for suppressed layer undulation in InGaAs/GaAsP superlattice on vicinal substrates", *Journal of Crystal Growth*, http://dx.doi.org/10.1016/j.jcrysgro.2014.10.043 (in press)

[8] <u>H. Fujii</u>, Y. Wang, H. Sodabanlu, K. Watanabe, M. Sugiyama, and Y. Nakano, "InGaAs/GaAsP superlattice solar cells with reduced carbon impurity grown by low-temperature metal-organic vapor phase epitaxy using triethylgallium", *Joural of Applied Physics* **116** (2014) 203101.

[9] <u>H. Fujii</u>, K. Toprasertpong, H. Sodabanlu, K. Watanabe, M. Sugiyama, and Y. Nakano, "Thickness modulated InGaAs/GaAsP superlattice solar cells on vicinal substrates", *Journal of Applied Physics* (under review).

Co-author

[1] M. Sugiyama, Y. Wang, <u>H. Fujii</u>, H. Sodabanlu, K. Watanabe and Y. Nakano, "A quantum-well superlattice solar cell for enhanced current output and minimized drop in open-circuit voltage under

sunlight concentration", Journal of Physics D: Applied Physics 46 (2013) 1-11.

[2] L.C. Hirst, <u>H. Fujii</u>, Y. Wang, M. Sugiyama, and N. J. Ekins-Daukes, "Hot Carriers in Quantum Wells for Photovoltaic Efficiency Enhancement", *IEEE Journal of Photovoltaics*, **4** (2014) 244-252.

[3] K. Toprasertpong, <u>H. Fujii</u>, Y. Wang, K. Watanabe, M. Sugiyama, and Y. Nakano, "Carrier Escape Time and Temperature-Dependent Carrier Collection Efficiency of Tunneling-Enhanced Multiple Quantum Well Solar Cells", *IEEE Journal of Photovoltaics*, **4** (2014) 607-613.

[4] A. Fukuyama, T. Aihara, Y. Yokoyama, M. Kojima, <u>H. Fujii</u>, H. Suzuki, M. Sugiyama, Y. Nakano, and T. Ikari, "Effect of internal electric field on non-radiative carrier recombination in the strain-balanced InGaAs/GaAsP multiple quantum well solar cells", *Physica Status Solidi A* **211** (2014) 444-448.

[5] D. Alonso-Álvarez, T. Thomas, M. Führer, N. P. Hylton, N. J. Ekins-Daukes, D. Lackner, S. P. Philipps, A. W. Bett, H. Sodabanlu, H. Fujii, K. Watanabe, M. Sugiyama, L. Nasi and M. Campanini, "InGaAs/GaAsP strain balanced multi-quantum wires grown on misoriented GaAs substrates for high efficiency solar cells", *Applied Physics Letters* **105** (2014) 083124.

[6] K. Toprasertpong, N. Kasamatsu, <u>H. Fujii</u>, T. Kada, S. Asahi, Y. Wang, K.Watanabe, M. Sugiyama, T. Kita, and Y. Nakano, "Carrier Time-of-Flight Measurement Using a Probe Structure for Direct Evaluation of Carrier Transport in Multiple Quantum Well Solar Cells", *IEEE Journal of Photovoltaics*, **4** (2014) 1518-1525.

[7] K. Toprasertpong, H. Fujii, T. Thomas, M. Führer, D. Alonso-Álvarez, D.J. Farrell, K. Watanabe, Y. Okada, N.J. Ekins-Daukes, M. Sugiyama, and Y. Nakano, "Absorption Threshold Extended to 1.15 eV Using InGaAs/GaAsP Quantum Wells for Over-50%-efficient Lattice-matched Quad-junction Solar Cells", *Progress in Photovoltaics: Research and Applications* (in press).

[8] W. Yanwachirakul, H. Fujii, K. Toprasertpong, K. Watanabe, M. Sugiyama, and Y. Nakano, "Effect of Barrier Thickness on Carrier Transport inside Multiple Quantum Well Solar Cells under High-concentration Illumination", *IEEE Journal of Photovoltaics* (in press).

(2) Conferences

(2-1) International conferences

First author

[1] <u>H. Fujii</u>, Y. Wang, Y. Nakano and M. Sugiyama, "Effects of Quantum Wells Position and Background Doping on the Performance of Multiple Quantum Well Solar Cells", 37th IEEE Photovoltaic Specialist Conference, A16-737, Seattle, June., 2011.

[2] <u>H. Fujii</u>, Y. Wang, K. Watanabe, M. Sugiyama and Y. Nakano, "Effects of Increasing Well Number on Carrier Transport in Eg = 1.2 eV InGaAs / GaAsP Multiple Quantum Well Solar Cells", 21st International Photovoltaic Science and Engineering Conference, 2B-4O-06, Fukuoka, December. 2011.

[3] H. Fujii, Y. Wang, K. Watanabe, M. Sugiyama and Y. Nakano, "A Large Number Stack of Eg = 1.2 eV InGaAs / GaAsP Multiple Quantum Wells with Graded Buffer Layers for Enhanced Infrared Response", 21st International Photovoltaic Science and Engineering Conference, 2D-4P-13, Fukuoka, December. 2011.

[4] H. Fujii, Y. Wang, K. Watanabe, M. Sugiyama, and Y. Nakano, "Doping-Compensation for Efficient Carrier Transport in InGaAs/GaAsP Multiple Quantum Well Solar Cells", 16th International Conference on Metal Organic Vapor Phase Epitaxy, WeA3-3, Busan, 2012.

[5] H. Fujii, Y. Wang, K. Watanabe, M. Sugiyama, and Y. Nakano, "High-aspect-ratio Structures for Efficient Light Absorption and Carrier Transport in InGaAs/GaAsP Multiple Quantum Well Solar Cells", 38th IEEE Photovoltaic Specialist Conference, Austin, 2012.

[6] H. Fujii, Y. Wang, K. Watanabe, M. Sugiyama, and Y. Nakano, "Enhanced Carrier Collection Efficiency in InGaAs/GaAsP Quantum Well Solar Cells by Compensation Doping", 27th European Photovoltaic Solar Energy Conference, 1AO.7.2, Frankfurt, 2012.

[7] H. Fujii, Y. Wang, K. Watanabe, M. Sugiyama, Y. Nakano "Carrier collection efficiency in multiple quantum well solar cells", SPIE Conference 8620, Physics, Simulation, and Photonic Engineering of Photovoltaic Devices II, 8620-52, San Francisco, 2013.

[8] H. Fujii, K. Toprasertpong, K. Watanabe, M. Sugiyama, Y. Nakano, "Comprehensive Validation of Carrier Collection Efficiency in Multiple Quantum Well Solar Cells: For More Effective and Direct Evaluation of Carrier Transport Dynamics", 39th Photovoltaic Specialist Conference, Tampa, 2013 .

[9] H. Fujii, K. Toprasertpong, Y. Wang, K. Watanabe, M. Sugiyama, and Y. Nakano, "Structure optimization of 1.23 eV bandgap InGaAs/GaAsP quantum wells in GaAs single junction solar cells for absolute efficiency enhancement", 2013 JSAP-MRS Joint Symposia, 18a-M2-6, Kyoto, 2013 (Oral).

[10] H. Fujii, K. Toprasertpong, K. Watanabe, M. Sugiyama, and Y. Nakano, "100-period, 1.23 eV Bandgap InGaAs / GaAsP Quantum Wells for Efficiency-enhanced GaAs Solar Cells: Toward Current-matched Ge-based Tandem Cells", 28th European Photovoltaic Solar Energy Conference, 1DO.4.4, Paris, 2013.

[11] H. Fujii, H. Sodabanlu, Y. Wang, K. Watanabe, "In-situ reflectance monitoring in MOVPE growth of InGaAs/GaAsP superlattice on misoriented GaAs substrate", 23rd International Photovoltaic Science and Engineering Conference, 4-O-14, Taipei, 2013.

[12] H. Fujii, H. Sodabanlu, M. Sugiyama, and Y. Nakano, "Ga precursor dependent growth of InGaAs/GaAsP strain-balanced quantum wells on 6°-off substrate", 17th International Conference on Metal Organic Vapor Phase Epitaxy, Lausanne, 2014.

[13] H. Fujii, K. Toprasertpong, H. Sodabanlu, K. Watanabe, M. Sugiyama, and Y. Nakano, "InGaAs/GaAsP Superlattice Solar Cells on Vicinal Substrates for Current-matched Triple Junction Cells on Ge", 29th European Photovoltaic Solar Energy Conference, 4BO.10.1, Amsterdam, 2014.

[14] H. Fujii, K. Toprasertpong, H. Sodabanlu, K. Watanabe, M. Sugiyama, and Y. Nakano, "1.2 eV bandgap InGaAs/GaAsP superlattice solar cells on vicinal substrates for current-matched Ge-based triple junction cells", 7th International Symposium on Innovative Solar Cells, R-19, Tokyo, 2015.

Co-author

[1] M. Sugiyama, Y. Wang, H. Sodabanlu, S. Ma, H. Fujii, K. Watanabe, and Y. Nakano: "Optical in situ monitoring of strain evolution and relaxation in lattice-mismatched InGaAs/GaAsP multiple quantum wells by MOVPE", 15th U.S. Biennal Workshop on Organometallic Vapor Phase Epitaxy, Monterey, California, 2011.

[2] Y. Wang, K. Watanabe, H. Fujii, S. Ma, M. Sugiyama, and Y. Nakano: "Carrier transport through super-lattice region in a multiple quantum well solar cell", Technical Digest of 21st International Photovoltaic Science and Engineering Conference (PVSEC-21), 4D-4P-07, Fukuoka, Japan, 2011.

[3] M. Sugiyama, Y. Wang, H. Sodabanlu, S. Ma, H. Fujii, K. Watanabe, and Y. Nakano: "Defect management in III-V nanostructure solar cells for higher efficiency by strain control based on in situ monitoring of MOVPE", 2012 MRS Spring Meeting & Exhibit, G11.1, San Francisco, 2012.

[4] A. Fukuyama, Y. Nakano, T. Aihara, H. Fujii, M. Sugiyama, Y. Nakano, and T. Ikari, "Non-radiative carrier recombination mechanism in the InGaAs/GaAsP strain-balanced quantum well solar cells with different number of stacks by using a piezoelectric photothermal method", 8th International Conference on Concentrating Photovoltaic Systems, Toledo, 2012.

[5] L.C. Hirst, M. Fürher, D.J. Farrell, A.L. Bris, J.F. Guillemoles, M.J.Y. Tayebjee, R. Clady, T.W. Schmidt, M. Sugiyama, Y. Wang, H. Fujii, N. J. Ekins-Daukes, "InGaAs/GaAsP quantum wells for hot carrier solar cells", SPIE Photonics West 2013, 82560X, San Francisco, 2012.

[6] M. Sugiyama, Y. Wang, H. Fujii, H. Sodabanlu, Y. Wen, K. Watanabe, Y. Nakano, "Exploring the potential of quantum wells for efficiency enhancement in photovoltaic cells", SPIE Photonics West 2013, 82560D, San Francisco, 2012.

[7] M. Sugiyama, H. Fujii, Y. Wen, Y. Wang, "InGaAs/GaAsP quantum-well superlattice solar cell for better carrier collection and higher efficiency", 2012 Conference on Optoelectronic and Microelectronic Materials & Devices, Melbourne, 2012.

[8] Y. Wang, H. Sodabanlu, S. Ma, H. Fujii, K. Watanabe, M. Sugiyama, and Y. Nakano, "A Multi-step superlattice solar cell with enhanced subband absorption and open circuit voltage", 38th Photovoltaic Specialist Conference, Austin, 2012.

[9] Y. Wang, K. Watanabe, H. Fujii, H. Sodabanlu, M. Sugiyama, and Y. Nakano: "Observation of a strong open-circuit voltage enhancement in a super-lattice solar cell under concentration: a potential scenario for a high efficiency single junction cell", 27th European Photovoltaic Solar Energy Conference and Exhibition (EU PVSEC 27), Frankfurt, 2012.

[10] Y. Wang, S. Ma, H. Sodabanlu, H. Fujii, K. Watanabe, M. Sugiyama, and Y. Nakano: "Smart interface management to implement a high quality strain balanced super-lattice solar cell", 22nd International Photovoltaic Science and Engineering Conference (PVSEC-22), Hangzhou, 2012

[11] K. Watanabe, K. Toprasertpong, H. Fujii, H. Sodabanlu, M. Sugiyama, and Y. Nakano "Temperature-dependent photoluminescence analysis for InGaAs/GaAsP multiple quantum wells solar cell", 22nd International Photovoltaic Science and Engineering Conference (PVSEC-22), Hangzhou,

2012.

[12] M. Sugiyama, K. Watanabe, Y. Wang, H. Sodabanlu, H. Fujii, B. Kim, K. Miyano, and Y. Nakano "Efficiency gain of quantum-well solar cells by light-trapping structure and sunlight concentration", SPIE Conference 8620, Physics, Simulation, and Photonic Engineering of Photovoltaic Devices II, 8620-48, 2013.

[13] Y. Wang, H. Fujii, H. Sodabanlu, K. Watanabe, M. Sugiyama and Y. Nakano, "Investigation on the role of inserted ultra-thin GaAs layer in a strain balanced superlattice solar cell", 2013 JSAP-MRS Joint Symposia, 18a-M2-8, Kyoto, 2013.

[14] M. Sugiyama, K. Watanabe, Y. Wang, H. Sodabanlu, H. Fujii and Y. Nakano, "Can quantum wells provide efficiency gain for a single-junction cell?", 2013 JSAP-MRS Joint Symposia, 18a-M2-4, Kyoto, 2013.

[15] K. Toprasertpong, H. Fujii, Y. Wang, K. Watanabe, M. Sugiyama, and Y. Nakano, "Carrier Escape Time and Temperature-Dependent Carrier Collection Efficiency of Tunneling-Enhanced Multiple Quantum Well Solar Cells", 39th Photovoltaic Specialist Conference, Tampa, 2013.

[16] Y. Wang, K. Watanabe, H. Sodabanlu, S. Ma, H. Fujii, M. Sugiyama, and Y. Nakano, "A superlattice solar cell for enhanced current output and minimized drop in open-circuit voltage under sunlight concentration", 39th Photovoltaic Specialist Conference, Tampa, 2013.

[17] K. Toprasertpong, H. Fujii, Y. Wang, K. Watanabe, M. Sugiyama and Y. Nakano, "Carrier Collection Enhancement by Barrier Design in InGaAs/GaAsP Strain-Balanced Quantum Well Solar Cells", 2013 JSAP-MRS Joint Symposia, 18a-M2-7, Kyoto, 2013.

[18] Y. Wang, H. Sodabanlu, H. Fujii, K. Toprasertpong, K. Watanabe, M. Sugiyama, Y. Nakano, "Management of GaAsP related hetero-interface in strain-balanced MQWs solar cells", 23rd International Photovoltaic Science and Engineering Conference, Taipei, 2013.

[19] K. Toprasertpong, H. Fujii, Y. Wang, K. Watanabe, M. Sugiyama and Y. Nakano, "Thermionic Behavior of Carrier Transport in InGaAs/GaAsP Multiple Quantum Well Solar Cells", 23rd International Photovoltaic Science and Engineering Conference, Taipei, 2013

[20] Y. Wang, K. Watanabe, H. Sodabanlu, S. Ma, H. Fujii, K. Toprasertpong, M. Sugiyama, and Y. Nakano "Superlattice cell under sunlight concentration", 5th International Symposium on Innovative Solar Cells, Tsukuba, Japan, 2013.

[21] K. Toprasertpong, N. Kasamatsu, H. Fujii, T. Kada, S. Asahi, Y. Wang, K. Watanabe, M. Sugiyama, T. Kita, Y. Nakano, "Carrier Time-of-Flight Measurement Using a Probe Structure for Direct Evaluation of Carrier Transport in Quantum Structure Solar Cells", 40th Photovoltaic Specialist Conference, Denver, 2014

[22] W. Yanwachirakul, H. Fujii, K. Watanabe, M. Sugiyama, Y. Nakano, "Effect of Barrier Thickness on Carrier Transport inside Multiple Quantum Well Solar Cells under High-concentration Light Illumination", 40th Photovoltaic Specialist Conference, Denver, 2014.

[23] K. Toprasertpong, H. Fujii, M. Führer, D. Alonso-Álvarez, D.J. Farrell, K.Watanabe, Y. Okada, N.J. Ekins-Daukes, M. Sugiyama, and Y. Nakano, "Absorption Threshold Extended to 1.15 eV Using

InGaAs/GaAsP Quantum Wells for Over-50%-efficient Lattice-matched Quad-junction Solar Cells" 29th European Photovoltaic Solar Energy Conference, Amsterdam, 2014

[24] Y. Wang, H. Sodabanlu, <u>H. Fujii</u>, K. Toprasertpong, K. Watanabe, M. Sugiyama and Y. Nakano, "Influence of barrier thickness and potential of barrier on carrier extraction mechanism for strain balanced MQWs (InGaAs/GaAsP) solar cell", 29th European Photovoltaic Solar Energy Conference, Amsterdam, 2014.

[25] W. Yanwachirakul, K. Toprasertpong, <u>H. Fujii</u>, K. Watanabe, M. Sugiyama, and Y. Nakano, "Open-circuit voltage behavior in multiple quantum well solar cells with different barrier thickness illuminated under high concentrated sunlight", The 6th World Conference on Photovoltaic Energy Conversion, Kyoto, 2014.

[26] Y. Wang, H. Sodabanlu, <u>H. Fujii</u>, K. Toprasertpong, K. Watanabe, M. Sugiyama and Y. Nakano, "InGaP-based multiple-quantum-well solar cell fabricated using metal-organic-vapor-phase- epitaxy", The 6th World Conference on Photovoltaic Energy Conversion, Kyoto, 2014.

(2-2) Domestic conferences

First author

[1] <u>藤井宏昌</u>，王云鵬，杉山正和，中野義昭，「GaAs / InGaAs 緩衝層を用いた InGaAs / GaAsP 多重量子井戸の成長」，第 72 回応用物理学会秋季学術講演会，31a-ZA-14，山形，2011.

[2] <u>H. Fujii</u>, Y. Wang, Y. Nakano, and M. Sugiyama, "Effects of Quantum Wells Position on Carrier Transport in Multiple Quantum Well Solar Cells with P-type Background Doping", 第 30 回電子材料シンポジウム，Th1-5，滋賀，2011.

[3] <u>藤井宏昌</u>，渡邉健太郎，杉山正和，中野義明，「補償ドーピングによる InGaAs/GaAsP 量子井戸太陽電池のキャリア回収効率向上」，第 59 回応用物理学会春季学術講演会，18a-C1-5，東京，2012.

[4] <u>藤井宏昌</u>，王云鵬，渡辺健太郎，杉山正和，中野義昭，「（講演奨励賞受賞記念講演）InGaAs/GaAsP 量子井戸太陽電池におけるバックグラウンドドーピングの影響」，第 73 回応用物理学会秋季学術講演会，12a-HB-1，松山，2012.

[5] <u>藤井宏昌</u>，杉山正和，王云鵬，渡辺健太郎，中野義昭「補償ドーピングによる InGaAs/GaAsP 量子井戸太陽電池のキャリア回収効率向上」，第 44 回化学工学会秋季大会，G217，仙台，2012

[6] <u>藤井宏昌</u>，トープラサートポン・カシディット，渡辺健太郎，杉山正和，中野義昭，「量子井戸太陽電池におけるキャリア回収効率の妥当性検証」，第 60 回応用物理学会春季学術講演会，29a-G4-4，厚木，2013

[7] <u>H. Fujii</u>, K. Toprasertpong, K. Watanabe, M. Sugiyama, and Y. Nakano, "Efficiency enhancement of GaAs solar cells with 100-period InGaAs/GaAsP quantum wells with a bandgap of 1.23 eV", 32nd Electronic Materials Symposium, Th5-3, 滋賀, 2013

[8] <u>藤井 宏昌</u>，王 云鵬，ソダーバンル ハッサネット，渡辺 健太郎，杉山 正和，中野 義昭「微

傾斜基板上 InGaAs/GaAsP 超格子太陽電池の作製」，第 61 回応用物理学会春季学術講演会，18p-PG4-3，相模原，2014

[9] 藤井 宏昌, 王 云鵬, ソダーバンル ハッサネット, 渡辺 健太郎, 杉山 正和, 中野 義昭「TEGa を用いた低温 MOVPE による微傾斜基板上 InGaAs/GaAsP 超格子太陽電池」，第 75 回応用物理学会秋季学術講演会，19a-S1-2，札幌，2014

Co-author

[1] トープラサートポン カシディット，藤井 宏昌，渡辺 健太郎，杉山 正和，中野 義昭，「InGaAs/GaAsP 量子井戸太陽電池における障壁層厚さがキャリア脱出に与える影響」第 60 回応用物理学会春季学術講演会，29a-G4-5，厚木，2013

[2] 王 雲鵬，藤井宏昌，ソダーバンル ハッサネット，渡辺健太郎，杉山正和，中野義昭，「InGaAs/GaAsP 歪み補償超格子セルにおけるヘテロ界面処理」，第 60 回応用物理学会春季学術講演会，29a-G4-8，厚木，2013

[3] K. Toprasertpong, H. Fujii, Y. Wang, K. Watanabe, M. Sugiyama, and Y. Nakano, "Carrier Transport in Tunneling-Enhanced Multiple Quantum Well Solar Cells", 32nd Electronic Materials Symposium, 滋賀, 2013.

[4] トープラサートポン カシディット，笠松直史，藤井宏昌，加田智之，朝日重雄，王云鵬，渡辺健太郎，杉山正和，喜多隆，中野義昭，「プローブ構造を用いた量子構造太陽電池におけるキャリア走行時間の測定」第 61 回応用物理学会春季学術講演会，18p-D7-11，相模原，2014

[5] ヤンワチラーコン ワラーコン，藤井宏昌，渡辺健太郎，杉山正和，中野義昭，「高倍集光下の多重量子井戸太陽電池におけるキャリア輪送評価」第 61 回応用物理学会春季学術講演会，18p-D7-18，相模原，2014

[6] K. Toprasertpong, N. Kasamatsu, H. Fujii, T. Kada, S. Asahi, Y. Wang, K. Watanabe, M. Sugiyama, T. Kita, and Y. Nakano, "Carrier Time-of-Flight Measurement for Evaluating Carrier Collection in Quantum Well Solar Cells", 33nd Electronic Materials Symposium, 静岡, 2013.

(3) Awards

[1] Student Paper Award, 21st International Photovoltaic Science and Engineering Conference, Fukuoka, 12/2/2011.

[2] Best Student Presentation Award, 38th Photovoltaic Specialist Conference, Austin, 6/8/2012.

[3] Young Scientist Presentation Award, 73rd JSAP (Japan Society of Applied Physics) Autumn Meeting (応用物理学会講演奨励賞), 9/11/2012.

[4] Student Award, 28th European Photovoltaic Solar Energy Conference, Paris, 10/3/2013.

Acknowledgements

<div align="right">

December 1, 2014

Hiromasa Fujii

藤井 宏昌

</div>